



HAL
open science

Applications and development of acoustic and microwave atomic force microscopy for high resolution tomography analysis

Pauline Vitry

► **To cite this version:**

Pauline Vitry. Applications and development of acoustic and microwave atomic force microscopy for high resolution tomography analysis. Physics [physics]. Université de Bourgogne, 2016. English. NNT : 2016DIJOS046 . tel-01635664

HAL Id: tel-01635664

<https://theses.hal.science/tel-01635664v1>

Submitted on 15 Nov 2017

HAL is a multi-disciplinary open access archive for the deposit and dissemination of scientific research documents, whether they are published or not. The documents may come from teaching and research institutions in France or abroad, or from public or private research centers.

L'archive ouverte pluridisciplinaire **HAL**, est destinée au dépôt et à la diffusion de documents scientifiques de niveau recherche, publiés ou non, émanant des établissements d'enseignement et de recherche français ou étrangers, des laboratoires publics ou privés.

UNIVERSITE DE BOURGOGNE FRANCHE-COMTE

FACULTE DES SCIENCES

Laboratoire Interdisciplinaire Carnot de Bourgogne UMR CNRS 6303

Département Nanosciences

APPLICATIONS AND DEVELOPMENT OF ACOUSTIC
AND MICROWAVE ATOMIC FORCE MICROSCOPY
FOR HIGH RESOLUTION TOMOGRAPHY ANALYSIS

Thèse présentée à l'Université de Bourgogne Franche-Comté

pour obtenir le grade de Docteur (Mention Physique)

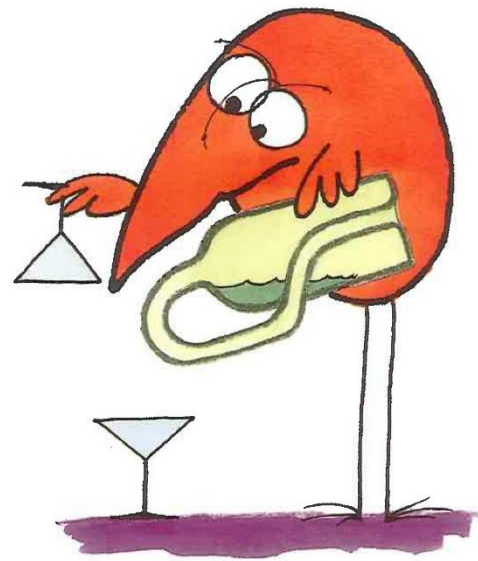
par

Pauline VITRY

Soutenue publiquement le 10 juin 2016 devant la commission d'examen composée de :

Milhet P.E.	Directeur de recherche CNRS, CBS Montpellier	Rapporteur
François M.	Professeur, Univ. Technologique de Troyes	Rapporteur
Dereux A.	Professeur, Univ. de Bourgogne	Examineur
Tetard L.	Assistant Professor, Univ. of Central Florida	Examineur
Virolle M-J.	Directeur de recherches, Univ. Paris Sud	Examineur
Bourillot E.	Maitre de conférences, Univ. de Bourgogne	Co-encadrant de thèse
Lesniewska E.	Professeur, Univ. de Bourgogne	Directeur de thèse

« En essayant continuellement on finit par réussir. Donc : plus ça rate, plus on a de chance que ça marche. »



S'IL N'Y A PAS DE SOLUTION
C'EST QU'IL N'Y A PAS DE PROBLÈME.

Remerciements

L'aboutissement de ces années de thèse a pu être possible grâce aux nombreuses personnes qui y ont contribué que ce soit scientifiquement ou personnellement.

Cette thèse a été réalisée au sein de l'équipe Optique Submicronique et Nano-capteurs (UMR CNRS 6303) du laboratoire Interdisciplinaire Carnot de Bourgogne (ICB). Je remercie le Pr. Alain Dereux, directeur du laboratoire, de m'y avoir accueilli durant ces années.

Un grand merci à mes directeurs de thèse que sont le Pr. Eric Lesniewska et le Dr. Eric Bourillot de m'avoir donné le goût de la recherche et permis de m'épanouir dans mon travail. Merci pour vos enseignements, votre patience, votre gentillesse et la confiance que vous m'avez accordée.

J'exprime toute ma gratitude à Monsieur Pierre-Emmanuel Milhiet, Directeur de Recherche au Centre de Biochimie Structurale de Montpellier ainsi qu'à Monsieur Manuel François, Professeur à l'Institut Charles Delaunay de l'Université de technologie de Troyes qui ont accepté de rapporter mon travail de thèse.

Merci à Monsieur Alain Dereux, Professeur à l'Université de Bourgogne d'avoir présidé mon jury de thèse et d'avoir examiné mon travail avec Madame Laurène Tétard, Assistant Professor au Nanoscience Technology Center de l'Université Centrale de Floride et Madame Marie-Joëlle Virolle, Directeur de recherches au laboratoire de Chimie Physique de l'Université Paris Sud d'Orsay.

Durant ces 5 années (stages et thèse réunis) j'ai eu l'occasion de rencontrer des personnes marquantes que je tiens à remercier plus personnellement.

Eric, j'ai passé des années riches en émotions avec vous deux. Outre le domaine professionnel je tiens ici à vous remercier pour les qualités humaines dont vous avez fait preuve.

« Riké », vous qui ne tremblez pas face à un alligator croisé sur une route de Floride, je tiens à vous remercier pour votre gentillesse et les bons moments passés ensemble (Grand-huit, Restos et Laser Games entre collègues).

Eric B, vous avez été sur tous les fronts: parties de badminton, taxi, voyage nocturne aux urgences et interprétations scientifiques aiguisées.

Merci et Merci !

Laurène et Cisco, merci de m'avoir accueilli à bras ouverts chez vous en Floride. J'espère que nous aurons encore plein d'autres occasions de se voir. Docteur Laurène, je me souviendrai des excellents moments de travail, discussions, visites et divertissements ainsi que de ton aide si précieuse dans mon travail. Merci d'avoir pris le temps de m'enseigner et d'avoir su m'aider dans la rude tâche de la rédaction scientifique. On se refait une soirée galette des rois quand tu veux ! Merci pour tout !

Il fallait bien dans ces remerciements deux paragraphes distincts pour deux personnes particulièrement marquantes :

Elly, si c'est ton aversion du Gouda qui t'a poussé à venir en France alors je le remercie car sans lui je ne t'aurais jamais rencontré. Durant toutes ces années tu as toujours été à mon écoute, disponible, gentille et d'un grand soutien dans les moments difficiles (à l'occasion fournisseuse officielle de nouilles chinoises) : je remercie la maman du labo !

Yvon (le roi des échantillons), n'ayant jamais pu déterminer si vous pensiez tout ce que vous disiez je m'accorde le droit de supposer que nous sommes dans le même camp puisque nous avons la même définition de la sociabilité (A+ partout !) et que vous ne m'avez jamais posé un lapin au Campanile. Alors que je bascule du côté obscur de la frontière, j'espère que vous saurez faire la part des choses et me garder dans votre estime !

Cette thèse ne se serait certainement pas si bien passée sans toutes les personnes de l'équipe qui y ont contribué. Merci à vous tous ! à Gérard (le seul Breton toulousain que je connaisse), à Alex (merci de m'avoir toujours soutenu et encouragé dans mes réalisations culinaires – on s'appelle et on se fait une bouffe), à Aymeric, à Thierry avec une mention toute spéciale pour Kamel (merci pour ta gentillesse et ta disponibilité : je n'oublierai pas toutes nos discussions passionnantes. Tu as été mon sauveur sur *Comsol* et la porte de ton bureau ne m'a jamais été fermée. Je te souhaite tout le bonheur possible pour toi et ta petite famille et une bonne continuation dans ta carrière politique).

Pour continuer, je remercie de façon non exhaustive : Tony Montesin, Virgil Optasanu, Vincent Duquesne (pour l'opéra que tu ne nous as jamais apporté), Kanjer !! (fournisseur de mirabelle avec un grand sens de l'optimisme ;) Raphaël (le super collègue aux fameuses quatre consonnes et trois voyelles), Ece (pour ton amitié, ta gentillesse et tes gâteaux à la carotte inoubliables !), Cédric et Nicolas (mais oui vous êtes les plus beaux), Audrey, ainsi que David, Karim, Cédric P., Thomas B., Simon D. (tiens moi au courant dès que tu casses ton iPhone6 – on se verra peut-être en Belgique), Anne (ce fut trop court mais intense. Nous avons formé une équipe de choc (et de chic) et partagé bien plus que des fous rires), Marie et Brice (je vous souhaite plein de beaux projets à trois).

Pour terminer ces remerciements je dédierai le paragraphe suivant à ma famille et mes amis :

Mon plus vieil ami Sébastien (alias Seb) ainsi que les incroyables Laura, Elodie, Laetitia et Jiji.

Et évidemment, car je n'aurais jamais pu en arriver là sans eux, ma famille qui m'a toujours aimé et soutenu.

Mamie Tété et Papi Moujot: « des chercheurs qui cherchent on en trouve mais des chercheurs qui trouvent on en cherche ! » J'ai déjà trouvé le plus important : votre amour et votre soutien.

Je continue en embrassant Tonton, Sylvie, Maude, Alexis, Clément et Maeva. Merci à vous !

Une dédicace spéciale pour моя любовь Levon-Chmevon qui est toujours présent pour sa հունհունկ ;-)

Pour terminer, je remercie de tout cœur mes parents qui m'ont toujours soutenu et sans qui tout cela n'aurait jamais été possible. Merci de m'encourager et de m'aimer comme vous l'avez toujours fait. Merci maman de ton amour et soutien continuel ainsi que de tes conseils avisés.

Même si tu n'es plus là aujourd'hui Papa je sais que tu es fier de moi.

Résumé

La microscopie à force atomique (AFM) est un outil de caractérisation d'échantillons tant organiques qu'inorganiques d'intérêt en physique, en biologie et en métallurgie. Le champ d'investigation de la microscopie AFM reste néanmoins restreint à l'étude des propriétés surfaciques des échantillons et la caractérisation sub-surfacique à l'échelle nanométrique n'est pas envisageable au-delà de la nano-indentation. Lors de ce travail, nous nous sommes intéressés à deux techniques de sonde locale complémentaires pour l'investigation volumique haute résolution.

La première technique proposée est la microscopie de champ proche ultrasonore (MS-AFM), mise en place et exploitée en collaboration avec Dr. L. Tétard de l'Université Centrale de Floride. Cette technique fournit des informations localisées en profondeur en utilisant des ondes acoustiques dans la gamme de fréquences du MHz. Une étude complète de l'influence des paramètres de fréquences a été réalisée sur des échantillons de calibration et a permis de valider un modèle d'interprétation numérique. Cette technique ultrasonore, non invasive, a été appliquée à la caractérisation de vésicules lipidiques au sein de bactéries lors d'une collaboration avec les Pr. A. Dazzi et M.-J. Virolle, de l'Université Paris Sud Orsay. Un couplage a été réalisé avec la microscopie AFM infra-rouge (AFM-IR). Cette étude a démontré le potentiel d'investigation et d'analyse volumique et chimique d'échantillons biologiques.

La seconde technique étudiée est la microscopie micro-onde (SMM), développée en collaboration avec la société Keysight. Cette technique, tout comme la microscopie acoustique, est non invasive et conduit à une caractérisation physico-chimique basée sur l'interaction de micro-ondes (0.2-16 GHz) avec la matière. Dans le cas de métaux, un lien entre la fréquence et la profondeur d'investigation a été mis en évidence. Cette technique a été appliquée à l'étude de la diffusion d'élément chimique léger au sein de métaux et à la mesure des propriétés mécaniques des matériaux.

L'ensemble de ces résultats ouvre un nouveau champ d'investigation de la tomographie 3D dans l'analyse volumique à l'échelle nanométrique que ce soit dans le domaine de la biologie ou de la métallurgie.

Mots clés : Microscopie à force atomique (AFM), Microscopie à force atomique micro-onde (SMM), Microscopie à force atomique acoustique (MSAFM), tomographie et reconstruction 3D.

Abstract

The atomic force microscope (AFM) is a powerful tool for the characterization of organic and inorganic materials of interest in physics, biology and metallurgy. However, conventional scanning probe microscopy techniques are limited to the probing surface properties, while the subsurface analysis remains difficult beyond nanoindentation methods. Thus, the present thesis is focused on two novel complementary scanning probe techniques for high-resolution volumetric investigation that were developed to tackle this persisting challenge in nanometrology.

The first technique considered, called Mode Synthesizing Atomic Force Microscopy (MSAFM), has been exploited in collaboration with Dr. Laurene Tetard of University of Central Florida to explore the volume of materials with high spatial resolution by means of mechanical actuation of the tip and the sample with acoustic waves of frequencies in the MHz range. A comprehensive study of the impact of the frequency parameters on the performance of subsurface imaging has been conducted through the use of calibrated samples and led to the validation of a numerical model for quantitative interpretation. Furthermore, this non-invasive technique has been utilized to locate lipid vesicles inside bacteria (in collaboration with Pr. A. Dazzi and M.-J. Virolle of Université Paris Sud, Orsay). Furthermore, we have combined this ultrasonic approach with infra-red microscopy, to add chemical speciation aimed at identifying the subsurface features, which represents a great advance for volume and chemical characterization of biological samples.

The second technique considered is the Scanning Microwave Microscopy, which was developed in collaboration with Keysight society. Similar to acoustic-based microscopy, this non-invasive technique provided physical and chemical characterizations based on the interaction of micro-waves radiations with the matter (with frequency ranging from 0.2 and 16 GHz). Particularly, for metallic samples we performed volumetric characterization based on the skin effect of the materials. On the other hand, we have used this technique to analyze the diffusion of light chemical elements in metals and measured the effect of changes in mechanical properties of materials on their conductivity.

Overall, these results constitute a new line of research involving non-destructive subsurface high resolution analysis by means of the AFM of great potential for several fields of research.

Key words: Atomic force microscopy (AFM), Mode Synthesizing atomic force microscopy (MSAFM), Scanning microwave microscopy (SMM), tomography and 3D reconstruction.

Table des matières

General Introduction	2
Chapter 1 – <i>State of the Art</i>	7
1.1. Needs for having access to subsurface information	9
1.1.1. Current limitation in biology and life sciences	9
1.1.1.1. Health	9
1.1.1.2. Toxicity	9
1.1.2. Current limitations in material science	10
1.1.2.1. Security issues	10
1.1.2.2. Economic issues	10
1.1.2.3. Scientific issues	11
1.2. Current non-destructive techniques used for subsurface characterization	12
1.2.1. Techniques used in biology	12
1.2.1.1. Fluorescence microscopy	12
1.2.1.2. Radio-elements imaging	16
1.2.2. Tomography techniques	18
1.2.2.1. Electronic tomography	18
1.2.2.2. Ultrasound tomography (Non-contact techniques)	20
1.2.2.3. Eddy-current testing (ECT)	22
1.2.2.4. Infrared stimulated thermography	24
1.2.3. Elements analysis techniques	25
1.2.3.1. Scanning Electronic Microscopy (SEM) for elements analysis	25
1.2.3.2. Energy dispersive spectrometry (EDS)	27
1.2.3.3. Electron Backscattered Diffraction (EBSD) technique	29
1.2.3.4. Nuclear microprobe	30
1.3. Local probe techniques for surface characterization	33
1.3.1. Photon Scanning Tunneling Microscopy (PSTM)	35
1.3.2. Conventional Atomic Force Microscopy	38
1.3.2.1. Working principle	38
1.3.2.2. Different working modes	39
1.4. Development of near-field microscopes for subsurface investigation	45
1.4.1. Scanning Thermal Atomic Force Microscope	45
1.4.2. Nano-Infrared Microscopy (nanoIR)	47
1.4.3. Acoustic microscopy	49
1.4.3.1. Far field acoustic microscopy	49
1.4.3.2. Near field acoustic microscopy	53
1.5. Conclusion	56
Chapter 2 – <i>From topographic study to the development of tomographic high resolution tools.</i>	59
2.1. Mode Synthesizing Atomic Force Microscopy (MSAFM)	61
2.1.1. Advances in Quantitative Nanoscale Subsurface Imaging by Mode-Synthesizing Atomic Force Microscopy	64
2.2.1.1. Theoretical approach	64
2.2.1.2. Relationship between the frequency difference and the investigation depth	68
2.2.1.3. Influence of the order relationship between f_p frequency and f_s frequency	68
2.2.1.4. Influence of a change in frequency range	69

2.2.1.5. Experimental validation of the numerical model	70
2.2.1.6. Conclusion.....	79
2.1.2. Mode-Synthesizing Atomic Force Microscopy for volume characterization of mixed metal nanoparticles.....	80
2.2.2.1. Sample fabrication.....	80
2.2.2.2. Study of nanoparticles with a special metal core	82
2.2.2.3. Conclusion.....	84
2.2. Scanning Microwave Microscopy (SMM).....	85
2.2.1. Far and near-fields microwave techniques for the detection of defects.....	85
2.2.2. Micro-wave microscope.....	88
2.2.2.1. Microscope model.....	89
2.2.2.2. Definition of the reflection coefficient Γ	90
2.2.2.3. Return loss.....	90
2.2.2.4. Penetration depth.....	91
2.2.3. Scanning Microwave Microscope (by <i>Agilent</i>).....	93
2.2.4. Modelisation of the microwave probe.....	97
2.2.5. Evidence of in-depth investigation by SMM	103
2.2.6. Conclusion.....	105
2.3. Conclusion.....	106
Chapter 3 – <i>Advances in the understanding of tomography microscopy through the study of dielectric and biological samples.</i>	109
3.1. Study of the sensitivity of MSAFM – Analysis of a model sample.....	111
3.1.1. Methods.....	112
3.1.1.1. Material	112
3.1.1.2. Peak Force QNM and Lateral Force Microscopy	113
3.1.1.3. Raman spectroscopy mapping.....	114
3.1.1.4. Sample preparation.....	114
3.1.2. Results and discussions	115
3.1.3. Conclusion.....	122
3.2. Study of the action of an alcoholic stress on <i>Oenococcus oeni</i> bacteria.....	124
3.2.1. Introduction	124
3.2.2. Characterization of <i>Oenococcus Oeni</i> bacteria under stress by MSAFM.....	125
3.2.3. Conclusion.....	128
3.3. Combining AFM-IR and Mode Synthesizing Atomic Force Microscopy: Application to the study of Triglyceride vesicles inside <i>Streptomyces</i> bacteria.....	130
3.3.1. Introduction	130
3.3.2. Samples preparation	132
3.3.2.1. Bacterial strains and growth conditions	132
3.3.2.2. Sample preparation for AFM-IR measurements	132
3.3.3. Results	132
3.3.4. Conclusion.....	138
3.4. Conclusion.....	139
Chapter 4 – <i>Application and development of tomography on metallic samples by Scanning Microwave Microscopy.</i>	141
4.1. Study of various factors influencing Scanning Microwave Microscopy Measurements	143
4.1.1. Realization of a tomographic reconstruction by SMM	144
4.1.2. Study of the influence of metal conductivity on SMM measurements	145
4.1.2.1. Fabrication of the calibrated sample with buried metal patterns	145
4.1.2.2. Results	146

4.1.2.3. Conclusion.....	148
4.2. Study of various factors influencing conductivity by SMM	149
4.2.1. Study of light elements in metals: Diffusion of a light element in a metal	149
4.2.2.1. Preparation of the oxidized Zirconium sample preparation	150
4.2.2.2. SMM results	151
4.2.3. Conclusion.....	162
4.3. Introduction to the nanoscale non-destructive characterization of residual stress by Scanning Microwave Microscopy.....	163
4.3.1. Residual stress definition ^{225,226}	164
4.3.1. Residual stresses measurements	166
4.3.1.1. Destructive techniques (or semi-destructive techniques).....	166
4.3.1.2. Non - destructive techniques	166
4.3.1. Study of shot-peening influence on stress profile	169
4.3.1.1. Shot-peening treatment ²⁴¹	169
4.3.1.2. Obtaining of the stress profile by incremental hole-drilling method	172
4.3.1.3. Scanning Microwave Microscopy for residual stress measurements.....	173
4.3.2. Study of shot-peening treatment on a brass sample	176
4.3.2.4. Conclusion.....	177
4.4. Conclusion.....	178
Conclusion.....	181
References	187
List of publications.....	199
Conferences and Contributions	200

List of figures

Figure 1: Conventional fluorescence microscopy. A selected combination of excitation and emission filters are selected to collect wavelength of interest.	13
Figure 2: Fluorescence confocal microscopy image showing <i>E. coli</i> bacteria (red fluorescence) with synthetic adhesins targeting an antigen (green fluorescence) expressed on the surface of human tumor cells (nuclei and bacterial DNA stained in blue) ¹⁵	13
Figure 3: Conventional far-field microscope. Incoming light is focused onto the sample with the objective and collected by the detector.	15
Figure 4: Schematic of conventional confocal microscope. The pinholes are used to restrict the rays of light on the focal plane and to the detection.....	15
Figure 5: Illustration of the data acquisition scheme in brain gamma scintigraphy ²² . Gamma rays are collected by the camera, data analysis is performed to form an image representing the analyzed organ.....	16
Figure 6: Scintigraphy of a cross-section of human brain obtained in Positron-Emission Tomography.	17
Figure 7: Illustration of the 3D electron tomography principle.	18
Figure 8: Image of a multilyosomal body obtained by conventional TEM image.....	19
Figure 9 : The two modes of photothermic generation.	20
Figure 10: Laser detection of ultrasounds. The laser light is focused on the point of impact of the generation laser beam on the surface of the material. Any motion of the analyzed at the impact point of the detection laser is recorded on the reflected light as a frequency (or phase) variations ³⁴	21
Figure 11 : Principle of acoustic wave generation by Piezoelectric and EMAT sensors ³⁸ . Piezoelectric crystal generates acoustic waves under an electrical stimulation which causes mechanical distortion of the crystal and EMAT sensor is a transducer that employs a magnetostrictive effect to transmit and receive ultrasonic waves.....	22
Figure 12: Principle of an eddy-current device.....	23
Figure 13 : Different excitation sources in infrared stimulated thermography: a) by flash lamps or b) halogen lamps.....	24
Figure 14: Diagram of the electrons/matter interactions used in nanocharacterization with electron beam.	26
Figure 15: Energy Dispersion Spectroscopy (EDS) principle. The incident electron constitutes an external stimulation that results in an electron being kicked out of inner shell. An electron from an outer shell transitions to the hole created. The difference in energy results on the emission of a X-ray photon that can be detected to determine the energy of the transition for elemental analysis.....	27
Figure 16 : EDS spectrum of silver nanoparticles showing Ag L α and Ag L β signatures ⁵⁵	28
Figure 17: Example of a diffraction diagram (La ₂ Zr ₂ O ₇ , 20 kV, $\lambda = 0.086$ Å) (NEEL institute CNRS/UGA UPR2940).....	30
Figure 18: Schematic of the EBSD principle (NEEL institute CNRS/UGA UPR2940).	30
Figure 19: Schematic diagram of a nuclear microprobe: the ion beam is collimated and focused to form a spot with a micrometric diameter in the focal plane. An electrostatic deflection system allows scanning point by point the area to be analyzed in order to obtain a 2D or 3D map of the atomic percentage of the element analysed.....	31
Figure 20: Representation of Airy discs and their associated intensity distribution.....	34
Figure 21: Illustration of far and near-field regions around an emitting antenna.	35

Figure 22: PSTM setup for near-field optical collection of the light emitted by the sample excited by incoming polarized LASER light in Total Internal Reflection configuration ⁷⁶	36
Figure 23: Comparison of AFM and PSTM images on a same sample.....	37
Figure 24: Atomic Force Microscopy setup including the read-out system used to monitor the cantilever deflection and the electronics for feedback loops and sample rastering.	38
Figure 25: SEM view of the DNP cantilevers (Bruker) (left) and high resolution view of the cantilever tip (right) ⁸¹	39
Figure 26: Cantilever deflection vs the piezo z displacement curve. (1-3) are representative of the approach and (4-6) of the withdraw phase.	40
Figure 27: Lateral Force Microscopy principle: the lateral variation of the cantilever deflection is captured to extract the friction profile across the sample.	41
Figure 28: Topography (a) and (b) LFM image of human hair. (20 μm scan size). One can clearly observe the difference in frictional areas of keratin protein in (b) ⁸³	42
Figure 29: Schematic of tapping mode AFM. The cantilever oscillates close to the surface and the tip intermittently touches or taps the sample. The advantage of tapping the surface is improved lateral resolution on soft samples. Lateral forces such as drag, common in contact mode, are virtually eliminated ⁸⁷	42
Figure 30: AFM Peak Force QNM images of a multilayer film composed of polymer multilayers. (Scan size 10 x 10 μm).	43
Figure 31: AFM image of human monocyte rafts obtained by Peak Force Mode.....	44
Figure 32: Thermal AFM setup ⁹⁵ . A special AFM cantilever constitutes the fourth leg of the Wheatstone bridge for temperature measurements.	45
Figure 33: Thermal measurements from a SEBS polymer sample.	47
Figure 34: NanoIR setup: molecular vibrations in the sample are excited by illumination in the infrared range using a total internal reflection configuration. The ringing of the cantilever resulting from the pulse of light interacting with the matter is captured by an oscilloscope. Next FFT is performed to extract the absorption spectrum or chemical measurements. .	48
Figure 35: Results obtained with the AFM-IR system on <i>S. lividans</i> bacteria.	48
Figure 36: Far-field acoustic microscopy principle. The top and bottom interfaces of the buried defects lead to a reflection of the wave that can be captured by the pulse/detection.	49
Figure 37: Schematic of the Scanning Acoustic Microscope (SAM) using an acoustic lens to focus the waves onto the sample.	50
Figure 38: Acoustic (a) and SEM (b) images of a concrete samples made with granitic aggregate grains and Portland cement paste. The acoustic image was set at 400 MHz ¹¹⁸	52
Figure 39: Optical (in color) and overlaid acoustical (in grey) images of embryonic chicken heart muscle cells. The acoustical images have dimensions of 65 x 65 μm and were acquired with a center frequency of 860 MHz ¹¹⁷	52
Figure 40: Near-field acoustic microscope setup showing the mechanical actuation of the sample using a piezoelectric crystal connected by a frequency generator.	54
Figure 41: UFM images of Ge dots on Si substrate.	55
Figure 42: AFAM images of a piezoelectric lead zirconate ceramic at sample actuations of 600 kHz and 750 kHz ¹³³	55
Figure 43 : MSAFM setup.	62
Figure 44: Detection principle of a subsurface defect (purple sphere) in a homogeneous material (yellow slab). The acoustic wave of f_p frequency is represented in blue and the f_s frequency wave in green. The resulting wave of the nonlinear interaction is represented in red and presents a $ f_p - f_s $ frequency.	63
Figure 45: Predicted evolution of the investigation depth $z_{\Delta f}$	67

Figure 46: Experimental setup of MSAFM used to validate our model. The structures designed were probed using a tip and sample actuators of f_p and f_s , respectively. The signal of the difference $ f_p - f_s $ was monitored heterodyne detection. The phase was captured to successive Δf . The reconstruction of the depth profile was obtained by measuring the width of the features on each image.	70
Figure 47: Calibration of the reactive ion etching (RIE) step used for fabrication of the sample.	71
Figure 48: Two model samples developed for quantitative nanoscale subsurface imaging with MSAFM.	72
Figure 49: MSAFM phase images at various Δf frequencies (Scan size $10 \mu\text{m}$ acquired at scan rate of 0.5 Hz).	73
Figure 50: Subsurface composition reconstructions of the depth profile of calibration samples #1 and #2 based on MSAFM measurements and numerical model for the case in which $f_s > f_p$	74
Figure 51 : Subsurface composition reconstructions of of calibration samples #1 and #2 based on MSAFM measurements and numerical model – $f_s < f_p$ case.	76
Figure 52: Frequency spectrum of the Bruker DNP-S cantilever ($k = 0.12 \text{ N/m}$). The peaks of the blue curve correspond to the natural resonance frequencies of the free cantilever ($f_0 = 20 \text{ kHz}$, $f_1 = 120 \text{ kHz}$). The difference frequencies used in the measurements presented in Figure 3-5 are indicated in the graph (yellow dots), ranging from 20 kHz to 300 kHz by step of 10 kHz . The selected frequencies are represented by the green triangular markers (i.e. 20 kHz , 30 kHz , 70 kHz , 200 kHz , 270 kHz , 370 kHz , and 420 kHz).	77
Figure 53: “Contact” frequency spectrum of Bruker DNP-S cantilever ($k = 0.12 \text{ N/m}$). The peaks of the blue curve correspond to the resonance frequencies of the cantilever in contact with the sample. The difference frequencies used in the measurements presented are indicated in the graph (yellow dots), ranging from 20 kHz to 300 kHz by step of 10 kHz . The selected frequencies are represented by the green triangular markers (i.e. 20 kHz , 30 kHz , 70 kHz , 200 kHz , 270 kHz , 370 kHz , and 420 kHz).	78
Figure 54: MSAFM phase images for sample 2 with $f_s > f_p$ (f_s fixed at 4.3 MHz).	79
Figure 55: Schematic of the sample fabrication.	81
Figure 56 : MSAFM study of sample at different Δf frequencies.	83
Figure 57: Evolution of the core diameter with the Δf frequency.	83
Figure 58: Representation of various near field microwave characterization techniques.	86
Figure 59: Electrical circuit associated to the microwave microscope.	89
Figure 60: Illustration of the skin effect. The radiation frequency applied for the detection of defects buried inside the metallic sample should be tuned according to the depth of the defect. Depending on the electrical and magnetic properties of the metal, a frequency that is too high does not give access to a skin depth (δ_1) large enough for detection of the defect. The frequency has to be adapted for each material and defect.	92
Figure 61: Picture of the microscope used for SMM measurements. SMM, Agilent Technologies.	93
Figure 62: Frequency spectrum obtained at the output of the resonant circuit in the SMM setup.	94
Figure 63 : Influence of the tip-sample interaction on the SMM amplitude signal.	95
Figure 64: SMM cone nose and tip holder.	96
Figure 65: SMM setup: (left) microscope head and (right) data acquisition scheme.	96
Figure 66: SEM image of SCM-PIT cantilever (Bruker) used in our measurements: (left) cantilever and (right) tip ⁸¹	97

Figure 67: Geometry of the coaxial cable used in the model. Axes values are given in mm. Inner and outer radii as well as length of the cable were fixed for the calculations.....	98
Figure 68: List of parameters used for the Comsol model.....	98
Figure 69: Representation of the absolute value of the electric field $ E $ at the coaxial cable output. Highest intensity (in yellow) were found at the outer perimeter of the cable output.	99
Figure 70: Representation of the absolute value of the electric field $ E $ variations in the system. The system modeled is composed of the coaxial cable and the probe (and tip) for a 8 GHz frequency. Field concentration was observed at the probe location.	100
Figure 71: Average value of the absolute value of the electric field $ E $ for the 4 GHz, 6 GHz, 8 GHz and 12 GHz frequencies at the out of the coaxial cable in the presence or not of probe and tip.....	101
Figure 72: Absolute value of the electric field at the out of the coaxial cable in presence or not of probe and tip.	102
Figure 73: Electric field confinement provided by the presence of the probe and the tip.	102
Figure 74: Calibration sample: buried structures of aluminum under a calibrated nickel layer.	104
Figure 75: SMM images (phase) of buried Al under a calibrated Ni layer at different frequencies. Scan size: 10 x 10 μm . Phase scale: 0.1 deg.....	104
Figure 76: MSAFM experimental setup used in the characterization of dielectric materials, including multi-frequency actuation and heterodyne detection.	112
Figure 77: Nanofabrication process of the PMMA/Exposed (non-developed) PMMA patterned calibration samples.	114
Figure 78: AFM characterization of the sample.....	115
Figure 79: Influence of the scan rate on MSAFM phase (a,c,e) and amplitude (b,c,e) response of the difference mode of the MSAFM signals.....	116
Figure 80: MSAFM characterization of the calibration samples.	117
Figure 81: Calibration sample characterization by Peak Force QNM.	118
Figure 82: 3D reconstruction of subsurface structure and composition of the PMMA/exposed calibration samples. The 3D reconstruction is obtained by extracting the diameter for a ten successive MSAFM phase image.....	121
Figure 83: Highlighting the contrast change effect in MSAFM images with the Δf frequency difference.....	122
Figure 84: Overview of the response mechanisms of Lo18 protein to external stress. Under a stress, the Lo18 protein is produced by <i>O. Oeni</i> bacteria and acts like a molecular chaperon to avoid the denaturation of the other proteins present in the bacteria and like a lipochaperon to preserve the integrity of the membrane.....	124
Figure 85: Non-stressed <i>O. Oeni</i> bacteria.	126
Figure 86: Topographical dimensions of non-stressed and stressed bacteria.	127
Figure 87: Stressed <i>O. Oeni</i> bacteria.....	128
Figure 88: MSAFM and AFMIR imaging (Range 10 μm).	133
Figure 89: Comparison between MSAFM and AFM elasticity measurements.	135
Figure 90: MSAFM phase images in depth investigation – Evolution of the lipid vesicles size with the frequency (Range 4 μm) at frequency $\Delta f= 40$ kHz, $\Delta f= 50$ kHz and $\Delta f= 70$ kHz.	136
Figure 91: 3D reconstruction of a bacteria containing lipid vesicles. The reconstruction is obtained by stacking MSAFM images for 10 different Δf frequencies.....	137
Figure 92: Resolution comparison between AFM-IR and MSAFM techniques.....	138

Figure 93: Three-dimensional tomographic image reconstruction of the volume of the metal sample according to the frequency applied onto the SMM probe ¹⁸¹	144
Figure 94: Calibration sample with buried metal patterns.	145
Figure 95: Schematic of the cross section of the Zr/ZrO ₂ sample analyzed.	151
Figure 96: Analysis and composition of the zirconium sample enriched in oxide.	152
Figure 97: Depiction of SMM measurements on the cross-section of an oxidized zirconium sample probed. At a given frequency ($f_1= 11.83$ GHz) the attenuation of the wave changes as a function of the material conductivity (= oxygen concentration). Various frequencies ($f_2= 6.87$ GHz and $f_3= 2.21$ GHz) are used to probe deeper levels in the material.	153
Figure 98: Topography and phase shift cartography acquired at various frequencies (scan area 80 μm).	154
Figure 99: AFM and SMM characterization of pure Zr area.	156
Figure 100: Superimposed phase shift profiles (red, blue and green) for several depths with the location of the interface and compared with NRA results for the oxygen concentration (yellow).	158
Figure 101: NRA versus SMM phase shift measurements. The slope of the fitted curve was 0.94 indicative of a linear relationship between the two values.....	160
Figure 102: Successive SMM images obtained at frequencies (top) 11.83 GHz; (middle) 6.87 GHz; (bottom) 2.21 GHz, corresponding to different depth in the material.	161
Figure 103: Profile of the data corresponding to the different orders of residual stresses with σ_R^I , σ_R^{II} and σ_R^{III} the residual stresses of first, second and third order.....	165
Figure 104: Bragg's law principle: in a material with crystal planes separated by d ; d can be determined using the relationship between the angle and wavelength of the incoming beam and the n index of the refraction of the medium.	167
Figure 105: Residual stress measurements techniques presented with respect to the measurement depth they can probe and the amount of material removed ²⁴⁰	168
Figure 106: Illustration of shot-peening method used to prepare our samples ²⁴⁴ High speed impact between the small balls and the materials modifies the surface by generating residual stresses in the material.	170
Figure 107: Characteristic profiles used in shot peening ²⁴⁵	170
Figure 108: Schematic of the effect of some parameters on the shot-peening stress profile ²⁴⁵	171
Figure 109: Residual stress profile of shot-peened Zr obtained by incremental hole-drilling method ²¹⁷	172
Figure 110: SMM amplitude images realized on the shot peened Zr sample (image full size: 80 x 400 μm). Repions (1) to (5) represent successive images obtained across the region of interest.	173
Figure 111: Phase profile on a shot-peening sample realized by SMM.....	174
Figure 112: Representation of the SMM amplitude peaks versus frequency. Each peak provide from a different area of the shot peened sample to analyze.	175
Figure 113: SMM measurements compared to the indentation profile showing a good agreement.	175
Figure 114: Influence of the shot-peening time - Comparison between 20min and 40min shot peened samples (the shot-peened surface is located on the left part of the graphic representation) showing a shift in frequency and a change in amplitude that may be used for quantitative analysis.	176

General Introduction

General Introduction

One of the major challenges of nanotechnology is the non-destructive characterization of materials with high sensitivity and high spatial resolution. In this context, Atomic Force Microscopy (AFM) is an outstanding tool, because of its high spatial resolution for surface characterization and its versatility to explore properties of dielectric and biological samples, as well as solid-state materials, such as metals.

However, time-consuming data acquisition (limited by the processing time of the acquisition loop and the bandwidth of the piezoelectric scanners) and lack of sensitivity for non-surface features constitute two major drawbacks of standard atomic force microscopy.

Data acquisition has been greatly improved in the 2010s with the development of high-speed atomic force microscopy, by Professor T. Ando at the University of Kanazawa. Other groups have since exploited and developed this technique. Currently, acquisition speed of 25-50 frames/sec can be reached, making it possible to capture the dynamics of biological samples such as proteins in real time.

In this thesis, we present a new approach for high resolution tomographic characterization based on atomic force microscopy. We focus on two technologies operating with two different sample actuations: acoustic atomic force microscopy and scanning microwave microscopy. Specifically, the acoustic nanoscale microscopy prototype, called Mode Synthesizing Atomic Force Microscope (MSAFM), has been exploited in collaboration with Dr. Laurene Tétard from Nanoscience Technology Center of University of Central Florida. Acoustic microscopy is particularly effective to study changes in the volume of soft samples, such as biological and organic materials, and of dielectric materials. However, we found that it was quite challenging the access subsurface information in metals with acoustic microscopy. For our purpose, this limitation could be overcome using scanning microwave microscopy (SMM).

We also found that MSAFM and SMM are limited in obtaining the local chemical properties of the materials, which we address by implementing the MSAFM measurements on a platform developed for nanoscale IR spectroscopy. This has been achieved in collaboration with Professor Alexandre Dazzi and Marie-Joelle Virolle from the University of Paris Sud, Orsay. The development of SMM using tunable frequencies was inspired from macroscopic measurements. In 2008, the AREVA Company decided to invest in this technique for the investigation of defects in metallic samples. The proof of concept was established. For this reason we focused on the characterization of metallic samples by SMM.

Metal products are commonly used in automobile, aeronautic, aerospace, railway, construction and nuclear industries. In some structures, they represent the first mechanical resistance barrier subjected to wear. Non-destructive testing (NDT) methods are used to monitor their condition. The optimization of the service life of such metallic components evolving in fluctuating environments (temperature, pressure, electric and magnetic fields, gas, etc.) would require the detection, identification and monitoring of defects formed beneath the surface. However, conventional NDT techniques only permit the detection of wear or defective areas at late stage of their development (i.e., macro-cracking), while early stages of defect formation (micro-cracking) remain overlooked.

Material degradation of metallic components can also be accelerated by the diffusion of light chemical elements such as oxygen, helium, hydrogen or nitrogen. The presence and migration of these light elements in solids can induce substantial local changes with macroscopic irreversible effects such as residual stress, ductility loss or change in mechanical strength. Most of these changes are detrimental to the components functionality. However, mapping the distribution of light chemical elements near and below the surface of a metal is not straightforward with the most common surface analysis techniques. This is due to the lack of

sensitivity of the techniques, and to the volatility and mobility of the species (hydrogen H, helium He), or the surface contamination by the surrounding environment (oxygen O).

Overall, the detection limit of conventional systems capable of probing volume properties of complex heterogeneous materials makes early defect formation quite challenging. This constitutes a major drawback when the parts operate under extreme conditions (high temperature, high pressure, mechanical stress, radiation exposure, etc.), as the propagation of defects is often greatly accelerated, leading to the emergence of critical defects with higher incidence rate. Thus, improving this detection limit of imaging and spectroscopic techniques is crucial to understand the processes of defect propagation and to improve materials quality.

We thus propose to overcome these existing limitations of non-destructive methods by developing a platform capable of monitoring local changes in mechanical properties in heterogeneous materials, as it is well known that mechanical constraints can be generated during components production due to residual stress, hardening and surface chemical composition.

To address the above needs, on the basis on an AFM platform, an acoustic-based microscope (MSAFM) and a micro-wave-based microscope (SMM) have been implemented. Acoustic AFM works in a MHz frequency range while SMM works in a frequency range between 0.2 GHz and 16 GHz. On the one hand MSAFM is mainly used to study soft samples. On the other hand, SMM can be used to study the evolution of the behavior and aging of solid and metallic components, in particular regarding:

the non-destructive early detection of defects that can evolve from nanometer to micrometer size, the indirect measurement of gradual changes in materials properties engendered by the diffusion of light chemical elements and the effect microstructural changes such as residual stress, dislocation or nanocrystallization.

In this respect, the thesis focuses on the acoustic and microwave microscopes as well as on their development towards the access to a more comprehensive high-resolution tomographic characterization of soft or solid samples.

This work is organized as follows:

In the first chapter, the state of the art of non-destructive methods on soft and hard materials is discussed. The description of the foundations of NDT techniques for volume and three-dimensional investigations is carried out via the review of the main techniques used in laboratories and in the industry.

The second chapter is focused on the review of near-field techniques used and implemented in this work to achieve tomographic exploration of heterogeneous samples with a nanometric spatial resolution.

The third chapter presents the results obtained on soft samples using acoustic atomic force microscopy and its coupling to the infrared atomic force microscope (AFM-IR).

The fourth chapter discusses the advances realized using SMM to achieve near field tomography on solid and metallurgical samples to tackle industrial problems concerning the non-destructive early detection of defects and the effect of light chemical elements contaminations on metal lattice and on its mechanical properties. A part of the chapter will discuss the promising use of microwave microscopy for the detection of residual stress inside materials to establish connections to the performance of the components being produced.

Finally, the conclusion confers the promising use of near-field microscopy for non-destructive testing at the nanoscale and provides an overview of the possibility of transforming SMM into a portable version, in order to achieve high-resolution in-situ analyzes for industrial use.

Chapter 1 – *State of the Art*

Having access to sub-surface high information with high-spatial resolution via non-destructive characterization techniques is a real challenge in various scientific fields such as biology, material science, or even metallurgy. Early detection of the presence of particles, or viruses in host cells remains a challenge in biology. Moreover, highlighting diffusion in materials would improve the optimization treatments for better efficiency in material development. Tomographic techniques have emerged for the characterization of buried structures inside solid or soft matter. In this chapter we present the state of the art of existing volumetric techniques useful either in biology or in material sciences. Then, we discuss the near-field techniques presently being used for surface and subsurface characterization and we conclude on the need to develop new local probe techniques for high spatial resolution, subsurface investigation.

1.1. Needs for having access to subsurface information

1.1.1. Current limitation in biology and life sciences

1.1.1.1. Health

Volume investigation of biological elements such as bacteria or cells would allow a better understanding of the various fundamental mechanisms such as the internal processes in bacteria or the effect of chemical and physical stresses on them. Monitoring and characterizing virus/cell interactions, or the influence of the external environment on live biological systems is of a great interest for fundamental science¹ and also for applications such as the development of new pharmaceutical treatments².

1.1.1.2. Toxicity

With the swift development of nanotechnology and particularly the use of nanoparticles in health and other industry, safety and toxicity issues arise. Assessing the toxicity caused by such small particles at the single cell level remains challenging. This is due to the lack of suitable tools to probe their local interactions with the material/tissue³. In the case of targeted drug delivery using nanoparticles on the interaction of stress agents with cells, the following mechanisms remain unclear, including the characteristics of the functionalized nanoparticles-cells interactions, or the mechanisms of penetration of the nanoparticles through the membrane. Consequently, tools that would allow us to characterize cell properties with high spatial resolution and to monitor their behavior *in situ*, both at their surface and in their volume, is of a great importance.

1.1.2. Current limitations in material science

1.1.2.1. Security issues

Early detection of damages in industrial metallic components is of great interest to optimize the lifetime of parts subjected to harsh environments (temperature, pressure or other) ⁴. Detecting material failure and cracks in their early stages is all the more important in the nuclear field to avoid major accidents like the one that occurred in March 2011 on the site of the Fukushima plant⁵. Non-destructive methods are needed at different stages of an event related to part failure.

Before the accident: More accurate non-destructive methods would have permitted to have an understanding of the state of the components (minor defects and physical characteristics of materials). The desired tools could assess the limits of current parts in operation. This would facilitate predictions of minor accidents to plan timely repairs.

During the accident: Monitoring the status of the materials will feed calculation algorithms useful to predict the behavior of the structure during the accident.

After the accident: After the accident happened, an accurate diagnosis of the components involved is performed. Non-destructive characterization methods are aimed to facilitate the analysis of the components to support the decision making about the future of the structure and its potential reconstruction.

1.1.2.2. Economic issues

The maintenance and replacement operations are generally triggered only if the component in use in the reactor system is found to be significantly damaged, or if a component of the same type was damaged on another similar installation. As a result, the maintenance and renovations can be costly. For instance, AREVA replaced 32 old steam generators in France for a total cost of 1.1 billion euros.

Superior non-destructive methods would permit the early detection of defects in components already in use or ideally when they just come out of production. This will enable the

development of strategies for predictive servicing that would be much less expensive than the strategies currently in place. This approach would also be much “greener” as it would prevent early replacement of some pieces.

1.1.2.3. Scientific issues

In recent decades, scientific and technical advances have been reported in defectology⁶. Among them we find ultrasonic and electromagnetic sensors, adaptive probes (conformable or flexible), contactless sensors (LASER and electro-magneto-acoustic) as well as simulation and image reconstruction tools. However, there is still a lack in understanding the mechanisms involved in fatigue and defect formation. This is partly due to the lack in sensitivity and reproducibility of the conventional techniques available, as well as difficulties encountered to interpret the measurements performed with traditional sensors.

Moreover, although methods of good potential exist, few are applied today in line or on-site to study degraded service materials. There are several main reasons for this lack of implementation in the field. First, most publications are limited to qualitative observations and do not interpret the evolution of signals related to the metallurgical analysis of the mechanisms of damage and aging^{7 8}. Furthermore, most methods of physical measurement used in non-destructive control fail to benefit from a straightforward relationship between the measured signal and the desired characteristic of the phenomenon studied and many methods are sensitive to various intrinsic material parameters (dislocation density, residual stress strain, the presence and nature of precipitates, surface state...) or extrinsic (stress level, temperature...). The decorrelation of these important parameters is often difficult. In addition to that, the signal variations are generally small and often marred by high uncertainty related to the measurement or to the heterogeneity of the material⁹. Finally, the information collected by conventional methods are sometimes local and the connection to the behavior of the entire component to determine a maintenance plan remains an uncertain leap.

1.2. Current non-destructive techniques used for subsurface characterization

1.2.1. Techniques used in biology

1.2.1.1. Fluorescence microscopy

Fluorescence microscopy^{10,11} is currently the most commonly used method for the study of structures and dynamics inside biological systems such as cells¹². It is based on conventional light microscopy, with added features to detect selected fluorescence properties of the sample. In a conventional microscope the light source used is in the visible range (wavelength from 400 to 700 nm), while in a fluorescence microscope a light source with much higher intensity (as a laser source, Xenon or Mercury arc-discharge lamp) is used to excite the sample at a specific wavelength. With sufficient energy, molecules in the sample undergo electronic transitions, followed by relaxation resulting in the emission of photons with lower energy (longer wavelength). These photons are detected to form the fluorescence images. Fluorescent microscopy is often used to image small entities inside biological systems such as living cells¹³. This can be accomplished by attaching fluorescent tags to antibodies that in turn attach to targeted antigens. The reflected and background fluorescence light is filtered in order to detect only the targeted species. We can then have access to a distribution map of the tagged entities inside a biological sample with a lateral resolution of up to 200 nm¹⁴. Note that the spatial resolution is directly related to the wavelength used to illuminate the sample. The description of the microscope is presented in **Figure 1** and an example of fluorescence image of a bacteria can be seen in **Figure 2**.

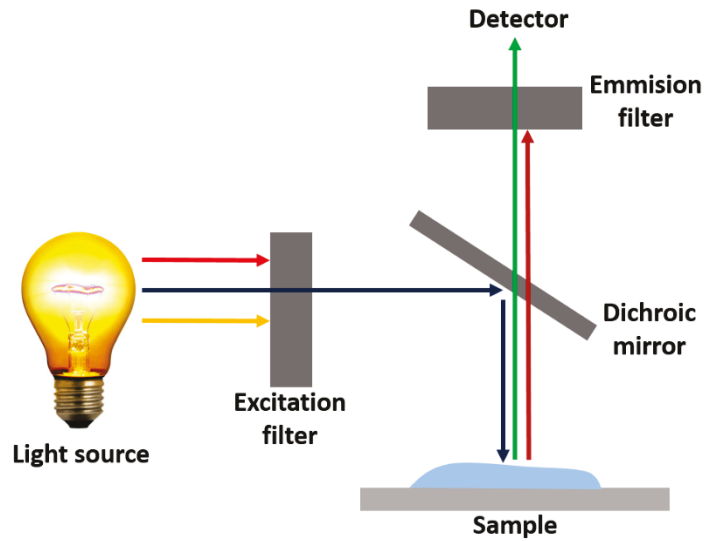


Figure 1: Conventional fluorescence microscopy. A selected combination of excitation and emission filters are selected to collect wavelength of interest.

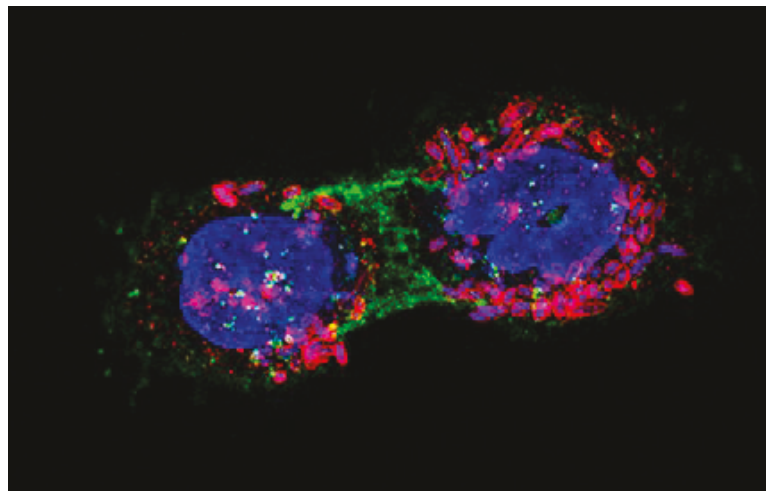


Figure 2: Fluorescence confocal microscopy image showing *E. coli* bacteria (red fluorescence) with synthetic adhesins targeting an antigen (green fluorescence) expressed on the surface of human tumor cells (nuclei and bacterial DNA stained in blue)¹⁵.

Fluorescence measurements can be achieved with different kinds of configurations:

Epifluorescence microscopy¹⁶: the excitation light comes from the objective and the fluorescence signal collected by the same objective, in a reflection configuration as shown in Figure 3. This configuration is of interest to limit the interference from the incoming light, since the materials studied are mostly transparent. The fluorescence emission being isotropic, a reflection collection does not impede the signal measured.

Confocal microscopy¹⁷, shown in **Figure 4**, offers better lateral (up to half of the excitation wavelength) and volume (up to 400nm) resolution than classical optical microscopy. In fact, confocal imaging has long been the platform of choice for 3D imaging of biological samples¹⁸. Samples should also be tagged to visualize the structures of interest. The fluorescent tag should be selected in conjunction with the excitation wavelengths available. To collect an image, the laser is rastered across the selected region. This results in fluorescence emission, which can be collected to form an image of the select plane. Due to the combination of pinholes in the system, the light emitted from “out of pane” are blocked, making images more resolved compared to conventional microscopy.

Total internal reflection microscopy allows a better depth of field (200nm) than confocal microscopy (400nm) but only at the interface between the sample and the sample support¹⁹ due to the evanescent nature of the field at the substrate interface used for imaging. This is used to monitor small entities such as fibrils or interfaces such as the membrane of a bacterial cell in the vicinity of the substrate.

The fluorescence correlation spectroscopy (FCS)²⁰ which allows to study the diffusion and the interaction of the molecules.

Figure 3 and **Figure 4** illustrate the difference between far field microscopy and confocal microscopy which offer a better resolution.

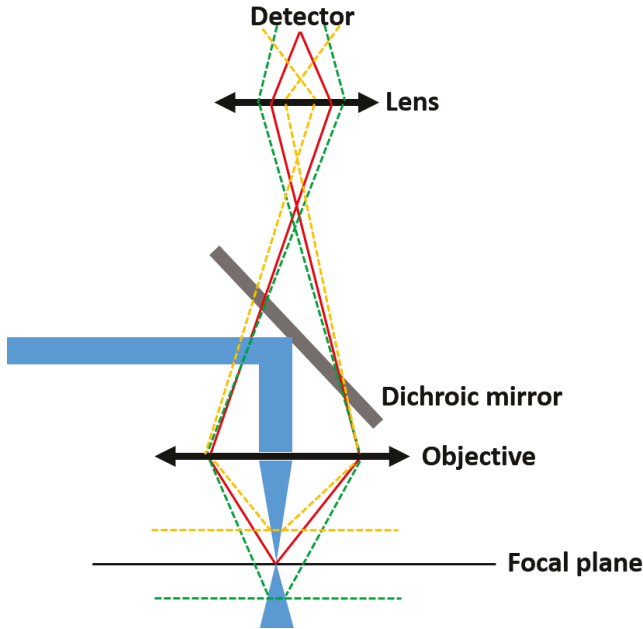


Figure 3: Conventional far-field microscope. Incoming light is focused onto the sample with the objective and collected by the detector.

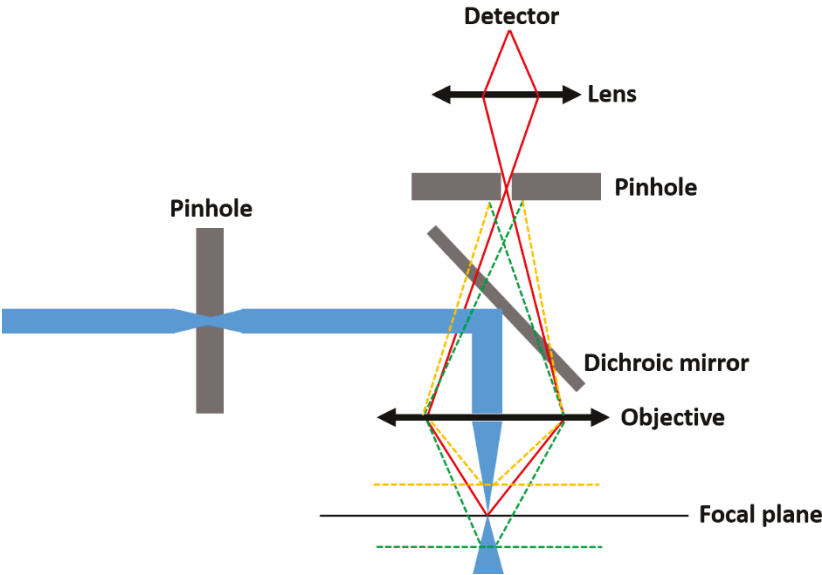


Figure 4: Schematic of conventional confocal microscope. The pinholes are used to restrict the rays of light on the focal plane and to the detection.

1.2.1.2. Radio-elements imaging

Scintigraphy²¹ is an imaging technique to follow a radioactive isotope. This is classified as emission imaging because the radiation originates from the organ after the tracer is injected, which is the association of a carrier molecule and a radioactive label, is injected to the patient. The radioactive marker serves as a "transmitter spy" that makes it possible to track the particles by detecting the gamma rays emitted using an external detector called gamma camera (**Figure 5**).

Scintigraphy is widely used in nuclear medicine, it allows detection of many diseases, such as early screening for cancer, for example. Each organ setting isotopes in different, we do not use the same isotopes for all organs. A scintigraphy image is presented in **Figure 6**.

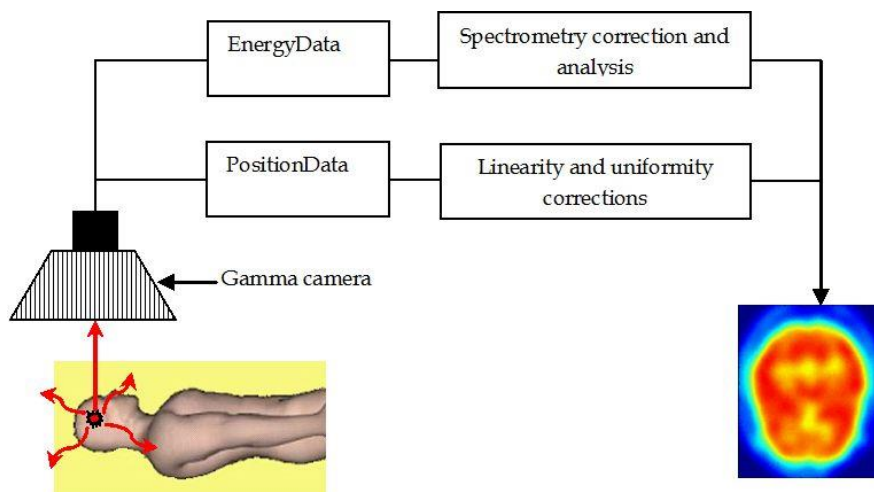


Figure 5: Illustration of the data acquisition scheme in brain gamma scintigraphy²². Gamma rays are collected by the camera, data analysis is performed to form an image representing the analyzed organ.

This detection has different stages:

1 - Selection by a collimator of only photons emitted perpendicular to the camera.

2 - Gamma photons interacting with a NaI (Tl) crystal. This step permits to transform the gamma photons into electrons and electrons into visible light (scintillation). Each gamma photon is responsible for hundreds of light photons emitted in all directions.

3 - Transformation of photons into electrical current at the photocathode of the photomultiplier positioned behind the crystal.

4 - Spatial and energy selection of photons. The above processing leads to the formation of signals from which it is possible to accurately determine the initial position of each photon, and their energy.

5 - Following this selection, it is possible to reconstruct the image of the photon distribution in the studied organ.

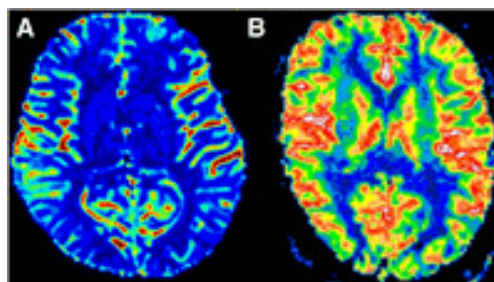


Figure 6: Scintillography of a cross-section of human brain obtained in Positron-Emission Tomography: (a) diseased brain with low neuronal activity and (b) healthy brain²³. The image is formed by reconstruction using false-color representation.

1.2.2. Tomography techniques

1.2.2.1. Electronic tomography

The transmission electronic microscopy (TEM) is mostly used for cellular and intra-cellular imaging^{24,25}. However, a lot of intracellular structures cannot be apprehended in one time, with a single image. Only the combination of several views taken in several directions or in depth can allow reconstructing the geometry of these structures. Electronic tomography allows having access to the tridimensional volume of a sample in electronic microscopy.

The general principle of electron tomography is based on the collection of projection images of a sample taken at different orientations²⁶. A projection image contains the information of the projected 3D volume, i.e. summed on the 2D image. By varying the angle of the projection, it is possible to obtain different views of this 3D information. With a sufficient number of views the 3D reconstruction of the original volume can be obtained using a set of projections (**Figure 7**).

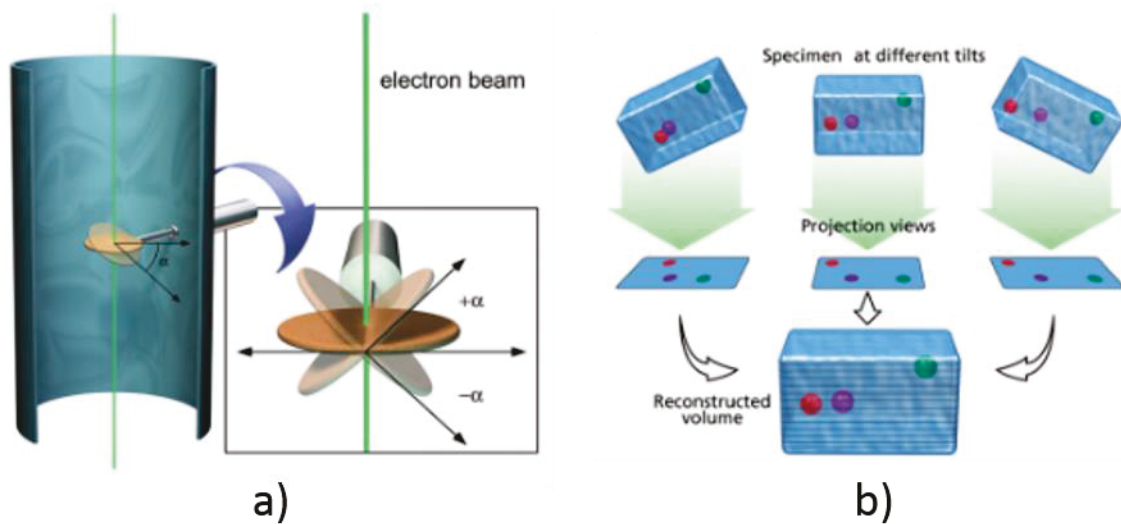


Figure 7: Illustration of the 3D electron tomography principle. (a) The sample is tilted to selected angles around an axis perpendicular to the electron beam. A series of corresponding projection images is recorded. (b) Schematic of a set of 2D projection views generated by tilting a 3D object to different angles. The final volume is calculated by summation of all the back-projection profiles and represented as a series of stacked thin slices²⁷.

In the case of X-ray tomography (CT-scan) or micro-tomography (μ CT), the projection images are obtained through the use of X-rays, and the different orientations are obtained by turning the emitter and detector around the patient. In the case of electron tomography it is the sample that is rotated under the electron beam with a goniometer stage, by tilting the grid on which the specimen is deposited.

The final quality of the reconstructed volume depends on the number of projections and on the interval between acquisition angles. For X-ray acquisition, the span of the angles is 180° , which can provide a high quality 3D reconstruction with sufficiently small intervals²⁶. In the case of electronic tomography, the sample holder cannot have a 90° angle and the observation width increase as $1/\cos$ (observation angle), adding constraints to the reconstruction.

The samples to be observed by electron tomography undergo the same preparation as for conventional transmission electron microscopy, i.e. dehydration and inclusion in a resin. The attachment may be chemical or physical (high pressure followed by freeze-substitution fixation). For 3D reconstruction, thick sections of the order of 200 to 500 nm are preferred²⁸. This requires the use of microscope voltages of 200 keV to 120 keV²⁸.

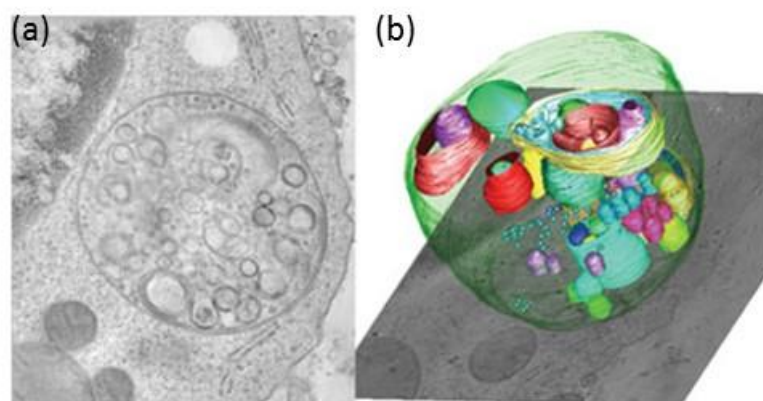


Figure 8: Image of a multilyosomal body obtained by conventional TEM image. (a) represents the complex 3D arrangement of the various membrane-bound structures in the interior of the organelle after electron tomography and (b) the modelling²⁹.

1.2.2.2. Ultrasound tomography (Non-contact techniques)

The laser ultrasonic technique³⁰⁻³²(LUT) consists of generating and detecting elastic ultrasound waves in a solid, liquid or gaseous medium, using a laser source. In general, short laser pulses (from tens of nanoseconds to femtoseconds) are used to locally heat the structure studied, causing expansion phenomena (thermoelastic regime)³³ or ablation. In thermoelastic regime the generation of ultrasounds is created by the sudden thermal expansion due to the heating of a small surface of the material by the pulsed Laser. In the ablation mode, if the laser power is enough high to heat the surface above the material boiling point, some material is evaporated (typically some nanometers). Following the ablation, a recoil force is generated, which is the source of a compression (longitudinal) ultrasonic wave (Figure 9).

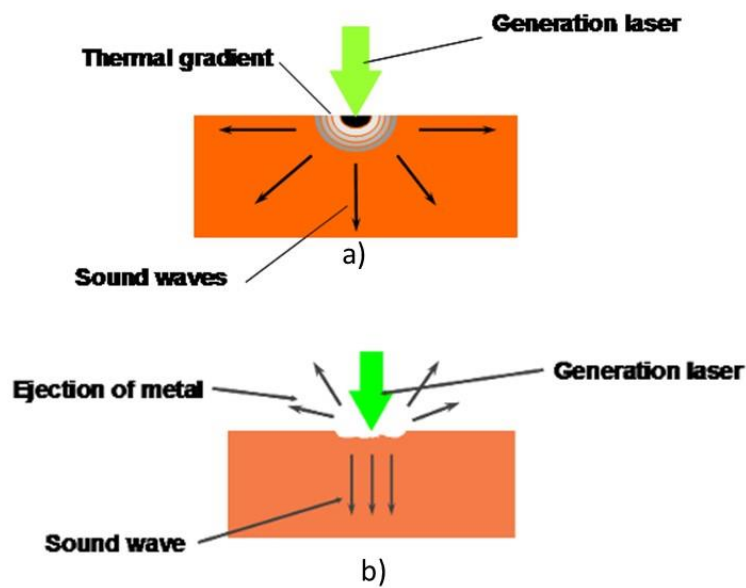


Figure 9 : The two modes of photothermic generation: (a) Thermoelastic mode where ultrasounds are created by the sudden thermal expansion due to the heating of a small surface of the material by the pulsed Laser and (b) Ablation mode where some of the material under test is evaporated³⁴.

Then the ultrasounds generated are detected by a Laser detection³⁵. This detection is based on the demodulation by an optical interferometer of the laser light reflected or backscattered from the surface of the material. A single frequency, laser light is focused on the point of impact of

the generation laser beam on the surface of the material. Any motion of the analyzed at the impact point of the detection laser is recorded on the reflected light as a frequency (or phase) variations - Doppler Effect - (Figure 10).

The laser ultrasounds allow ultrasonic inspection of materials in a wide variety of applications ranging from inspection of aerospace composite materials³⁶, to coating analysis³⁶.

There are numerous advantages of this method. Compared to traditional methods (piezoelectric transducers), no mechanical contact is required for photoacoustic generation and detection. Inspecting immersed materials in harsh environments (very high or low temperature) presenting complex geometries (cylindrical shapes) is possible³⁷. Hence, control of the structure can be done from a distance without causing any damage or favorable conditions for corrosion development since no coupling media is used. Lastly, the implementation of these methods is usually quite fast.

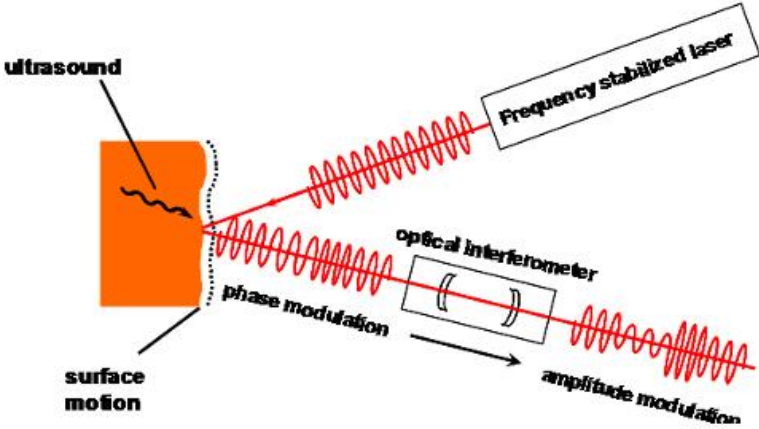


Figure 10: Laser detection of ultrasounds. The laser light is focused on the point of impact of the generation laser beam on the surface of the material. Any motion of the analyzed at the impact point of the detection laser is recorded on the reflected light as a frequency (or phase) variations³⁴.

Ultrasonic waves can also be generated and detected in metallic materials using EMAT (Electromagnetic Acoustic Transducer) transducers in a frequency range of several megahertz, much smaller than in ultrasonic Laser. EMAT is not a contact technique which is based on the

Lorentz force, which results from the combined actions of eddy currents and permanent magnetic field (**Figure 11**).

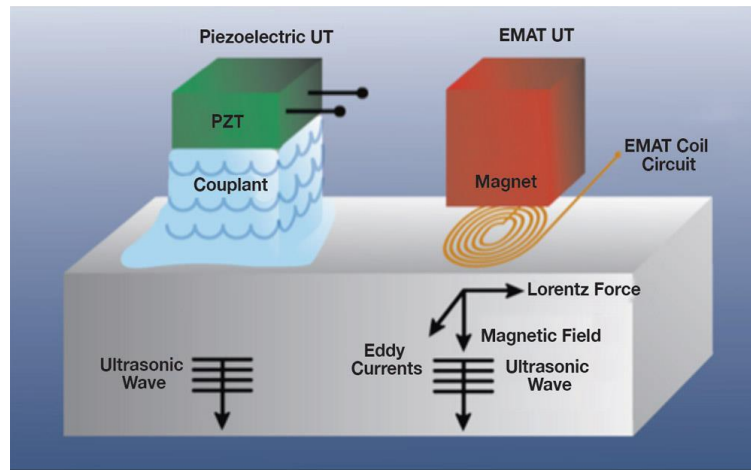


Figure 11 : Principle of acoustic wave generation by Piezoelectric and EMAT sensors³⁸. Piezoelectric crystal generates acoustic waves under an electrical stimulation which causes mechanical distortion of the crystal and EMAT sensor is a transducer that employs a magnetostrictive effect to transmit and receive ultrasonic waves.

1.2.2.3. Eddy-current testing (ECT)

Eddy Current testing is based on electromagnetic induction phenomenon³⁹ (ref). In the eddy current probe, an alternating current (AC) flows through a wire coil and generates an oscillating magnetic field (**Figure 12**). When the probe and the generated magnetic field are placed close to a conductive sample, induced currents are created inside the material, known as Eddy currents. Variations in the electrical conductivity and magnetic permeability of the test object as well as the presence of defects inside the material cause a change in Eddy current. Thus, a corresponding change in phase and amplitude that can be observed by measuring the impedance changes in the coil, which is a sign of the presence of defects⁴⁰.

However, due to the electrical nature of ECTB, this technique is limited to conductive materials with a depth investigation limited by the skin depth effect⁴¹.

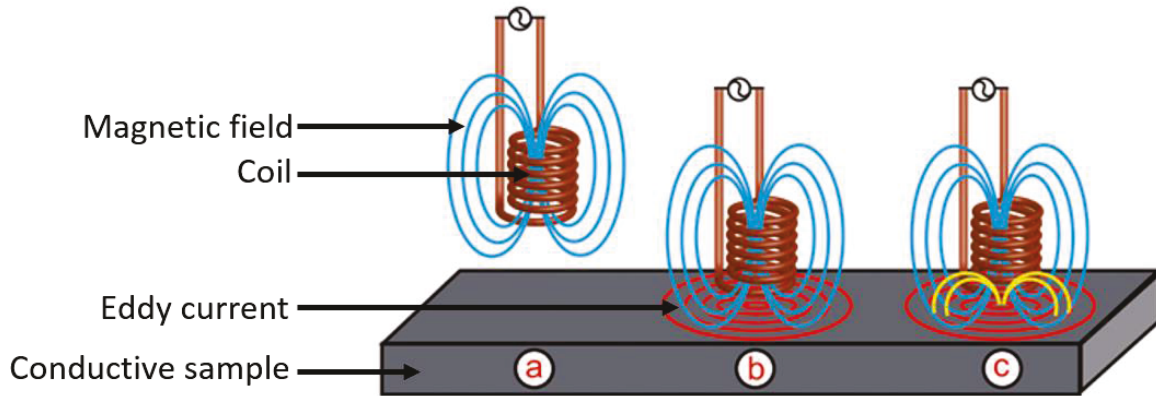


Figure 12: Principle of an eddy-current device. (a) The alternating current flowing through the coil at a chosen frequency generates a magnetic field around the coil. (b) When the coil is placed close to an electrically conductive material, eddy-current is induced in the material. (c) If a flaw in the conductive metal disturbs the eddy-current circulation, the magnetic coupling with the probe changes and a defect signal can be read by measuring the coil impedance variation.

The major parameters to take into include:

- Every local variation of the sample's electrical conductivity and magnetic permeability will lead to artifact of measurements.
- The distance between the probe and the sample has to be maintained constant to avoid disruptive effects.
- The excitation frequency of the coil has to be tuned to obtain the skin depth desired and a good signal from the sample.

This technique does not require any special sample preparation or any coupling media. The speed of analysis is very fast (up to several meters per second). However, the fast attenuation of Eddy current limits this technique to the skin depth, which varies from a few nm to μm depending on the frequency used and on the metal under test. Moreover, the quantitative interpretation of the signals can be complicated if the signal/noise ratio is not optimized and the characterization of a defect type crack is delicate.

1.2.2.4. Infrared stimulated thermography

Also called infrared radiometry⁴², this non-destructive method consists in illuminating the analyzed sample to a photon energy flux (visible or not, localized or widespread, in pulse form, sinusoidal, random). The illumination can be done in different ways: laser beam, flash lamp or halogen. The absorption of these photons produces an increase in temperature in the vicinity of the area of the material interacting with infrared photons due to the vibrational transitions taking place in the material. The resulting heating induces a transient variation of the infrared emission of the object. This variation is strongly dependent of optical and thermal properties of the material (thermal conductivity, thermal diffusivity, thermal emissivity, temperature, specific heat and density), and can be observed using an infrared thermography camera. Moreover, these parameters are correlated to the aspect of the surface (roughness), presence of delamination and cracks, and internal structure of the material. The principle of the method ensures it is non-destructive, without contact at the excitation and detection (**Figure 13**).

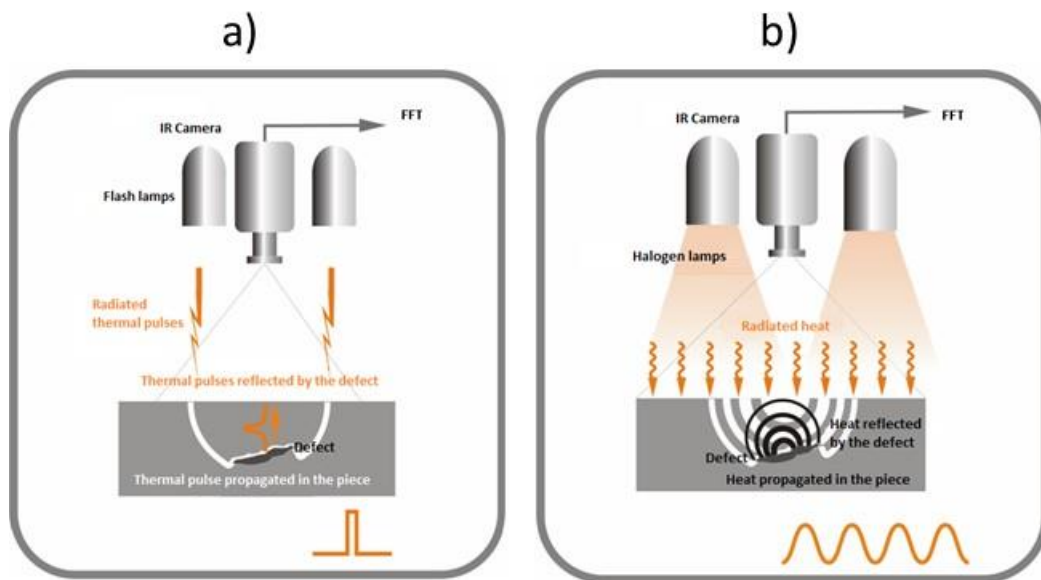


Figure 13 : Different excitation sources in infrared stimulated thermography: a) by flash lamps or b) halogen lamps.

The main advantages of this non-destructive method are non-contact, fast implementation and remote sensing. The photothermal signal collected is sensitive to homogeneities of the material and the presence of surface or underlying defects. Thus, the selection of the excitation source and its parameters (duration, amplitude, frequency ...) plays an important role depending on the material, size, depth and nature of the defect to be detected⁴³. Halogen light sources and flash lamps sources can be used to highlight delamination in composite materials^{44,45}, estimate coatings thickness⁴⁶ and detect cracks and defects inside materials⁴⁷.

In the field of thermo-elasticity, infrared thermography working in the passive mode can be used to measure stress of materials under mechanical stress as fatigue⁴⁸.

1.2.3. Elements analysis techniques

1.2.3.1. Scanning Electronic Microscopy (SEM) for elements analysis

The Scanning Electron Microscopy (SEM)^{49,50} is a powerful observation technique of sample topography developed in 1940 - 1960. It is mainly based on the detection of secondary electrons coming from the surface under the impact of a focused electron beam (energy between 1 MeV and 100 keV) produced by a cathode which scans the surface. Images with a lateral resolution until 5 nm and a great depth of field can be obtained. As the mean free path of electrons in the air is very low, a vacuum of at least 10^{-9} atmosphere is usually maintained in the microscope.

The electrons that provide from the primary electron beam penetrate in the material and affect a volume of the material. This volume depends on the average atomic number of the sample and on the energy of the incident electrons. Inside this interaction volume, the electrons will interact with the matter generating a lot of secondary phenomena that are described in **Figure 14**. As a result, other interactions of the electrons with the sample can also be studied to complement the measurements of secondary electrons⁵¹. Each of these interactions is related to the topography and/or the surface composition⁵¹.

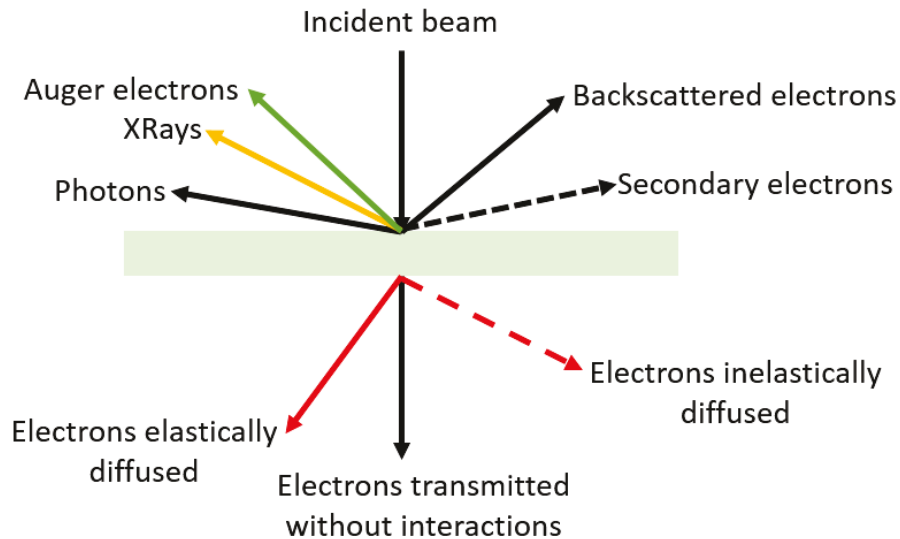


Figure 14: Diagram of the electrons/matter interactions used in nanocharacterization with electron beam.

SEM requires a conductive sample, thus non-conductive samples should be metallized by the evaporation of a few nanometer layer of a conductive material such as gold or chromium. The electron source requiring a high vacuum it is important to remove all the air presents in the sample before its introduction in the SEM observation chamber and to observe object with a reasonable size (a few mm^3 is possible). Nevertheless these difficulties can be overcome by working at a very low temperature (cryo-SEM)⁵². Cryo-SEM requires however a long and complex preparation of sample (samples with a thickness superior to 500nm have to be frozen and cut into thin sections - 40 nm to 200 nm thick- with a diamond knife in a cryomicrotome at temperatures lower than -135°C).

In the following sub-section, we focus on two analysis technique that can be provided by SEM microscopy: Energy Dispersive Spectrometry (EDS) and Electron Backscattered Diffraction (EDSD).

1.2.3.2. Energy dispersive spectrometry (EDS)

The electron beam from the SEM (possessing energy between 10 and 40 keV) interacts with the sample's atoms. Here we focus on inelastic collisions. As described in **Figure 15**, the atoms are ionized and as the incident electrons can eject an electron of the atom (usually valence one). This ejected electron is called secondary electron. Then, rearrangement of the atom's electronic cloud occurs and one of the atoms in the excited states decays to the lower energy state. This mechanism engenders the emission of X-ray photons, which are characteristic of the atom. By placing an X-ray detector in the microscope chamber, this radiation can be detected and recorded. Two types of detectors may be used operating either as energy dispersions (EDS)⁵³ or wavelength dispersion (WDS) spectrometries.

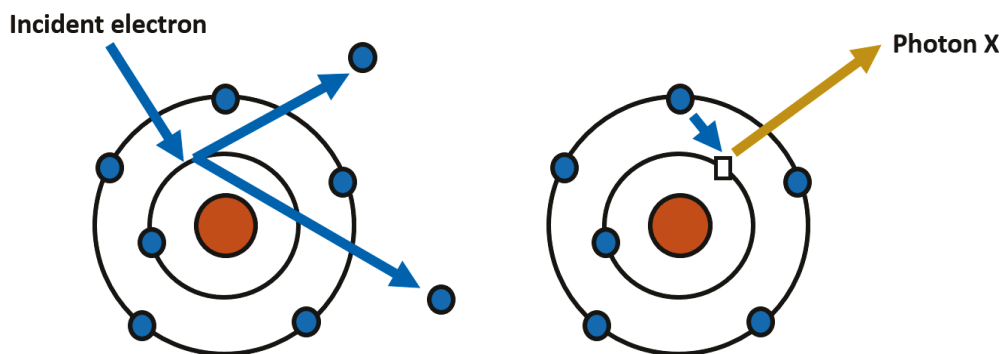


Figure 15: Energy Dispersion Spectroscopy (EDS) principle. The incident electron constitutes an external stimulation that results in an electron being kicked out of inner shell. An electron from an outer shell transitions to the hole created. The difference in energy results on the emission of a X-ray photon that can be detected to determine the energy of the transition for elemental analysis.

EDS detectors consist of an active portion of silicon. The incident X-ray photons generate electron-hole pairs in the crystal of the detector. With the polarization of the detector, electrons migrate toward the anode and a leakage current is recorded. This current is proportional to the photon energy of the incident X-ray. The data collected is in the form of a spectrum with the radiative transitions specific to each element, which can be identified by comparing the peaks

in the spectrum with existing databases for elements (**Figure 16**). The area of the peaks is correlated with the content of the element in the compound, and the energy of the primary beam. The limit of detection is typically between 1000 and 3000 ppm and the resolution is in the order of 300 nm for lateral resolution and 1 μm for depth information⁵⁴.

However, this technique presents some limitations. Due to the interaction of the electron beam with the matter, the analysis gives information about an integrated volume of the sample (included the surface and the oxide layer that is present in surface of the sample). In the case of samples that are not flat, polished and homogeneous, quantification of the results can be quite complicated. In addition, this technique is not suitable for low-Z elements. Finally, the sample size has to be adapted to the SEM sample holder and must be vacuum compatible.

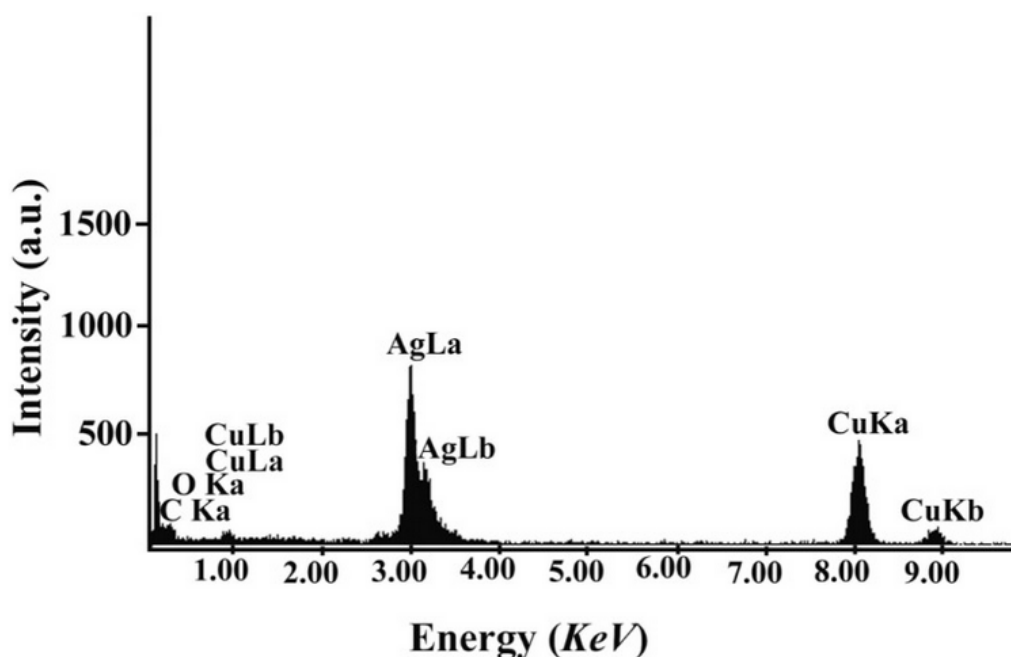


Figure 16 : EDS spectrum of silver nanoparticles showing Ag $L\alpha$ and Ag $L\beta$ signatures⁵⁵.

In order to obtain reliable measurements, an excellent surface flatness, a very well-polished surface, a sample that is conductive, stable under the electron beam and vacuum, and a homogeneous area for analysis are required.

These conditions exclude this technique as an overarching mean for chemical analysis. Moreover, in the case of quite rough samples, the topography can induce some absorption effects and lead to a wrong quantitative analysis. Cases of changes in the chemical composition of the sample under the electronic beam can also be reported. One example is the case of the migration of alkali metal ions under the beam influence ⁵⁶.

1.2.3.3. Electron Backscattered Diffraction (EBSD) technique

EBDS is a microstructural crystallographic technique⁵⁷ to measure the crystal orientation of crystalline materials. EBDS can be used to determine to preferential crystallographic orientation of any mono- or poly-crystalline material. It can also be used to identify the crystalline system in a material. EBDS can also be applied to study defects⁵⁸, phase identification⁵⁹, grain boundaries⁶⁰, examination of local heterogeneities⁶¹ and deformation cartography⁶² (**Figure 17**).

EBSD is commonly implemented in the SEM, provided that it is equipped with an appropriate detector ⁶³. The crystalline sample is first polished and positioned in the SEM vacuum chamber with a high inclination angle ($\sim 70^\circ$) to increase the contrast of the backscattered electrons. A phosphorescent screen is located inside the SEM chamber with a 90° angle from the electron beam and is coupled to an objective focusing the image produced on the screen of a CCD camera. Some of the electrons that interact with the sample are backscattered. A small amount of these electrons undergo a Bragg reflection on the lattice planes and strike the phosphorescent screen ⁶⁴. An electron backscatter diffraction pattern (EBSP) is created when several different planes diffract the electron to form the Kikuchi lines ⁶⁵, which correspond to each of the diffraction planes of the lattice (**Figure 17**). It is then possible to link the lines present in the EBSP diagram to the phase and the crystallographic orientation of the material (**Figure 18**).

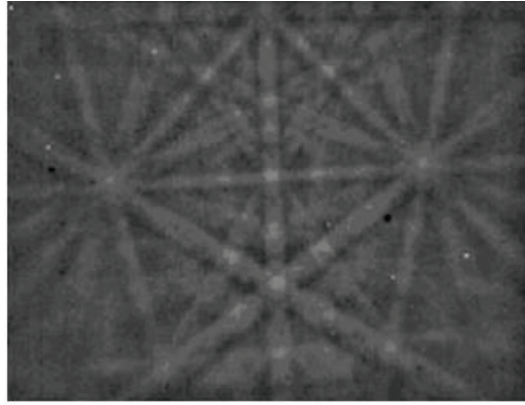


Figure 17: Example of a diffraction diagram ($\text{La}_2\text{Zr}_2\text{O}_7$, 20 kV, $\lambda = 0.086 \text{ \AA}$) (NEEL institute CNRS/UGA UPR2940).

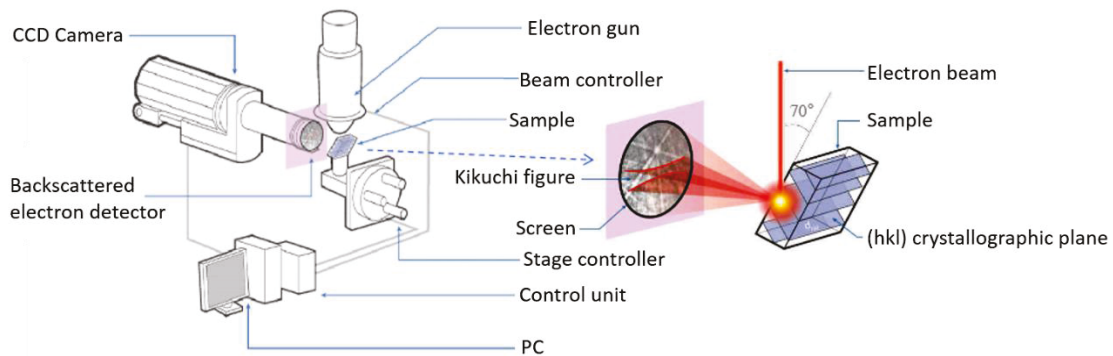


Figure 18: Schematic of the EBSD principle (NEEL institute CNRS/UGA UPR2940).

1.2.3.4. Nuclear microprobe

Nuclear microprobe appeared about fifteen years ago in the field of analytical and imaging techniques using ion beam. Taking advantage of multiple ion-matter interactions accessible at both nuclear and atomic scale, this instrument stands out for its versatility and its excellent analytical performance. The principle of operation of a nuclear microprobe is similar to that of a SEM. Simply, the "probe" is a focused beam of light ions (mostly protons, deuterons, alpha particles) instead of an electron beam. In general, the beam is delivered by a positive ion accelerator in order of energy of MeV. The spatial resolution obtained with such a technique is around a few micrometers (**Figure 19**).

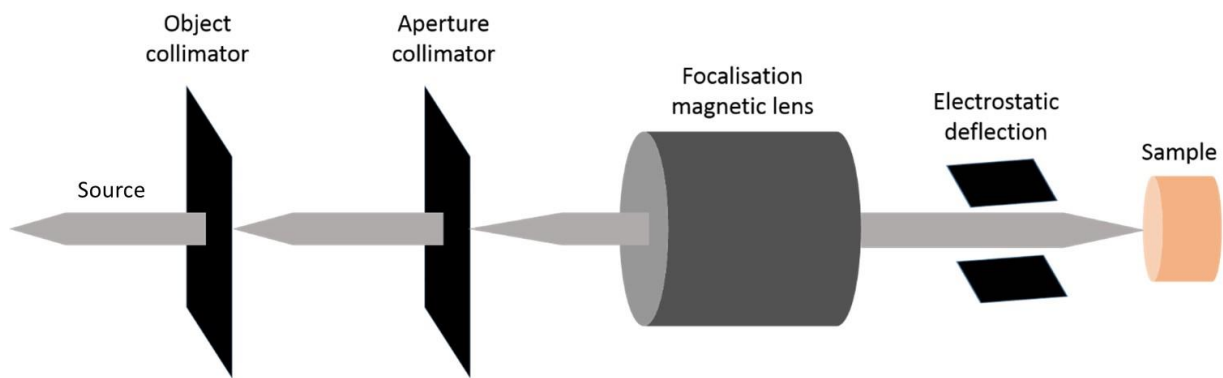


Figure 19: Schematic diagram of a nuclear microprobe: the ion beam is collimated and focused to form a spot with a micrometric diameter in the focal plane. An electrostatic deflection system allows scanning point by point the area to be analysed in order to obtain a 2D or 3D map of the atomic percentage of the element analysed.

Many characterization techniques can be used in conjunction with a nuclear microprobe. A few examples are described here.

Particle Induced X-ray Emission (PIXE)⁶⁶: The detection of characteristic X-rays emitted by the electronic clouds of the atoms excited by the incident ion beam allows to determine the proportion of all the heavier elements present such as sodium (Na). The X-rays emitted by the lighter elements are too low in energy to be detected. This analysis is elemental as it provides the Z number of protons with a sensitivity suitable to access concentrations of elements to the order of ppm.

Particle Induced Gamma-ray Emission (PIGE)⁶⁷: PIGE consists of measuring the gamma spectrum emitted by the nuclei of atoms excited (mainly Coulomb excitation) in order to detect light elements (typically Z less than 19). The identification is isotopic (access to Z and to the number of mass A).

Nuclear Reaction Analysis (NRA)⁶⁸: This characterization technique allows, by choosing the nature of the incident ions and their energy, to generate special nuclear reactions. With ions at few MeV energy, only light elements can be measured, because the Coulomb barrier of heavy nucleus is too high, which prohibits all nuclear interactions. The reaction probability presents

sometimes a narrow resonance depending on the energy of the incident beam. By varying this energy, we can then determine the concentration profile in depth (2-3 μm) in the sample. This method is also isotopic.

Rutherford Backscattering Spectrometry (RBS)⁶⁹: RBS consists in measuring the ion energy after their scattering on the target nuclei. This energy is characteristic of the nucleus mass and allows to determine the mass number A. Ions undergo an electronic deceleration in the crossing material. Hence, this method is sensitive to the topography and to the organization of the material in-depth (eg. organization and thickness of thin layers, impurities location, surface contamination).

1.3. Local probe techniques for surface characterization

It is in 1873, that the first limit of resolution in optics (for the study of a sub-wavelength object) was demonstrated. E. Abbe reported⁷⁰ that light cannot be focused on an infinitesimal point without being diffracted. Diffraction phenomena limit the resolving power of an optical microscope and do not give a point image of a point object, but rather an Airy disc as shown in **Figure 20**. The image of a perfectly circular hole gives a bright disc surrounded by concentric rings alternately bright or dark.

As the spatial resolution limit of an optical device is dictated by its resolving power, two very close points will appear as overlapping regions or as a larger disc when the distance between the two points is inferior to the resolving power of the microscope. In far field, the observation with optical instruments allow to discriminate two points of an object only if the center of the diffraction figure of one of the point is located on the first dark ring of the diffraction figure of the other point.

The resolving power of a far field optical device (R (in meters)) depends on the illumination wavelength λ (in meters), the refractive index n (no unit) and the half opening angle θ (in radians) of the optical device as:

$$R = \frac{\lambda}{2.n.\sin\theta}$$

Hence, in air ($n=1$), R is around $\lambda/2$. By playing with the numerical aperture (O.N. = $n.\sin\theta$) of the device it is possible to raise resolution up to $\lambda/3$ or $\lambda/4$.

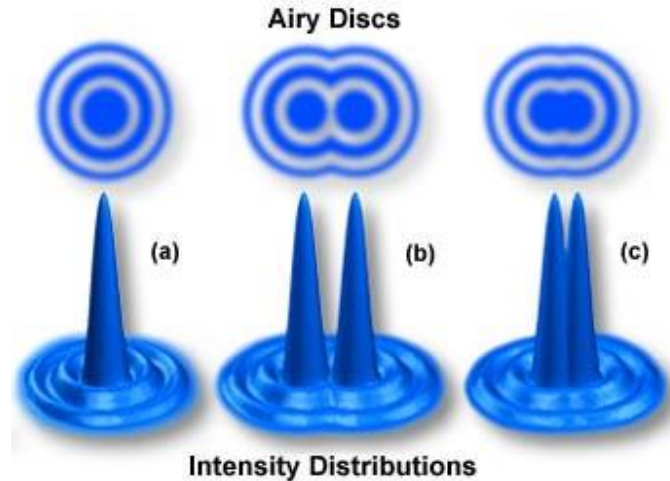


Figure 20: Representation of Airy discs and their associated intensity distribution. (a) Airy disk for a single object (diffraction pattern containing a central maximum surrounded by other orders 1st, 2nd ...). (b) Two overlapping Airy disks for two objects at the limit of optical resolution when the distance between the disks is larger than their radii and they are resolvable. (c) Two overlapping Airy disks in the case of the distance between centers of zero order maxima is less than the width of these maxima ⁷¹.

Figure 20 illustrates the resolution problem encounters by classical far field optical characterization techniques. The electromagnetic field diffracted by a sub-wavelength object is composed of a fundamental mode and several superior modes. The fundamental mode contains information related to large details of the object whereas superior modes contain information related to small details (high spatial frequencies) ⁷².

The superior modes are evanescent. As a result, far field characterization only measures the fundamental mode of the field diffracted by the sample. Thus, the information detected in far field measurements is not sensitive to small details of the object. To capture the contribution of superior modes it is necessary to get very close from the surface in the near field zone (**Figure 21**) ⁷³. Indeed, the amplitude of an evanescent wave decreases exponentially from the interface as a function of distance d . Dipolar model in air shows that the amplitude decrease of the radiated fields in near-field follows a $1/d^3$ law ⁷⁴. The spatial resolution depends on the distance between the observer and the sample but also on the dimensions of the extremities of the probe

used to perform the measurement. The sharper the probe, the narrower the region of field enhancements used as the illuminating beam to characterize the sample.

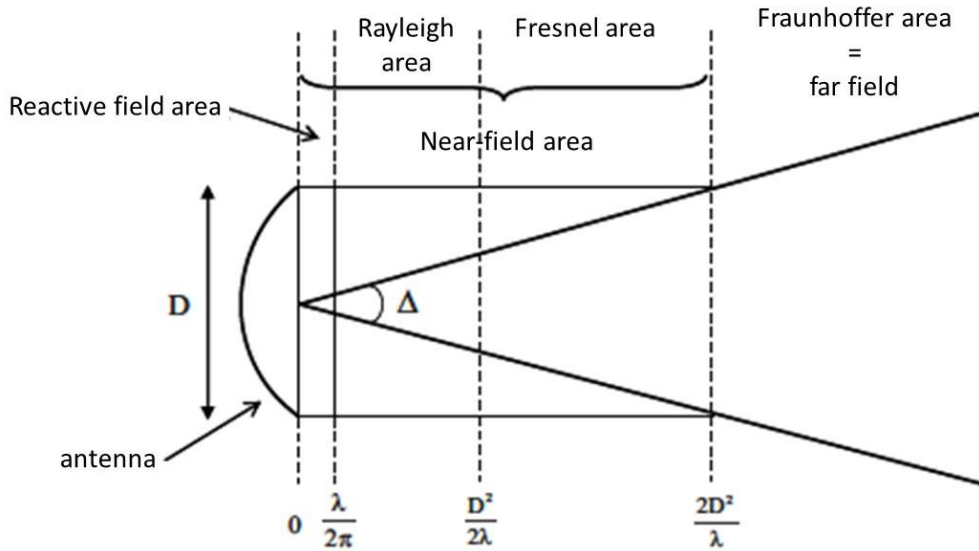


Figure 21: Illustration of far and near-field regions around an emitting antenna.

1.3.1. Photon Scanning Tunneling Microscopy (PSTM)

PSTM⁷⁵ platforms are composed of an optical fiber brought close to the surface of a sample placed on a prism by means of an index gel. The index gel provides optical continuity between the media as well as a good mechanical adhesion. The sample is illuminated by total internal reflection so that the optical fiber frustrates the evanescent part of the wave scattered by the sample surface, but the fundamental mode does not interfere with the measurement.

A schematic of the setup can be seen in **Figure 22**.

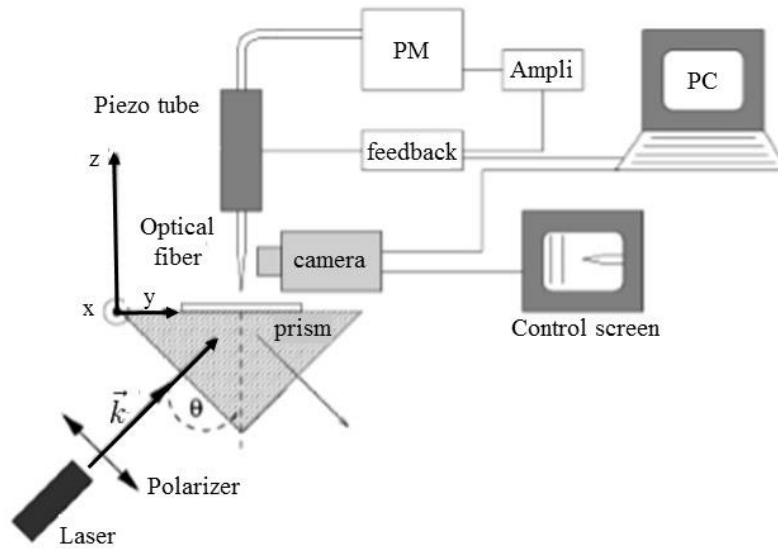


Figure 22: PSTM setup for near-field optical collection of the light emitted by the sample excited by incoming polarized LASER light in Total Internal Reflection configuration⁷⁶.

The interpretation of PSTM images is based on the study of the scattering of electromagnetic surface waves by defects at the sample's surface. Illuminating the sample in a total internal reflection configuration generates bi-dimensional surface waves: these waves propagate in the plane of the sample's surface and their amplitude decrease exponentially in the direction normal to the surface (z direction in the schematics in **Figure 22**). By approaching the local probe (optical fiber) very close to the surface, surface waves can be detected.

Figure 23 presents an example of PSTM images for the detection of optical index changes in a material.

The topographic and PSTM images are recorded simultaneously. In this configuration, the regulation between the tip and the sample is not based on the decay of the evanescent field but on the forces between the probe and the sample. This configuration facilitates the discrimination of the nature of the defects. In fact, for a volume defect, this mode acts as constant height detection whereas for a topographic defect the optical signal at constant height becomes constant. The experimental measurement was performed on a step of $400 \mu\text{m}$ height. Features

of different optical index were positioned on the sample. Topography and optical images are recorded simultaneously. One notice that the optical answer of the topographic step remains constant (excepted on the edge of the step) whereas the AFM image reveals it perfectly (**Figure 23a** and **Figure 23c**). The opposite phenomena is observed of the index step which is reveals by the optical image and not by the AFM one (**Figure 23b** and **Figure 23d**).

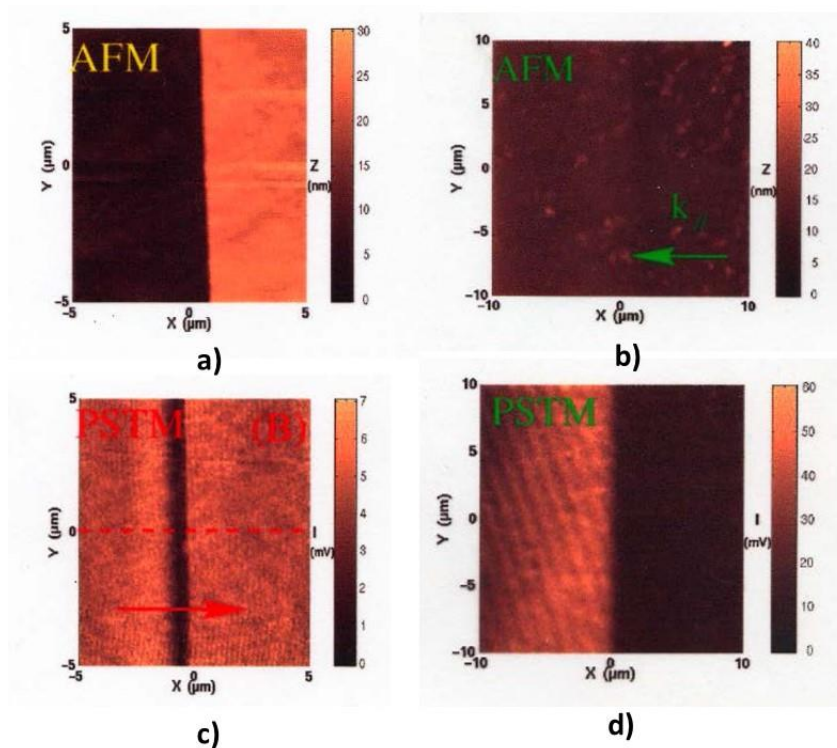


Figure 23: Comparison of AFM and PSTM images on a same sample. (a) Topography AFM image. (b) AFM image of the sample presenting optical index differences. (c) PSTM image of a topographical variation without any optical changes. (d) PSTM image of the sample presenting variations in the optical index⁷⁷.

1.3.2. Conventional Atomic Force Microscopy

1.3.2.1. Working principle

Atomic Force Microscopy (AFM) is a near-field microscopy technique developed in 1986 by Binnig, Quate and Gerber^{78, 79}. AFM belongs to the family of near-field techniques. Its principle is based on the interatomic forces between the sample and the surface with a very fine tip attached to the AFM cantilever. The schematic of the dispositive is represented in **Figure 24**. Before AFM, scanning tunneling microscope (STM) was developed to study conductive or semi-conductive samples by detecting a tunneling current between the tip and the analyzed surface⁸⁰. AFM was developed to overcome the conductivity requirement limitation so that all types of samples (from metal to soft matter) can be analyzed. The major advantage this technique consists in its versatility, in particular to analyze samples in various environments. Thus, studies in liquid medium can be conducted in order to be close to physiological conditions in biology.

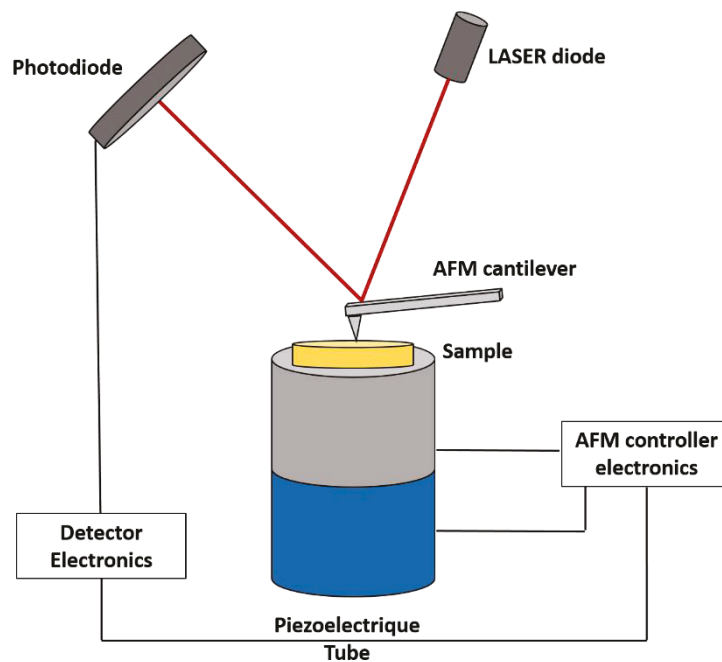


Figure 24: Atomic Force Microscopy setup including the read-out system used to monitor the cantilever deflection and the electronics for feedback loops and sample rastering.

The choice of cantilever's spring constant is a crucial parameter – generally conditioned by the nature of the sample or the type of measurement performed - to realize high quality measurements and AFM images (**Figure 25**). Furthermore, the tip has to be very sharp (a few nanometers) to get the high spatial resolution. The cantilever possesses a spring constant (from 0.01 N/m to 15 N/m) and a natural resonance frequency ranging from 10 kHz to the MHz.

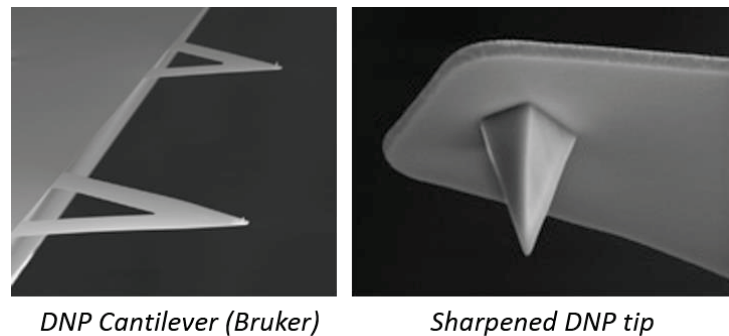


Figure 25: SEM view of the DNP cantilevers (Bruker) (left) and high resolution view of the cantilever tip (right)⁸¹.

AFM is sensitive to forces in the order of piconewtons (10^{-12} N). By adjusting the position (X, Y, Z) of the piezoelectric tube to maintain a constant force between the tip and the surface, through a feedback loop, the topographic information of the sample surface can be unveiled. In conventional systems, scan rate of the order of Hertz is used for the cantilever raster.

1.3.2.2. Different working modes

Contact mode and Lateral Force Microscopy (LFM)

The contact mode or constant force mode consists in monitoring the cantilever/sample force during the scanning of the tip over the sample surface as described above.

The vertical deflection of the cantilever is monitored using a readout system composed of a Laser diode and of a four quadrant photodetector. The cantilever deflection is monitored in focalizing the Laser beam on the cantilever which is then reflected on the photodetector.

To investigate the nature of the force between the tip and the sample, one can perform a “force curve” at a fixed point by varying the tip-sample distance incrementally and recording the vertical deflection of the cantilever. The profile of the resulting curve is presented in **Figure 26**.

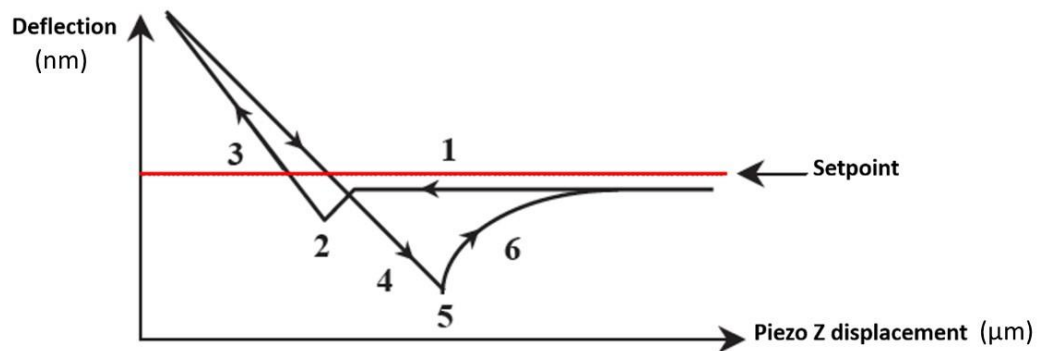


Figure 26: Cantilever deflection vs the piezo z displacement curve. (1-3) are representative of the approach and (4-6) of the withdraw phase.

The different phases illustrated in **Figure 26** can be described as following:

- 1- The tip/sample distance decreases. There is no interaction between the tip and the sample.
- 2- The cantilever bends downward as a result of the attractive forces of the surface. The deflection of the cantilever ‘decreases’ as the tip engages in contact with the surface (electrostatic attraction and/or capillarity forces).
- 3- The tip presses the surface, the cantilever bends upward. The repulsive forces are predominant in the regime.
- 4- The pressure exerted by the tip decreases. The motor initiate the steps to withdraw the cantilever. The tip remains in contact with the sample, now bound by adhesion forces.

5- The tip-sample distance increases further, the tip is subjected to the surface adhesions until the “jump out of contact” point.

6- The tip is free, there is no more (or negligible) interactions between the tip and the sample.

Lateral Force Microscopy (LFM)⁸² is also based on the AFM contact mode. In LFM we measure the cantilever horizontal component of the deflection. The lateral deflection is the result of the friction forces. Their contribution is accentuated when the cantilever moves in a direction normal to the direction (length) of the cantilever (sweep with a 90° angle). This mode is very useful for studying a sample whose surface is composed of inhomogeneous compounds and to enhance contrast at a boundary between different compounds (**Figure 27** and **Figure 28**). Friction signal can be represented as the difference in the signals recorded in the right (A+B) and left (C+D) cells.

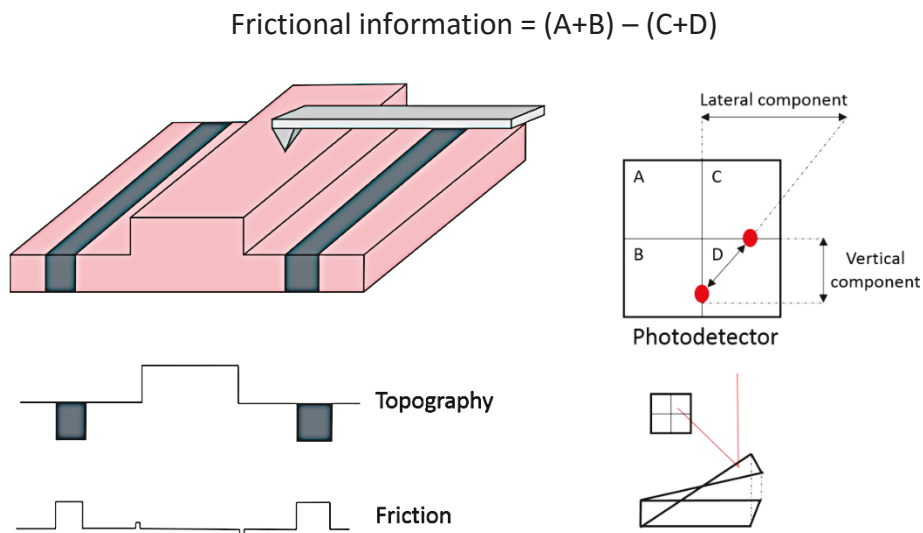


Figure 27: Lateral Force Microscopy principle: the lateral variation of the cantilever deflection is captured to extract the friction profile across the sample.

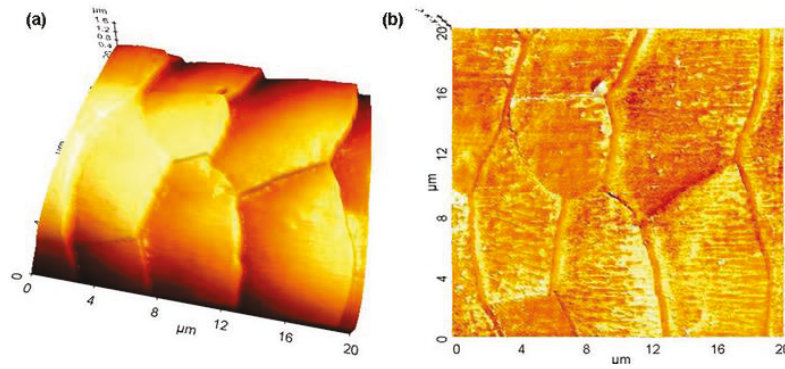


Figure 28: Topography (a) and (b) LFM image of human hair. (20 μm scan size). One can clearly observe the difference in frictional areas of keratin protein in (b) ⁸³.

Oscillant Tapping mode

The friction phenomena between the tip and the sample in contact mode may damage the sample surface, especially for soft materials. Tapping mode was developed to overcome the capillary and friction forces ⁸⁴. Later, it was demonstrated that this mode provides access to the nano-mechanical properties (measured point by point) of the surfaces such as variations in elastic properties of materials regardless the medium used for the study (air or liquid medium) ⁸⁴⁻⁸⁶ (Figure 29).

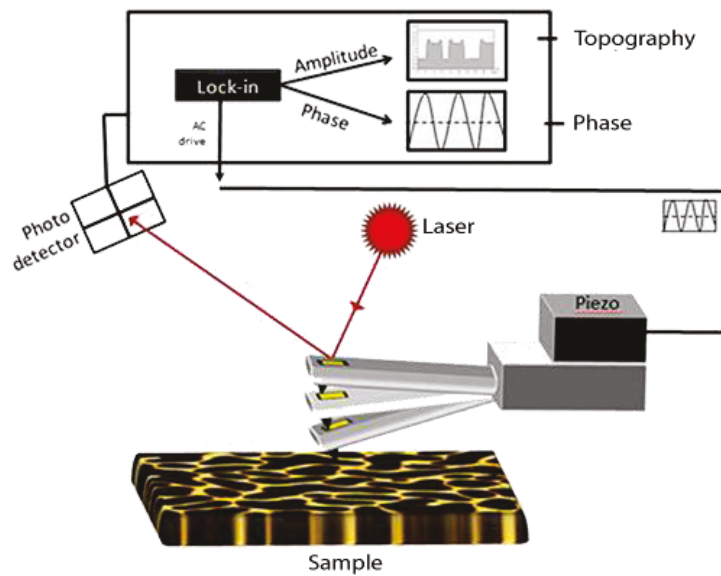


Figure 29: Schematic of tapping mode AFM. The cantilever oscillates close to the surface and the tip intermittently touches or taps the sample. The advantage of tapping the surface is improved lateral resolution on soft samples. Lateral forces such as drag, common in contact mode, are virtually eliminated ⁸⁷.

Peak Force QNM mode (Quantitative NanoMechanics)

Peak Force QNM mode⁸⁸ is based on Tapping mode but allows to measure the mechanical properties of materials such as adhesion, deformation or elasticity⁸⁹ (**Figure 30**). In this configuration, force curves at a frequency range of 0.5 - 4 kHz are acquired at each pixel of the image. Force curves are then used as retro-control for imaging. Resolution equivalent to the classic tapping mode has been demonstrated⁸⁹. This can be used on all types of materials from the inorganic to the organic.

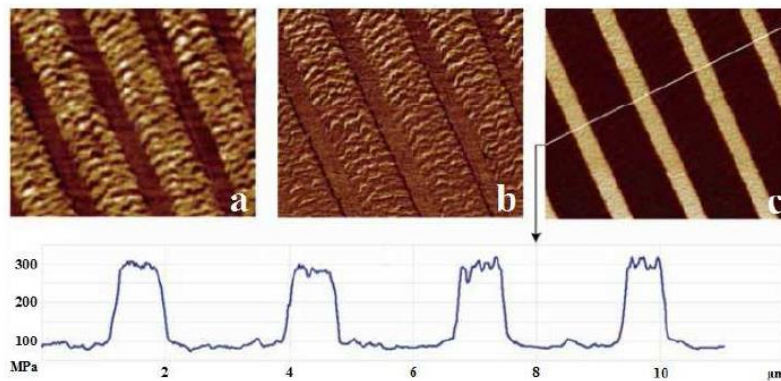


Figure 30: AFM Peak Force QNM images of a multilayer film composed of polymer multi-layers. (Scan size 10 x 10 µm). (a) Topography (b) Adhesion (c) Elasticity⁸⁹.

Force curve modeling for Young modulus extraction

Derjagin, Muller, Toropov (DMT)⁹⁰ is a standard model used to fit tip-sample force curves in Peak Force QNM. The retract part of the force curve, when the cantilever-sample distance increases, is fitted using the DMT model, and the result of the fit corresponds to the reduced modulus E^* calculated by:

$$F - F_{adh} = \frac{4}{3} E^* \sqrt{R(d - d_0)^3}$$

where $F - F_{adh}$ is the force applied on the cantilever, $d - d_0$ the sample deformation and R is the tip radius.

An example of different surface properties provided by Peak Force NM mode (including elasticity) is given in **Figure 31**.

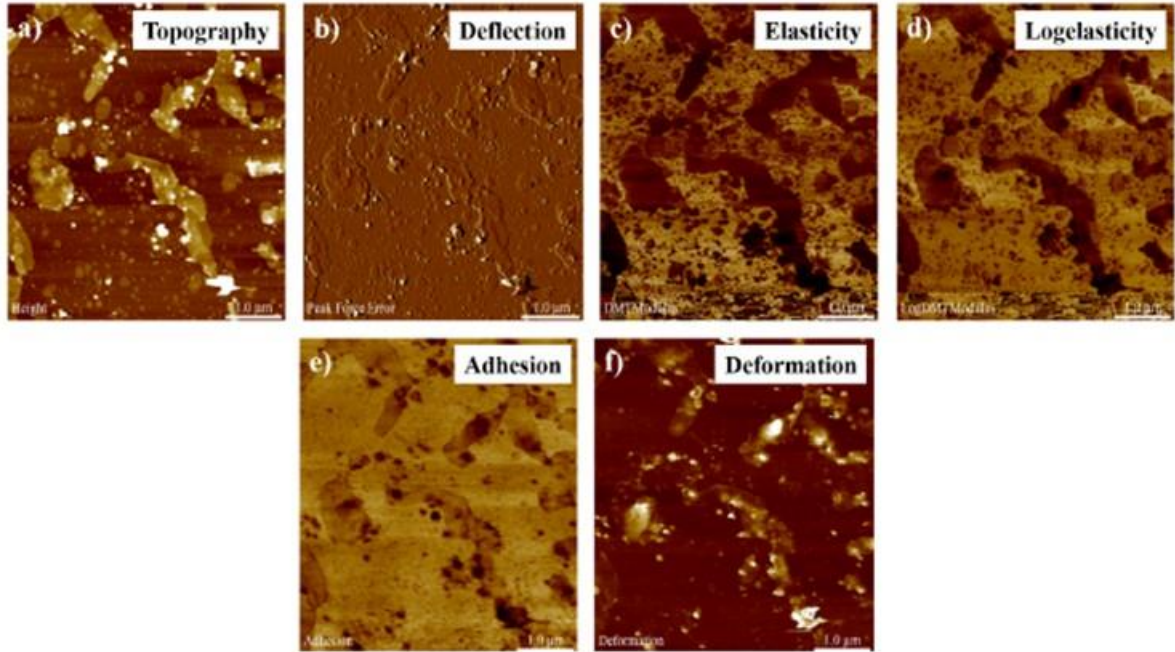


Figure 31: AFM image of human monocyte rafts obtained by Peak Force Mode. (a) Topography, (b) signal error, (c) modulus (elasticity), (d) LogModulus, (e) adhesion, (f) deformation (images Ece Abayke).

1.4. Development of near-field microscopes for subsurface investigation

1.4.1. Scanning Thermal Atomic Force Microscope

Scanning Thermal Microscopy (S_{Th}M)⁹¹ mode was developed to probe thermal properties at the nanoscale level. This technique maps the thermal properties of a sample by using a nanofabricated thermal probe that contains a resistive element near the apex of the probe tip^{92, 93, 94}. This resistor is incorporated into a Wheatstone bridge circuit, which allows the system to monitor the resistance.

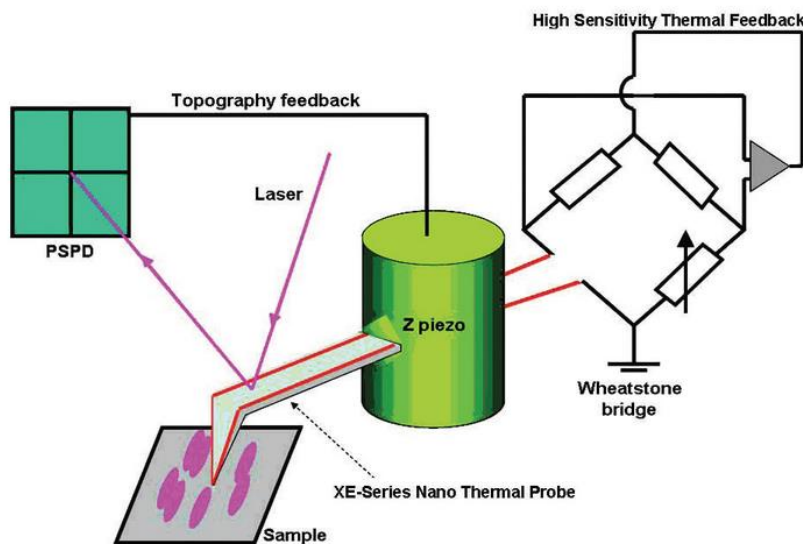


Figure 32: Thermal AFM setup⁹⁵. A special AFM cantilever constitutes the fourth leg of the Wheatstone bridge for temperature measurements.

Figure 32 represents the experimental device of S_{Th}M AFM. A “V” shaped resistive element is mounted at the end of a cantilever. While the distance between the probe tip and sample surface is controlled by usual AFM scheme, the thermal probe forms one leg of a Wheatstone bridge. It is this Wheatstone bridge which is used as a feedback to adjust and balance the bridge voltage in order to measure the probe’s temperature (TCM) or maintain a constant probe temperature (CCM). A topographical AFM image can also be generated from changes in the

cantilever's amplitude deflection. Thus, topographic information can be separated from local variations in the sample's thermal properties, and the two types of images can be collected simultaneously.

Two qualitative sub-modes are available for SThM, the Temperature Contrast Mode (TCM) that allows measuring the temperature variations of the sample and the Conductivity Contrast Mode (CCM) that provides measurement of thermal conductivity variations. Sample temperatures are typically measured on active device structures such as magnetic samples, laser diodes or electrical circuits⁹⁶. Conversely, thermal conductivity is more typically measured on composite samples⁹⁷. In these measurements, a higher voltage is applied to the probe increasing it further the room temperature. The thermal conductivity of the sample will affect the temperature of the probe by draining more or less heat away from the tip.

Although the preferred method for SThM operation is via solid-to-solid direct conduction, it is possible that conduction occurs within the liquid meniscus at the tip surface in the presence of aqueous species, which can also be affected by gas conduction. For this reason the preferred method of operation is to perform the measurements under vacuum conditions. The fundamental limit of resolution of the measurements is proportional to kT , where k is the Boltzman constant and T the temperature. At room temperature, kT is between 10 and 21 Joules. Some of the major applications for SThM are for defect and "hot spot" detection in semiconductors⁹⁸ or the detection of subsurface features⁹⁹, which cannot be observed by AFM. Typical material parameters that can be observed include the thermodynamic characterization of material properties such as conductance, specific heat capacity, and glass transition temperatures¹⁰⁰. The technology is also of particular relevance to pharmaceutical compounds and for the analysis of biomolecules¹⁰¹. **Figure 33** illustrates the potential of this technique with the characterization of local phase transitions in a polymer that are not detectable by classical AFM.

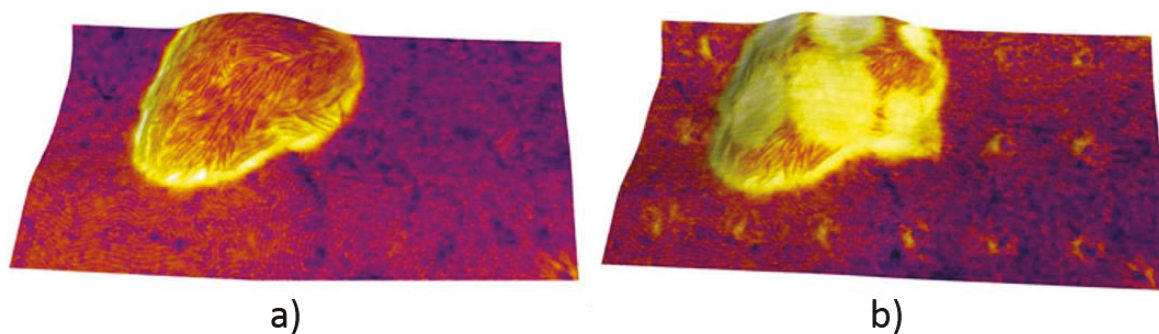


Figure 33: Thermal measurements from a SEBS polymer sample. (a) Topography before thermal measurements. (b) Thermal image which shows induced local phase transitions in the SEBS materials (Scan size: $1 \times 2 \mu\text{m}$)¹⁰².

1.4.2. Nano-Infrared Microscopy (nanoIR)

The nanoIR microscope (developed by Anasys Instruments) combines the high resolution imaging capability of an AFM with the power of infrared spectroscopy to perform chemical characterization¹⁰³.

NanoIR consists of a near-field technique based on photothermal^{104, 105, 106} expansion of a sample due to the absorption of IR radiations^{107, 108}. The sample is placed on an IR-transparent prism and irradiated with an IR nanosecond pulsed laser tuned to a wavelength corresponding to an absorption band of the sample. The absorbed light induced a temperature increase and consequently a rapid thermal expansion of the absorbing material. This local deformation (or expansion) is detected with the AFM tip in contact with the sample. As the expansion is related to the nanosecond scale, the cantilever undergoes a pulse and oscillates on its eigenmodes (**Figure 34**). Mapping this oscillation amplitude versus position creates a spatially resolved map of IR absorption that can be used to localize specific chemical species with sub-100 nm lateral. Tracking the oscillation amplitude while tuning the wavelength leads to the formation of a spectrum for a fixed position of the AFM. We work with the nanoIRTM microscope from Anasys Instruments using an optical parametric oscillator (OPO) as a benchtop tunable IR laser (range $4000\text{-}1000 \text{ cm}^{-1}$). Topographic images were acquired in contact mode with cantilever of 0.03 N/m ($\mu\text{masch HQ:CSC/AIBS}$).

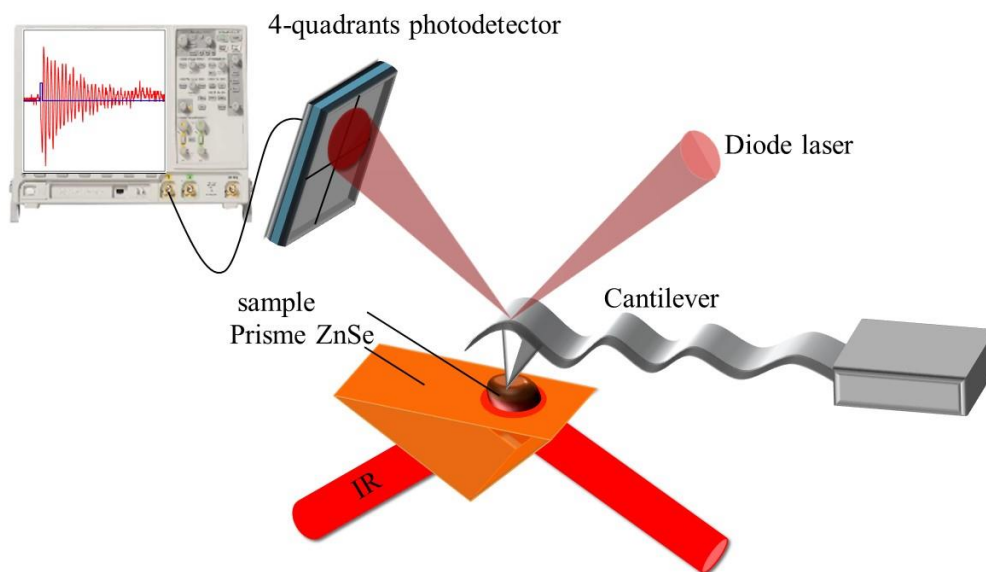


Figure 34: NanoIR setup: molecular vibrations in the sample are excited by illumination in the infrared range using a total internal reflection configuration. The ringing of the cantilever resulting from the pulse of light interacting with the matter is captured by an oscilloscope. Next FFT is performed to extract the absorption spectrum or chemical measurements.

Figure 35 illustrates the use of nanoIR microscopes for mapping the distribution of lipids inside bacteria.

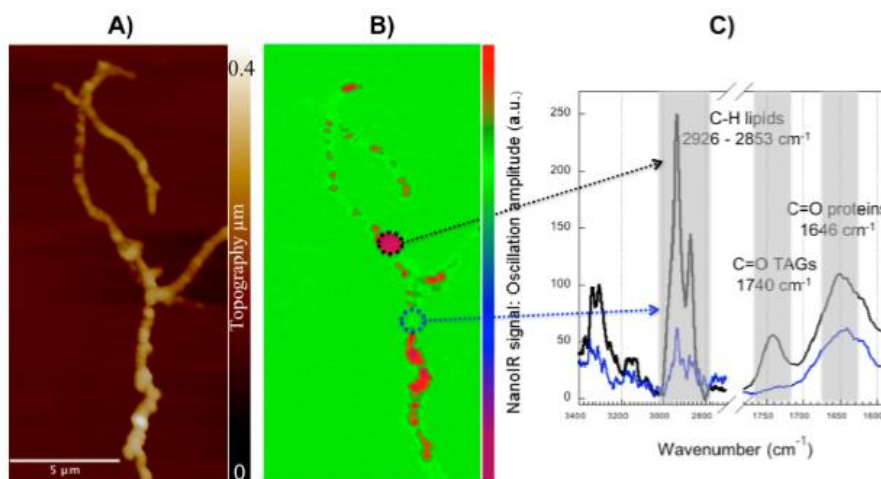


Figure 35: Results obtained with the AFM-IR system on *S. lividans* bacteria: (a) AFM topography, (b) chemical map at 1740 cm^{-1} , and (c) local IR spectra acquired at selected points: on and off a lipid inclusion¹⁰⁹.

1.4.3. Acoustic microscopy

1.4.3.1. Far field acoustic microscopy

Sergei Y. Sokolov, was the first who proposed in 1928 (and later demonstrated) a technique based on through-transmission of sound for detecting irregularity and defects in solids such as metals (sounds waves travel as longitudinal, vibrations whose velocity depends on the elasticity and temperature of the medium) ¹¹⁰. He also proved that high frequency sounds wave could be used to create a new kind a microscope based on a reflective principle ¹¹⁰.

In the far field reflection technique, a pulsed acoustic wave is generated from one side of the sample through the sample and reflected on far side to return to a receiver located at the emission point. When it encounters a defect or a crack inside the material, the acoustic signal is reflected and its traveling time is modified. The traveling time delay can provide a measure of the defect's location. Thus, a map of the material can be generated to illustrate the location and geometry of the defects (**Figure 36**).

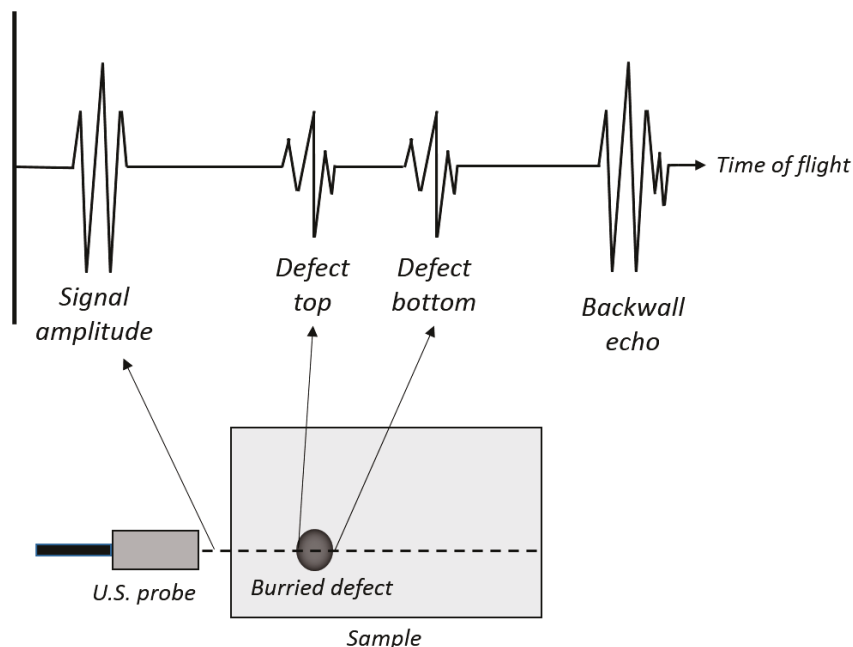


Figure 36: Far-field acoustic microscopy principle. The top and bottom interfaces of the buried defects lead to a reflection of the wave that can be captured by the pulse/detection.

Moreover, in 1937, Sokolov described a technique for underwater imaging called “Sokolov tube” also known under the name of Acoustic Electron-Ray Converter (AERC)¹¹¹. This device is composed of a special Piezoelectric Element Matrix (PEM) lens composed of about 1000 square elements electrically connected to a vacuum cathode-ray tube or Cathode-Ray Converter (CRC). An electron beam scanning this surface converts the electrical image into a time dependent output signal that can be processed and displayed as an image^{112, 113, 114}. In 1955, the first successful experiments were carried at the Andreev’s Acoustical Institute, Moscow, Russia¹¹⁵.

The first scanning acoustic microscope (SAM) was developed in 1973 by A. Lemon and C.F. Quate at Stanford University¹¹⁶. The acoustic microscope principle relies on the fact that the speed of sound in a medium is directly related to physical properties of that medium such as density and elasticity.

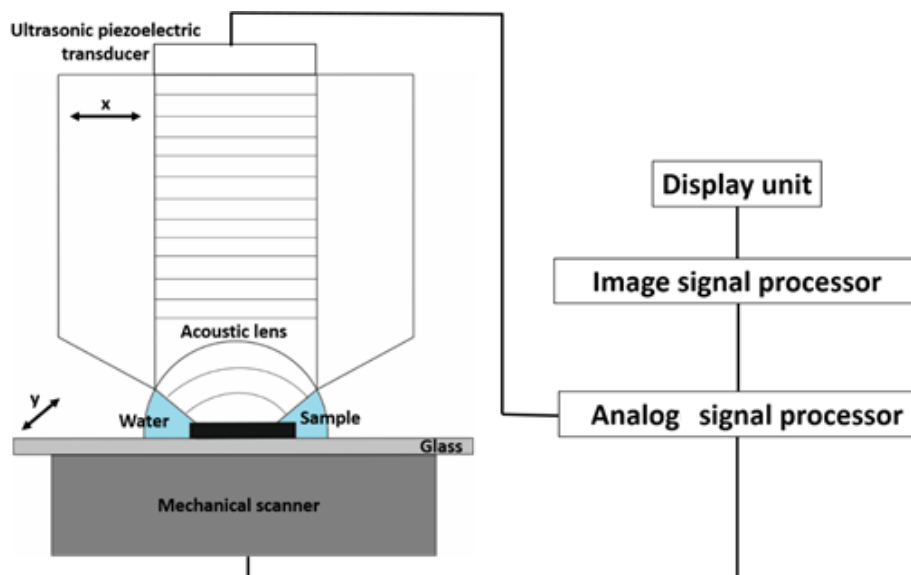


Figure 37: Schematic of the Scanning Acoustic Microscope (SAM) using an acoustic lens to focus the waves onto the sample.

The schematic of the SAM microscope is presented in **Figure 37**. The acoustic wave is transmitted due to a piezoelectric crystal and is propagated inside the sample via a sapphire focalization lens. A suitable coupling liquid is required. SAM image formation is based on a sequential radiofrequency (RF) electrical pulse with a 50-500 ns period and 10-1000 MHz frequency, which is used to excite a piezoelectric transducer fixed on the top of an acoustic lens body. The transducer converts the RF pulse into an ultrasonic wave with the same frequency that is emitted into the lens body. This ultrasonic wave propagates to a spherical cavity coated with a quarter-wavelength-matching layer to increase transmission. The lens cavity is coupled by liquid (usually water) to the sample surface, which is located at the focal point of the spherical lens (the lens with the spherical cavity). The ultrasonic pulse is transmitted and focused by the spherical lens to steer the acoustic wave onto a spot whose size is comparable with the acoustic wavelength in the fluid. Then, the wave is reflected back by the sample. The amplitude of the reflected pulse is proportional to the difference between the acoustic properties of the sample and that of the water at the focal point, so that the amplitude gives a measure of the microscopic properties of the sample at that point. The pulse is reconverted into a RF pulse by the inverse piezoelectric effect of the RF receiver, tuned to the appropriate frequency. The average amplitude of the pulse is determined, converted into a digital signal and sent to a computer imaging system. The lens is then mechanically displaced by a small distance and the process is repeated, usually at 500 *500 points, to form an image¹¹⁷.

This type of microscope can be used both for the observation of hard material and biological sample because unlike light and electron microscopy, biological specimens can be examined without any alteration during sample preparation. **Figure 38** and **Figure 39** illustrate the imaging possibilities of SAM on hard and soft matter, respectively, at different frequencies. As can be seen on the images, the resolution is somewhat limited. Similar to optical techniques, the diffraction limit dictates the spatial resolution of the microscope, hence the resolution is

dependent on the wavelength of the acoustic wave and the artifacts generated by the lens. Another limitation of SAM microscopy is the need to couple the acoustic lens and sample with water, preventing the analysis of water sensitive samples.

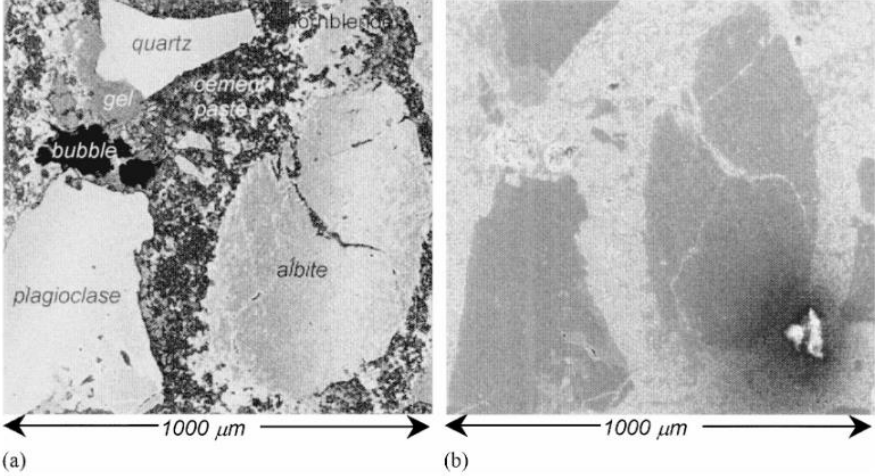


Figure 38: Acoustic (a) and SEM (b) images of a concrete samples made with granitic aggregate grains and Portland cement paste. The acoustic image was set at 400 MHz ¹¹⁸.

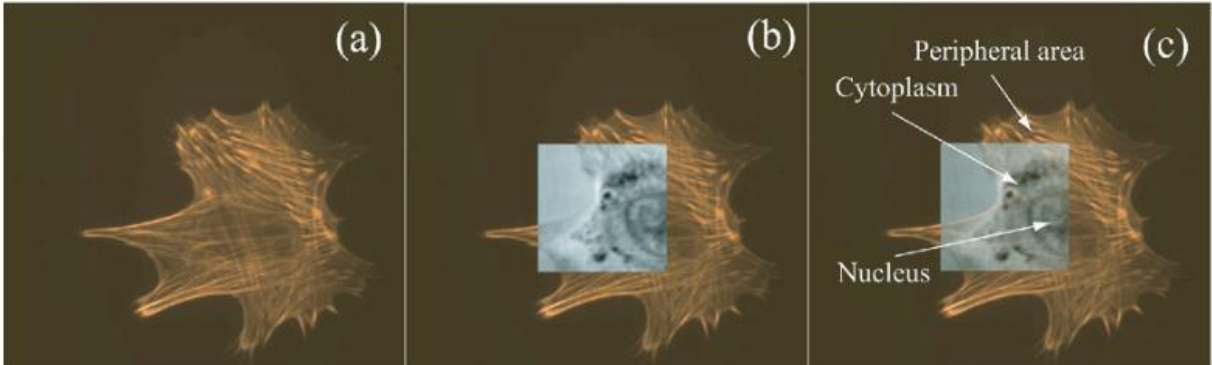


Figure 39: Optical (in color) and overlaid acoustical (in grey) images of embryonic chicken heart muscle cells. The acoustical images have dimensions of 65 x 65 μm and were acquired with a center frequency of 860 MHz ¹¹⁷.

1.4.3.2. Near field acoustic microscopy

We mentioned in previous sections that the apex of the AFM cantilever sensor has a curve radius of only a few nanometers to several hundred of nanometers. The lateral resolution is given by the contact area between the tip radius and the sample radius, which is much smaller than what can be obtained with the wavelength of the acoustic waves.

In order to use the capabilities of ultrasound waves for the volume investigation with nanometer resolution, such as what is offered by the local probe effect of the AFM, idea of coupling acoustic and AFM techniques was explored.

Since 1993, several AFM microscopes combining ultrasound imaging have been developed, including ultrasound force microscopy (UFM)¹¹⁹, scanning acoustic force microscopy (SAFM)¹²⁰, atomic force acoustic microscopy (AFAM)¹²¹, and ultrasonic atomic force microscopy (UAFM)¹²². These techniques can be seen as special types of dynamic force microscopy techniques or as near field microscopy techniques in the scope of “nanoscale ultrasound imaging”. We will describe them here briefly.

UFM was the first acoustic near field microscope reported¹²³. UFM combines the principle of acoustic microscopy with the resolution of the AFM operating in contact mode. As represented in **Figure 40**, UFM can be designed on the basis of a conventional AFM. To implement the acoustic actuation on the sample, the substrate is placed on a piezoelectric transducer connected to a radio frequency (RF) signal generator. Longitudinal waves with a frequency range of few hundred kHz to several MHz selected so that the cantilever response is negligible^{119,124,125} (far above the first resonant mode and away from the higher resonant modes) are launched through the sample. The acoustic wave causes high frequency surface. The sensor tip of the AFM is in contact with the vibrating sample surface and when the threshold amplitude is reached, the sensor tip lifts off from the surface. The deflection and/or torsional vibration of the cantilever

due to its interaction with the acoustic wave are then monitored via a lock-in detection and gives nanometer resolution elastic or subsurface images¹²⁶.

This ultrasonic method can be used to evaluate the elasticity of stiff samples and to detect subsurface defects (**Figure 41**)^{119, 123}, which are not possible by force curves¹²⁷ or force modulation modes^{128, 129}. Although the force modulation mode using a very stiff cantilever (> 1000 N/m) can be used to evaluate a stiff sample, such a cantilever is not suitable for soft samples. UFM can overcome this shortcoming. UFM detection is performed both in liquid medium and in air. UFM is however limited for the characterization of samples that are too large or heavy as the piezoelectric crystal cannot effectively vibrate.

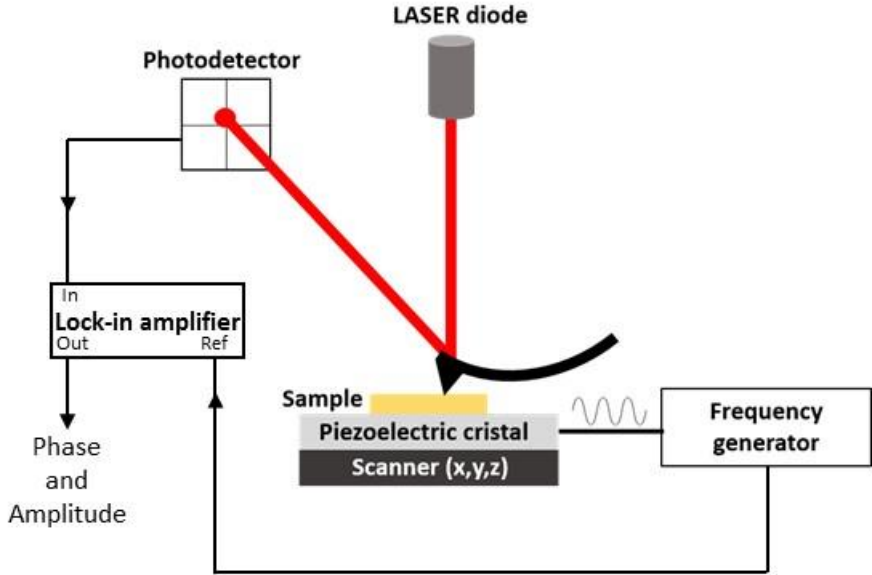


Figure 40: Near-field acoustic microscope setup showing the mechanical actuation of the sample using a piezoelectric crystal connected by a frequency generator.

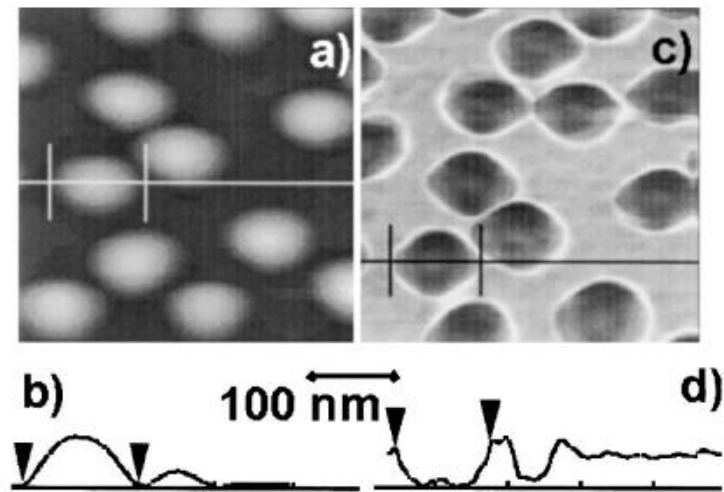


Figure 41: UFM images of Ge dots on Si substrate. (a) Topography (c) UFM image at 3 MHz of Ge dots on a Si substrate (Scan size 400 x 400 nm). The cross section on the UFM image (d) reveals the sharp change in signal at the periphery of the round structure corresponding to a cavity in the center of the Ge dot, while the topography profile (b) is perfectly smooth. Height of the dots is about 15 nm¹³⁰.

AFAM¹³¹ principle is very similar to UFM microscopy with a frequency range limited from 0.1 MHz to 2.5 MHz¹³². Moreover, the configuration can be adapt to excite the sample with acoustic waves generated by piezoelectric crystal located on the AFM probe¹³¹ instead of the excitation of the sample described in UFM. **Figure 42** illustrates images of a piezoelectric lead zirconate ceramic by AFAM.

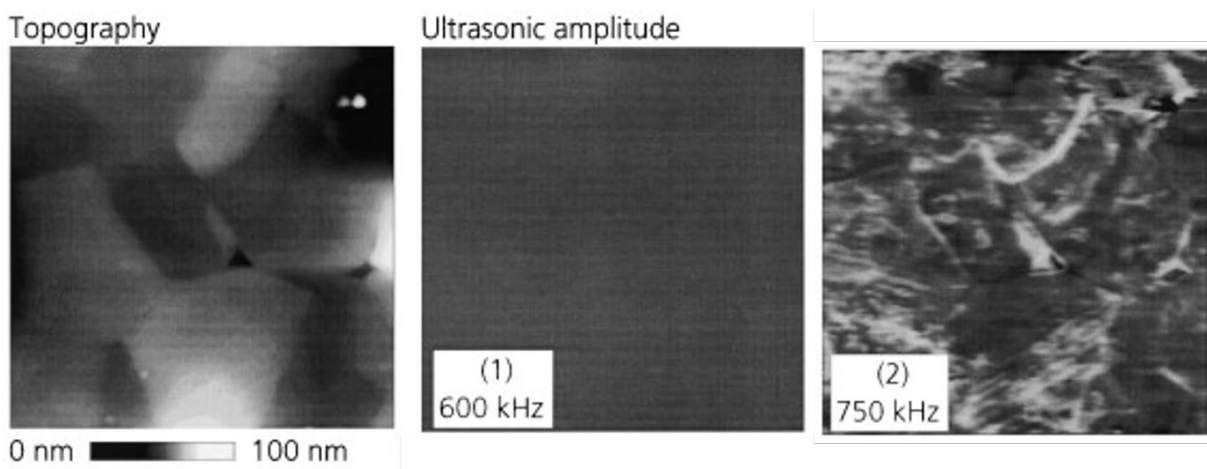


Figure 42: AFAM images of a piezoelectric lead zirconate ceramic at sample actuations of 600 kHz and 750 kHz¹³³.

1.5. Conclusion

Although a multitude of characterization techniques for non-destructive investigation of the volume of materials are available ¹³⁴, most of them do not provide sufficient resolution to achieve early detection of defects at the nanoscale. Conventional techniques offering great sensitivity and spatial resolution do not provide access to subsurface information or consist of destructive analysis of the sample.

The purpose of this work is to achieve continuity of the non-destructive analysis to reach nanoscale resolution in order to understand defect formation and propagation in materials. We aim to develop an early detection and nanoscale resolution technique to characterize both solid materials and biological samples. Moreover, despite the fact that sensitive techniques are available for biology analysis, they generally require the use of markers which may have an impact on biological elements that cannot be assessed. Consequently, the idea is to observe these interactions with high resolution in a non-invasive way is very stimulating. In this work we will focus on two techniques– Mode Synthesizing AFM (MSAFM) and Scanning Microwave Microscopy (SMM) – which we believe can address some of these issues.

Chapter 2 – *From topographic study to the development of tomographic high resolution tools.*

Since the development of near-field techniques in 1982⁸⁰, the need for powerful high-resolution characterization tools capable of probing properties of materials of increasing complexity continued to increase. In 1986, the emergence of atomic force microscopy (AFM) paved the way to surface information with a lateral resolution of a few nanometers for all materials irrespectively of their conductivity^{78, 79}. The rise of AFM then led to new demands in characterization of condensed matter beyond morphological studies, for both solid state and soft materials (i.e. in the biological field). For instance, the ability to study systems in real time requires to significantly increase the image acquisition speed as the performance of about one picture in five minutes in conventional AFM platforms hinders the study of fast dynamic phenomena such as self-assembly or protein conformational changes. Acquisition time saw a breakthrough discovery in 2008 with the development of high speed atomic force microscopy (HS-AFM) by the group of Professor Toshio Ando^{135, 136} (Kanazawa University, Japan), capable of imaging the dynamics of myosin and dynamic molecular processes in photoactivated bacteriorhodopsin using 1 frame per second^{135,136}. Another limitation of AFM is its limitation to surface characterization. Hence research efforts in near-field techniques are very active in developing new tools for non-destructive and non-invasive volumetric investigations, while maintaining the nanoscale resolution of AFM. New techniques such as acoustic microscopy and microwave microscopy emerged from these efforts^{112, 113, 137, 138}.

This chapter is centered on the description of the capabilities of two new near-field techniques to realize high resolution characterization with the aim of achieving 3D tomographic studies. Namely, we focus on the techniques developed in the context of this work based on acoustic and microwave microscopy for non-invasive and non-destructive volume characterization^{139,140}.

2.1. Mode Synthesizing Atomic Force Microscopy (MSAFM)

Acoustic microscopy is a technique that enables in-depth imaging due to the propagation of ultrasonic waves and the change in their propagation in the presence of defects. Ultrasound waves propagating through the sample are sensitive to material properties such as stiffness or density^{141, 142, 143}. A change in these properties is likely to cause variations of amplitude and phases of the incident sound wave.

In the present work, we used AFM to circumvent the diffraction limit of conventional acoustic microscopy¹⁴⁴. We show here that using this novel approach, it is possible to analyze the sample in-depth while maintaining the inherent atomic resolution of AFM¹³⁹.

The first AFM devices coupled with acoustic waves such as Ultrasonic Force Microscope (UFM)^{123, 126} and Atomic Force Acoustic Microscope (AFAM)^{131, 121} were based on the interaction a single ultrasound wave launched below the sample with the subsurface defects inside the sample, and monitoring the amplitude and phase of the wave detected at the surface of the sample by the cantilever. Then, to increase the detection sensitivity the technique was improved by adding a second ultrasound wave. The two-wave actuation AFM technique is called Scanning Near Field Ultrasound Holography (SNFUH)¹⁴⁵ and Mode Synthesizing Atomic Force Microscopy (MSAFM)¹⁴⁴ was introduced next as a generalization of the multi-wave actuation and nonlinear mixing.

The principle of MSAFM is based on the study of amplitude and phase variations of the surface waves generated by the interference of two ultrasonic waves carried out by the imaging system. In the first report of MSAFM¹⁴⁶, two (or more) forces were exerted on the system through forced oscillations of the cantilever probe and/or the sample at frequencies, noted f_p and f_s , respectively (Figure 43a). In the case of the microscope developed our laboratory, the actuation frequencies applied were varied from 1 MHz to 10 MHz. Using this approach, a subsurface

inhomogeneity can be detected due to variation in amplitude and phase of the mixing signal at frequency $|f_p - f_s|$ (from several kHz to hundreds of kHz) monitored using lock-in detection to perform the appropriate analysis of the signal from the AFM photodetector¹⁴⁷. Using calibration samples, the signals were shown to be sensitive to subsurface defects such as nanoparticles and nanostructured defects^{142, 148, 149, 139, 150}. **Figure 44** illustrates this phenomenon in a simple schematic. The synthesized wave is modified by the presence of a buried particle inside the sample. The heterodyne detection used is sensitive to such changes. Heterodyne detection consists in transposing the energy of a part of the spectrum at a lower frequency (called intermediate) to make the detection possible. Heterodyne scheme of detection was used for all MSAFM measurements in order to circumvent the limitation of the AFM detection (cut-off after a few MHz) and to make it possible to tune the MSAFM modes synthesized (difference in particular) with the resonance of the cantilever in contact with the sample when necessary.

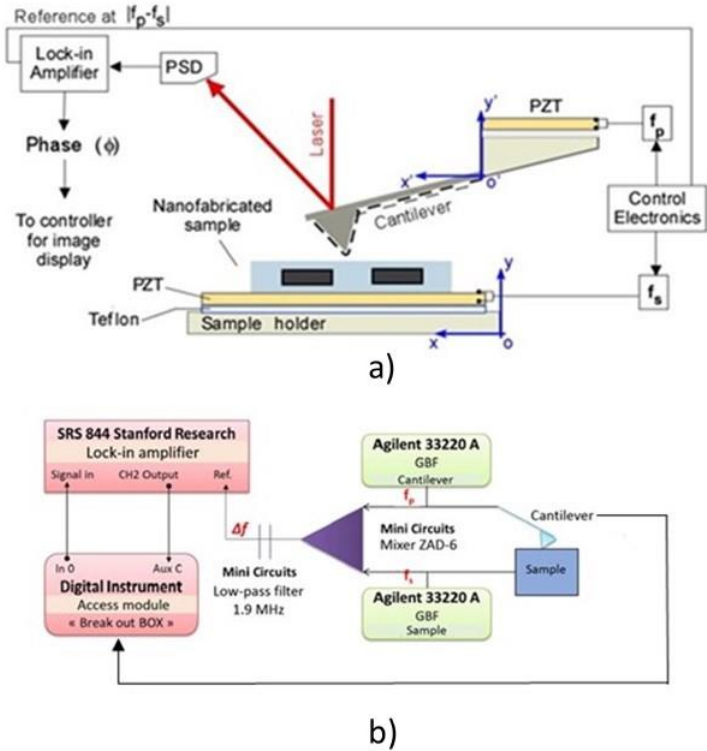


Figure 43 : MSAFM setup. (a) Experimental setup of MSAFM¹⁴⁴. (b) Electronic setup for AFM in acoustic mode¹⁴⁴.

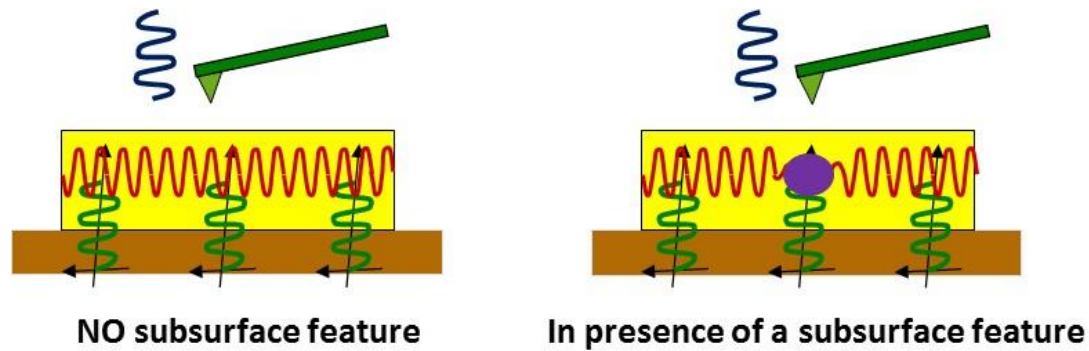


Figure 44: Detection principle of a subsurface defect (purple sphere) in a homogeneous material (yellow slab). The acoustic wave of f_p frequency is represented in blue and the f_s frequency wave in green. The resulting wave of the nonlinear interaction is represented in red and presents a $|f_p - f_s|$ frequency.

In our experimental setup, acoustic waves are generated by two frequency generators (AGILENT 33220A) connected to piezoelectric ceramic (PI France) components of a 0.5 mm thickness and resonances in the MHz range (CuNi electrode, ceramic PZT PIC 151). A lock-in detection is used (SRS 844 Lock-in Amplifier from Stanford Research Systems). The two outputs of the frequency generators are also connected to a mixing circuit (Mini circuits mixer ZAD-6) followed by a low pass filter (DC 1.9 MHz) to isolate the reference signal Δf (defined by the difference in frequency $\Delta f = |f_p - f_s|$) for the lock-in measurement. The input of the lock-in is the signal from the AFM detector. The acoustic image is formed by displaying the amplitude and phase reading performed at each point after rerouting the signal measured to the auxiliary input channel (Aux C) of the acquisition board of the microscope AFM using the AFM signal access module. The image appears on the canal "Aux C" whereas the topographical image remains on the canal "Height". The setup of the experiment is represented in **Figure 43**.

2.1.1. Advances in Quantitative Nanoscale Subsurface Imaging by Mode-Synthesizing Atomic Force Microscopy

This part reports on advances towards quantitative non-destructive nanoscale subsurface investigation of a nanofabricated sample based on mode synthesizing atomic force microscopy (MSAFM) with heterodyne detection addressing the need for a quantitative approach to correlate the role of actuation frequencies of the probe f_p and the sample f_s with depth resolution for 3D tomography reconstruction. By developing a simple model and validate the approach experimentally through the study of the nanofabricated calibration depth samples, consisting of buried metallic patterns¹³⁹, we demonstrate new avenues for quantitative nanoscale subsurface imaging. Our findings enable the reconstruction of the depth profile of the sample and allow high fidelity resolution of the buried nanostructures. Non-destructive quantitative nanoscale subsurface imaging offers great promise in the study of the structures and properties of complex systems at the nanoscale¹³⁹.

2.2.1.1. Theoretical approach

AFM and related techniques mostly provide surface properties, while the observation of subsurface nanoscale defects remains a challenge. Detection of nanoscale structures buried under several hundreds of nanometers, well below the contact radius of the AFM tip, was demonstrated using acoustic based methods^{144, 151, 152}. As the operating principle of MSAFM is founded on the nonlinear mixing of two ultrasonic waves, in this study one wave is launched at the base of the AFM probe at frequency f_p , and a second wave is launched at the sample base at frequency f_s ^{153, 154} (**Figure 43**). The mixing product occurring as a result of the nonlinear tip-sample interaction thus contains subsurface information^{130, 155, 156, 157}. Furthermore, previous works on biological samples^{158,159} underline the interest for quantitative volume characterization. However, the development of a theoretical model and the design of calibration samples for volume investigations are quite challenging^{160, 152, 161}. Here we study the impact of

frequency difference $\Delta f = |f_p - f_s|$ and ultrasonic frequency range (used for actuation) on the investigation depth $z_{\Delta f}$ using a simple theoretical model and verify the results experimentally. Although considered in previous work^{162, 150}, a thorough determination of the effect of Δf on $z_{\Delta f}$ is still lacking. To overcome this, a predictive calculation based on the evaluation of the attenuation coefficients of the respective ultrasonic waves, is established here to link $z_{\Delta f}$ with the applied frequencies (f_s and f_p) and the difference frequency Δf . We consider two ultrasonic waves S_p and S_s , launched at the base of the probe and the sample, respectively, and assume that their respective amplitudes A_p and A_s are such that:

$$S_p(t) = A_p e^{-\frac{\alpha_p z}{v}} \cos(\omega_p t + \varphi_p) \quad (1)$$

$$S_s(t) = A_s e^{-\frac{\alpha_s z}{v}} \cos(\omega_s t + \varphi_s) \quad (2)$$

where α_p and α_s are the attenuation coefficients, and $\omega_p = 2\pi f_p$ and $\omega_s = 2\pi f_s$ the frequencies of the respective waves. v is the velocity of ultrasonic waves in the material (in our case the velocity is considered the same for both waves). As it was reported by Verbiest et al¹⁵² and Cantrell et al¹⁵³ that the subsurface information is contained in the oscillation at the difference frequency Δf , we focus here on the mixing product resulting in the resulting signal detected S . Under the assumption that $A_p = A_s$ as the tip and the sample interact, S is such that:

$$S = 2A(z) \cos(\Delta\omega t + \Delta\varphi_a) \cos(\Delta\Omega t + \Delta\varphi_p) \quad (3)$$

with $\Delta\omega = \frac{|\omega_s - \omega_p|}{2} = 2\pi \frac{|f_s - f_p|}{2} = \pi\Delta f$ and $\Delta\Omega = \frac{\omega_s + \omega_p}{2}$,

and the attenuation amplitude of the mixed wave $A(z)$ is:

$$A(z) = A_0 e^{-\left(\frac{|\alpha_p - \alpha_s|z}{v}\right)} \quad (4)$$

In heterodyne detection, one only monitors the oscillation at frequency Δf , so we simplify the expression:

$$S'(t) = A(z) \cos(\Delta\omega t + \Delta\varphi_a) \quad (5)$$

Eq. (5) shows the role of the attenuation amplitude $A(z)$, which depends in turn on the attenuations coefficients α_p and α_s as shown in **Eq. (4)**. Hence, $S'(t)$ will be maximal when $A(z)$ is maximal, i.e. when $|\alpha_p - \alpha_s|$ reaches its minimum value. We detected the changes in amplitude and phase of the oscillation at Δf and linked the results to propose a relationship between the frequency difference Δf and the investigation depth $z_{\Delta f}$. The results are presented in **Figure 45** for a selected combination of parameters.

It is important to precise that **Eq. (3)** describes the mixing product occurring as a result of the tip-sample interaction. In previous studies, the behaviour of nanomechanical frequency difference mode generation by developing a numerical simulation of the semi-analytical results obtained for the amplitude of oscillation at the difference frequency resulting from such mixing was explored¹⁶³. The results point out that:

(1) Such mixing is optimum as the force verifies a volume integrated Lennard-Jones (LJ) potential;

(2) The oscillation at the difference frequency is expected to be more sensitive to long-range Van der Waals power form than to the short-range power form¹⁶³. The results predicted by the theory were validated experimentally and the study also showed the effect of tip-sample distance d on the amplitude of the difference mode resulting from such mixing¹⁶³. In addition, other works including recent theoretical study by Verbiest et al¹⁶¹ and Cantrell et al¹⁶⁴ described other aspects of the dynamical aspect of the technique, including replacing the LJ potential by

a Derjaguin-Muller-Toporov (DMT model) interaction and demonstrating the importance of the repulsive regime in the system. Here, our attempt is to offer a simplified approach of the mixing and focus on understanding the "depth perception" of the technique. As it was reported in previous works that the subsurface information is contained in the oscillations at the difference frequency, we decided here focus on the mixing product.

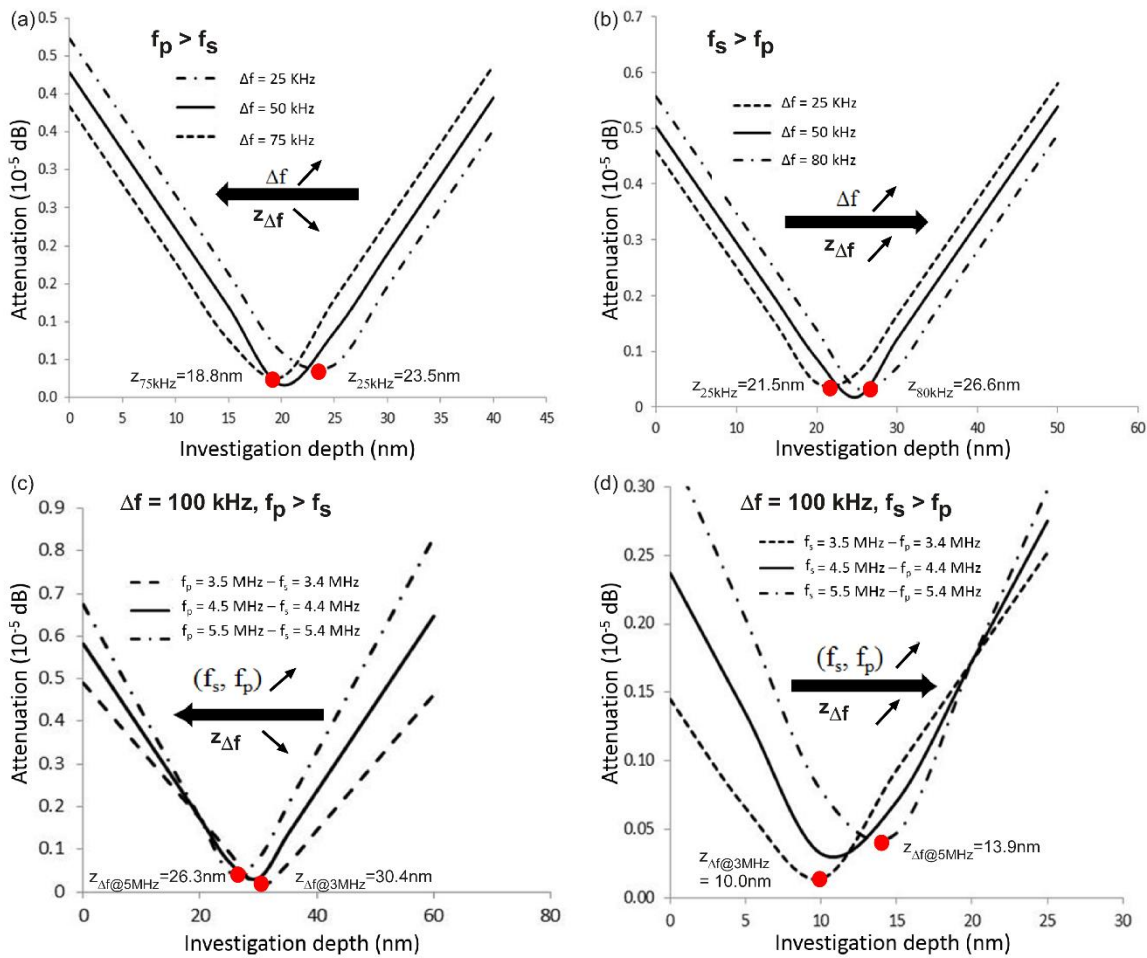


Figure 45: Predicted evolution of the investigation depth $z_{\Delta f}$. (a) Evolution of the attenuation coefficient in case of $f_s < f_p$. The value of tip frequency f_p was fixed at 4.500 MHz while the sample frequency f_s progressively decreased from 4.475 to 4.425 MHz. (b) Evolution of the attenuation coefficient in case $f_s > f_p$. The sample frequency was fixed at $f_s = 4.500$ MHz while the tip frequency f_p increased from 4.525 MHz to 4.580 MHz. (c) Influence of change of frequency range on the investigation depth z_f in case $f_s < f_p$ for a fixed $\Delta f = 100$ kHz. (d) Influence of change of frequency range on the investigation depth z_f in case $f_s > f_p$ for a fixed $\Delta f = 100$ kHz

2.2.1.2. Relationship between the frequency difference and the investigation depth

During its propagation in the bulk of the material, the energy of ultrasonic waves is attenuated via various mechanisms (reflection, refraction, scattering, absorption...). Overall, attenuation $A_z(dB)$ (which is related to $|A(z)|^2$) follows an exponential law that can be expressed in terms of intensity I_0 at the entrance of the material and the intensity I_z at the depth z : $A_z(dB) = 10\log(I_0/I_z)$. Consequently, for a given material and a given ultrasonic frequency, the attenuation $A_z(dB)$ increases linearly with investigation depth $z_{\Delta f}$ such that: $A_z(dB) \propto \alpha z_{\Delta f} \propto fz$ where α is the attenuation coefficient (in $dB \cdot cm^{-1}$), f is the frequency (in Hz), and $z_{\Delta f}$ (in cm). In addition, the attenuation coefficient α expressed for each component α_p and α_s , depends on the depth $z_{\Delta f}$ as follows:

$$\alpha = e^{-\frac{f \cdot z_{\Delta f} \cdot \ln(10)/10}{v}} \quad (6)$$

Thus, calculating the minimum resulting from attenuation of the mixed waves is connected to the absolute value of the difference $|\alpha_p - \alpha_s|$ of the attenuation coefficients. This coefficient is calculated for each Δf value under various sets of parameters (**Figure 45**).

For example, if considering $f_p = 4.500$ MHz and $f_s = 4.450$ MHz, i.e. a difference $\Delta f = 50$ kHz as depicted in **Figure 45a** (solid curve), by plotting $A_z(dB)$ as a function of the investigation depth $z_{\Delta f}$, a minimum in attenuation can be observed at $z_{\Delta f} = 20$ nm. This investigation depth $z_{\Delta f}$, can be linked to the attenuation amplitude $A(z)$ according to the Eq. (1.2). We then repeat this calculation for systematic combinations of parameters to understand the evolution of the attenuation and $z_{\Delta f}$ as a function of f_p , f_s , their difference and frequency range.

2.2.1.3. Influence of the order relationship between f_p frequency and f_s frequency

We now explore how the depth of investigation $z_{\Delta f}$ varies as a function of the difference frequency Δf and on whether $f_s < f_p$ or $f_s > f_p$ (**Figure 45a** and **Figure 45b**).

Case of sample frequency lower than probe frequency

The value of probe frequency f_p was fixed at 4.500 MHz and the sample frequency f_s progressively decreased from 4.475 to 4.425 MHz. The numerical model applied in the case of decreasing values of f_s highlights a shift of the minimum of absorption as a function of the difference frequency Δf used (**Figure 45a**). Note that for a fixed f_p , a decrease in f_s corresponds to an increase of the frequency difference Δf , from 25 kHz to 75 kHz respectively. We observed a shift of the minimum attenuation to lower depths during sample investigation. These results suggest that (all other parameters considered here being set) for an increase of Δf equal to 25 kHz, we observed a decrease of the depth of investigation $z_{\Delta f}$ in the sample of about 4-5 nm.

Case of sample frequency higher than probe frequency

The sample frequency was fixed at $f_s = 4.500$ MHz while the probe frequency f_p increased from 4.525 MHz to 4.580 MHz. As can be seen in **Figure 45b**, an increase in difference frequency Δf leads to a shift of the minimum attenuation, in the direction of the greater investigation depths. For an increase of $\Delta f = 25$ kHz, the depth of investigation in the sample augmented of 4-5 nm.

2.2.1.4. Influence of a change in frequency range

To complete the study of the influence of the frequency sets used in MSAFM on the investigation depth $z_{\Delta f}$, the impact of the frequency ranges used on $z_{\Delta f}$ was explored. By maintaining Δf constant, the behavior of the attenuation coefficient is given from the curves in **Figure 45c** and **Figure 45d** as a function of $z_{\Delta f}$ for three different frequency ranges : 3 MHz range, 4 MHz range and 5 MHz range. For the two cases considered $f_s > f_p$ or $f_s < f_p$, $z_{\Delta f}$ appeared to change with the range of frequency used. For example, when $f_s < f_p$ (**Figure 45c**), a smaller $z_{\Delta f}$ was measured for (f_s, f_p) in the 5 MHz range than for (f_s, f_p) in the 3 MHz range. The opposite behavior was predicted in the case of $f_s > f_p$ (**Figure 45d**).

Thus, our results show that the shift of the attenuation curve, and consequently $z_{\Delta f}$, depends not only on the frequency difference Δf but also on the range of the frequencies f_s and f_p . In addition, we unveil a change in behavior for the two cases $f_s > f_p$ or $f_p > f_s$.

2.2.1.5. Experimental validation of the numerical model

For experimental verification of the model, we used the MSAFM technique described below (see schematic in **Figure 46**). Silicon nitride cantilevers (DNP-S, Bruker, $k=0.12\text{N/m}$) were used for all the experiments. We estimated the contact radius of $30\pm 10\text{ nm}$ after MSAFM analysis on standard diamond calibration sample. The phase response of the oscillation was monitored and sent to the AFM controller to display the image for each step of Δf . After acquiring a sequence of images at various Δf , the corresponding depth information could be extracted from each image to reconstruct a depth profile of each sample.

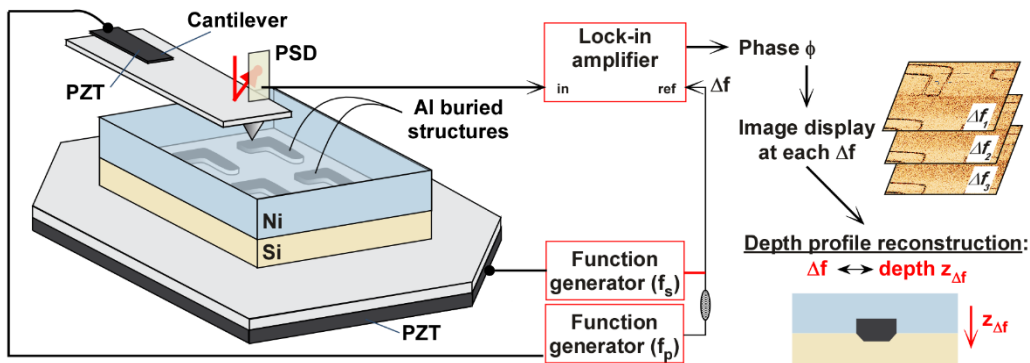


Figure 46: Experimental setup of MSAFM used to validate our model. The structures designed were probed using a tip and sample actuators of f_p and f_s , respectively. The signal of the difference $|f_p - f_s|$ was monitored heterodyne detection. The phase was captured to successive Δf . The reconstruction of the depth profile was obtained by measuring the width of the features on each image.

To that end, two sets of calibration samples with buried metallic patterns were fabricated by nanolithography using electron-beam lithography (e-Line^{Plus}, Raith). A layer of 300 nm thick electro-sensitive polymer poly(methyl methacrylate) (PMMA) was deposited on a silicon

substrate. The electro-sensitive resin was then insulated point by point by electron beam exposure. Next, a combination of solvents was used to dissolve the marked areas of the polymer, therefore revealing the desired patterns. Reactive ion etching (RIE) was performed to etch the design patterns into the Si substrate. The patterned silicon surface was controlled by AFM to determine the etch depth in silicon (34 ± 2 nm) and the angle edge α ($79\pm 1^\circ$) (**Figure 47**), which was verified for 10 different samples per set.

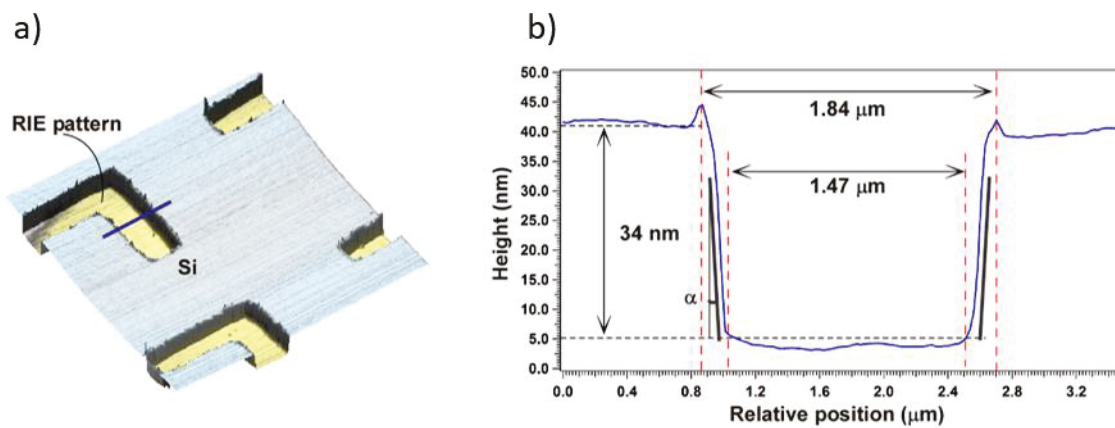


Figure 47: Calibration of the reactive ion etching (RIE) step used for fabrication of the sample. (a) Topography AFM image after reactive ion etching. (b) Cross section extracted at the selected blue line on (a).

The buried structures were obtained by Al deposition, polymer lift-off and a final Ni layer deposition. The calibration samples thus consist of buried aluminum (Al) structures covered by a nickel (Ni) layer. In the first set of samples (**Figure 48a**), the Al structures were 114 ± 2 nm in height, covered by 95 ± 2 nm thickness of Ni. The cross section of the pattern, obtained from the topographical AFM image, reveals a height difference of 80 nm resulting from the mismatch between the thicknesses of Al deposited and the initial depth etched in the silicon substrate (**Figure 48b**). The second set of samples (**Figure 48c**) was obtained by deposition of a 17 ± 1 nm Al layer and coating with a 95 ± 2 nm Ni layer. This pattern exhibited dips of 17 ± 1 nm on the surface, resulting from the mismatch between the Al thickness and the depth silicon etching

(**Figure 48d**). In addition the width of the surface features in after Ni deposition were measured by AFM and are indicated on the respective schematics (1.96 μm in sample series 1 and 1.83 μm in sample series 2).

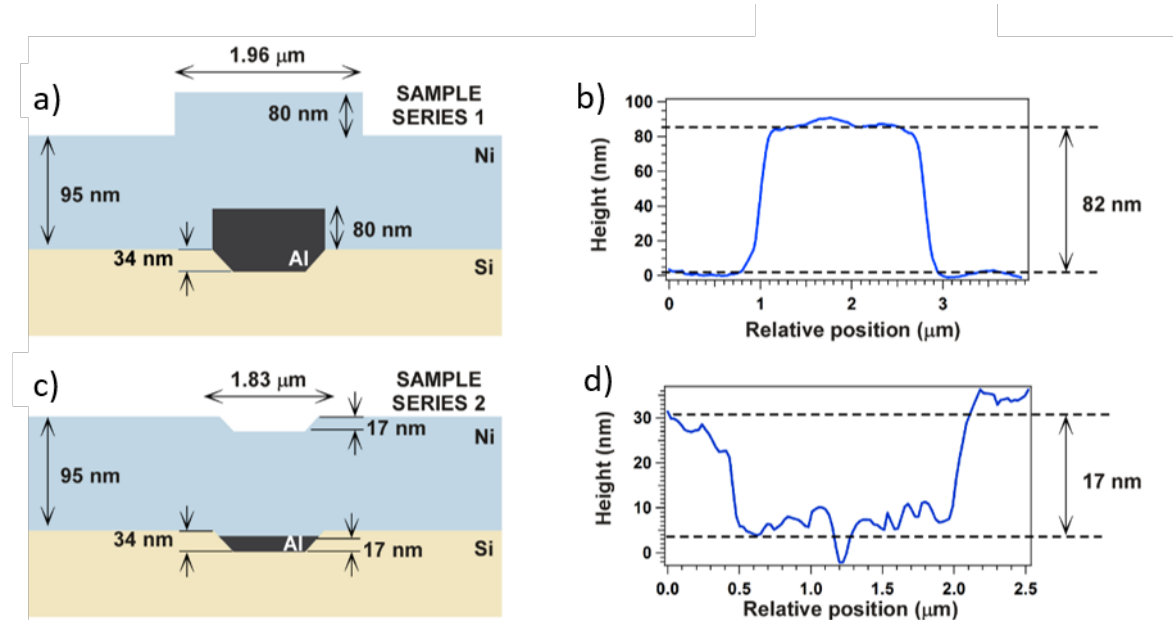


Figure 48: Two model samples developed for quantitative nanoscale subsurface imaging with MSAFM. (a) Schematic of the design of sample 1. (b) Profile representative of the topography of sample 1. (c) Schematic of the design of sample 2. (d) Profile representative of the topography of sample 2.

To determine the relevance of the numerical model in the study of buried samples, we compared the results presented in **Figure 45** with experimental results obtained on the calibrated samples, using the same parameter as those considered for the numerical study. In all cases we fixed the driving amplitude $A_p = A_s = 4 V_{pp}$. MSAFM phase images were acquired for a set of frequencies from 20 kHz to 420 kHz at each step of 10 kHz. The results are described in **Figure 49** to **Figure 51**. Note that the set of frequencies selected to acquire the images presented here did not coincide with the natural resonances of the cantilever.

Case of sample frequency higher than probe frequency

Here f_s was fixed at 4.300 MHz and Δf was increased by decreasing f_p . The MSAFM phase images were obtained at different Δf , starting from 20kHz and sequential increase of 10kHz. Three of the images obtained during this sequence are depicted in Figure 49: (a) at $\Delta f=20$ kHz, (b) at $\Delta f=70$ kHz, and (c) at $\Delta f=420$ kHz. We observed that each one of the MSAFM images corresponds to a specific investigation depth $z_{\Delta f}$ as the contour of the buried pattern (highlighted by the dashed blue line on the MSAFM images in **Figure 49** appears clearly on the images due to phase variation induced by the interface. The structures exhibited different dimensions (width and length) for each Δf . To measure the width of the patterns, as indicated by the solid blue line on the MSAFM images, the cross-section was extracted for each image (right column in **Figure 49**) to perform the width measurement.

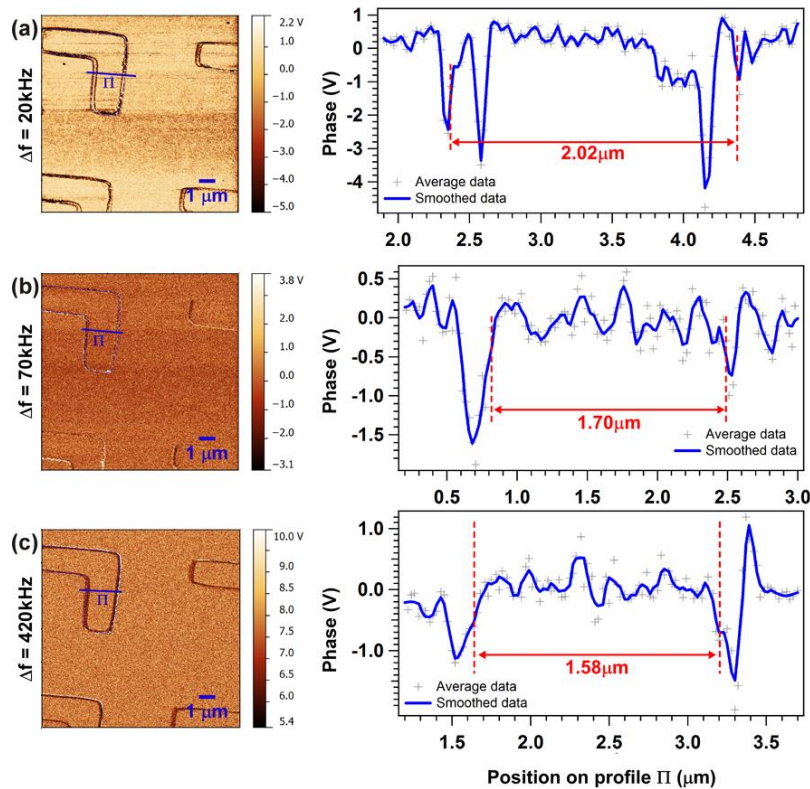


Figure 49: MSAFM phase images at various Δf frequencies (Scan size $10 \mu\text{m}$ acquired at scan rate of 0.5 Hz). (a) $\Delta f = 20$ kHz – width extracted at the section $\pi = 2.02 \mu\text{m}$. (b) $\Delta f = 70$ kHz – width extracted at the section $\pi = 1.70 \mu\text{m}$. (c) $\Delta f = 420$ kHz – width extracted at the section $\pi = 1.58 \mu\text{m}$. Phase were measured in a specified range ($\pm 10\text{V}$) corresponding to a range in degrees of ($-180/+180$ degrees).

A clear variation in width of the pattern with respect to Δf was measured. It may be noted that in this case, in **Figure 49**, the width decreases when Δf increases. The width profile of the buried pattern was described in **Figure 47** i.e. etching angle of $\alpha \sim 79^\circ$, and the width of the pattern decreased from $1.84 \mu\text{m}$ at the surface to $1.47 \mu\text{m}$ at the bottom of the structure. According to the dimensions of the patterns in the calibration sample and the behavior we predicted from the numerical model, the change in width observed in the acoustic phase images is in good agreement with a tunable investigation depth $z_{\Delta f}$. In order to quantify $z_{\Delta f}$ in the experimental data, the frequency values used in the experiment were applied to the numerical model discussed in previous sections. With this approach, Δf step of 10 kHz could be correlated to a depth variation through a nearly linear relationship as shown in **Figure 50a**.

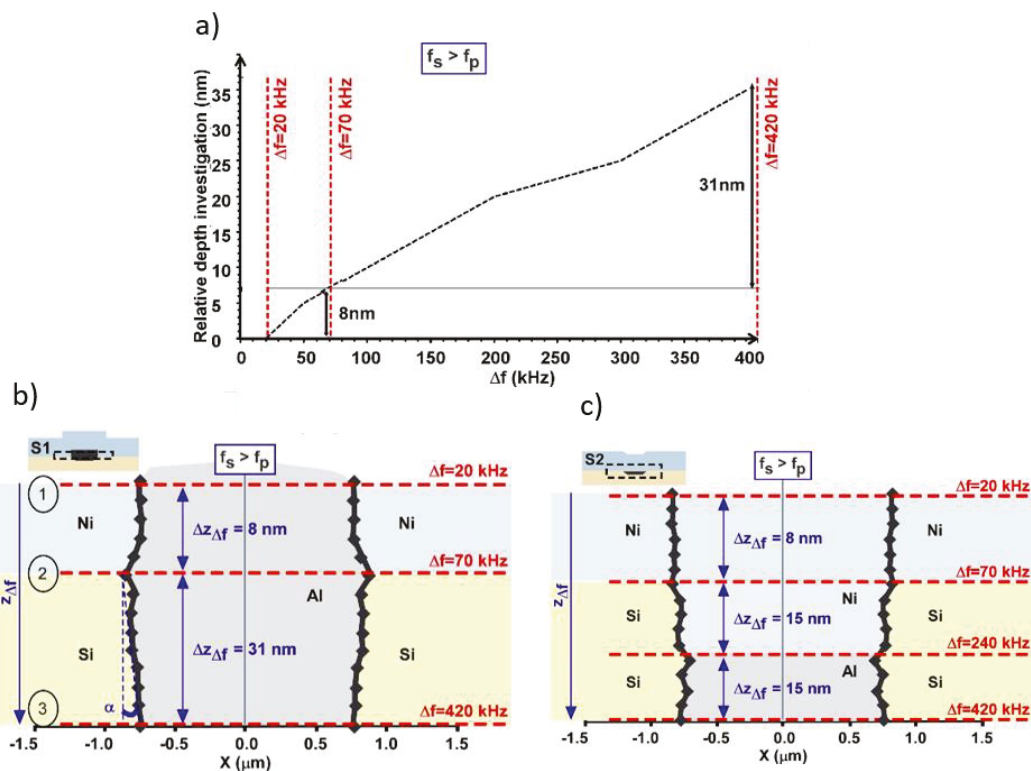


Figure 50: Subsurface composition reconstructions of the depth profile of calibration samples #1 and #2 based on MSAFM measurements and numerical model for the case in which $f_s > f_p$. (a) Representation of the dependence of relative depth investigation as a function of Δf in the case $f_s > f_p$ with fixed $f_s = 4.300 \text{ MHz}$. (c) Reconstruction of the depth composition of sample #2 (area depicted in inset) profile pattern in case $f_s > f_p$ based on the compilation of MSAFM data with (f_s, f_p) in the 4 MHz range.

By combining the width of the buried structures extracted from the cross-sections of the MSAFM phase images and the investigation depth $z_{\Delta f}$ for each Δf using the numerical model, we could reconstruct the depth profile characteristic to the samples (**Figure 50a** and **Figure 50b**). Note that the depth scale (z) is not respected on the graph. Line 2 in **Figure 50b** indicates the Si/Ni interface. The experimental results used to reconstruct the pattern profile agree well with the tapered angle resulting from the RIE etch. In addition, the etching depth obtained from the reconstruction using the numerical model is equal to 31 ± 2 nm (in the Si layer in **Figure 50b**), which is in agreement with the AFM profile in **Figure 47** (34 ± 2 nm). As a confirmation of the approach, we also verified the angle: the angle measurement between the points 2 and 3 in **Figure 50b** indicated an angle of $79 \pm 2^\circ$, instead of $79 \pm 1^\circ$ measured experimentally on ten different samples. As a whole, these results are in good agreement with the profile of sample calibration.

Case of sample frequency lower than probe frequency

The experiment was repeated in the case $f_s < f_p$ with a fixed f_p equal to 4.300MHz. The profile pattern is obtained in a similar manner as the previous case with the assumption that a Δf increasing corresponds to a diminution of the investigation depth (**Figure 49c** to **Figure 49d**). Under these conditions, there is a good correlation between the profile and the numerical model. However investigation takes place at a closer vicinity of the surface. The smallest value of Δf corresponds to the deepest investigation depth and we could find the boundary delimitation Si-Ni (dotted red line in **Figure 51**) at $\Delta f = 30$ kHz.

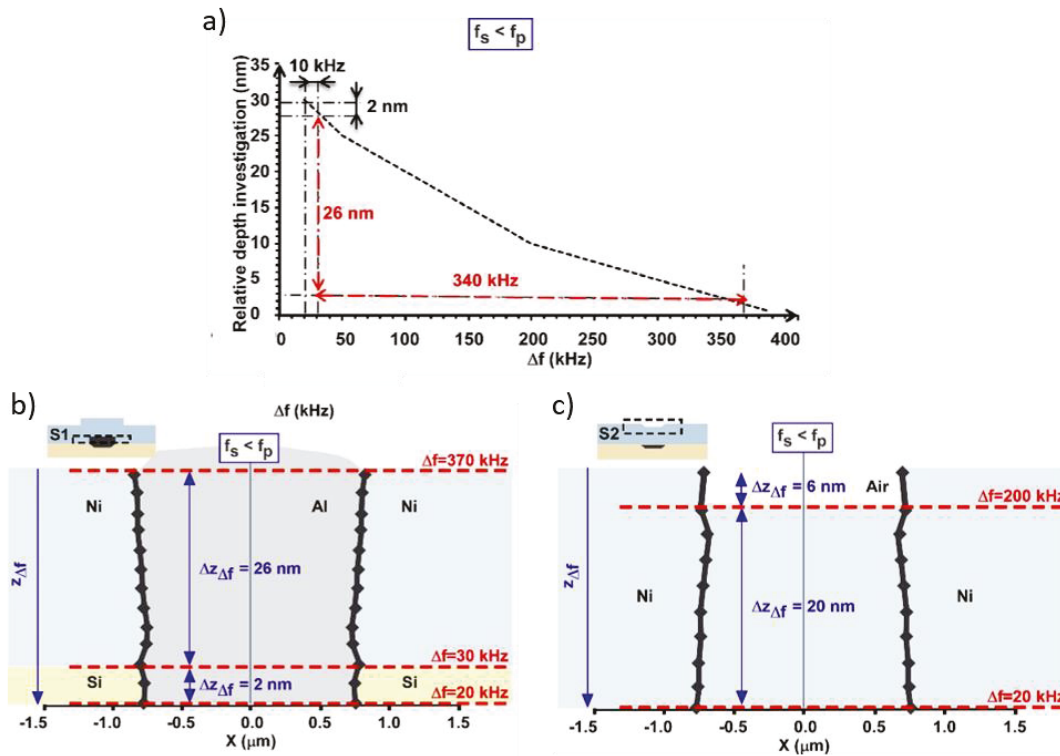


Figure 51 : Subsurface composition reconstructions of of calibration samples #1 and #2 based on MSAFM measurements and numerical model – $f_s < f_p$ case. (a) Curve calculated to link the relative depth investigation to Δf (b) Reconstruction of the depth composition of sample #1 pattern (area depicted in inset) in case $f_s < f_p$ based on the compilation of MSAFM data with fixed $f_p = 4.300$ MHz. The depth was extracted from the curve in (a) as indicated by the markers of Δf and relative difference in height. (c) Reconstruction of the depth composition of sample #2 profile (area depicted in inset) pattern in case $f_s < f_p$ based on the compilation of MSAFM data with (f_s, f_p) in the 3 MHz range.

The same study is realized on sample #2, together with the numerical modeling. Thus, the two cases $f_s > f_p$ (with f_s fixed at 4.3 MHz) and $f_s < f_p$ (with f_p fixed at 3.6 MHz) were studied and the results are presented in **Figure 50c** and **Figure 51c**, respectively. In **Figure 50c** the results show that the values of the profiles (obtained by MSAFM) associated with the investigation depth calculated with the numerical model provide a value of 30 nm of total silicon etching, including a 15 nm of aluminum thickness (the border of each zone is identified by the dotted boundary in **Figure 50c**, in good agreement with AFM measurements presented in **Figure 47**. In the last experiment, the frequency was in the 3 MHz range. The results (**Figure 51c**) show,

in accordance with the numerical model results, that the variation in the depth investigation was modified. In this case, the investigation occurs less deeply in the sample.

In the MSAFM configuration, the difference mode synthesized upon tip-sample interaction is very sensitive to characteristics of the tip-sample interactions and provides higher spatial resolution compared to conventional AFM methods. Here we took advantage of all the previous works mentioned above to extract and quantify the volume information contained in the rich dynamics of the system. In addition, we have also taken into account other components of the system to confirm our results.

For instance, the frequency difference used to form the images presented here does not coincide with any of the eigenmodes (natural resonance frequencies) of the cantilever used, both away from the sample (free cantilever) and in contact with the sample (see two spectra below presented in **Figure 52** and **Figure 53**).

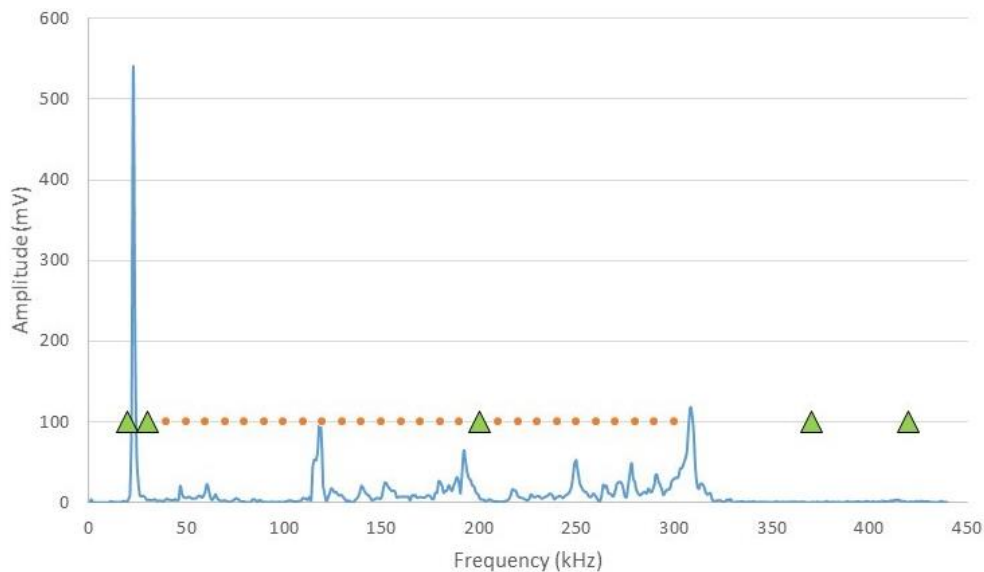


Figure 52: Frequency spectrum of the Bruker DNP-S cantilever ($k= 0.12\text{N/m}$). The peaks of the blue curve correspond to the natural resonance frequencies of the free cantilever ($f_0 = 20\text{kHz}$, $f_1 = 120\text{ kHz}$). The difference frequencies used in the measurements presented in Figure 3-5 are indicated in the graph (yellow dots), ranging from 20 kHz to 300 kHz by step of 10 kHz. The selected frequencies are represented by the green triangular markers (i.e. 20 kHz, 30 kHz, 70 kHz, 200 kHz, 270 kHz, 370 kHz, and 420 kHz).

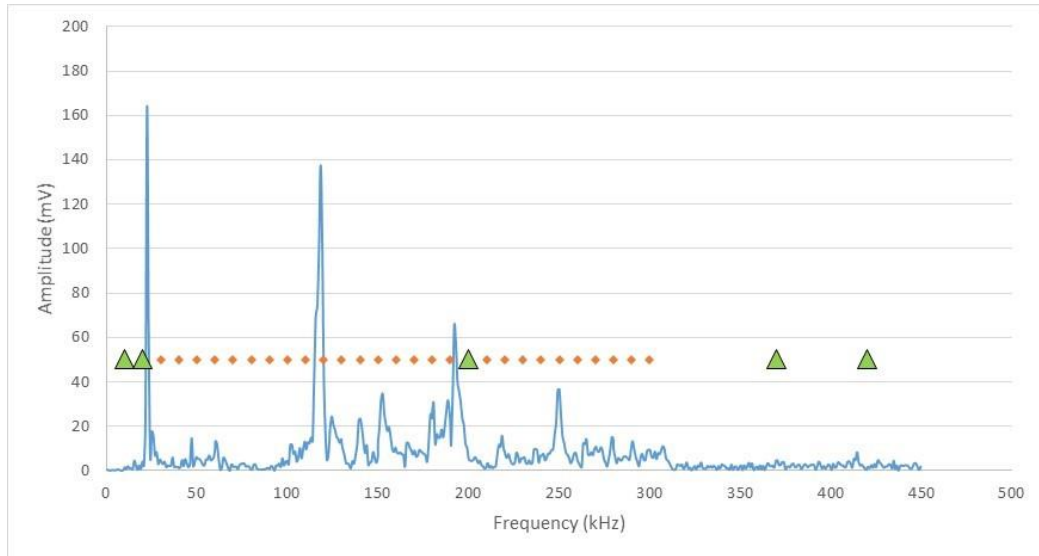


Figure 53: “Contact” frequency spectrum of Bruker DNP-S cantilever ($k= 0.12\text{N/m}$). The peaks of the blue curve correspond to the resonance frequencies of the cantilever in contact with the sample. The difference frequencies used in the measurements presented are indicated in the graph (yellow dots), ranging from 20 kHz to 300 kHz by step of 10 kHz. The selected frequencies are represented by the green triangular markers (i.e. 20 kHz, 30 kHz, 70 kHz, 200 kHz, 270 kHz, 370 kHz, and 420 kHz).

The force applied by the probe on the sample was carefully controlled. With a tip-sample interaction greater than 100pN, topography was found to influence the signal detected by the cantilever, likely due to increasing nonlinearity in the interaction.

Finally, the results reveal the presence of the defects in the sample. On the AFM images (**Figure 54**), it is possible to note that these contours exhibit (**Figure 54a**) a lower contrast than the images obtained in the etch area (**Figure 54b**). This phenomenon may be due to the wave propagation in nickel in presence of subsurface stacking fault, showing depression on the topographical AFM image ¹⁶⁵ (**Figure 48c**). We observe that on the two samples, for the same range of frequency and when $f_s > f_p$, the investigation depth is equivalent (39 nm for sample #1 and 38 nm for sample #2). In both cases, the MSAFM phase images revealed the same etching area in silicon with Al depositing. On the other hand, when $f_s < f_p$, we used a different range of frequency (f_s, f_p) with the same Δf . The results show that the relative investigation depth is

equivalent in both cases and equal to 28 nm for Δf equal to 350 kHz, but not for the same area in the sample. In accordance with the numerical prediction, when the couple (f_s, f_p) is in a lower range of frequency, the MSAFM mode used probes a smaller depth of the sample, which explains the transition zone air-nickel on the graph of sample #2 (**Figure 51c**).

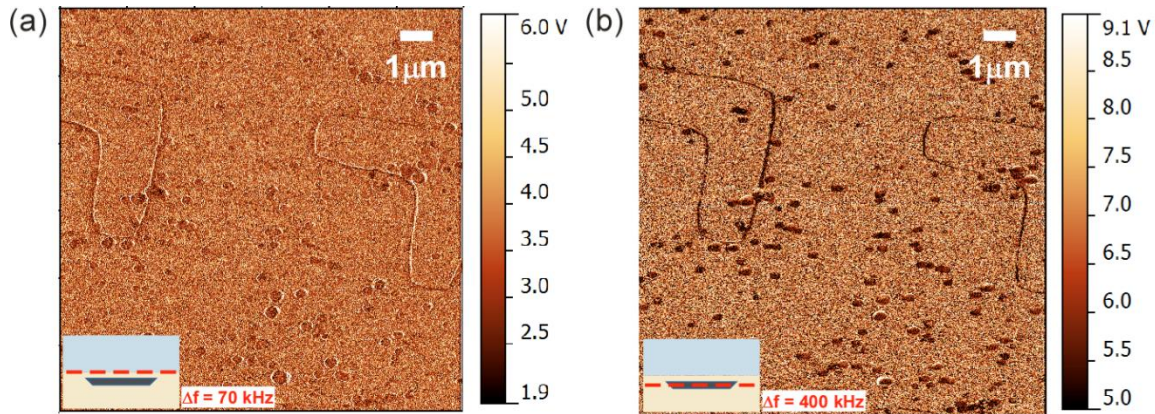


Figure 54: MSAFM phase images for sample 2 with $f_s > f_p$ (f_s fixed at 4.3 MHz). (a) Phase image at $\Delta f = 70 \text{ kHz}$: the investigation depth is in the nickel layer. (b) Phase image at $\Delta f = 200 \text{ kHz}$: the investigation depth is in the etched area of silicon. Phases were measured in a specified range ($\pm 10\text{V}$) corresponding to a range in degrees of $(-180/+180)$ degrees).

2.2.1.6. Conclusion

In summary, through the development of a numerical model, we unveiled the influence of various actuation parameters, such as the range of frequencies used (f_s, f_p) and the variations in Δf , on the investigation depth of the sample during MSAFM imaging. This numerical study has been validated by experiments on metallic calibration samples with buried patterns. Therefore, the relationships of the frequencies range and Δf on the investigation depth $z_{\Delta f}$ advances the capabilities for quantitative subsurface studies. Based on this discovery, the different dimensions of the buried structures were identified to reconstruct the depth profile of the sample using width variations and theoretical predictions. Importantly, the phase images were not related to the sample topography. Overall, we demonstrated that MSAFM has the potential to become a very powerful tool for non-destructive control and 3D reconstruction of buried objects with high (nanoscale) spatial resolution (lateral resolution, depth resolution).

2.1.2. Mode-Synthesizing Atomic Force Microscopy for volume characterization of mixed metal nanoparticles

To better understand the sensitivity of MSAFM, we characterized a structure with subsurface variations in the nanometer range. The nanoparticle was composed of two layers of different metal materials. We showed that the reconstruction of the depth profile is possible thanks to a simple model to connect the actuation waves and the corresponding frequency difference to the depth of investigation when probing the sample. We also demonstrate that it is possible to discriminate metallic materials of different properties within a nanoparticle¹⁶⁶.

2.2.2.1. Sample fabrication

The sample fabrication process is described in **Figure 55a** to **Figure 55f**. First, a silicon wafer was recovered of Polymethacrylate methyl (PMMA) resin by spin coating. The nanostructures were then patterned by e-beam lithography on the PMMA film by Scanning Electronic Microscopy (SEM – e-Line^{plus}, Raith) (**Figure 55a** to **Figure 55b**). The resin exposed to e-beam was lifted off and 43 nm of Nickel were deposited by sputtering (**Figure 55c** to **Figure 55d**). Next, the silicon wafer was etched by Reactive Ion Etching (RIE –model GIR 300 Alcatel) to create a base supporting the nickel dots (**Figure 55e**). Finally, a gold film (about 55 nm thick) was deposited by thermal evaporation onto the entire structure (**Figure 55f**). SEM images were realized before and after the gold evaporation (**Figure 55f** and **Figure 55h**) to have a full view of the steps of fabrication.

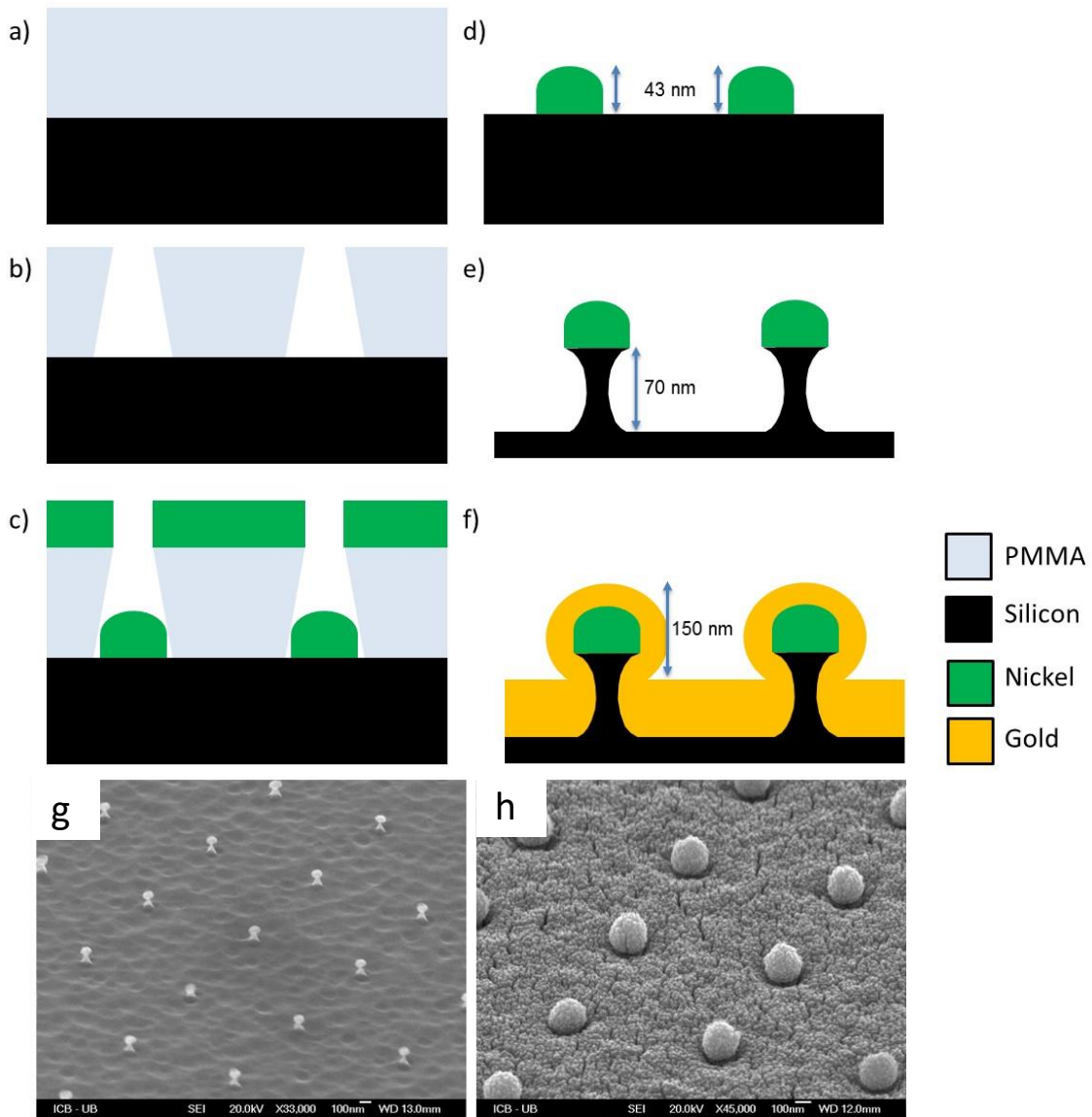


Figure 55: Schematic of the sample fabrication (a) Deposition of a PMMA resin. (b) E. beam exposure by SEM and lift-off. (c) Evaporation of about 43 nm of Nickel. (d) Development of the PMMA resin. (e) Etching of the Silicon substrate by Reactive Ion Etching (RIE). (f) Final design after evaporation of a 55 nm gold layer. (g), (h) SEM images of the sample g) SEM image of the sample before the deposition of the gold layer (after (e) step). (h) SEM image of the final sample structures (after (f)).

2.2.2.2. Study of nanoparticles with a special metal core

We first characterized the arrays of nanoparticles composed of nickel and gold using AFM and SEM standard procedures for surface imaging. The SEM images in **Figure 55g** show the Ni sphere sitting on top of the Si post prior to Au deposition. After Au deposition, the sample consists of an array of Au nanoparticles evenly spaced, as shown in **Figure 55h**. The topography AFM image (**Figure 56a**) reveals only the size of the global particle (without any distinction between the core and the envelope). A structure height of 150 nm and a diameter of about 580 nm were measured across the sample (**Figure 56**), in good agreement with the initial design (**Figure 55**).

MSAFM phase images were acquired (**Figure 56b to Figure 56e**) and unveil the presence of the core inside the nanoparticles. Standard protocol was followed for data acquisition, as detailed in the previous section (2.2). After varying the frequency we could observe a variation of the core diameter (**Figure 56b to Figure 56e**). According to the numerical calculation presented above, an increase in Δf corresponds to a decrease in the volume investigated, i.e. the plane of the image acquired is closer to the surface. Thus, by adjusting the frequency we could observe great variations in the diameter of the core (**Figure 57**). For a frequency difference Δf of 140 kHz a core diameter of 233 nm was measured. While at $\Delta f = 100$ kHz an increase of the core diameter to 516 nm could clearly be observed. Finally, the diameter in the image decrease to 290 nm at $\Delta f = 90$ kHz. The levels investigated at each Δf are labeled in the inset of **Figure 56**. As can be seen, the change in dimension observed is in good agreement with the sample design and follows the evolution predicted by the numerical model.

The results are all the more significant that both layers of the structures are made of metals, thus could not be characterized by elasticity measurements or any other non-destructive techniques. In force investigation, the dual constitution between nickel and gold could not be distinguished in the elasticity modulus map due to the limitation in depth sensitivity. The results

shine light on the special capability of MSAFM to gain access to non-destructive characterization of such structures that cannot be studied by conventional ways.

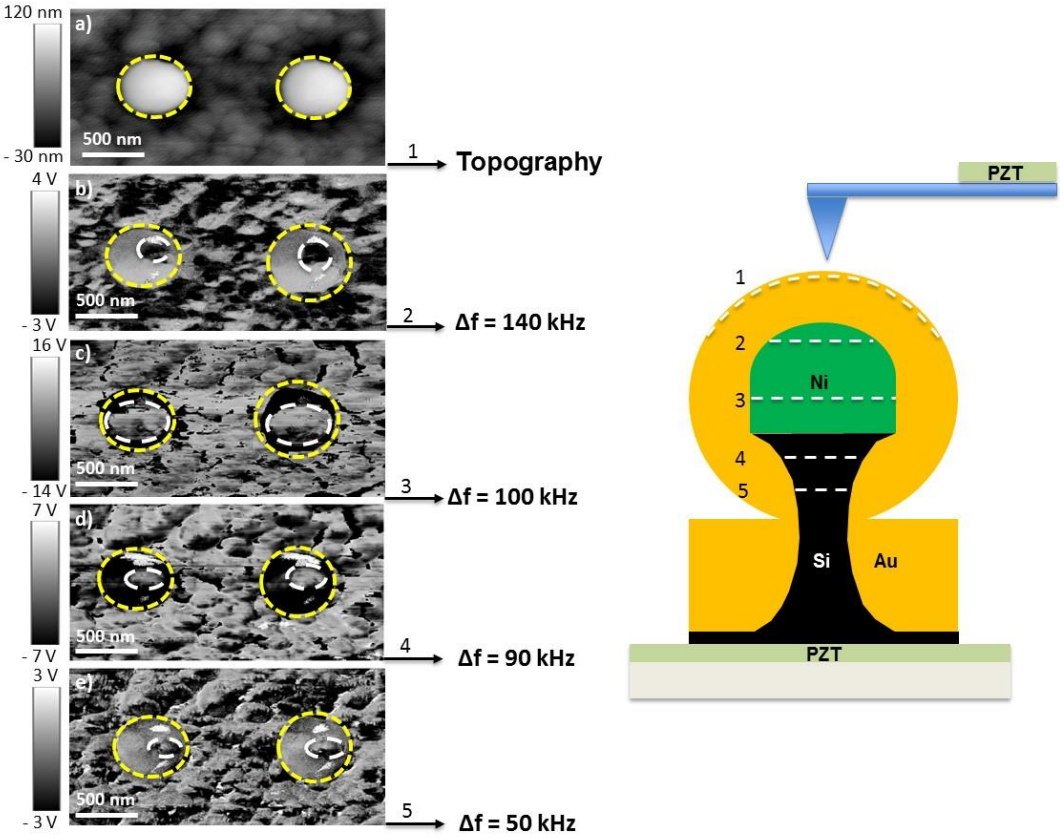


Figure 56 : MSAFM study of sample at different Δf frequencies. (a) Topography image of two Ni-Au nanoparticles and corresponding MSAFM phase images at $\Delta f=140\text{kHz}$ (b), $\Delta f=100\text{kHz}$ (c), $\Delta f=90\text{kHz}$ (d), and $\Delta f=50\text{kHz}$ (e).

Δf (kHz)	Core diameter (nm)	Level on Figure 56
140	233	2
100	516	3
90	290	4
50	258	5

Figure 57: Evolution of the core diameter with the Δf frequency.

2.2.2.3. Conclusion

Through the development of the numerical model, we unveiled the influence of the variation in Δf on the investigation depth during MSAFM characterization. The inner features of the new 3D calibration sample made of a metal nickel core encapsulated in a gold layer could be successfully characterized by MSAFM at different frequencies. We showed the presence of the core inside the nanoparticle with its diameter variations according to the Δf variations. This numerical model offers special interest for the 3D characterization of complex systems, particularly in biological field as in metallic nanoparticles in cells for possible tailored nanotechnology-driven therapy. However, this technique does not provide any chemical information. There is no phase or amplitude contrast allowing to discriminate different kind of metals. This is explained by the sensitivity of MSAFM to differences of density (see Chapter 3) and not to differences in electric properties of the materials (such as conductivity).

Consequently, for studies in which more advanced characterization of metallic components was required we had to employ electromagnetic (EM) waves propagations through the sample, as unlike acoustic waves, EM waves are sensitive to changes in the conductivity of the material. In the second part of this chapter we will focus on the second technique developed during this thesis: Scanning Microwave Microscopy (SMM).

2.2. Scanning Microwave Microscopy (SMM)

Scanning microwave microscope is a near-field technique possessing an extended microwave frequency range (usually limited to a 1GHz frequency). The first experimental observation of sub-wavelength defects in the microwave domain was presented in 1972 by E.A. Ash and G. Nicholls¹⁶⁷. Using a hemispheric cavity resonating at a 3 cm wavelength and a flat reflector perforated with a sub-wavelength hole (1.5 mm diameter) variations in the cavity resonance frequency, and by moving a probe at a distance of 500 μm above metallic lines (width 2 mm) and monitoring the, spatial resolution of $\lambda/60$ could be achieved.

2.2.1. Far and near-fields microwave techniques for the detection of defects

Due to the limitation of their spatial resolution (around $\lambda/2$), far field characterization techniques are only used for the detection of millimeter defects. The probes used in conventional microwave techniques are directive antenna acting as emitter and receptor for microwaves. The sample under test is located in the antenna far field zone, i.e. at a distance d from the antenna defined by:

$$d > \frac{2 \cdot D^2}{\lambda} \quad (7)$$

D is the antenna biggest dimension, λ the illuminating wavelength. So, if a defect bigger than $\lambda/2$ is located in the illuminating beam of the antenna, one can observe a variation of the reflection coefficient (S_{11}) of the antenna.

By using the Abbe limit, we can calculate the spatial resolution of the defects detected with such techniques. With λ in air comprised between 1 mm (for $f = 300$ GHz) and 1m (for $f = 300$ MHz), the limit of spatial resolution of far-field microwave techniques varies from 0.5 mm (for $f = 300$ GHz) to 0.5 m (for $f = 300$ MHz). Thus, the methods based on far-field detection of defects are not adapted for the detection of micro (and nano)-defects.

On the other hand, near field microwave techniques provide a spatial resolution superior to that of conventional far-field methods, making them the approach of choice to study microscale defects. The spatial resolution of near-field methods depends principally on the probe dimensions as well as the probe/sample distance. A number of near field measurements capitalized on this particular regime to observe surface and subsurface features in a large range of materials. These techniques were used in a very large range of frequencies from a few GHz to 100 GHz with spatial resolution up to $\lambda/750\,000$ reported¹⁶⁸. Two categories of near-field characterization methods are presented in the literature:

- a) The non-resonant techniques: amplitude and phase of the reflection coefficient (S_{11}) or transmission coefficient (S_{21}) are measured.
- b) The resonant techniques: resonator frequency and quality factor are measured.

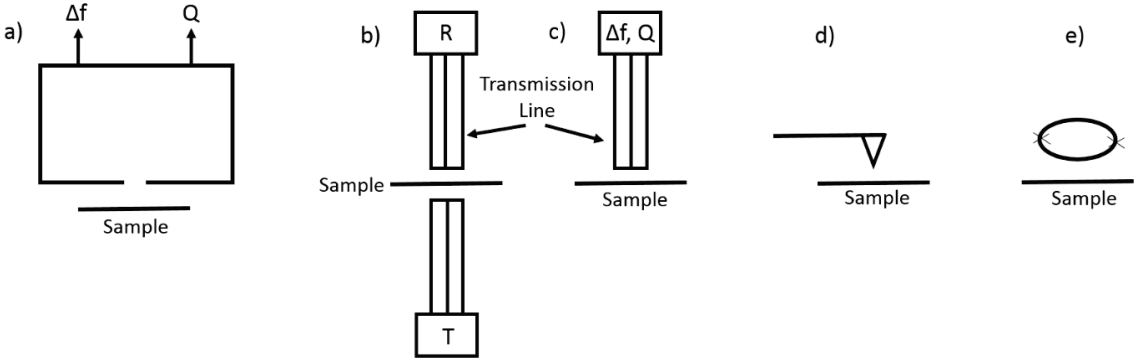


Figure 58: Representation of various near field microwave characterization techniques. (a) Microwave cavity resonator. (b) Non-resonant microscopy techniques. (d) Microwave measurement with AFM. (e) Scanning superconducting quantum interference device (SQUID) method.

An illustration of few configuration of microwave near-field characterization is provided in **Figure 58**. In **Figure 58a**, the scheme represents the traditional microwave cavity resonator with a small hole in one of its wall¹⁶⁹. The sample is localized close to the wall and a small region of the sample, defined by the diameter of hole, perturbs the resonant frequency causing

a frequency shift Δf and affects the quality factor (Q) of the resonator. This method uses an evanescent mode to couple the resonant cavity to a local part of the sample. The most important development on this technique was developed by Ash and Nichols¹⁷⁰, they were able to sensitively recover the signal from the resonator to reconstruct an image of the sample scanned under the hole¹⁷⁰.

Figure 58b represents a non-resonant microscopy technique which is based on the measurement of complex resistivity R or transmission coefficient T from which properties of the sample can be deduced. The most common configuration is the measurement of reflectivity from a coaxial transmission line terminated by the sample¹⁷¹. Transmission measurements were also reported¹⁷². This technique is suitable to map metallic conductivity, sheet resistance and dielectric constant¹⁷¹.

In the configuration presented in **Figure 58c**, the sample is located near the open end of the transmission line resonator and the changes in resonant frequency and quality factor are monitored while scanning sample. This configuration uses a field enhancing feature at the end of the transmission line, rather than an evanescent aperture in the resonator. The first application of this setup was to measure moisture content in paper¹³⁷.

The system configuration presented in **Figure 58d** combines the nanometer resolution of an AFM with microwave microscopy. Three different variations of this configuration were reported in the literature^{173, 174, 175}. The first one is used to perform localized electron-spin resonance measurements¹⁷³. The second one consists in generating a magnetic field gradient on the sample (e.g. with a small magnetic particle on the tip) while immersing it in a radio-frequency (RF) magnetic field. The sample locally satisfies the magnetic resonance condition and exerts a force on the cantilever^{174, 175}. The third scanning probe method uses a sharp metallized tip to perform “apertureless” near-field microscopy¹⁷⁶. The sharp tip, in close

proximity to a metallic sample, will locally enhance radiation introduced by a focused far-field beam.

Finally, **Figure 58e** represents a method called scanning superconducting quantum interference device (SQUID) method. SQUID generates circulating radio frequency currents when a DC bias is placed across the loop. The frequency of these currents is directly proportional to the applied bias voltage. The currents in turn generate RF magnetic fields, which then impinge on the sample. The sample generates its own response currents which modify the inductance of the SQUID loop. By monitoring the magnetic-field feedback signal required to keep the SQUID in a constant flux state, one can map the electromagnetic response of the sample¹⁷⁷.

In that work, we focused of the AFM coupled with microwave frequencies.

2.2.2. Micro-wave microscope

Properties of the sample including complex permittivity, permeability and conductivity affect the detection parameters such as the reflection/transmission coefficients, the quality factor, and the resonant frequency measured. A good theoretical modeling of the system can support the establishment of a relationship between the quantities detected and the sample properties. Here, the near-field tip is considered as an antenna (two terminal, linear, passive system) which is connected to the detection apparatus¹⁷⁸.

2.2.2.1. Microscope model

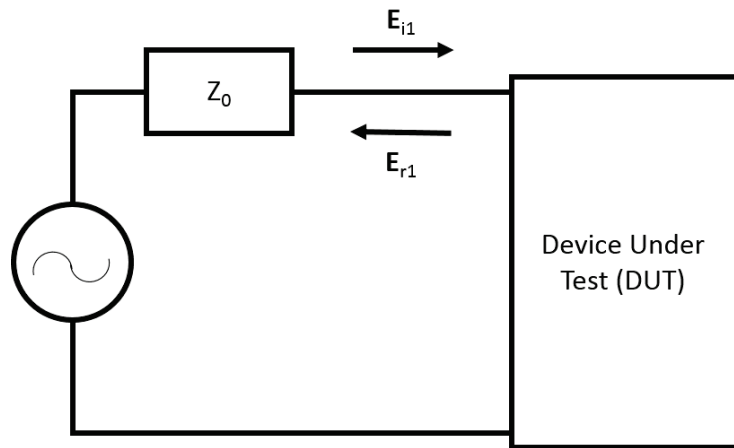


Figure 59: Electrical circuit associated to the microwave microscope.

We consider a source of characteristic impedance Z_0 alimenting the device under-test (DUT) as depicted in **Figure 59**.

The DUT is composed of two elements¹⁷⁶, namely an incident wave E_{i1} and a reflected wave E_{r1} such as:

$$V_1 = E_{i1} + E_{r1}, \text{ and } I_1 = (E_{i1} - E_{r1})/Z_0 \quad (8)$$

The DUT is connected to the source through a certain length of transmission line of impedance Z_0 . The voltage along the line is called V_1 and the current is called I_1 . The voltage V_1 and current I_1 .

Furthermore, we note that: $a_1 = \frac{E_{i1}}{\sqrt{Z_0}}$ and $b_1 = \frac{E_{r1}}{\sqrt{Z_0}}$

Where a_1 and b_1 are the square of the incident and reflected powers.

We also introduce S_{11} as: $S_{11} = b_1/a_1$

The impedance of the DUT is noted Z_L and can be expressed as:

$$\text{With } Z_L = [(1+S_{11}) Z_0]/ (1-S_{11}) \quad (9)$$

2.2.2.2. Definition of the reflection coefficient Γ

When the signal travelling in a coaxial cable encounters an impedance mismatch, a portion of the signal will be reflected back to the source. This reflected signal has an amplitude and a phase and is measured as the reflection coefficient:

$$\Gamma = |\Gamma| \cdot e^{j\phi} = (Z_L - Z_0) / (Z_L + Z_0) \text{ (in our case } Z_0 = 50 \Omega) \quad (10)$$

Γ represents the charge adaptation quality to the source impedance. It is a complex value with an amplitude ρ and an angle θ . Z_L is the impedance mismatch of Z_0 the impedance of the line. A good adaptation is realized when Γ tends to 0.

By using the normalized impedance $Z = Z_L / Z_0$, we have:

$$\Gamma = (Z - 1) / (Z + 1) \text{ and } Z = (1 + \Gamma) / (1 - \Gamma) \quad (11)$$

Thus, S_{11} can also be expressed as $S_{11} = (Z - 1) / (Z + 1) = \Gamma$

2.2.2.3. Return loss

The return loss is defined as the loss of power in the signal returned/reflected by a discontinuity in the transmission line and it usually expressed as a ratio in decibels (dB)

$$RL (dB) = 10 \log \frac{P_i}{P_r} \quad (12)$$

where $RL (dB)$ is the return loss, P_i is the incident power and P_r the reflected power.

The return loss is the negative of the magnitude of the reflection coefficient in dB and is given by the following relation:

$$RL(dB) = -20 \log |\Gamma| \quad (13)$$

Thus, a large positive return loss indicated the reflected power is small relative to the incident power which indicated a good impedance adaptation.

2.2.2.4. Penetration depth

The penetration depth δ , or so-called skin depth, is a measure of the depth of microwave penetration in a material. The penetration depth of the EM field is defined as the distance from the surface of the material at which the magnitude of the field strength decreases to $1/e$ ($= 0.368$) of its value at the surface¹⁷⁹. The penetration depth of the electric field can be expressed by the equation: $\delta = \frac{1}{\alpha}$

where α is the attenuation factor and can be represented as:

$$\alpha = \omega \left(\frac{\mu_0 \mu_r \sigma}{2} \right)^2 \left[(1 + (\tan\Delta)^2)^{1/2} - 1 \right]^{1/2} \quad (14)$$

With μ_0 is the permeability of the vacuum ($4\pi 10^{-7}$ H/m), μ_r the permeability relating to the conductor, σ the electric conductivity (in S.m^{-1}), ω the radial frequency - $\omega=2\pi f$ - in rad.s^{-1} and $\tan\Delta$ the loss tangent factor which represents the efficiency of the material to convert absorbed energy into heat.

Hence, the penetration depth is inversely proportional to the frequency of the electromagnetic field.

In the particular case of the penetration depth of the electromagnetic field for a conducting material – which is high loss medium - the previous equation can be expressed as:

$$\delta = \frac{1}{\alpha} = \frac{1}{\sqrt{\pi \mu_0 \mu_r \sigma f}} \quad (15)$$

with δ the skin depth (in m), σ the electrical conductivity (in S.m^{-1}) and f the frequency (in Hz).

Thus, the potential of the microwave microscope lies its ability to differentiate the microwave images obtained at different frequencies for volume exploration. The microwave images will

provide information about the differences in phase and amplitude of the reflected waves at various frequencies, which is directly related to the nature of the material. The frequency of the EM wave will influence the skin depth, which we optimized to detect defects in the volume of the samples (**Figure 60**).

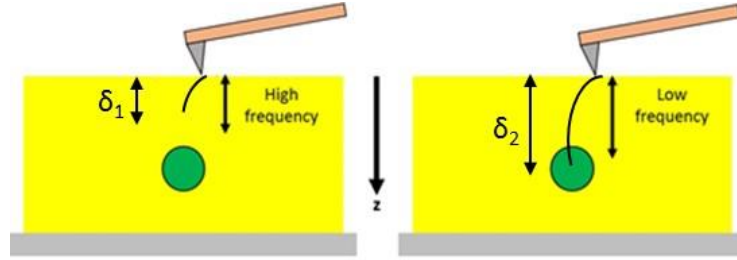


Figure 60: Illustration of the skin effect. The radiation frequency applied for the detection of defects buried inside the metallic sample should be tuned according to the depth of the defect. Depending on the electrical and magnetic properties of the metal, a frequency that is too high does not give access to a skin depth (δ_1) large enough for detection of the defect. The frequency has to be adapted for each material and defect.

The electric field of the reflected wave through a good conducting material can be written as¹⁸⁰:

$$E_r = E_{r0} e^{i(\omega t - \frac{z}{\delta}) - \frac{z}{\delta}} \quad (16)$$

with E_r the reflected electric field, E_{r0} the attenuated reflected electric field, ω the angular frequency ($\omega = 2\pi f$), t the instant considered, z the component of the direction of propagation and δ the skin depth¹⁸⁰.

The phase Φ of the wave defined by **Eq. 16** is defined as:

$$\varphi = \frac{z}{\delta} \quad (17)$$

Thus, in a fixed location z and for all other fixed parameters, the phase will be modified if the skin depth varies. Based on **Eq. 15**, the skin effect is dependent, at constant frequency, on the

permeability (δ decreases with increasing permeability) and on the conductivity (δ increases with decreasing conductivity) of metallic materials.

2.2.3. Scanning Microwave Microscope (by Agilent)

In 2008 Agilent Technologies developed a new scanning probe microscopy (SPM) technique that combines the electromagnetic measurement capabilities of a microwave vector network analyzer (VNA N5230A, Agilent Technologies) and an AFM (AFM 5600LS, Agilent Technologies) to offer nanometer spatial resolution. This new technique, called Scanning Microwave Microscopy (SMM), is shown in **Figure 61**. This nondestructive technique allows the characterization of defects located in the volume of a metal sample.



Figure 61: Picture of the microscope used for SMM measurements. SMM, Agilent Technologies.

The principle of operation of SMM is the following: a microwave signal is sent directly from the network analyzer and transmitted through a resonant circuit to a conductive AFM probe that is in contact with the sample under investigation. **Figure 62** illustrates the signal obtained outside of the resonant circuit and cantilever, which exhibits frequency peaks.

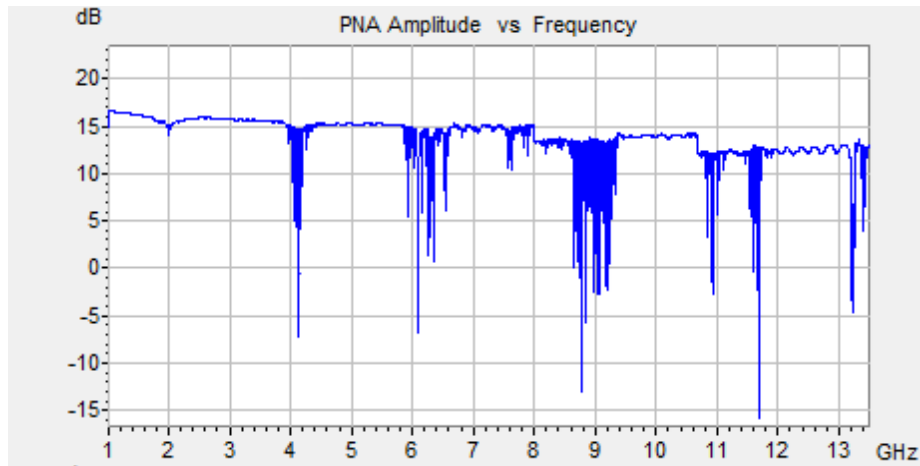


Figure 62: Frequency spectrum obtained at the output of the resonant circuit in the SMM setup.

From this frequency spectrum, one of the peaks is selected to decide the frequency at which the analyses will be conducted.

The conductive tip attached to a solid metal cantilever acts as both as a nanometer-scale AFM probe and as a GHz emitter-receiver antenna. The transmitter–receiver system is limited to the accessible frequency range given by the cantilever/resonator system and by the interactions between the tip and the surface sample (see the example presented in **Figure 63**), which makes it possible to capture the reflected microwave signal locally, from the contact point. By directly measuring the complex reflection coefficient from the network analyzer, the impedance representing the probe–sample interaction amplitude and the phase at each point probed can then be recorded, simultaneously with the surface topography.

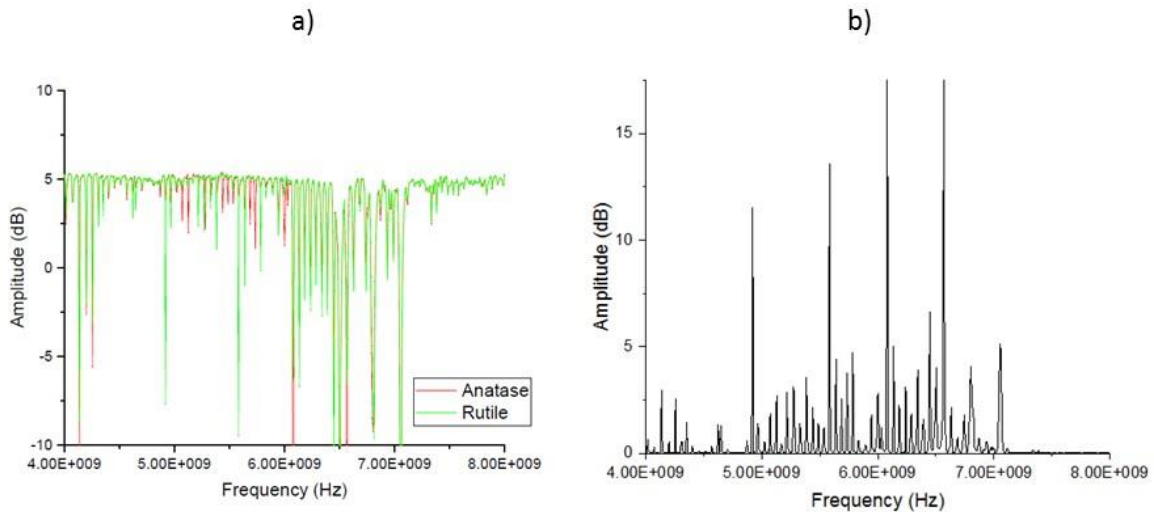


Figure 63 : Influence of the tip-sample interaction on the SMM amplitude signal. (a) Comparison between TiO₂ samples. (b) Difference of the amplitude signal obtained on the anatase and rutile TiO₂ sample obtained by subtracting the two signals in (a).

The AFM tip scans the surface sample and in every measurement point of the scan, the S_{11} scattering parameter is acquired by the VNA. The high-frequency signal travels from the VNA to the conductive probe, which is in contact with the sample to characterize. Depending on the electrical properties of the sample (ie. the impedance of the sample), the sample partly absorbs or reflects the high-frequency wave. The reflected wave travels through the transmission line back to the VNA where it is compared with a copy of the incident wave.

By analogy with an optical technique such as Scanning Near-Field Optical Microscopy (SNOM), and like many SPM techniques, the transmitter-receiver system depends on the nature of the interaction between the tip and the surface sample. SMM images are acquired in real space, as in photon scanning tunneling microscopy.

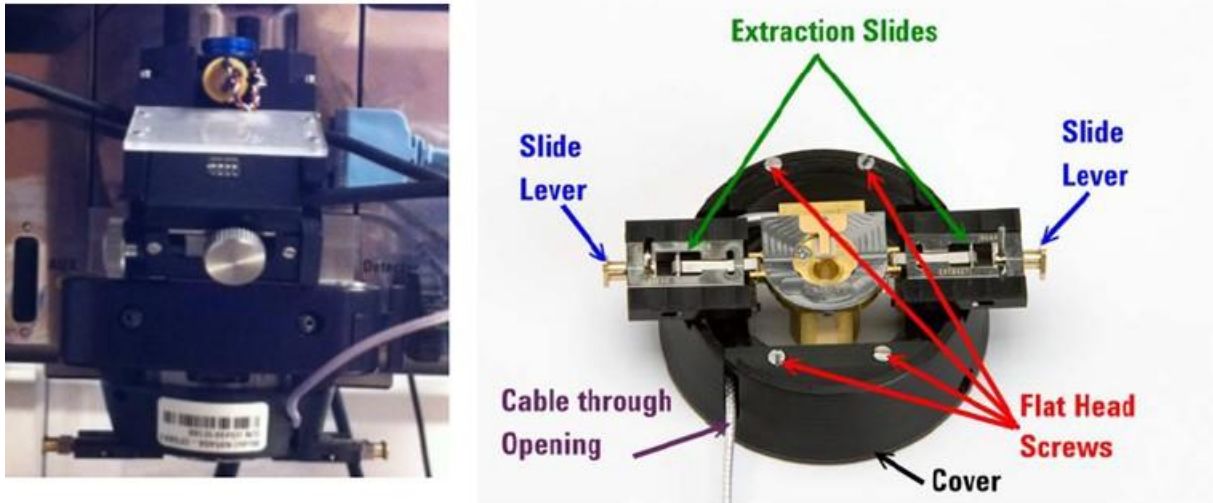


Figure 64: SMM cone nose and tip holder.

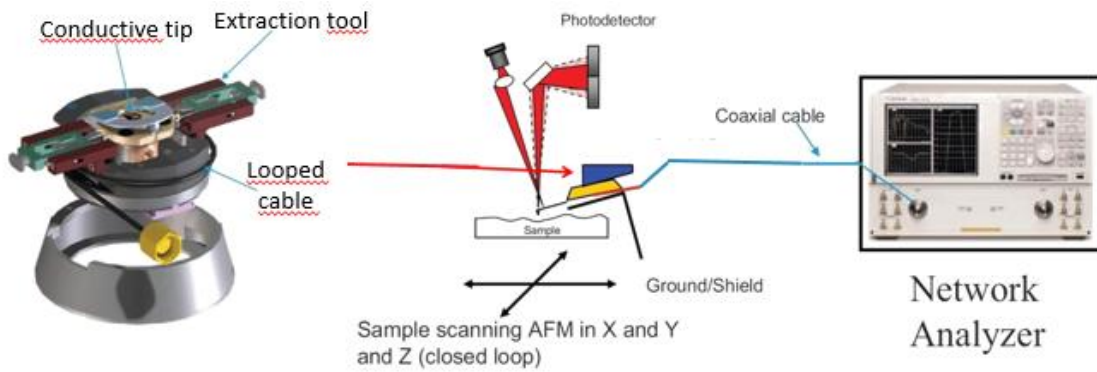


Figure 65: SMM setup: (left) microscope head and (right) data acquisition scheme.

The cantilevers used for microwave measurements are SCM-PIT probes from Bruker. Built on the model of FESP probe (about 225 μm length), SCM-PIT have a Platinum-Iridium coating on the front side of the cantilever to provide a metallic electrical path from the cantilever die to the apex of the tip. The coating on the back side of the cantilever compensates for the stress created by the front side coating and also enhances laser reflectivity by a factor of up to 2.5 times (**Figure 66**). The resonance frequency of the SCM-PIT cantilever is about 75 kHz for a spring constant in the range 1 to 5 N/m.

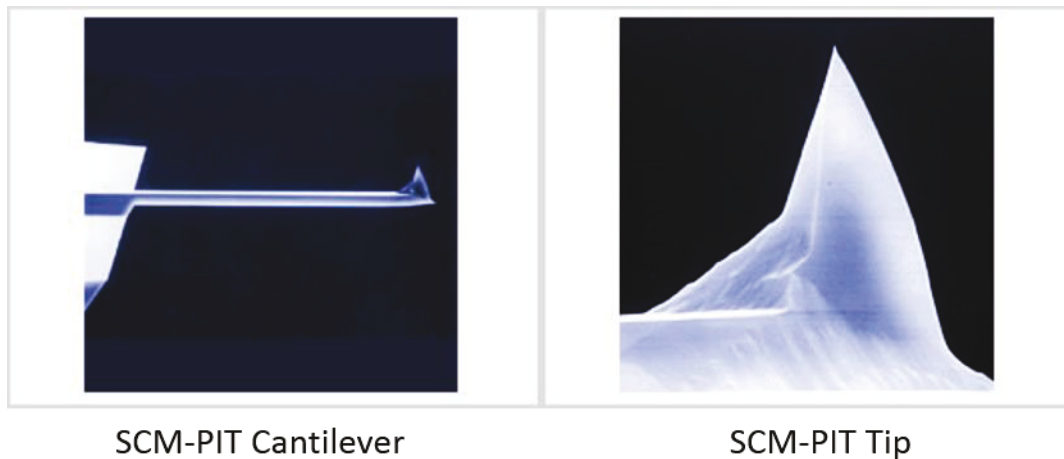


Figure 66: SEM image of SCM-PIT cantilever (Bruker) used in our measurements: (left) cantilever and (right) tip ⁸¹.

2.2.4. Modelisation of the microwave probe

In order to illustrate the confinement of the electromagnetic field (in this case the electromagnetic is defined as transverse electric) and its exaltation by the SMM tip, we performed simulations using the Comsol Multiphysics software.

The geometry of the model is presented in **Figure 67**. It consists of a coaxial cable of a given length (L_{coax}) composed of a perfect conductor of radius noted r_{coax} surrounded by a dielectric materials of radius noted R_{coax} . At the end of the cable, a typical conductive - here perfect conductor - STM probe (h_p in length and d in diameter) is modeled. A conical tip (h_{tip} in height and r_{tip} in inferior diameter) is added at the extremity of the STM probe. The list of the different parameters used by the model is provided in **Figure 68**.

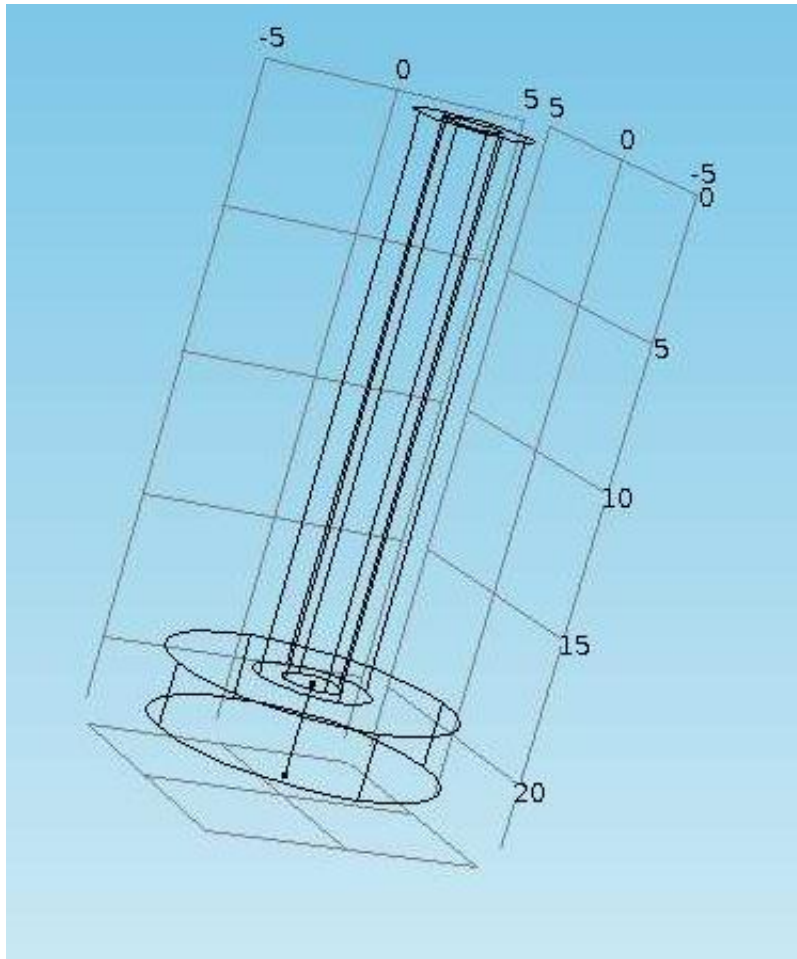


Figure 67: Geometry of the coaxial cable used in the model. Axes values are given in mm. Inner and outer radii as well as length of the cable were fixed for the calculations.

	Model 1	Model 2
Coaxial cable		
R_coax	2 [mm]	2 [mm]
r_coax	1 [mm]	1 [mm]
L_coax	20 [mm]	20 [mm]
Cantilever		
d	0.1 [mm]	0.03 [mm]
h _p	From 1 to 20 [mm]	From 0.1 to 0.3 [mm]
Tip		
r _{tip}	0.1 [mm]	0.03 [mm]
h _{tip}	0.015 [mm]	0.015 [mm]

Figure 68: List of parameters used for the Comsol model.

We analyzed the distribution of the electric field at the end of the probe under various conditions. Calculations of the maximum of the electric field $|E|$ are realized without and with tip for different probe length h_p and various frequencies.

First, we analyzed the system composed of a single coaxial cable without any cantilever and tip. **Figure 69** shows the electric field distribution and reveals an important diffusion at the exit of the cable. The same calculations were then realized by adding a micrometer probe and a tip to the system. **Figure 70** represents the distribution of the electric field in presence of the probe, at an 8 GHz frequency. In **Figure 70** the electric field is concentrated at the apex of the probe with an intensity of about 20000 V/m. Moreover, the diffusion phenomena observed in the case of a single coaxial cable observed in **Figure 69** disappeared.

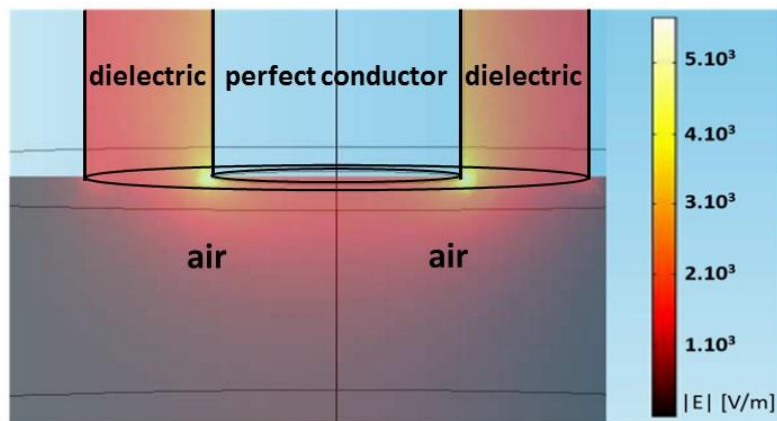


Figure 69: Representation of the absolute value of the electric field $|E|$ at the coaxial cable output. Highest intensity (in yellow) were found at the outer perimeter of the cable output.

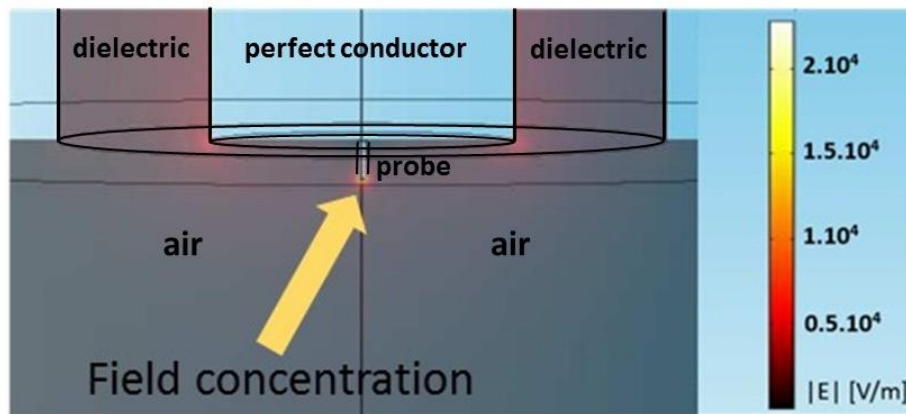


Figure 70: Representation of the absolute value of the electric field $|E|$ variations in the system. The system modeled is composed of the coaxial cable and the probe (and tip) for a 8 GHz frequency. Field concentration was observed at the probe location.

In order to evaluate this observation, we plotted the evolution of the calculated electric field as a function of different parameters. **Figure 71** represents the distribution of the electric field at the apex of the coaxial cable as a function of the frequency injected from 4 to 12 GHz. One can clearly see the high impact of the tip of the probe on the intensity of the electric field (blue curve in **Figure 71**). In the configuration of the coaxial cable without cantilever, the $|E|$ value remains less to 1000 V/m, but increased by a factor of 8 with the addition of a 300 μm length probe (red curve in **Figure 71**). Thus, we could confirm that the probe acts like an antenna and provides great exaltations of the electric field. This larger field was doubled with the addition of a tip. This model constitutes a strong confirmation of the high sensitivity of SMM microscope in the vicinity of the tip of the cantilever for near-field characterization. The cantilever tip enhances the electric field at the extremity of the tip. Consequently, contrary to the simple coaxial cable measurement, SMM will be of interest for local measurements with enhanced sensitivity.

Configuration	$ E $ (V/m)
Coaxial cable	1385
Coaxial cable and probe (300 μm)	8929
Coaxial cable, probe (300 μm) and tip	17269

Figure 71: Average value of the absolute value of the electric field $|E|$ for the 4 GHz, 6 GHz, 8 GHz and 12 GHz frequencies at the out of the coaxial cable in the presence or not of probe and tip.

Figure 72 and **Figure 73** represent the absolute value of electric field along the vertical and horizontal sections for a fixed frequency of 8 GHz at the out of the coaxial cable in presence or not of probe and tip . In the case of the coaxial-probe-tip system, the tip is modeled in contact with a perfect conductive (metallic) sample. **Figure 72** illustrates the skin effect by showing the brutal decrease of the electric field in a conductive material as the distance from the surface sample increases. As already illustrated in **Figure 71**, the enhancement of the field due to the presence of the probe and tip can be observed with a signal at the surface of the material nearly ten times higher than that of the measurement in absence of the probe.

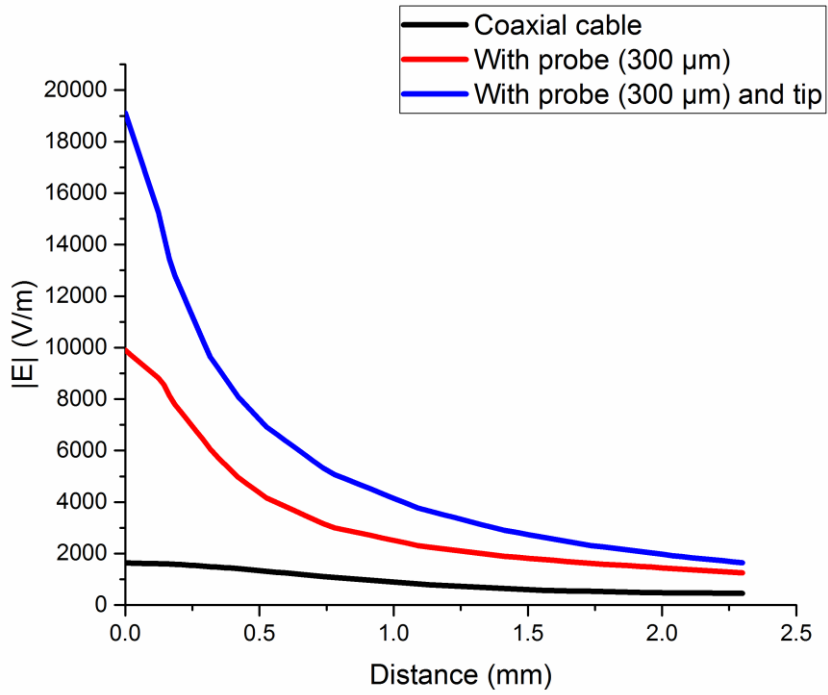


Figure 72: Absolute value of the electric field at the out of the coaxial cable in presence or not of probe and tip.

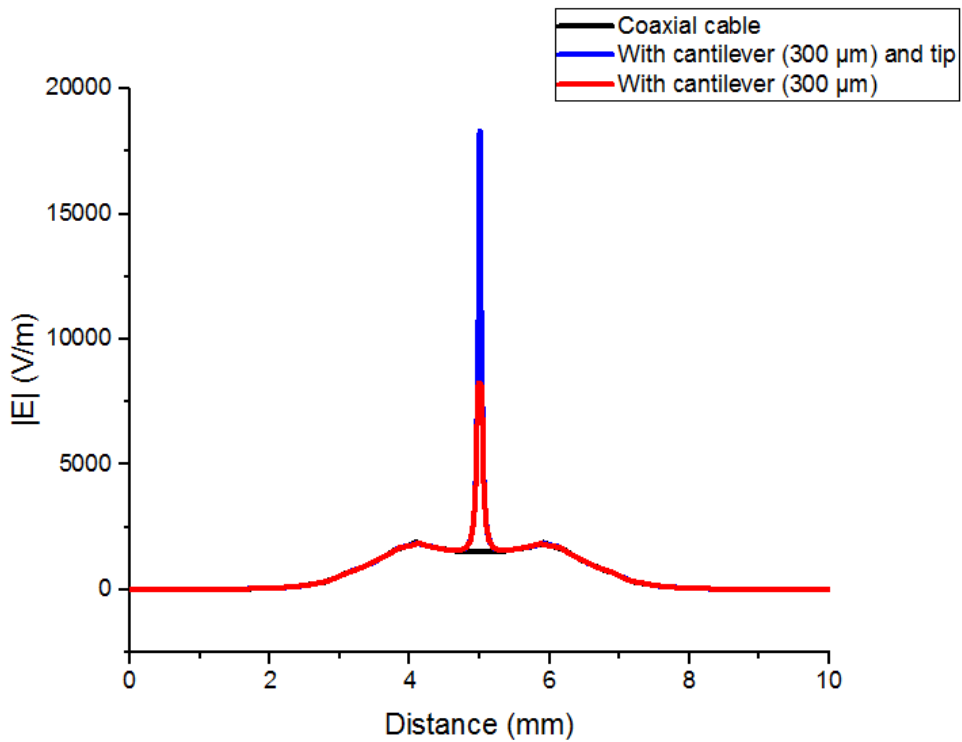


Figure 73: Electric field confinement provided by the presence of the probe and the tip.

Figure 73 represents the variation of the electric field distribution at varying distance from the coaxial-probe-tip system. The confinement of the electric field in the vicinity of the probe and the tip is clear. This phenomenon explains the high sensitivity detection of the SMM that cannot be achieved with a simple coaxial cable.

The model of the device highlight the great advantage of the local probe which consequently exalt the electric field and allow a great sensitivity detection. Thus, coupling the microwave spectroscopy with an AFM cantilever allows high resolution characterization with a sensitivity that cannot be achieved with a simple coaxial cable system.

2.2.5. Evidence of in-depth investigation by SMM

In order to evaluate the influence of microwave frequency on the investigation depth a calibrated sample was manufactured by Electron Beam Lithography (EBL) by using a Scanning Electron Microscope (SEM) coupled to a device of lithography management RAITH^{140, 181}.

The sample consists of L-shaped patterns of 30 nm depth were filled with aluminum (Al) film of 20 nm thickness. Then, a nickel (Ni) layer of 95 nm thickness was evaporated in order to cover these structures. Thus, we obtained buried structures of Al under a calibrated layer of Ni (**Figure 74a**). AFM observations at the final step show the surface of patterns (with height variations of 10 nm on the surface). On the topography (**Figure 74a**), the patterns appears at a lower level than on the non-treated surface.

Nevertheless, to show that the surface is only composed of nickel, an image of friction (scan at 90° compared to length of the cantilever) was carried out on this sample. Friction maps confirmed that the substrate and the patterns are of the same composition since the color contrast is identical (**Figure 74b**).

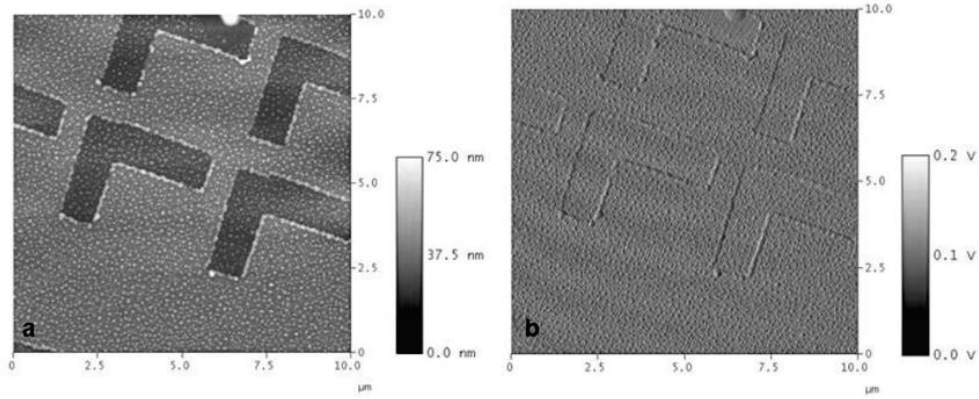


Figure 74: Calibration sample: buried structures of aluminum under a calibrated nickel layer. (a) AFM image. Scan size: 10 x 10 μm . (b) AFM friction image. Scan size: 10 x 10 μm .

The sample required using a large frequency to obtain probe appropriate thickness in the volume. For that, we estimated the depths likely to be probed with the frequencies used. Using the magnetic permeability and the electric conductivity of nickel (material constituting the superior layer of the sample) in the “skin depth” equation (Eq. 15), the values of depths corresponding to the various frequencies were calculated (Figure 75).

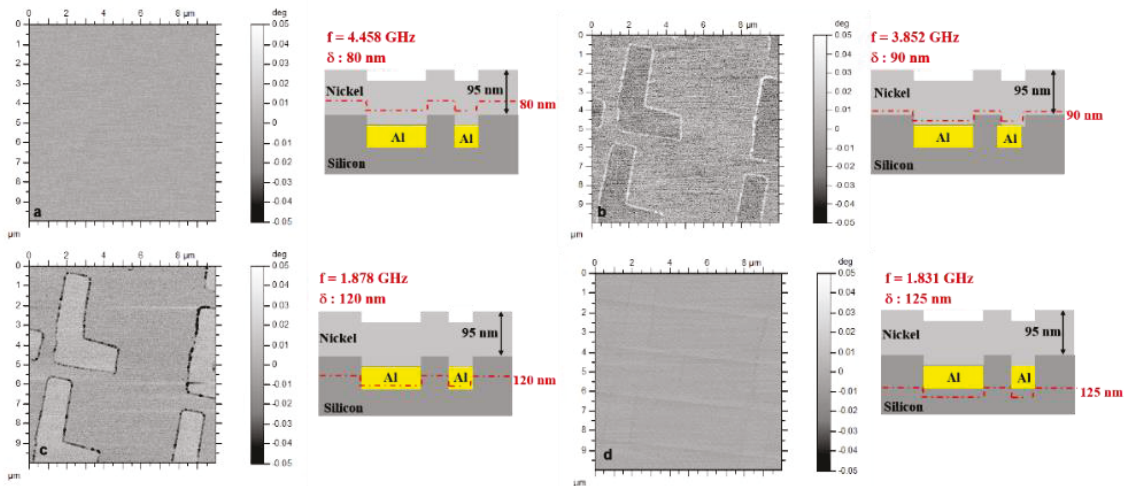


Figure 75: SMM images (phase) of buried Al under a calibrated Ni layer at different frequencies. Scan size: 10 x 10 μm . Phase scale: 0.1 deg. (a) SMM phase image at 4.485 GHz. (b) SMM phase image at 3.852 GHz. (c) SMM phase image at 2.103 GHz. (d) SMM phase image at 1.831 GHz. The red dotted line in the inset in each section indicates the position of the image acquired in the volume of the sample.

The SMM phase images obtained at various frequencies are presented in **Figure 75**. For frequency $f = 4.485$ GHz (corresponding to a depth, $\delta = 80$ nm), the SMM phase image did not show any features as the EM wave is probing the homogeneous Nickel layer. For frequency $f = 3.852$ GHz (corresponding to a depth, $\delta = 90$ nm), the plane probed is located at the Si/Ni interface. The SMM phase image shows a light contrast of color between the Ni layer and the proximity of the Si patterns, thus revealing the presence of different materials. The outline of the patterns also appeared with a contrast of color much more distinguishable. For frequency $f = 1.878$ GHz ($\delta = 120$ nm) the system probe a plane located inside the Al patterns. The SMM phase image clearly shows a difference in nature between the Al patterns and the Si substrate. Si being a semiconductor, it was expected to show a weaker electric conductivity than that of metals. These differences in properties are found on the SMM image in the color contrast. For frequency $f = 1.831$ GHz, corresponding to an investigation depth of 125 nm, the scanned plane reached the level below Al patterns, inside the Si substrate. On the SMM phase image, no pattern could be observed. This sample made it possible to correlate the depth investigated at each frequency used and indicate that it will be possible to carry out an in-depth cartography in a representative thickness of the volume of the sample.

2.2.6. Conclusion

In conclusion, the capacity of SMM to detect defects located in the volume of a metal sample was established. The theory and modeling developed make it possible to connect the investigation depth associated to the frequency used. Moreover, the measurements at successive frequencies give access to information located at different depths below the sample surface with potential for tomographic study with an in depth resolution 80 nm and beyond.

2.3. Conclusion

In this chapter, we highlighted strong evidence in favor of volume investigation at the nanoscale by means of ultrasound-based and microwave-based scanning probe techniques. Both approaches were shown to be capable of providing lateral and volume resolution of a few nanometers. At the next stage, the practical implementation of these microscopes shall be achieved, which then can be applied to the analysis of samples that are of specific interest for biology and material sciences. This will be the purpose of the next chapters.

Chapter 3 – *Advances in the understanding of tomography microscopy through the study of dielectric and biological samples.*

This Chapter is focused on the MSAFM capabilities for the characterization of dielectric and biological samples. Through the study of polymer, we highlighted the sensitivity of the technique to low density changes in the matter. Then, we applied the technique to the characterization of bacteria in order to visualize the action of an alcoholic stress on the bacterial membrane. Finally, the last part of the chapter is focused on the coupling of AFM-IR and MSAFM for the detection of lipid vesicles inside bacteria.

3.1. Study of the sensitivity of MSAFM – Analysis of a model sample

Outstanding challenges in nanoscale characterization call for non-invasive, yet sensitive sub-surface characterization of low-density materials such as polymers. In this work, we present new evidence that Mode Synthesizing Atomic Force Microscopy (MSAFM) can be tuned to detect minute changes in low-density materials such as the ones engendered in an electro-sensitive polymer during electron beam lithography (EBL), surpassing all common nanoscale mechanical techniques.

Moreover, we propose a 3D reconstruction of the exposed polymer regions using successive high-resolution frames acquired at incremental depths inside the sample. In addition, the results clearly show the influence of increasing dwell time on the depth profile of the nano-sized exposed regions. Hence the simple approach described here can be considered an unprecedented capability for sensitive nanoscale tomography of soft materials with promising applications in material sciences, and biology¹⁴³.

In this section, we designed and studied calibration samples with series of low-density variations patterns created in the volume of an electro sensitive polymer poly-(methy methacrylate) (PMMA) layer using various doses and dwell time parameters of controlled electron beam lithography (EBL). PMMA is routinely used in EBL as a sacrificial layer for positive resist in direct write processes. During e-beam exposure, the primary electrons entering the resist layer loose energy by means of inelastic scattering or collisions with other electrons and produce secondary electrons. The resulting electron cascade can engender a non-uniform spread of the energy deposition. The aim of this study is to track how electron-matter interactions modify the conformation of the material in the depth of the PMMA layer (i.e. below the surface). First, we show that, compared to AFM Peak Force Quantitative NanoMechanical

property mapping (QNM), Lateral Force Microscopy (LFM) and confocal Raman spectroscopy, MSAFM exhibits a combination of higher sensitivity and improved depth resolution. Second, we studied the influence of parameters such as driving frequency and scan rate on image contrast. Then, we evaluated their impact on resolution and on sensitivity of the subsurface components of the MSAFM measurements. The study highlights the potential of MSAFM for sensitive differentiation of materials presenting similar elastic properties, which is of prime interest in material sciences and biology^{182, 119}.

3.1.1. Methods

3.1.1.1. Material

Mode Synthesizing AFM was set up as depicted in **Figure 76**^{144, 160}. Previous reports show that one could obtain images of buried defects with high resolution, although comprehensive calibration of the method for volumetric characterization of materials is still lacking. In addition, the interpretation of the results obtained with the multi-frequency apparatus proves to be quite challenging, in particular for dielectric samples with low-density differences^{183, 156, 184}. For all experiments presented in this chapter, silicon nitride cantilevers (DNP-S, Bruker, $k=0.12\text{N/m}$), with an estimated contact radius of $10\pm 30\text{ nm}$ ⁸¹. The profiles of the nanoholes were determined using the cross section data analysis tool (Nanoscope Analysis).

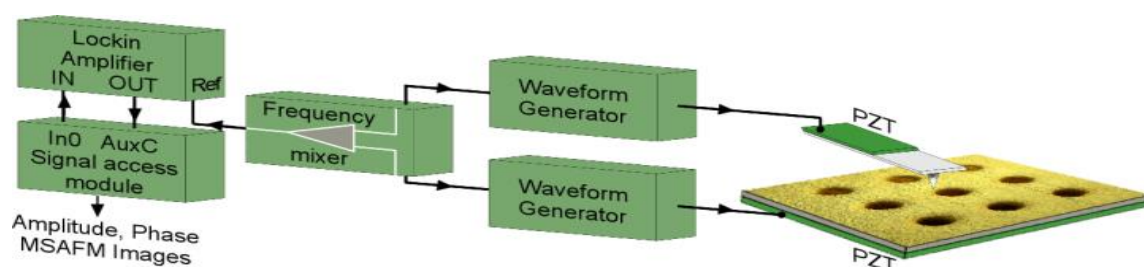


Figure 76: MSAFM experimental setup used in the characterization of dielectric materials, including multi-frequency actuation and heterodyne detection.

The cantilever and that sample are mechanically actuated by piezo actuators at their bases connected to respective waveform generators. The frequency mixer is used to select the reference frequency of the lock-in amplifier for amplitude and phase.

3.1.1.2. Peak Force QNM and Lateral Force Microscopy

Peak Force QNM and Lateral Force Microscopy studies were performed on a Multimode AFM (Bruker), with Nanoscope IV controller. Lateral force microscopy (LFM) consists in measuring the torsional bending of the AFM cantilever engaged in contact mode. Torsional bending of the cantilever is related to the friction force acting on tip. This mode is sensitive to mechanical and chemical properties of the material near the surface, underneath the tip of the cantilever. Peak Force Quantitative Nanomechanical Property Mapping (QNM), on the other hand, is based on force curve mode, which records four force curves at every point (pixel) of the image. This mode allows extracting the Young modulus of the sample, with simultaneous topography reconstruction.

Derjagin, Muller, Toropov (DMT) is a standard model used to fit tip-sample force curves in Peak Force QNM⁹⁰. The retract part of the force curve, when the cantilever-sample distance increases, is fitted using the DMT model, and the fit corresponds to the reduced modulus E^* calculated by:

$$F_{tip} - F_{adh} = \frac{4}{3} E^* \sqrt{R (d - d_0)^3} \quad (18)$$

Where F_{tip} is the force with which the tip is pressed on the surface, F_{adh} the adhesive force between the AFM tip and the sample, $d - d_0$ the sample deformation depth with correspond to the value indented by the tip in the sample (measured on the force curves) and R is the tip radius.

3.1.1.3. Raman spectroscopy mapping

Raman mappings of the calibration samples were performed at the University of Central Florida (UCF) in Dr. Laurene Tetard's group. The results were obtained on a confocal Raman system (WITec alpha300 RA) under ambient conditions with an excitation wavelength of 532 nm. The spectra were collected with a 100x objective and acquisition time of 0.1s with about 10 points per micrometer. The depth profiles were collected by performing XZ scans along the center axis (diameter) of the exposed regions.

3.1.1.4. Sample preparation

Sets of calibration samples were produced by depositing a 300 nm-thick layer of electrosensitive polymer (poly-(methy methacrylate) (PMMA)) on silicon (**Figure 77**).

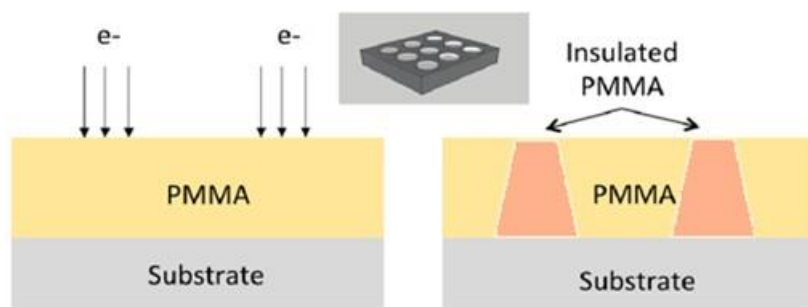


Figure 77: Nanofabrication process of the PMMA/Exposed (non-developed) PMMA patterned calibration samples.

The resin was then treated using electron beam lithography (EBL) to obtain 100x100 μm matrices of disks with doses ranging from 2.5 to 8.0. EBL was performed on a JEOL 6500 scanning electron microscope (SEM). The following parameters were then selected for the EBL process: the step size corresponding to the distance between two exposure points (defined in pixel) by the electron beam is adjusted in accordance with the desired structures for a given acceleration voltage current of the electron beam on the sample, and the dwell time for exposure time per pixel was defined for each step of the electron beam. The dose corresponds to the exposure time coefficient that can be locally applied on part of the pattern in order to control

the proximity effects and thus the size of exposed features. For instance, dose 1.0 is obtained with a step size equal to 20 nm, a dwell time of 0.017 ms, an acceleration voltage of 10 kV and a current of 20 pA. Hence, the dose is directly proportional to the dwell time:

$$\text{dose} = a \times 0.017 \text{ms}.$$

3.1.2. Results and discussions

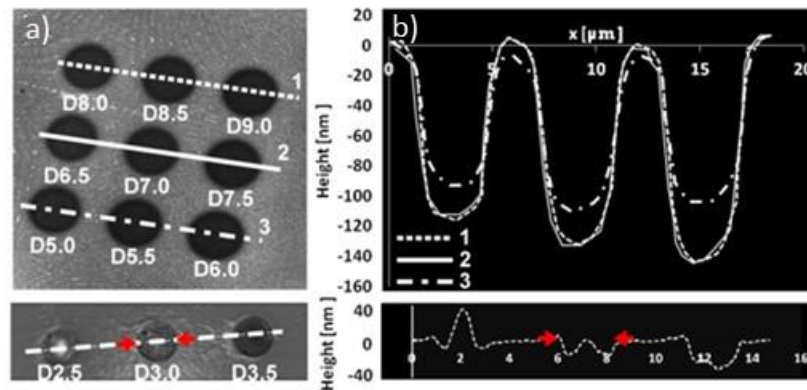


Figure 78: AFM characterization of the sample. (a) AFM images of the exposed PMMA dots resulting from e-beam treatment. (b) AFM cross-sections realized for lines across dots of different doses, as labeled in (a).

The nanofabricated structures (**Figure 77**) were first characterized by AFM (**Figure 78a**). From the profiles of the nanoholes (**Figure 78b**) it can clearly be seen that the depth of the structures and their lateral sizes vary with the dwell time and the dose. Under e-beam exposure, the main PMMA polymer chain undergoes scission. As a result, a change in the molecular mass of the PMMA is expected in the patterns of exposed dots, inducing a reduction of the space volume occupied by the polymer. This exposure induces topographical modifications as can be seen from the change in thickness of the treated region. Moreover, due to electrons forward- and back-scattering, the resulting shape of the nanostructures modified by the electron beam display a classical inverse V-shaped profile (**Figure 78b**).

During the MSAFM measurements, we found that a good synchronization of the scan rate with the sensitivity of the lock-in detection increased image quality. Although the scan rate did not influence the width of the exposed areas measured on each MSAFM frame. The optimization of the signals led to sharper amplitude and phase maps. Accordingly, we acquired the data with 4 Hz scan rate (**Figure 79**).

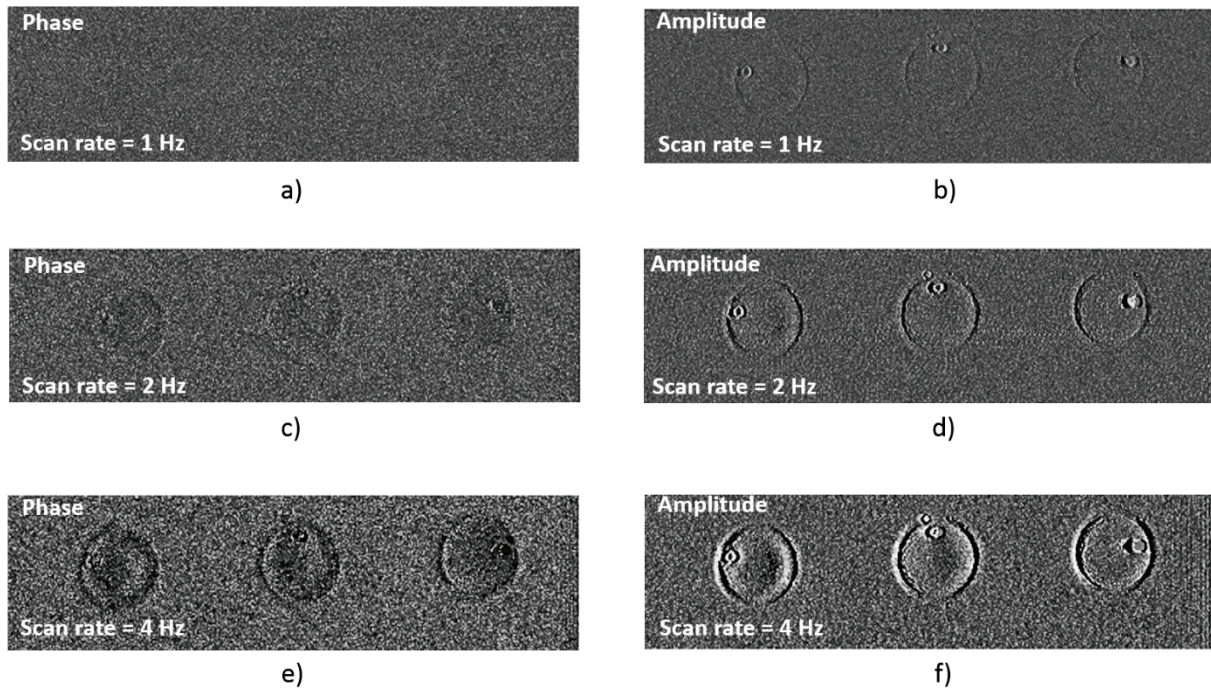


Figure 79: Influence of the scan rate on MSAFM phase (a,c,e) and amplitude (b,c,e) response of the difference mode of the MSAFM signals.

Next, we characterized the same region using MSAFM with varying Δf . The resulting maps are presented in **Figure 80(a-c)**.

By direct comparison of the MSAFM images obtained (**Figure 80**), a clear variation in the phase signal between the treated and non-treated PMMA can be observed. In addition, the diameter of the structures exhibited significant changes with increasing Δf . In the matrices exposed at doses varying from 2.5 to 3.5 (**Figure 80e, f**), the diameter of the dot exposed with dose 3.0 (middle dot) varied from 3.0 μm when probed with $\Delta f = 50 \text{ kHz}$ (**Figure 80e**) to 3.3 μm

when imaged with $\Delta f = 110$ kHz (**Figure 80f**). Overall, the minimum size was found for Dose=2.5 at $\Delta f = 50$ kHz while the largest was found for Dose = 3.5 at $\Delta f = 110$ kHz (**Figure 80d**). In the series of patterns with dot exposed at higher doses (**Figure 80b**), the diameter of Dose = 7.0 varied from $4.1\mu\text{m}$ at $\Delta f = 50$ kHz to $4.7\mu\text{m}$ at $\Delta f = 140$ kHz. The smallest observed structures were found with $\Delta f = 50$ kHz of the Dose = 5.0 dots, while the largest diameters were found for Dose = 9.0 at $\Delta f = 140$ kHz (**Figure 80 c-g**). It was necessary to increase Δf to 140 kHz to probe the bottom of the structure, suggesting larger volume of modified PMMA with higher doses.

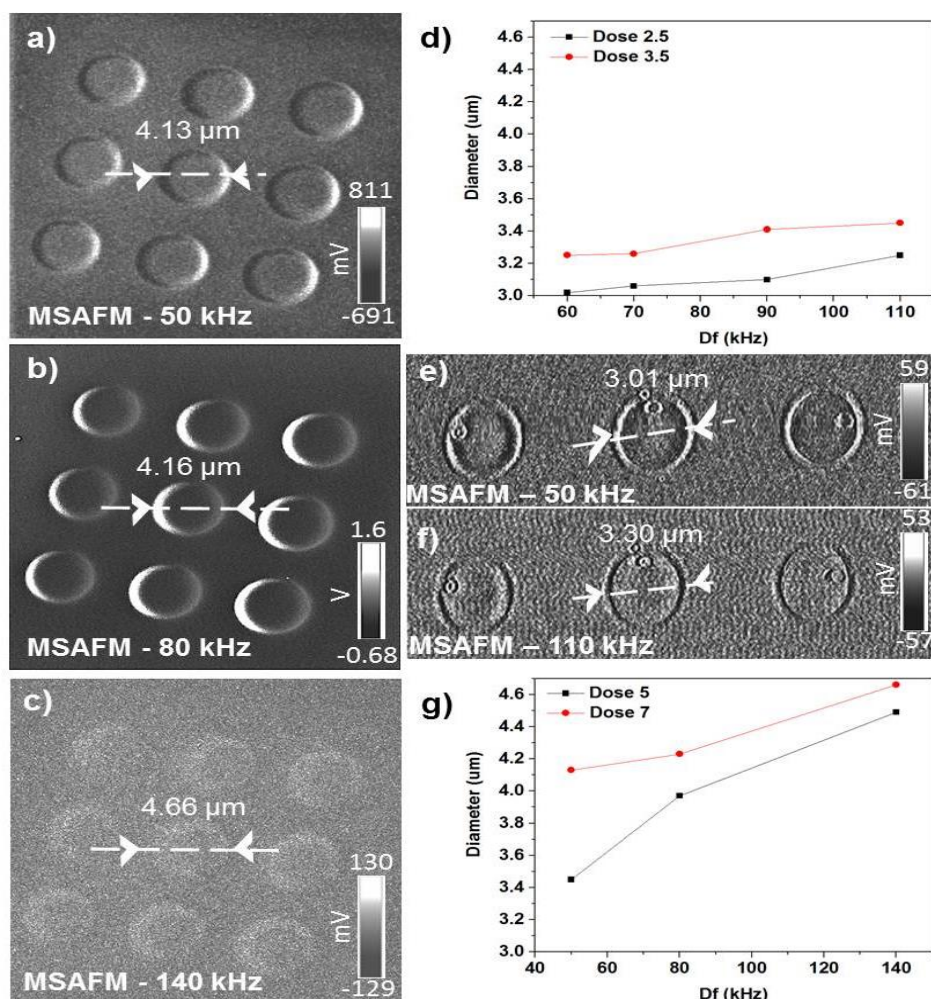


Figure 80: MSAFM characterization of the calibration samples. (a-c) MSAFM images for high doses (D5.0-D9.0) acquired at (a) $\Delta f = 50\text{kHz}$, (b) $\Delta f = 80\text{kHz}$, and (c) $\Delta f = 140\text{kHz}$. (d) Evolution of exposed PMMA dots diameters as a function of frequency Δf for doses D2.5 and

D3.5. (e,f) MFAFM images for lower doses (D2.5-D3.5) acquired at (e) $\Delta f = 50\text{kHz}$, and (f) $\Delta f = 110\text{kHz}$. (g) Relationship between dot diameter and Δf frequency for doses D5.0 and D7.0.

To better understand the nature of the local polymer conformation change induced by electron-matter interaction and related MSAFM image formation mechanisms, we performed Peak Force QNM, Lateral Force Microscopy (LFM), and Raman spectroscopy on the same regions of the sample.

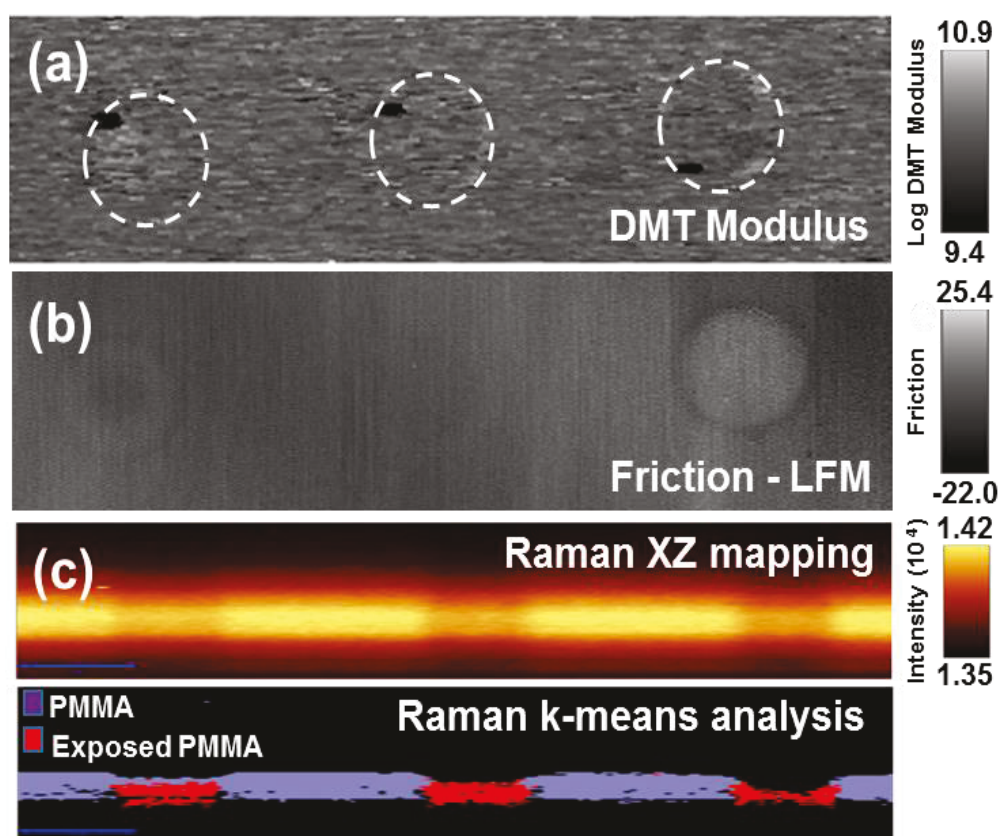


Figure 81: Calibration sample characterization by Peak Force QNM (a), Lateral Force Microscopy (b) and Raman spectroscopy (c) including Raman XZ mapping and corresponding k-means analysis.

After Peak Force QNM mapping, we extracted the reduced Young modulus E^* across the sample using the DMT-based model (see methods), which is an accepted model for standard AFM-based measure of the Young's modulus in materials. Peak Force QNM measurements did

not reveal significant variations of the Young modulus (**Figure 81a**), showing no differences inside and out of the dots: this proves that the nature of materials was modified and that polymer remains inside the dots. The absence of change in the Young modulus between the exposed and the non-exposed polymer suggests that the variations measured by MSAFM are not caused by a change in modulus of the material. As the speed of the ultrasonic waves depends on the propagation medium and varies with the material, the wave speed expression is defined as the ratio of the bulk modulus K related to the stiffness of the medium and its resistance to being compressed over the density (ρ) of the medium:

$$v = \sqrt{\frac{K}{\rho}} \quad (19)$$

$$\text{with } K = \frac{1}{3} \frac{E}{(1 - 2\nu)}$$

and ν the Poisson coefficient (between 0.4 and 0.43 for the PMMA). With a constant modulus E , an increased propagation velocity in the e-beam exposed PMMA can be caused by a decrease in density ρ . This would agree with a higher acoustic response, as the one observed in the MSAFM map. Thus we infer that the changes observed in **Figure 80** are related to the difference of density ρ resulting from EBL on PMMA, which is also coherent with a smaller molecular weight of the irradiated polymer compared to that of the unexposed polymer. Further, we acquired LFM maps of the same region of the sample. LFM is commonly used to detect changes in chemical composition or viscosity changes in materials. As can be seen in **Figure 81b**, no contrast could be observed on the LFM images acquired on the calibration samples, except at a higher dose (Dose = 3.5), which may be due to topographical variations inducing a peripheral friction response. Hence, the results confirm that EBL exposure of PMMA does not affect the viscosity and likely does not modify the chemical composition of the thin layer. However, while the Peak Force QNM and LFM can provide some insight on the properties of the sample

surface, they cannot access depth information. Thus, to gain some insight on the volume properties of the exposed PMMA film, we acquired Raman depth profile across the dots of the matrix (**Figure 81c**). A comparison of the individual Raman spectra in the exposed and non-exposed regions confirms that PMMA chains are preserved after e-beam treatment. However, the exposed regions exhibit a lower signal in the map, in good agreement with the idea of the lower density of the treated material. Thus, MSAFM complemented of Peak Force QNM, LFM and Raman data demonstrate and confirm that density is the only parameter changing in the sample. We explored the Raman signal further to obtain some information on the in-depth profile of the exposed regions. K-means analysis on the Raman data sets revealed a low resolution profile of the depth cross section of the exposed dots (**Figure 80d**). Although with poor spatial resolution, the slight enlargement observed is in agreement with the expected profile of an electro-sensitive resin by EBL. Therefore the changes in diameter of the exposed dots resolved with MSAFM show that the technique is sensitive to depth information and can probe the volume information of the sample. By extracting the changes in volume density from each MSAFM map and representing it as a function of driving frequencies and difference frequency Δf , we propose a simple procedure for the 3D reconstruction of the sample¹³⁹. In short, by considering the attenuation resulting from the acoustic waves (launched by the mechanical actuators located at the base of the cantilever and below the sample) propagation through the medium, attenuation amplitude (z) of the mixed wave Δf resulting from the nonlinear tip-sample interaction can be formulated:

$$A(z) = A_0 e^{-\left(\frac{\alpha_p + \alpha_s |z|}{v}\right)} \quad (20)$$

with α_i ($i=s,p$) = $\alpha_i(f)$ the attenuation coefficients (depending on frequency f) of the probe and the sample, z the investigation depth, and v the velocity of the ultrasonic wave. By calculating

the minimum of attenuation for each combination of Δf in MSAFM, it is then possible to link the actuation frequencies and their difference with the investigation depth.

Experimentally, the changes in diameter are extracted for the sequence of MSAFM images obtained at each Δf . By assigning an investigation depth (obtained with the simple numerical model) for each Δf , it is then possible to reconstruct the three-dimensional profile of the exposed region inside the PMMA film. The resulting reconstruction, acquired with ten successive MSAFM frames, is presented in **Figure 82**. The 3D reconstruction of the sample is in good agreement with the expected plum shape of exposed PMMA region below the surface.

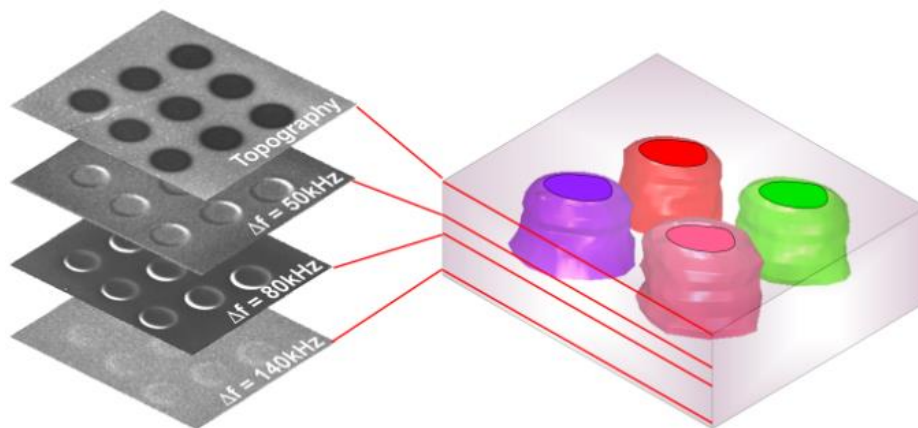


Figure 82: 3D reconstruction of subsurface structure and composition of the PMMA/exposed calibration samples. The 3D reconstruction is obtained by extracting the diameter for a ten successive MSAFM phase image.

Another point that is important to notice is the contrast changes that can appear between MSAFM images taken at different Δf frequencies (**Figure 83**). One can notice a contrast inversion between the phase images **Figure 83c** and **Figure 83e** when the Δf frequency changes from 50 kHz to 80 kHz. On the contrary, this phenomenon is not visible on amplitude images (**Figure 83b** and **Figure 83d**). These observations confirm that the contrast change is not due to a modification of the interaction tip/sample (because the amplitude signal is not affected) but

is the result of the ultrasound waves interaction. Two hypothesis could explain this contrast inversion observed in phase: a difference between the length travelled by the waves that can be assimilated to a difference between optical path in the optical field; or the jump around a resonance peak induced by the frequency change of the cantilever leading to a phase shift as well.

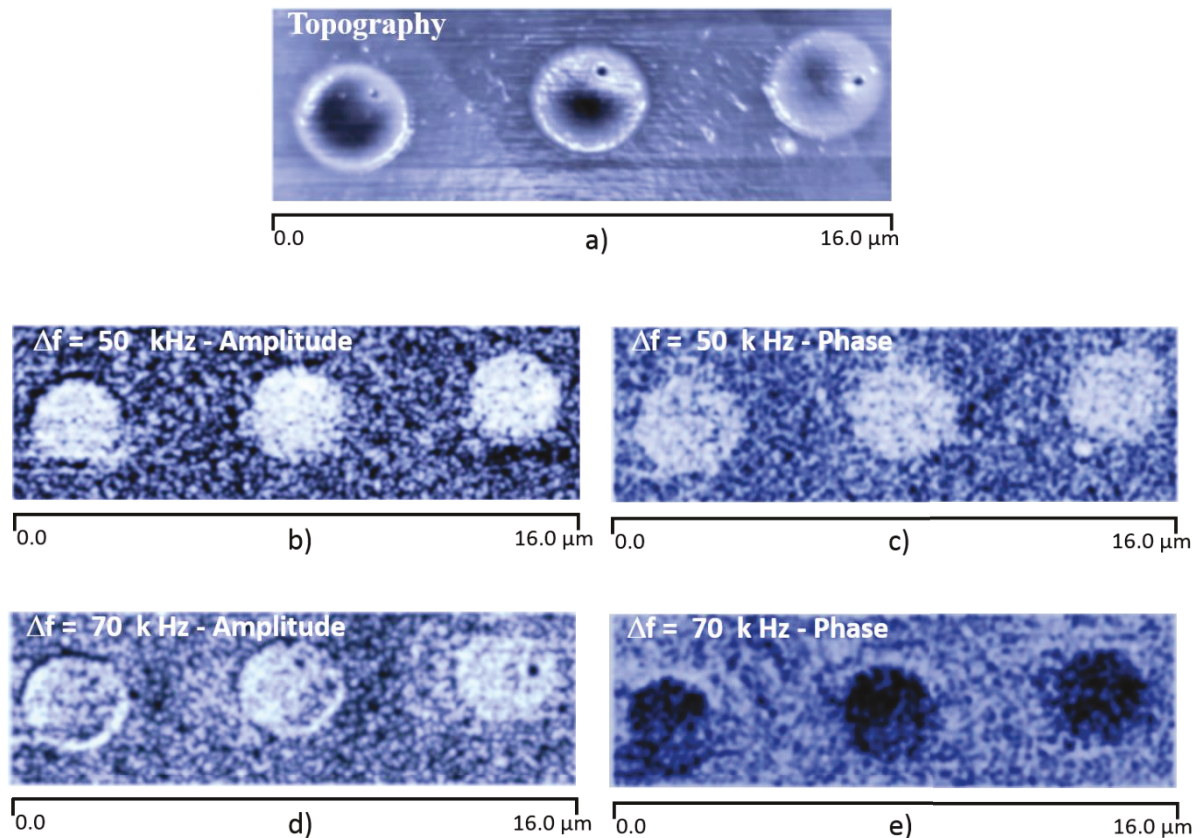


Figure 83: Highlighting the contrast change effect in MSAFM images with the Δf frequency difference. (a) Topography image (Scan size 16 μm). (b) and (c) Amplitude and phase images at $\Delta f = 50$ kHz. (d) and (e) Amplitude and phase images at $\Delta f = 70$ kHz.

3.1.3. Conclusion

MSAFM is well adapted for the characterization of low density material and offers the possibility to create a 3D reconstruction of the device undergoing testing. Its sensitivity was compared to three standard characterization techniques Peak Force QNM, LFM and Raman spectroscopy. Our study shows that MSAFM offers the best sensitivity and spatial resolution

in presence of low density variations. In addition, different parameters such as frequencies and scan rate were found to play a significant role in the quality of the acoustic picture. The ability to image complex systems with low density changes is especially important in biology. Indeed, it is a central in the behavior of dynamic entities in intracellular organisms and conformational changes in response to various external agents such as chemical or thermal stresses. Consequently, our results highlight the great potential of MSAFM for ground breaking discoveries in soft matter and life sciences.

The next parts of this chapter are focus on the use of MSAFM for the study of complex biological samples presenting volume elements can cannot be resolved by conventional microscopy technique in a non-destructive way.

3.2. Study of the action of an alcoholic stress on *Oenococcus oeni* bacteria

3.2.1. Introduction

Oenococcus Oeni bacteria play a crucial role in the malolactic fermentation involved in the vinification process¹⁸⁵. The conditions of development of this bacteria in wine are not favorable mainly due to the high ethanol concentration (12%)¹⁸⁶.

It was shown that the bacteria strain possesses high adaptation capabilities in this environment and thus represents a good model for the study of bacteria stress responses¹⁸⁷. One of the resistance mechanism involves a small heat shock Lo18 protein (sHsp Lo18), which is expressed under various stress conditions (temperature variations, presence of alcohol...)¹⁸⁸.

The sHsp Lo18 protein is expressed during the alcoholic fermentation process in *Oenococcus Oeni* bacteria. As the alcohol induces stress on the bacteria membrane and content, the sHsp Lo18 protein will protect the membrane and the intracellular material of the bacteria, as response mechanisms presented in **Figure 84**.

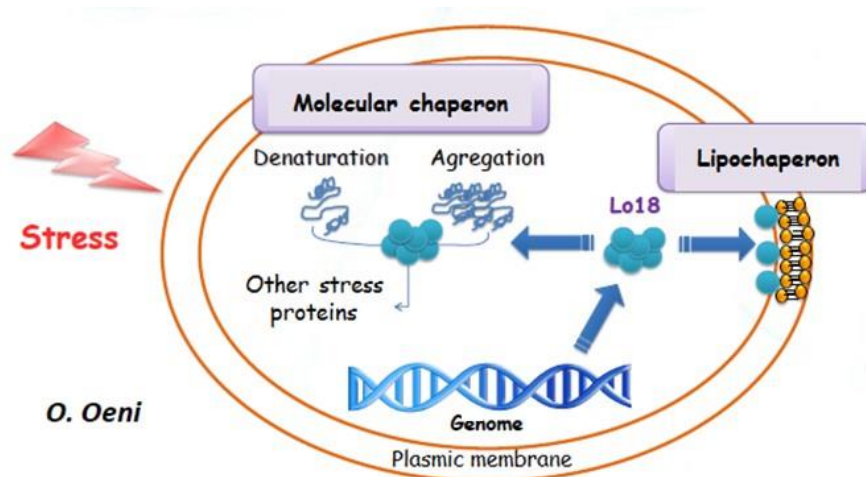


Figure 84: Overview of the response mechanisms of Lo18 protein to external stress. Under a stress, the Lo18 protein is produced by *O. Oeni* bacteria and acts like a molecular chaperon to avoid the denaturation of the other proteins present in the bacteria and like a lipochaperon to preserve the integrity of the membrane.

Recently, a lipo-chaperon activity of the sHsp Lo18 protein was discovered. This lipo-chaperon activity is characterized by the association – under thermal stress condition - of a part of the protein with the membrane to rigidify it and thus protect the intracellular bacteria material from the stress attack^{189,190}.

The expression of this protein is induced not only upon thermal stress but also under the action of some chemical agents, such as benzyl alcohol (BA) or ethanol, responsible of membrane fluidizing¹⁹¹.

In this part, we present our study of the action of an alcoholic stress on the bacteria by MSAFM. Next, to mimic the rigidizing of the membrane in presence of the sHsp Lo18 protein induced by the stress, we reconstructed an artificial membrane by Langmuir-Blodget technique as a model of the *Oenococcus Oeni* bacteria.

3.2.2. Characterization of *Oenococcus Oeni* bacteria under stress by MSAFM

The characterization of *Oenococcus Oeni* bacteria is realized by MSAFM in different environmental conditions: first when the bacteria are subjected to no stress and second after the bacteria has undergone a 36 hours' stress imposed by Benzyl alcohol (BA) treatment.

For MSAFM observations the bacteria are deposited on stainless steel support and analyzed in air.

Figure 85 presents the *Oenococcus Oeni* bacteria with no stress in both topography and acoustic imaging. The topography is common, with a height of 457nm (± 35 nm), a length of 1.5 μ m ($\pm 0.2\mu$ m) and a width of 1.3 μ m ($\pm 0.2\mu$ m). Interestingly, acoustic imaging revealed internal structures of the bacteria with high resolution: one can observe compartments and a cell wall of about 70nm thick, which is in agreement with the values of cell walls in Gram positive bacteria¹⁹².

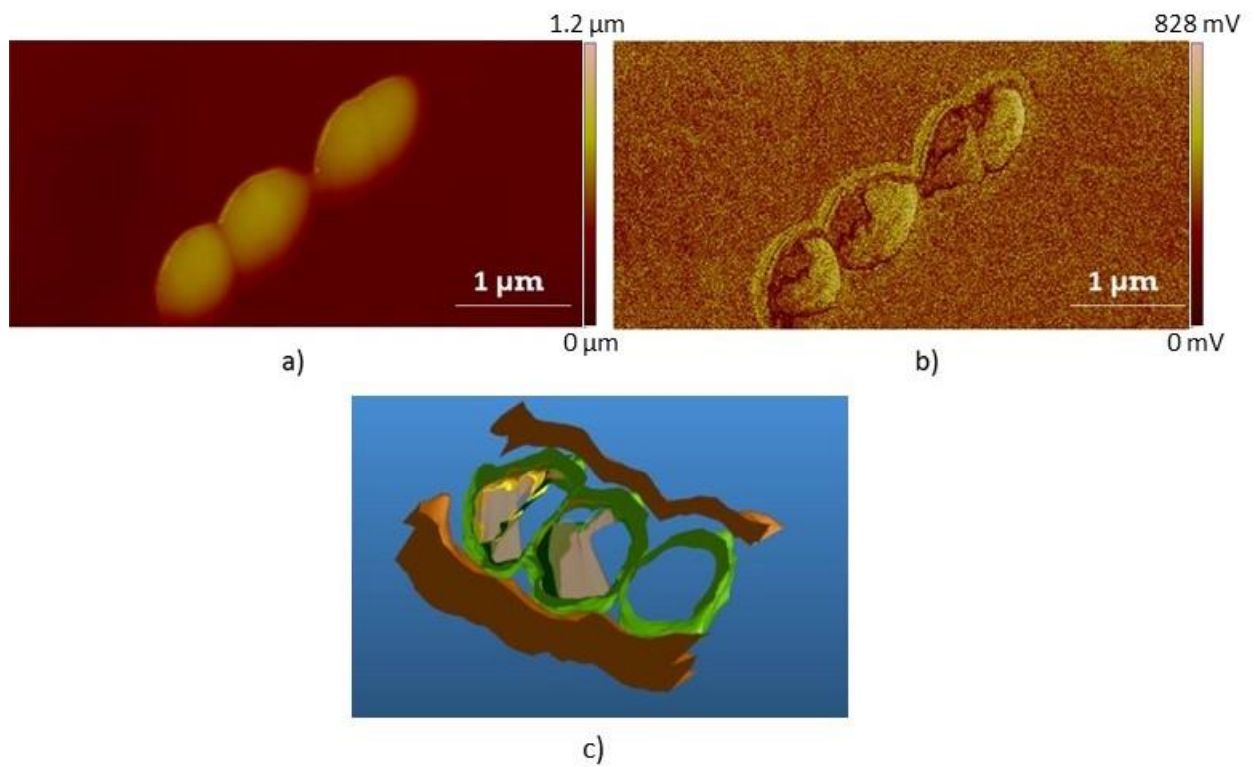


Figure 85: Non-stressed *O. Oeni* bacteria. (a) Topography. (b) Acoustic MSAFM image – $f_1 = 4.3$ MHz, $f_2 = 4.350$ MHz - $\Delta f = 50$ kHz revealing inner structures. (c) Tomographic reconstruction of the bacteria.

Next, to observe the impact of alcoholic stress on a bacterial structure, we realized MSAFM images of the cells after a 36h alcoholic stress period. We noticed variations in the dimensions of the bacteria on stressed samples, which were not present in the control sample. The dimensions are summarized in **Figure 86**.

Stressed bacteria – Heterogeneous dimensions			Control bacteria – homogeneous dimensions
Height: 300±15 nm	Height: 229±25 nm	Height : 250±17 nm	Height : 474± 14nm
Length: 970±25 nm	Length: 1.6±0.2 μm	Length : 830±36 nm	Length : 1.5±0.10 μm
Width: 1.2±0.15 μm	Width: 918±45 nm	Width : 1.0±0.17 μm	Width : 1.3±0.17 μm

Figure 86: Topographical dimensions of non-stressed and stressed bacteria.

In addition to the changes observed in the topography – heterogeneity in the dimensions of the stressed bacteria – the structures observed with acoustic imaging, as shown in **Figure 87**, were quite different from the control cells in **Figure 85**. In addition, the frequency range of the acoustic signal required to detect the structures shifted from the 4MHz range to a 5MHz range. Moreover, the structures observed in the acoustic image of the stressed bacteria are not as well defined as the ones shown in **Figure 85**, and their dimensions changed significantly (**Figure 86**).

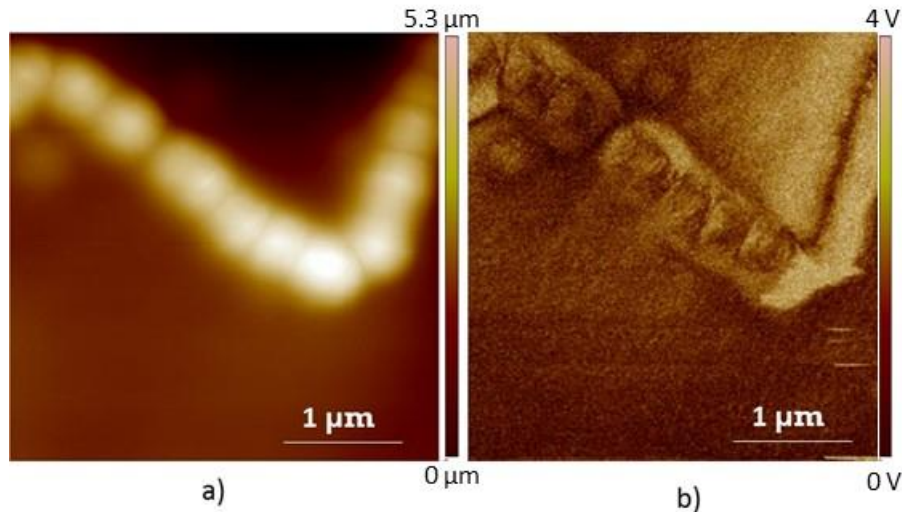


Figure 87: Stressed *O. Oeni* bacteria. (a) Topography. (b) Acoustic MSAFM image – $f_1=5$ MHz, $f_2 = 5.050$ MHz - $\Delta f = 50$ kHz revealing the inner structures of the bacteria that are different from **Figure 85**.

We surmised that the modifications unveiled by acoustic imaging are related to changes in the bacteria density as a result of the alcohol stress. In addition, we formulated the hypothesis that during the stress period, membrane rigidizing that result from the sHsp Lo18 protein action occurs, modifying the structures and mechanical properties of the bacteria.

3.2.3. Conclusion

This study unveiled significant changes in the morphology (height and length) of the *Oenococcus bacteria* as a result of stress on the culture during growth. MSAFM was used for in-depth characterization of the inner structures of the bacterial, and brought out modifications in the inner structures of the cell wall under stress. Moreover, we found that the acoustic signal detected can be significantly different in the case of stressed bacteria. Our current assumption is that the strong variations observed in the acoustic images and signals are related to the membrane rigidizing of the bacteria due to the lipo-chaperon activity of the sHsp Lo18 protein under stress conditions. This study strengthens our argument that MSAFM has the potential to

become a strong tool for in-depth characterization of biological elements, in particular to detect changes in density in complex biological material.

The next step of this work consists in using the MSAFM to realize 3D reconstruction of biological elements.

3.3. Combining AFM-IR and Mode Synthesizing Atomic Force Microscopy: Application to the study of Triglyceride vesicles inside *Streptomyces* bacteria

3.3.1. Introduction

We explored here another type of bacteria called *Streptomyces* which are of a great interest in the biofuel production¹⁹³.

Biofuel is an alternative energy source and a less toxic substitute for petroleum-based diesel fuel. Producing biodiesel in a sustainable way will allow this renewable and cost effective fuel to ease the world's high demand in petroleum, while providing economic and environmental benefits into the 21st century¹⁹⁴. Biofuel is produced from renewable biomass by transesterification of triacylglycerols¹ from plant oils, yielding monoalkyl esters of long-chain fatty acids with short-chain alcohols such as fatty acid methyl esters and fatty acid ethyl esters. Biofuel solutions promise to have important environmental benefits when used as a mainstream alternative to fossil fuels: they are carbon-neutral over their lifetime and are far less toxic than the petro-diesel derivatives¹⁹⁵. However biofuel solutions are being criticized because of high costs associated with production and because they are using agricultural land that could be used for alimentation. As an alternative, biologists recently engineered microorganisms to make biofuels, such as ethanol, butanol or octanol^{196, 197, 198}. However, the cells cannot produce the fuels at industrial scales since the fuel molecules are toxic to the microbes, killing the organisms before they can reach high yield production¹⁹⁹. Nonetheless, other potential biofuels such as oils are stored in specific organelles and are not as toxic for the producing micro-organisms²⁰⁰. While the earliest attempts to engineer biofuel-producing microbes were focused on well-known organisms such as yeasts and *E. coli*^{201, 202, 203}, scientists also hope to co-opt the unique metabolic functions of some other microbial species well known for their ability to grow at an

industrial scale. Indeed, *Streptomyces* bacteria grown in big fermenters for decades in the pharmaceutical industry to produce most of the antibiotics used in modern medicine^{204, 205, 206}. Furthermore, these soil-born bacteria have the natural ability to degrade various wastes of the agro-industry (lignocellulose, beat pulp...), hence limiting the consumption of products used for human alimentation. The group "Energetic Metabolism of *Streptomyces*" of the Institut de Biologie Intégrative de la Cellule (URA CNRS 1354 - leader: M.J. Virolle) identified different *Streptomyces* species as good candidates to generate bio-oils²⁰⁷. Interestingly, these *Streptomyces* species can store excess of carbon into TriAcylGlycerols (TAGs), a ready-to-use source of bio-diesel. These TAGs are chemically and structurally identical to those found in commercial fuels. Two patents were recently filed by this group with SOFIPROTEOL (one of the main industrial producer of vegetal bio-diesel in Europe) demonstrating the interest of *Streptomyces* as bio-fuel producers. The microbiology group in Orsay is now actively selecting the most promising *Streptomyces* species for bio-oil production and exploring genetic engineering strategies to enhance the natural ability of a model, *S. coelicolor*, whose genome was sequenced. This work is done in the framework of the ProBIO3 project, whose goal is to develop an industrial production of microbial bio-oil for bio-diesel/bio jet fuel generation.

To support the microbiology team, we need tools appropriate for the evaluation of density of TAGs accumulation in bacteria. Coupling the chemical imaging capability of Infra-Red Atomic Force Microscope and the subsurface detection capability of Mode Synthesizing Atomic Force Microscopy (MSAFM) was used to access a complete analysis of the lipids production in the bacteria.

In this section, we present a comparative study of AFM-IR (nanoIR microscope from Anasys Instruments) and MSAFM maps of the bacteria to detect triglycerides vesicles in *Streptomyces* bacteria and highlight the synergy between the two methods.

Using high-resolution infrared microscopy (nanoIR) with laser illumination at 1740 cm^{-1} and MSAFM with acoustic actuations in the MHz range, we detected the presence of the vesicles and we measured their size and position below the surface. We assessed the vesicle size distribution in the bacteria with accuracy of at least 50 nm. The chemical measurement confirmed that the structures detected with MSAFM were, indeed, vesicles. A 3D reconstruction of bacteria, showing the vesicles distribution inside the bacteria was performed to underline the great potential of the acoustic method²⁰⁸.

3.3.2. Samples preparation

3.3.2.1. Bacterial strains and growth conditions

The *Streptomyces* strains were *S. lividans*. 10^6 spores were spread on cellophane disks laid down on the top of agar plates. The solid medium was R2YE with no addition of phosphate salts. The plates were incubated at 30 °C for 72h.

3.3.2.2. Sample preparation for AFM-IR measurements

The cell suspension of each culture was spun down at 5000 x g for 2 min, the supernatant was removed, and the cell pellet was diluted in distilled water. To wash the bacteria thoroughly, this operation was repeated three times. Finally, a drop was deposited on a ZnSe (transparent in the mid-IR) prism and dried at room temperature.

3.3.3. Results

The AFM-IR images and MSAFM images of *Streptomyces* bacteria were realized in the same area (scan size 10 μm x 10 μm) to correlate the chemical information with the structures identified inside the bacteria. **Figure 88** shows a set of images obtained by these two different methods.

Several filaments characteristic to *Streptomyces* bacteria are detected in topography, showing bacteria of about 500 nm in width and filament assemblies of bacteria several micrometers in length (**Figure 88a**). **Figure 88b** represents the chemical mapping obtained when the energy

necessary to excite the of the triacylglycerol vesicles at 1740 cm^{-1} is used to illuminate the sample ¹⁰⁹. MSAFM images obtained on the same area, show dark spots that coincide with the regions identified as rich in ester carbonyl bonds by the AFM-IR measurements.

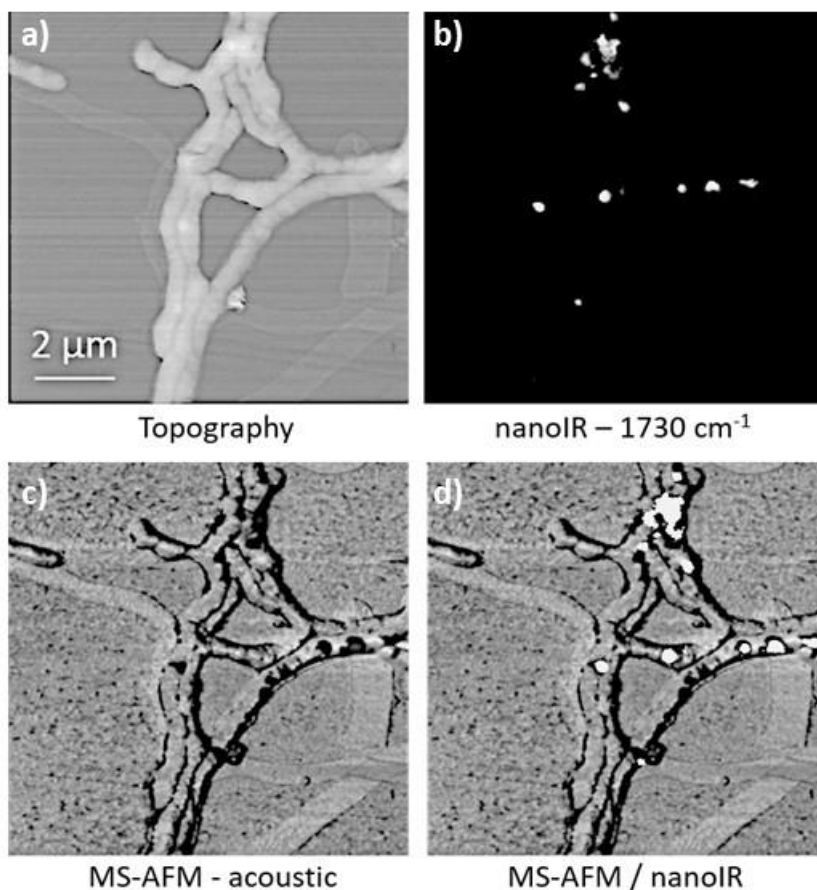


Figure 88: MSAFM and AFMIR imaging (Range $10\text{ }\mu\text{m}$). (a) AFM topography. (b) AFM-IR image at 1740 cm^{-1} . (c) MS-AFM ultrasound image ($\Delta f = 50\text{ kHz}$). (d) Overlay of IR and acoustic images.

This suggests that the dark features detected by MSAFM are the vesicles inside the bacteria. For vesicles buried deeper into the bacteria (i.e., not close to the membrane) the nano-IR signal (**Figure 88b**) appeared slightly blurry (or larger in diameter) compared to the features resolved by MSAFM (**Figure 88c**). The detection of the thermal expansion in AFM-IR is integrative as the signal detected will depend on the distance between the feature absorbing energy and the tip in contact with the sample. If the vesicle is small and buried into the bacteria then the signal

detected will be weaker and more diffuse than if the vesicle is close to the surface or in direct contact with the cantilever tip. On the other hand, the contrast of the acoustic image showed to be very strong and the vesicles could clearly be detected due to the dark contrast when compared to the filaments response. This strong contrast may be attributed to the low-density property^{139,143 14} of the lipid vesicles that are less dense than the dry matter of the bacteria filaments. This high contrast allows us to localize the vesicles, identify how many are located in each bacterium and estimate their lateral size.

However, we noted that a strong change in signal appeared along the filaments at the right border of the bacteria (**Figure 88c**), which was attributed to a shadow effect of the lateral acoustic waves and is not correlated to the lipid absorption (**Figure 88b**).

The superimposition of MSAFM images and AFM-IR images (**Figure 88d**) confirms the excellent correlation between the image of lipid identified by infra-red and the acoustic image. This was repeated over many different regions showing that the black contrast of the acoustic image is related to the light contrast of AFM-IR images induced by the presence of lipid vesicles (**Figure 88**).

After further study of the MSAFM images, we noticed that the acoustic signal inside the vesicles was constant, with no gradient or soft interface between the vesicles and the bacteria. The MSAFM cross-section (**Figure 89c**) realized on a vesicle (**Figure 89b**) the sharp transition (about 40-70 nm) compared to the cross section obtained on the AFM elasticity image obtained with Peak Force QNM on a bacterium containing lipid vesicle (**Figure 89d-f**).

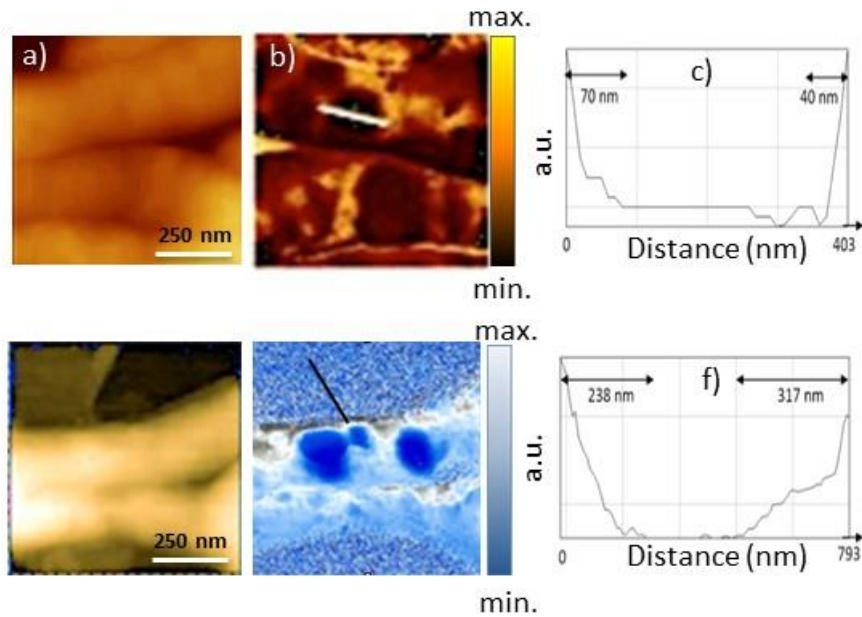


Figure 89: Comparison between MSAFM and AFM elasticity measurements. (a) AFM topography. (b) MSAFM image ($\Delta f = 50$ kHz). (c) MSAFM cross-section realized on a vesicle. (d) AFM topography. (e) Elasticity response of the bacteria containing lipid vesicles. (f) Cross-section realized on the elasticity response of a vesicle.

Figure 89d represents the morphology of the region inspected while **Figure 89e** shows the variations in elasticity detected in the same region. In **Figure 89f**, the cross-section showing the change in elasticity across the vesicle indicates that the transition of stiffness spans over 300nm.

These observations suggest that the acoustic signal is not directly proportional to the stiffness difference between the membrane surface and the vesicle itself. The MSAFM image contrast is induced by the density difference between the vesicle and the other elements of bacterium. For the vesicle, this density at a given level, probed by the fixed value of Δf for each MSAFM image, is constant.

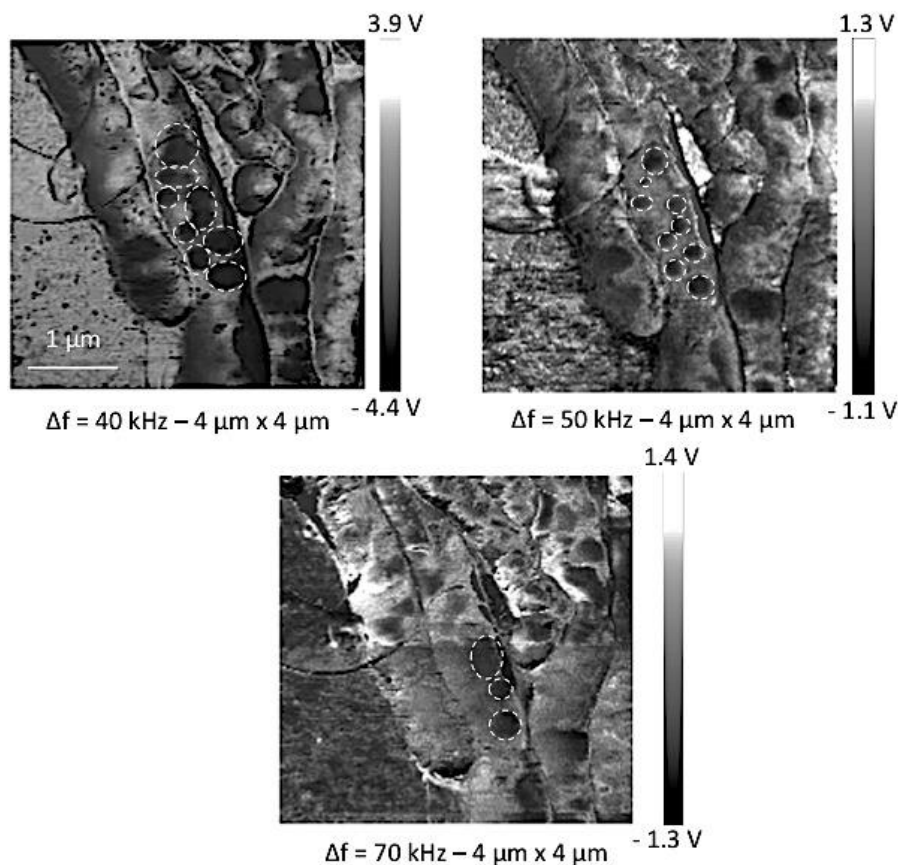


Figure 90: MSAFM phase images in depth investigation – Evolution of the lipid vesicles size with the frequency (Range $4 \mu\text{m}$) at frequency $\Delta f= 40 \text{ kHz}$, $\Delta f= 50 \text{ kHz}$ and $\Delta f= 70 \text{ kHz}$.

Then we analyzed a bacteria by MSAFM at different Δf frequencies. The results are presented in **Figure 90** where the evolution of the vesicles size with the frequency- and thus the depth- can be observed. From these results, we took advantage of the sensitivity to volume content to reconstruct the 3D profile of the bacteria and the vesicles. This was possible by varying the difference Δf in frequency by changing the ultrasound wave transferred into the specimen^{13, 156}. The resulting 3D reconstruction of a part of a bacterium with small lipid vesicles localized under the surface of the bacterium filament and other occupying the entire filament is presented in **Figure 91**. The results obtained are in good agreement with the vesicles production metabolism where we should detect vesicles with a wide range of size and volume.

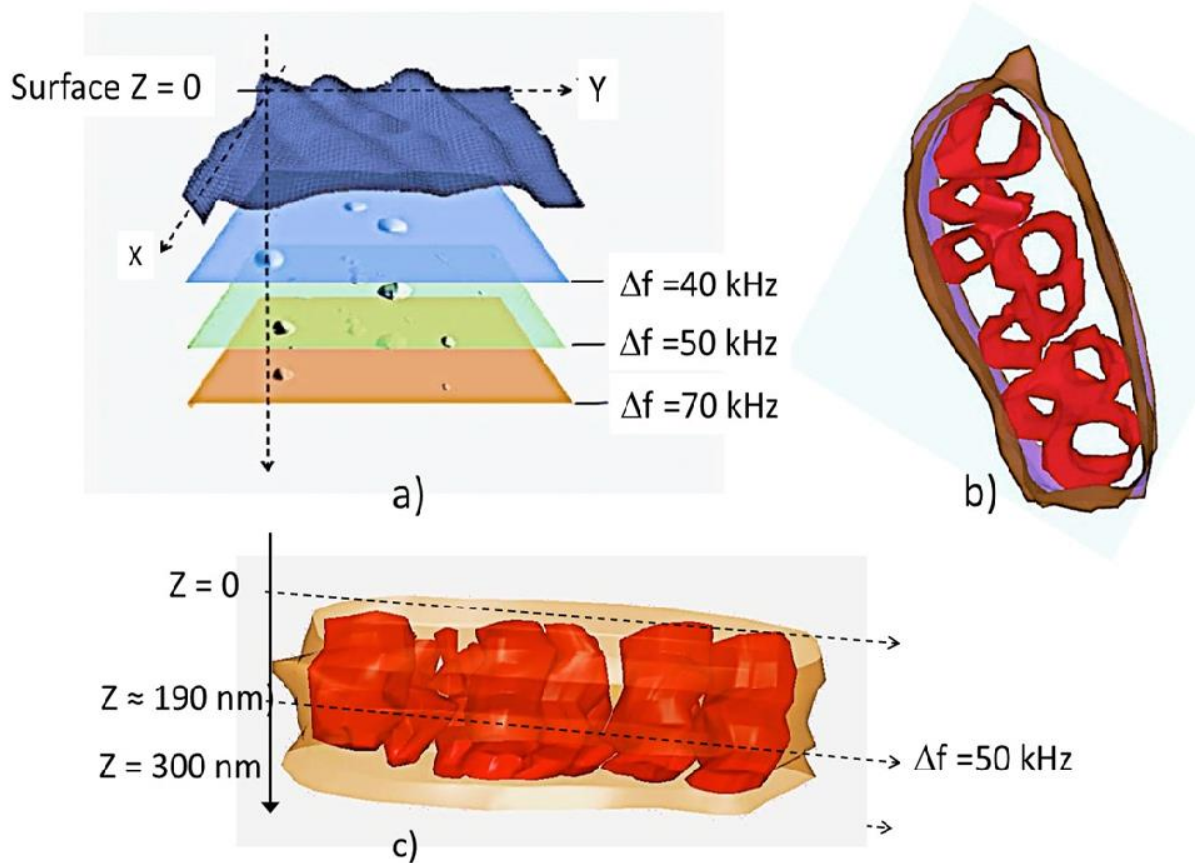


Figure 91: 3D reconstruction of a bacteria containing lipid vesicles. The reconstruction is obtained by stacking MSAFM images for 10 different Δf frequencies. (a) Stacking MSAFM images for 3 different Δf frequencies (40 kHz, 50 kHz and 70 kHz). (b) Top view of 3D reconstruction. (c) Lateral view of 3D reconstruction.

Finally, we further compared the MSAFM images and IR image hot spots corresponding to the strong local contrast difference observed in acoustics. As previously mentioned, the infrared absorption signal is linked to the sample-surface distance, leading to diffusion phenomenon around the position of the vesicles. We expect the diffusion to be more important in the areas where the vesicles are buried deeper into the bacteria. Indeed as can be seen in **Figure 92b**, one can notice the diffusion of the signal resulting from thermal expansion inside the system hindered the spatial resolution in that neighboring lipid vesicles inside the compact and complex absorption shape (inside dashed line mark) could not be resolved while acoustic images (**Figure 92c**) clearly reveal the vesicles boundaries.

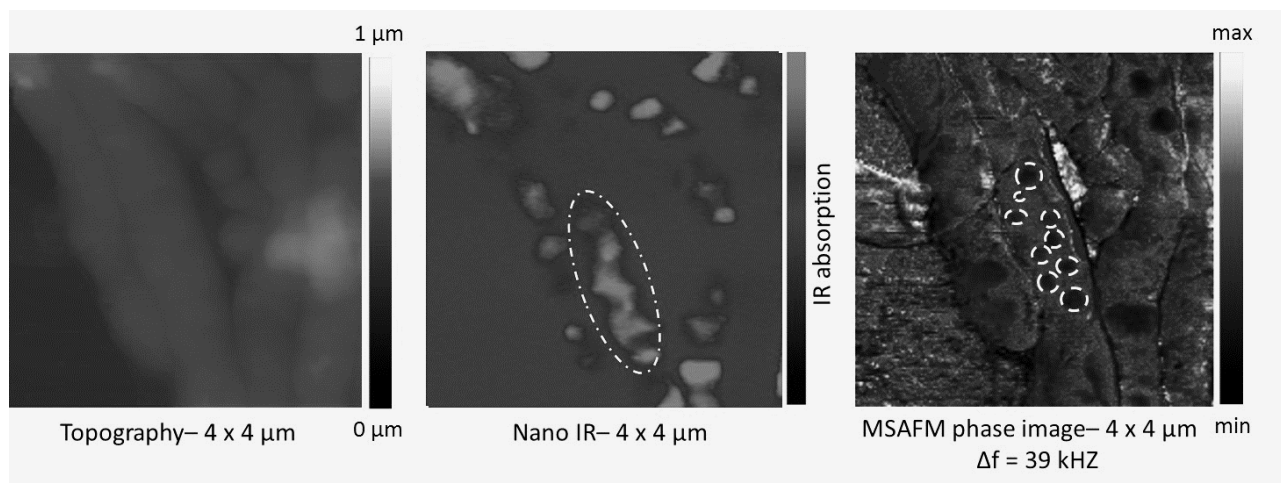


Figure 92: Resolution comparison between AFM-IR and MSAFM techniques. (a) AFM topography. (b) AFM-IR chemical mapping at 1740 cm^{-1} . (c) MSAFM phase image at $\Delta f = 50\text{ kHz}$ (Range $4\text{ }\mu\text{m}$).

3.3.4. Conclusion

The interest of coupling both techniques and showing their complementarity to identify and estimate the number and size of vesicles inside the bacteria was demonstrated in this study. We demonstrated the contribution of the acoustic and IR coupling in terms of subsurface and chemical information, respectively.

AFM-IR analysis is of great interest to screen the lipid content of the bacteria removing acoustic artifact inside the bacteria while MSAFM analysis improves the spatial resolution for smaller vesicles or vesicles lying inside the filaments.

As a result, we propose that the lack of discrimination between closer lipid vesicles in the IR images could be overcome with a technique taking advantage of both MSAFM and AFM-IR approaches. One aspect of this was recently reported by Dr. Tetard²⁰⁹. Furthermore, upon 3D reconstruction, with more advanced image learning methods, it will be possible to determine the real diameter of each vesicle in the volume, to build a distribution of the vesicle sizes in the bacteria.

3.4. Conclusion

This chapter highlights the high potential of MSAFM through the analysis of calibrated dielectric samples presenting embedded low-density dielectric nanostructures, bacteria and lipid vesicles. High resolution 3D tomographic reconstructions were realized as well as a first understanding of the influence of the frequency on depth investigation for dielectric samples. We also demonstrated that this approach, in combination with AFM-IR, can be used to tackle complex biological problems, such as bacteria membrane rigidizing or formation and evolution of lipid vesicles inside bacteria. MSAFM is a very promising tool in the characterization of biological samples but remains limited for the study of metals because it does not allow the discrimination of different chemical elements.

The next chapter will focus on the SMM technique in order to answer this problematic for a full characterization of metal materials.

Chapter 4 – *Application and development of tomography on metallic samples by Scanning Microwave Microscopy.*

This Chapter presents the application of near-field technique, SMM, to investigate subsurface properties in metallic components. We introduce several new approaches to access specific information describing the metallic components such as residual stress and present novel advanced methods for near-field microscopy. Subsequently, these studies reveal new possibilities for the use of the local probe of SMM in the industry.

4.1. Study of various factors influencing Scanning Microwave Microscopy Measurements

Predicting quality control and servicing of parts subjected to harsh environments (temperature, pressure, electric and magnetic fields, and gas) is a challenge in the characterization and optimization of metallic components. Major problems faced by industries include protection against corrosion, embrittlement, formation of bubbles of light chemical elements, and various chemical associations. These can, in turn, have significant effects on the mechanical integrity, structural stability and other properties of the material. However, early detection of structural or chemical changes in the material is not yet well established.

First, we focus on a simple case analyzing calibration samples to understand the capabilities of SMM. As previously discussed, SMM is based on the detection of the phase and amplitude variations of electromagnetic waves occurring upon their interaction with the features of the materials. Electrical, magnetic and geometric properties of the material affect the phase detected. In previous studies, we showed that SMM is sensitive to materials conductivity and that SMM can provide a tomographic view of buried patterns in a sample^{140, 181}.

According to the empiric Matthiessen law²¹⁰, the resistivity of a material is defined by the sum of three terms:

$$\rho = \rho_T + \rho_i + \rho_D \quad (21)$$

where ρ_T is the contribution to the thermal agitation, ρ_i the contribution of impurities present inside the material and ρ_D the contribution of atomic defects.

This law indicates the role impurities and atomic defects play on the electrical conductivity: inside metals, electrons collide with defects, leading to local conductivity variations.

In order to investigate the capability and the sensitivity of SMM, we considered factors (chemical diffusion, mechanical stress, thermal treatment...) that can influence the mechanical properties in materials, leading to conductivity variations that we could detect.

4.1.1. Realization of a tomographic reconstruction by SMM

Based on the measurements on buried calibrated samples presented in the Chapter 2, we decided to use SMM to reconstruct the volume – or 3D tomography - of the calibrated sample. By superimposing the successive phase images obtained at selected frequencies (from the sample surface to the volume) we associated each image with a depth profile of the sample, as shown in the 3D profile of the sample in **Figure 93**.

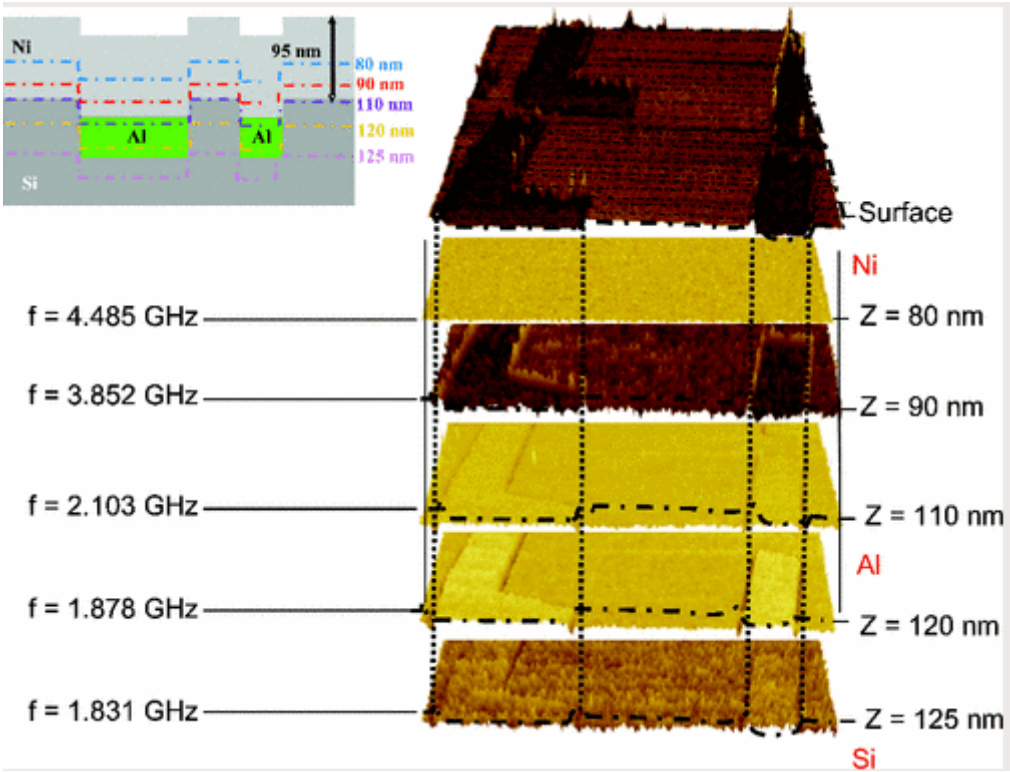


Figure 93: Three-dimensional tomographic image reconstruction of the volume of the metal sample according to the frequency applied onto the SMM probe¹⁸¹.

This result opened new possibilities for non-destructive, 3D reconstruction of metallic materials¹⁸¹. As a proof of concept that the signal measured in SMM is directly related to a variation in the conductivity for metallic materials, we then decided to realize a new set of calibration samples with materials presenting different conductivity embedded in a metal.

4.1.2. Study of the influence of metal conductivity on SMM measurements

4.1.2.1. Fabrication of the calibrated sample with buried metal patterns

The calibration sample was fabricated starting from a silicon substrate on which patterns (30 nm deep) were filled by two different materials of 20 nm thickness (aluminum and chromium), before being entirely covered with a 500 nm silicon layer (**Figure 94a**).

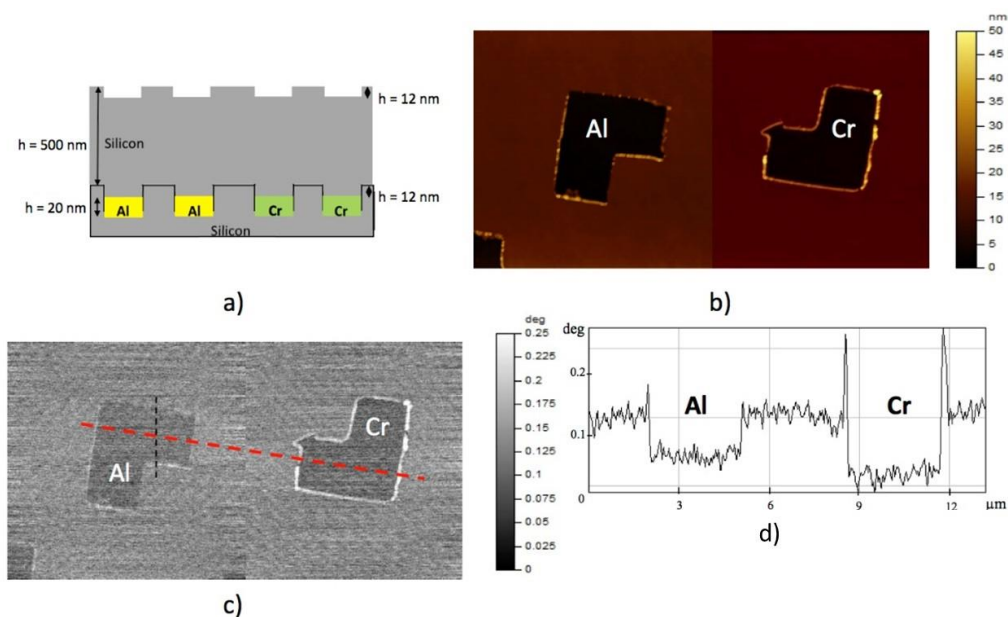


Figure 94: Calibration sample with buried metal patterns. (a) Schematic of the buried patterns of Al and Cr. (b) AFM image: topography. Scan size: 16 x 8 μm . Relative height: 50 nm. (c) SMM phase image ($f = 1.971$ GHz). Scan size: 16 x 8 μm . (d) Cross-section of the phase image revealing the phase difference between the structures of Al and Cr. (e) Profile of a section carried out on the phase image. Estimation of the lateral resolution (scan size: 8 μm).

To avoid any confusion between the two materials, the patterns were laid out in reverse positions. Traces that are thought to correspond to PMMA residues that were not fully dissolved by the solvents remain after evaporation of the silicon layer. We want to point out that it is very challenging to obtain samples without topographical effects on the surface. These residuals can be used as a reference marker for the investigation of the volume of the sample. AFM topography (**Figure 94b**) at this stage of fabrication, made it possible to measure a difference of 12 nm between the structures (Al or Cr) and the real height of the patterns.

4.1.2.2. Results

The objectives of this study were two-fold: 1) to investigate the potential of SMM to probe the depth of samples and 2) to assess the sensitivity of SMM to differentiate two or more types of materials in the sample.

Knowing the electrical conductivities and magnetic permeabilities of the two materials (Al and Cr) and considering that those remain constant in the frequency range used (1–6 GHz), it is possible to predict, for a frequency f and the same observation position z , the depth penetration δ and the phase φ relative to each material.

For the Al structures:

$$\varphi_1 = \frac{z}{\delta_1} \quad (22)$$

where

$$\delta_1 = \frac{1}{\sqrt{\pi\mu_0\mu_1 f}} \quad (23)$$

with the relative permeability $\mu_1 = 1$ and the electric conductivity ²¹¹ $\sigma_1 = 37.7 \times 10^6 \text{ S.m}^{-1}$.

For the Cr structures:

$$\varphi_2 = \frac{z}{\delta_2} \quad (24)$$

where

$$\delta_2 = \frac{1}{\sqrt{\pi\sigma\mu_0\mu_2f}} \quad (25)$$

with the relative permeability $\mu_2 = 1$ and the electric conductivity ²¹¹ $\sigma_2 = 7.74 \times 10^6 \text{ S.m}^{-1}$.

By comparing the penetration depth through the two materials (**Eq. 22**) and (**Eq. 24**) we obtain:

$$\frac{\delta_1}{\delta_2} = \sqrt{\frac{\sigma_2}{\sigma_1}} \quad (26)$$

Therefore, we can write:

$$\frac{\varphi_1}{\varphi_2} = \frac{\delta_2}{\delta_1} \quad (27)$$

Then, we realized SMM phase measurements at a frequency of 1.971 GHz. According to **Eq. 26**, we observed a dephasing introduced by chromium, which was higher than that of aluminum as shown in **Figure 93c**. From the cross-section (red dashed line, **Figure 93d**), we estimated that the dephasing introduced by chromium was about two times higher than that of aluminum. Thus, it is possible to identify the nature of the materials present on the patterns, using the microwave image phase signal given by SMM.

Another important parameter of the scanning microwave microscope lies in its resolution, lateral and in depth. The resolution of the microscope could be estimated while measuring, directly on the SMM images, the width of the outline on the buried Al pattern. On the phase

image (**Figure 93c**), a profile (black dashed line) was carried out while placing the two cursors with the middle height of the peak representing the outline of the patterns (**Figure 93e**). The result shows a resolution close to 35 nm, knowing that it can be still improved for recording images with smaller buried calibrated patterns. In depth, the result shows that SMM is sensitive to a buried defect whose thicknesses lay around 20 nm.

4.1.2.3. Conclusion

These studies proved the ability of SMM to detect metallic defects in the sample. Moreover, contrary to the other experimental techniques investigating the sample volume, SMM has the advantage of being completely nondestructive and of providing a complete tomographic view of the sample. Another advantage of the SMM technique is its capability to differentiate, via the analysis of phase and amplitude SMM signal, metals presenting different conductivities. Thus, for the next part of this work, we decided to highlight -in the case of metallic materials- properties that can introduce conductivity variations such as the diffusion of light elements or residual stress.

4.2. Study of various factors influencing conductivity by SMM

4.2.1. Study of light elements in metals: Diffusion of a light element in a metal

The presence and migration of light chemical elements (helium, hydrogen, nitrogen, and oxygen) in solids can induce important changes in materials properties, with macroscopic effects such as lattice swelling, creep, work hardening and high residual stress. In turn, these may lead to irreversible changes in the mechanical properties, such as loss of ductility or strength, ultimately causing loss of material functionality. Diffusion of light chemical elements is difficult to measure with most conventional high resolution techniques as described earlier chapters. However, measuring the spatial distribution of light elements in a metal is useful to reach a deeper understanding of the mechanisms governing diffusion or to validate models and their parameters. Nuclear reaction analysis facilities (NRA or nuclear microanalysis) are usually required to assess light elements distribution in a metal²¹². Moreover, most common techniques are limited to surface measurements (energy dispersive spectrometry – EDS, wavelength dispersive spectroscopy – WDS, X-ray photoelectron spectroscopy – XPS, and Auger electron spectroscopy). These techniques are essentially used for surface analysis because the interactions of the electron beam with the material limit their penetration depth to tens of nanometers below the surface^{213, 214, 215}. Hence, to precisely determine the concentration of light elements in a metal is nearly impossible with conventional surface techniques especially for very volatile species or when surface contamination occurring during surface preparation cannot be avoided. Two good examples are the study of hydrogen in metals and oxygen in reactive materials. Results obtained with conventional methods correspond to an average of the information obtained over a small volume ($1\mu\text{m}^3$ for EDS) including that of the contaminated surface, which can present a substantial drawback.

In this section, we characterized oxygen concentration in zirconium by Nuclear Reaction Analysis (NRA), with a special interest in the subsurface properties. This will constitute a good reference to determine the performance of SMM, which we propose to use here. The study was realized on a zirconium sample subjected to oxidation^{216, 140} because of the significant solubility of oxygen in this metal. The oxygen dissolved in zirconium produces noticeable differences in the physical and chemical properties of the metal²¹⁷. The oxidation of zirconium at high temperature takes place with the diffusion of oxygen atoms into the metal lattice, up to 29 atomic percent, followed by a transformation into ZrO₂. According to the theory of diffusion²¹⁸, in the Zr–O zone the oxygen concentration resulting from the diffusion processes exhibits a complementary error function (erfc) shape. This variation is expected to be the same at several depths under the scanned cross-section surface (which is normal to the oxidized face) beyond the first few hundreds of nm, as zirconium is well known for its high reactivity with oxygen, creating inevitable pollution during sample preparation. These conditions are associated with weak precision in the measurement of the diffusion length with conventional surface analysis techniques. In addition, measuring low values of oxygen concentration will be very challenging¹⁴⁰.

4.2.2.1. Preparation of the oxidized Zirconium sample preparation

For the study of zirconium oxidation, commercial pure zirconium plates (99.2% Zr from Goodfellow) were used. They were first annealed at 750 °C under a secondary vacuum (1.10⁻⁶ bar) for 2 hours and then oxidized in air under atmospheric pressure at 650 °C for 72 hours. After oxidation the samples were transversely cut and mirror-polished and then analyzed by SEM/EDS, NRA and the SMM technique. Two successive layers cover the pure original metal: a ZrO₂ exterior region and an intermediate oxygen-enriched metal (Zr–O). The oxygen concentration in the enriched zone shows a slow decrease from 29 at. % to 0 at. %. A schematic of the sample is presented in **Figure 95**.

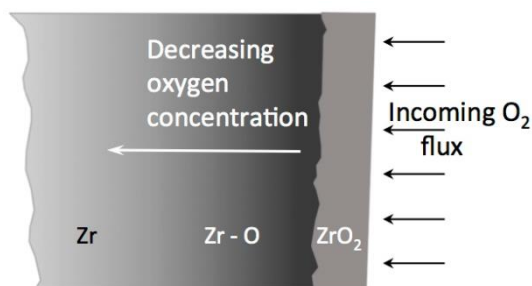


Figure 95: Schematic of the cross section of the Zr/ZrO₂ sample analyzed.

4.2.2.2. SMM results

Figure 96b presents a schematic of the sample and the cross-section used for analysis. **Figure 96a** shows the concentration of the oxygen in the sample in atomic percent. The results were obtained by EDS and NRA along a line on the cross-section perpendicular to the oxide–metal interface. For EDS, the analyzed volume is about 1 μm^3 and contains the sample surface, and the contaminated subsurface. Due to the high affinity of the zirconium with the oxygen, the surface was inevitably enriched with atmospheric oxygen during the cross-section preparation. This treatment results in a large quantity of oxygen content in the first few hundreds of nm under the surface scanned and can mask the original quantity present in the sample before the polishing process. The contamination of the surface with atmospheric oxygen and the over-evaluation of the light chemical elements by the EDS technique explains the apparent 12% oxygen concentration obtained in the pure metal zone. The residual apparent quantity of oxygen on the pure Zr can affect the measure of oxygen-enriched area and prevents the identification of regions with low oxygen content.

The nuclear reaction analysis was performed at the Institut Rayonnement Matière de Saclay, France, using a Van De Graaff linear accelerator (maximum 3.7 MeV). A 1.45 MeV deuteron beam was used to analyze the reaction $^{16}\text{O}(d,p_1)^{17}\text{O}$. Lateral resolution is directly related to beam size. In this case the beam size was $3 \times 3 \mu\text{m}^2$. And the size of the scanned area was $80 \times 120 \mu\text{m}^2$. The NRA measurements of the oxygen concentration presented in **Figure 96a** are

very accurate because NRA can eliminate the response of very superficial layers. The oxygen content in the pure Zr region is correctly measured and is close to zero. As expected, a longer diffusion region is found compared to what was observed with EDS. The spot size in NRA is about 3 μm and covers both Zr–O and ZrO₂ zones close to the interface. These considerations explain the apparent 45 at% oxygen content measured at the interface location. NRA measurements will serve as a control measurement to compare with the SMM results.

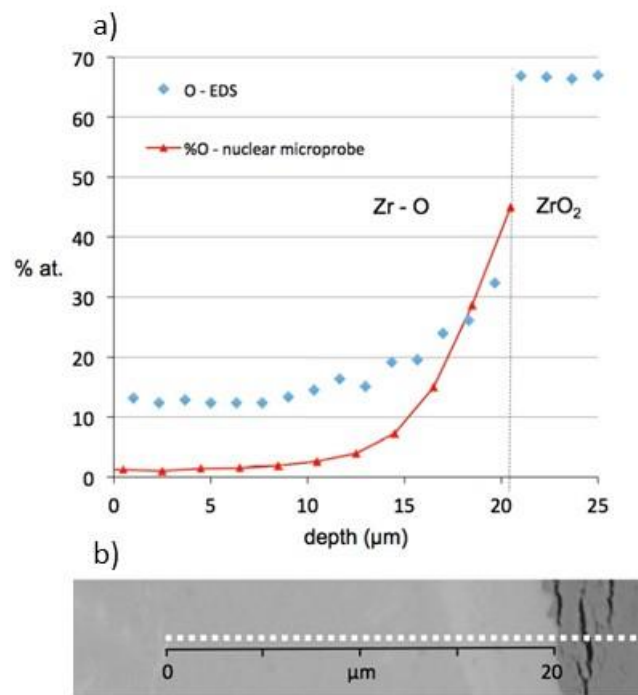


Figure 96: Analysis and composition of the zirconium sample enriched in oxide. (a) EDS and NRA measurements of the oxygen level as a function of depth. (b) Electronic microscope image of the analyzed area with line indicating the analysis trace.

To perform the SMM measurements, we selected a frequency range appropriate to obtain a profile investigation inside the sample and below the surface layer of pollution. Considering as a reference the deep layer of pure Zr, with the conductivity²¹¹ parameter $\sigma = 2.36 \times 10^6 \Omega^{-1} \text{m}^{-1}$, the frequencies 11.83 GHz, 6.87 GHz and 2.21 GHz were selected as they should allow an in-depth investigation between 3 and 7 microns below the sample surface. Then we avoid

the influence of the contaminated surface as shown in the scheme of **Figure 95**. We focus in this study mainly on the oxygen-enriched metal zone.

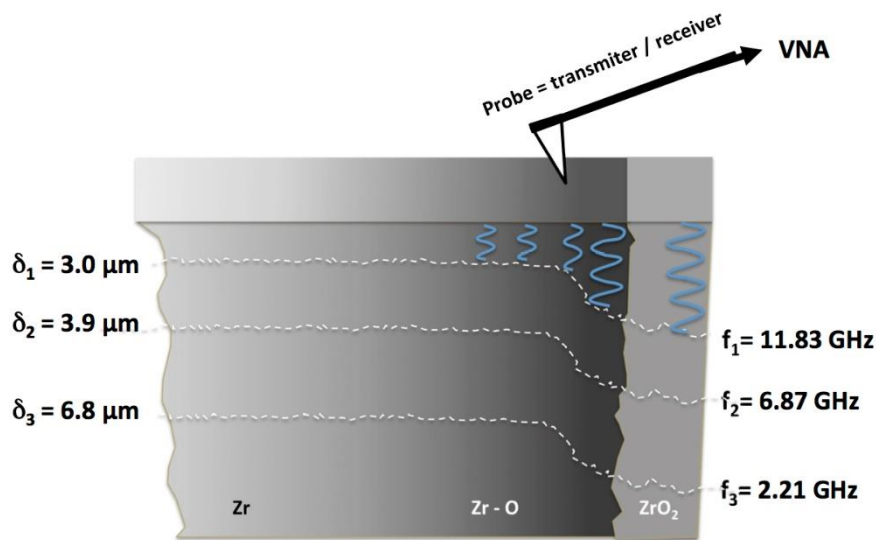


Figure 97: Depiction of SMM measurements on the cross-section of an oxidized zirconium sample probed. At a given frequency ($f_1= 11.83$ GHz) the attenuation of the wave changes as a function of the material conductivity (= oxygen concentration). Various frequencies ($f_2= 6.87$ GHz and $f_3= 2.21$ GHz) are used to probe deeper levels in the material.

SMM analysis of the same sample as the one probed with NRA was performed. AFM morphology of the sample and the SMM microwave signal phase shifts for several frequencies were recorded as can be seen in **Figure 97**.

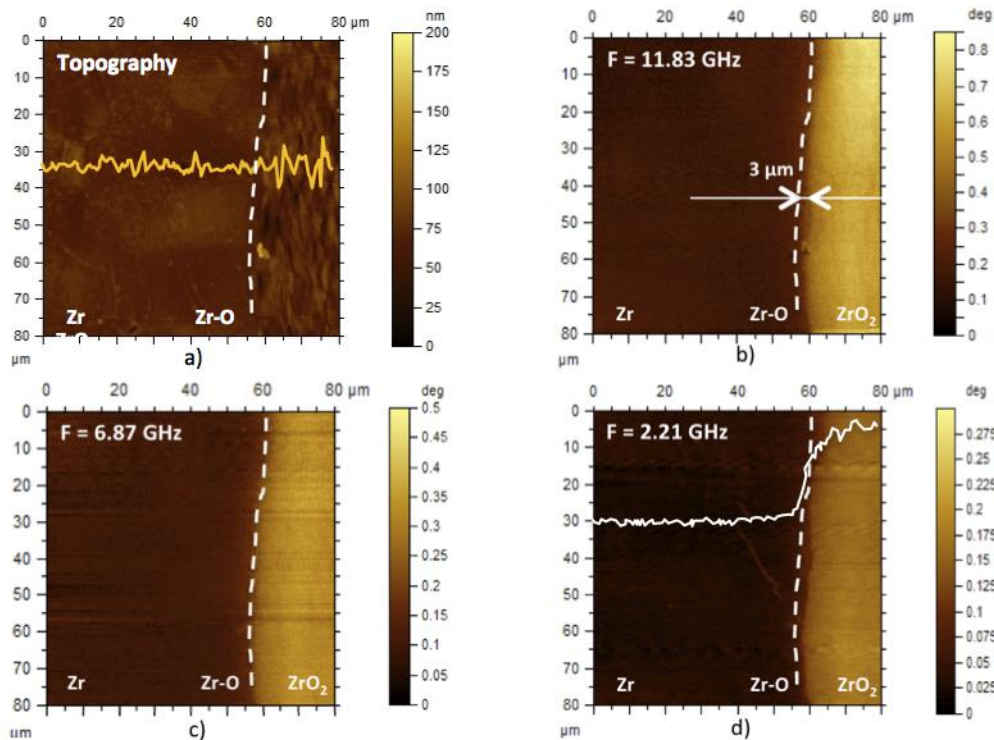


Figure 98: Topography and phase shift cartography acquired at various frequencies (scan area 80 μm). (a) Topography image of the sample and a selected cross-section of the change in height of the surface (yellow line). (b) SMM phase shift image at 11.83 GHz. (c) SMM phase shift image at 6.87 GHz. (d) SMM phase shift image at 2.21 GHz with profile of the measurement indicated by the white line.

Figure 98a presents the topographic cartography obtained from the amplitude signal and the profile along the dashed horizontal line. The topography clearly reveals the grains of the metal. The profile shows the roughness of the sample along a line. One can see that the ZrO_2 region shows a different roughness from the Zr–O and Zr zones. The amplitude of the roughness is about 20 nm, which is very low compared to the size of the scanned zone, 80 μm .

The SMM phase shift of the signal used to probe at selected frequencies can be seen in **Figure 98b** to **Figure 98d**. The SMM phase shift images clearly show variations in the phase signal, which is introduced solely by a conductivity change in the material, as the relative permeability is equal to 1 for Zr. Only oxygen dissolution in the zirconium lattice produces variations of the conductivity as it is well known that the mean free path of electrons is influenced by crystal

lattice imperfections²¹⁹ such as structural defects, foreign atoms or thermal agitation of the ions, and also the electron mobility μ , proportional to the mean free path of electrons, and thus the conductivity is defined by:

$$\sigma = nq\mu \quad (28)$$

with σ the conductivity (S m^{-1}), n the number density of electrons and q the elementary charge. Consequently, the electron mobility decreases as the temperature or the number of defects increases. The SMM phase shift is necessarily linked to a change in composition of the material as the wave propagates deeper into the oxygen-enriched zone in comparison with the area of pure Zr (**Figure 97**).

The position of the oxide–metal interface is materialized by the sudden change in the phase signal within a spatial range less than one micrometer. For a better localization, we used a white dashed line to indicate the position of the oxide–metal interface found on the topographic AFM image (**Figure 98a**) on all the phase shift cartographies. The phase shift starts to change close to the interface ($3 \mu\text{m}$, **Figure 98b**). The interface location can change for different depths as the interface is not perfectly planar. We can observe these changes in **Figure 98b** to **Figure 98d**. The transition zone between the oxide and the oxygen-enriched metal can be topographically perturbed by the strong difference of hardness of the ZrO_2 and Zr–O zones, giving rise to differences in the way the polishing/etching technique affects each zone. In this particular case the SMM phase shift signal can also be affected. A careful polishing of the sample could help avoiding these effects.

The variations of the phase shift signal in the Zr–O zones are very similar for each frequency. In the oxygen-enriched zirconium region, the concentration of the oxygen produces gradual modifications in the metal properties and implicitly in the SMM phase response. The size of the perturbed zone is about $18 \mu\text{m}$ for all the depths investigated here. This value is close to the

length of diffusion found on the EDS measurements considering that the latter is apparently shortened by the surface pollution effect. At different depths under the scanned surface the spatial variation of the material properties is similar. The changes in the properties result only from the quantity of oxygen dissolved in the zirconium lattice.

One can also observe that the value of the phase shift increases with the frequency. The deeper one looks, the lower the phase shift.

Figure 99a to **Figure 99b** present the topography and the phase shift of the pure Zr zone. The phase shift signal shows no gradient, as expected. This observation confirms that the SMM technique is only influenced by the chemical composition of the sample.

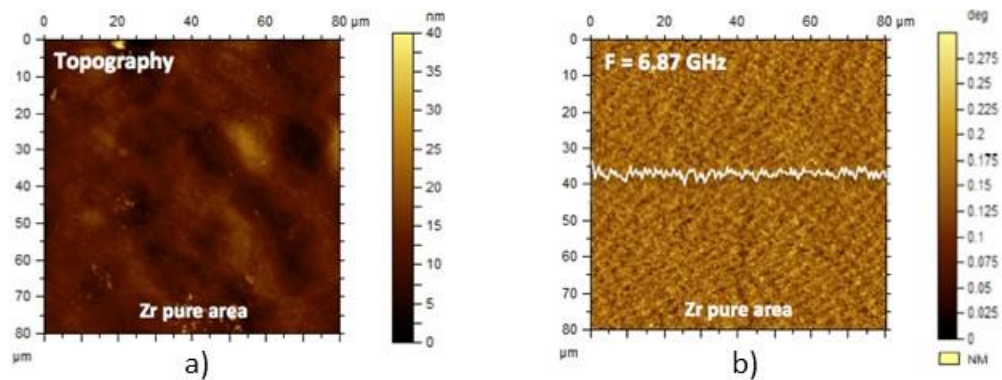


Figure 99: AFM and SMM characterization of pure Zr area. (a) Topography image of pure Zr. (b) SMM phase shift image of pure Zr at 6.87 GHz.

Using several frequencies one can obtain information at various depths. To compare the information between the signals obtained at various frequencies, a procedure of normalization is applied. Scale and shift are chosen in order to obtain 0 value for the pure Zr and 1 for the ZrO₂ zone. As pointed out in **Figure 98a**, the topography is flat. Since the signal is not influenced by the topography, the phase shift observed can only come from changes in the material properties as seen in **Eq. 21** and **Eq. 23**. The only parameter that changes along a line is oxygen concentration. As a result, the local enrichment of metal with oxygen is reflected in

the phase shift measurements obtained by SMM. The position of the metal–oxide interface is indicated by the sudden change in the phase shift signal. The location given by SMM is in agreement with the topographic picture. This study confirms that SMM can be used to probe oxidation layers in cases for which the topography image does not reveal the interface.

In the case of zirconium we know that at the oxide–metal interface the oxygen concentration should reach the solubility value, i.e. 29 at% ²²⁰. The oxygen concentration decreases progressively from 29 at% the interface to 0 at% in the pure metal zone.

According to the skin effect equation, the microwave signal penetration depends on the frequency used for the investigation: the lower the frequency, the deeper the penetration. **Figure 100** presents the results obtained at three different depths: 6.8 μm , 3.9 μm and 3 μm , i.e. respectively 2.21 GHz, 6.87 GHz and 11.83 GHz along a straight line that contains ZrO_2 , the oxide–metal interface and Zr–O zones.

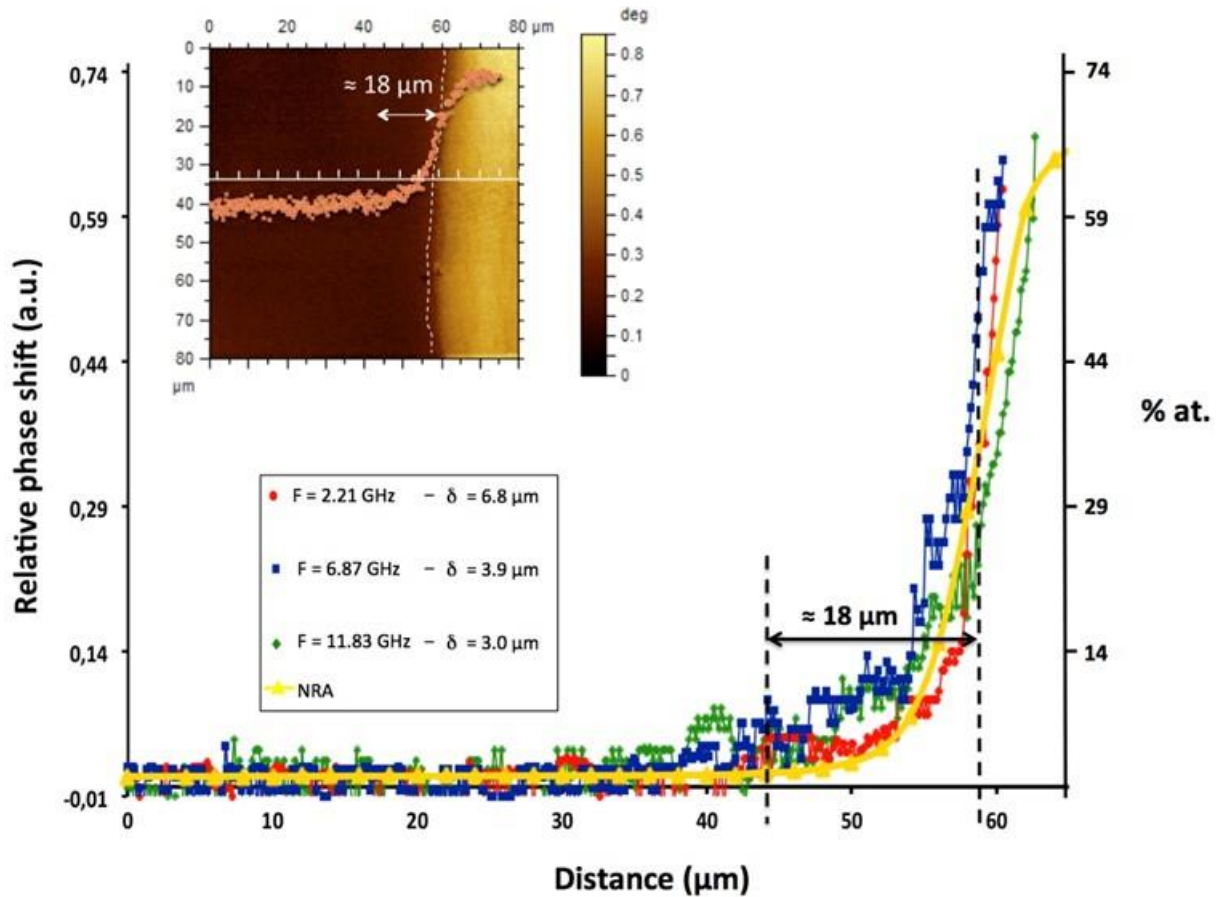


Figure 100: Superimposed phase shift profiles (red, blue and green) for several depths with the location of the interface and compared with NRA results for the oxygen concentration (yellow).

The phase shift profiles obtained for three different frequencies, i.e. at three different depths, are almost superposed, as can be seen in **Figure 100**. This confirms that the phase curves are only influenced by the chemical composition of the solid solution. We recall here that the normalization is performed using only information on the pure Zr (which is set to zero) and ZrO₂ (which is set to 1) and does not use the Zr–O zone. The phase shift profile can be used to reveal the presence of oxygen and to measure its diffusion length.

Figure 100 shows also the superposition of the SMM curves with the NRA measurements of the oxygen concentration in the Zr. One can note that the SMM response shows that the size of

the zone where the material has different properties compared to the original metal is sensibly the same as the oxygen-enriched zone revealed by NRA.

The NRA results are obtained with a lateral resolution imposed by the accelerator beam size (about $3 \times 3 \mu\text{m}^2$ and a depth of $3 \mu\text{m}$) for a step scan size of $2 \mu\text{m}$ between each measure point. Also this measurement represents an average value. By SMM, the lateral resolution is superior, since between two measure points the step scan size is 100 nm for 20 nm contact radius. This difference can explain the variations between the SMM curves and the NRA curve, in particular.

The small variations in the interfacial region for different investigation depths, as previously remarked in **Figure 98**.

In addition, the phase shift ϕ in SMM seems to be related to the oxygen concentration c as follows:

$$\phi = K(c)c \quad (29)$$

with $K(c)$ the proportionality factor which can be a function of the concentration. One can also propose the inverse form of the previous relation:

$$c = F(\phi)\phi \quad (30)$$

with $F(\phi)$ a factor to be found by calibration. After calibration, **Eq. 30** could be used to measure the oxygen concentration by SMM. The assumption of a proportionality relationship between the shift phase of SMM and the concentration of oxygen is confirmed when comparing the NRA measure with SMM measures. This rapid calibration, with the present measurements, shows a linear trend (**Figure 101**).

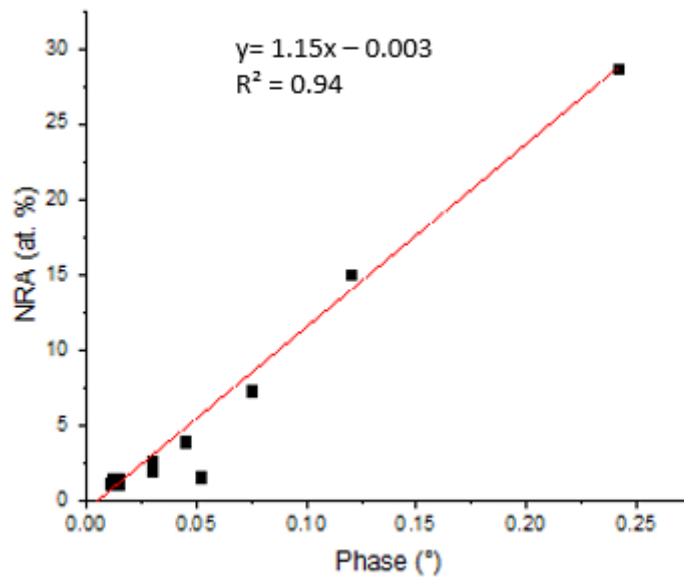


Figure 101: NRA versus SMM phase shift measurements. The slope of the fitted curve was 0.94 indicative of a linear relationship between the two values.

Furthermore, by referring with a white dashed line the border between ZrO_2 and Zr-O, one can observe an evolution of the border position depending on the frequency (and thus on the depth) (**Figure 102**). This highlights that the inhomogeneous nature of the boundary in the volume can only be achieved only by this tomographic SMM measurement.

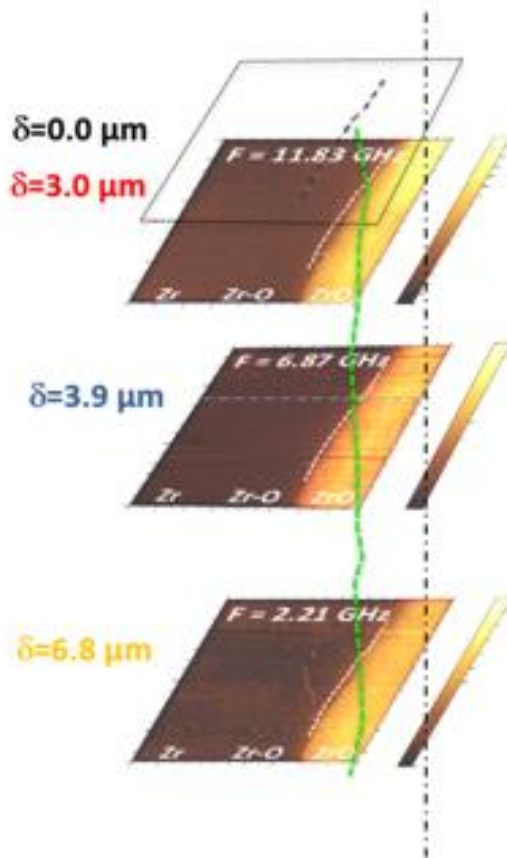


Figure 102: Successive SMM images obtained at frequencies (top) 11.83 GHz; (middle) 6.87 GHz; (bottom) 2.21 GHz, corresponding to different depth in the material.

Consequently, under the ZrO₂ layer, the SMM technique reveals a gradient of the metal properties. This gradient is related to the quantity of oxygen dissolved in the metal lattice. This method shows very encouraging results for the chemical characterization of the oxide–metal interface. SMM can facilitate the measure of the diffusion length of the oxygen in the zirconium lattice with a spatial resolution of about 50 nm.

4.2.3. Conclusion

In conclusion, the present work shows that the SMM technique not only allows the detection of subsurface defects with high resolution. Change in conductivity is associated with the diffusion of oxygen in metal. The possibility to characterize the in-depth distribution of the light chemical elements like oxygen in the metal represents an important feature of the SMM technique. The great advantage of this technique compared to those currently used is that measurements can be realized under the contaminated surface without any specific sample preparation.

Moreover, we noticed that the phase shift response seems to be proportional to the oxygen concentration, confirmed by NRA measurements. The calibration of the SMM phase signal with respect to the concentration of the chemical element dissolved in the metal lattice could lead to a quantitative technique with sub-micron spatial resolution. The authors are presently working on the calibration of the SMM method by comparing several oxygen concentration profiles measured by NRA with the corresponding SMM phase shift response.

As we noticed the sensitivity of SMM to the difference in chemical composition, we propose that SMM should be used for the exploration of other phenomena linked to a change in conductivity of the material. This includes stress in materials. In the following section of this chapter, we explored the performance of SMM to detect local changes in the conductivity due to residual stress in metals.

4.3. Introduction to the nanoscale non-destructive characterization of residual stress by Scanning Microwave Microscopy

Non-destructive characterization of residual stress is a major challenge in research on metallic materials. Indeed, its control is necessary to create material with the required properties. Major problem is that metals lifetime and properties are directly related to the stress condition that cannot be estimated by in situ, non-destructive, nanoscale methods. Anticipate the stress evolution in materials is a major issue, particularly for industry²²¹. The accurate measurements for the stress characterization inside materials are based on destructive methods such as Deep hole drilling (DHD)²²², or quantitative non-destructive analysis such as X-Ray Diffraction (XRD)²²³, or neutron diffraction²²⁴. However, these non-destructive techniques currently used take plenty of time (from hours to days) and do not permits the characterization of all kind of samples: a complex geometry and/or a not enough thick sample could be really problematic. Generally, the measurements correspond to an average of the information obtained on a small volume and correlated to the beam diameter (around 100 μm or more for XRD).

The main advantage of the SMM techniques lies in its precision. By coupling the nanoscale resolution of the AFM with the VNA analyzer, one can have access (as presented before) to the local conductivity of materials. Here, we present an introduction to a new way to use Scanning Microwave Microscopy (SMM) for the non-destructive, high resolution characterization of residual stress in metals.

4.3.1. Residual stress definition^{225,226}

Residual stresses are present in almost all solids, including metals, glasses, ceramic, or polymers. Mechanical and metallurgical events during the fabrication of the material can cause residual stress. Almost every manufacturing process leads to a new state of the residual stress, especially if the piece undergoes mechanical treatments. These residual stresses (σ_R) can be multi-axial, self-balanced, elastic static strains, existing in an isolated system of constant temperature and with a stable environment.

These stresses exist at different level. Due to the polycrystalline, multi-phased, nature of the majority of metallic materials, the deformations at the origin of residual stress can affect the material at the macroscopic, microscopic, or submicroscopic scales. Depending on the scale, one has to consider at least three different types of stress²²⁷ (**Figure 103**):

First order: *residual stress (also known as macroscopic)* σ^I_R : they are located at the scale of a multiple number of grains or at the scale of the entire component. These stresses are homogeneous (constant in intensity and direction on huge domains composed of a great number of grains). They can be characterized using gauges, which measure the deformations generated by the stress²²⁸.

Second order: *residual stress (homogeneous microscopic residual stress)* σ^{II}_R : they are homogeneous across domains corresponding to a grain or a part of a grain for mono-phased materials. They come from the difference of crystalline orientation between neighboring grains. During a mechanical sollicitation of the material, some grains will reach the elasticity limit which will lead to heterogeneity in the material behavior.

Third order: *residual stress (heterogeneous microscopic residual stress)* σ^{III}_R : at this level, we reach the limit of the stress definition. Stresses are heterogeneous across the crystal and even in a few interatomic distances areas. These stresses are generated by all the kind of crystalline

defects present in grains such as lack, interstitial defect, substitution of atoms, dislocations, sacking defect, or crystal twinning ²²⁹.

Second order residual stresses can be considered as fluctuations around an average value formed by the first order stresses, as shown in **Figure 103**. Third order residual stresses can be considered as fluctuations around an average value constituted of variations due to the second order stresses.

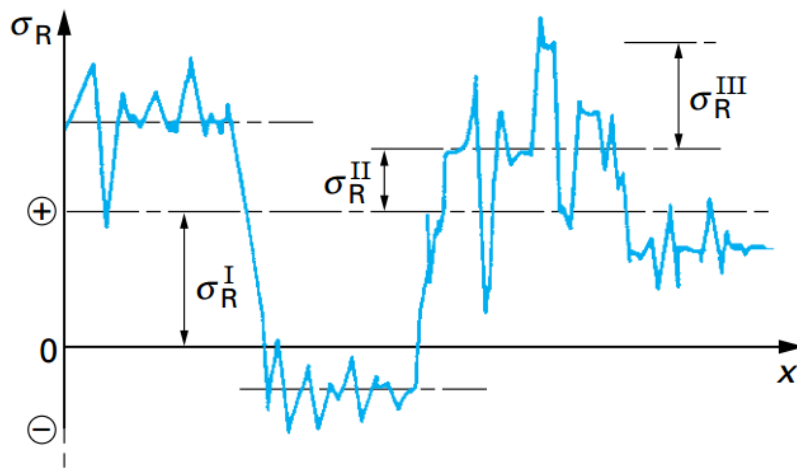


Figure 103: Profile of the data corresponding to the different orders of residual stresses with σ_R^I , σ_R^{II} and σ_R^{III} the residual stresses of first, second and third order.

Residual stresses have a great impact on the lifespan and quality of the materials and components. Large residual stresses may cause a material or component to break or fail. The defect inducing the rupture of the material often forms at the surface of the piece. Indeed, the roughness of the surface and its direct contact with the surrounding media can generate stress concentrations. As a result, surface treatments have emerged as an effective solution to improve the performance of materials in industrial applications ^{230 231}.

In some cases however, the presence of residual stresses may be beneficial ²³². For instance, compressive residual stresses can be introduced to increase the mechanical performance of the material ²³³. Surfaces treatments have been shown to introduce compressive residual stresses in

the material and to generate a superficial hardening of the surface (from a few hundredths of millimeter to some millimeters) ²³³. The impact of surface treatment with the case of shot-peening ²³⁴ will be discussed in the next session of this chapter.

4.3.1. Residual stresses measurements

4.3.1.1. Destructive techniques (or semi-destructive techniques)

Mechanical destructive investigation techniques are called relaxation methods. They consist of measuring the stress relaxation produced in a material when a portion of it is removed. By measuring the deformation resulting from such relaxation, the macro-residual stresses are determined by analyzing the successive equilibrium states. The most common techniques include hole drilling (determination of residual stress gradient up to 1.5mm) ²³⁵ and deep hole drilling (determination of residual stress gradient up to 750mm) ²³⁶.

4.3.1.2. Non - destructive techniques

There are a few non-destructive characterization techniques to determine residual stress in materials. The most common and accurate techniques are X-ray diffraction and neutrons diffraction techniques ^{237 238}. The analysis of X-ray or neutron spectra allow the determination of macro-residual stresses and also provides information on the micro-deformation.

X-Ray diffraction (XRD)

Elastic deformations resulting from stress in the material lead to modifications in the crystal planes distances of the material. With XRD it is possible to determine the distance between these planes and to determine the local elastic strain. Most of the metals are composed of grains, with specific orientation depending on their crystallographic arrangement. Polycrystalline metals that are submitted to a strain undergo a deformation in their crystal lattice. In the general case, the analysis of stress by XRD is based on the measure of the interplanar spacing variation of a crystal planes (**Figure 104**), also known as Bragg's law.

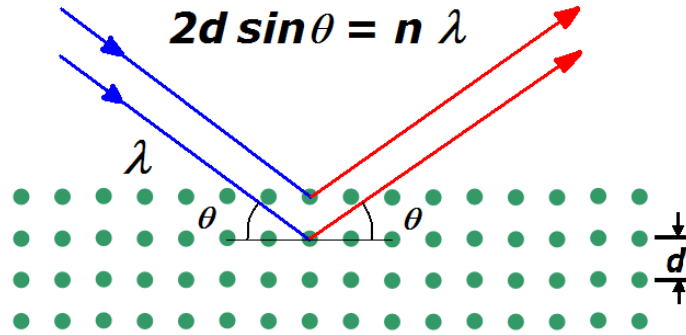


Figure 104: Bragg's law principle: in a material with crystal planes separated by d ; d can be determined using the relationship between the angle and wavelength of the incoming beam and the n index of the refraction of the medium.

Any modification in the interplanar spacing leads to a modification of the X-Ray diffraction spectrum in form of a shift of the diffraction peak²³⁹. Thus, using Bragg's law, the elastic deformation can be linked to the peak displacement. In addition, the plastic deformation will be detected by an enlargement of the diffraction peak²³⁹. Consequently, the stress can be related to the deformation measurements realized in XRD (the depth investigation can be adjusted from 20\AA to $30\mu\text{m}$ depending on the material properties and on the incidence of the X-rays, with a minimal spot size of $50\mu\text{m}$).

Neutrons diffraction

The neutron diffraction and the X-ray diffraction techniques are quite similar because they both allow measuring the elastic deformations of a polycrystalline material whose interplanar spacing is modified. However, the neutrons and the X-rays interact with the matter in very different ways. While X-rays interact with the electronic cloud making them sensitive to high atomic number atoms with their large electronic cloud, neutrons interact directly with the atom nucleus. Neutron penetration in metals is greater than X-rays. Neutrons allow measurements of residual stress up to a few centimeters ($30\mu\text{m}$ for X-ray). A 3D cartography of the residual

stresses inside the material can be achieved with a spot size of the neutron beam between 1mm and 5mm.

In Summary, techniques to study residual stresses at various scales, destructive or not, can range from 10µm for XRD to centimeters for all other techniques, as shown in **Figure 105**. However, a majority of these techniques remain destructive and do not provide direct measurement of residual stress in a material. Therefore, a non-destructive high resolution, accurate, and fast technique providing a direct measure of residual stress with simple of steps is still lacking. We will now present our contribution to this limitation.

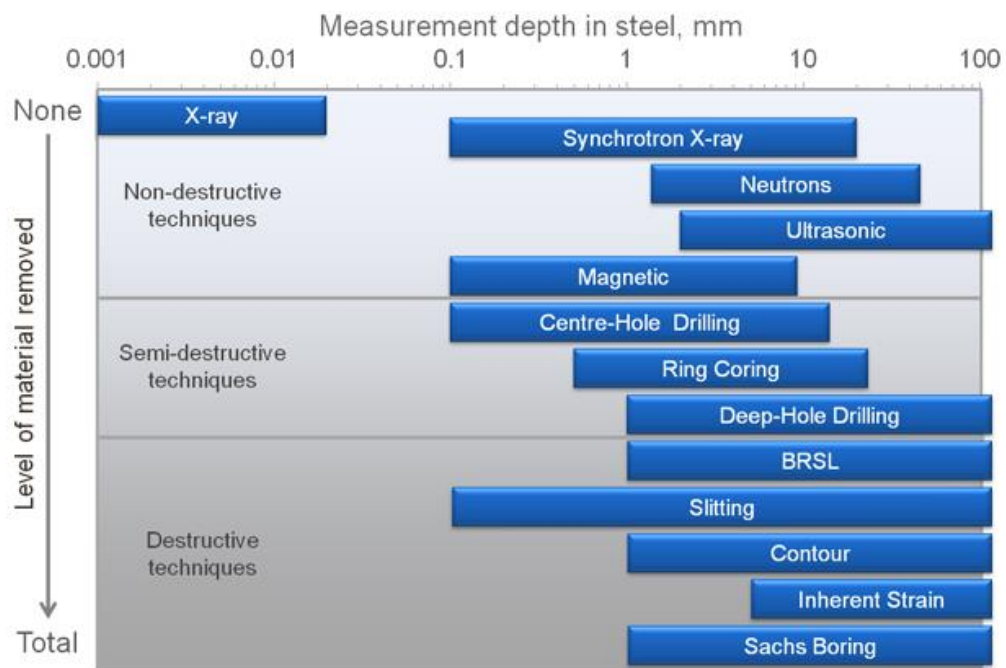


Figure 105: Residual stress measurements techniques presented with respect to the measurement depth they can probe and the amount of material removed²⁴⁰.

4.3.1. Study of shot-peening influence on stress profile

We decided to continue the studies on the same kind of material as the one used previously for the study of the diffusion of light chemical element. Thus, we will focus on the characterization of pure zirconium in order to investigate the influence of a shot-peening treatment on the stress profile of this material. The stress profile obtained by SMM will then be compared to the one realized by the incremental hole-drilling method²¹⁷.

4.3.1.1. Shot-peening treatment²⁴¹

Shot peening consist in a cold mechanical treatment used to produce a compressive residual stress layer and modify mechanical properties of metals (**Figure 106**). The surface to be treated is impacted with shot of metallic, glass or ceramic balls with a sufficient force to create a plastic deformation (**Figure 107**). The main objective of shot peening, as any surface treatment is to introduce compressive residual stresses²⁴² to increase resistance to fatigue and corrosion in order to improve the service performance of the mechanical components. However, its main disadvantage is the generation of a surface roughness by the impact of particles, which has a negative effect on the resistance to fatigue²⁴³. Optimization of treatment and compromise are needed for each type of materials to obtain high residual stresses over a large depth while maintaining acceptable roughness.

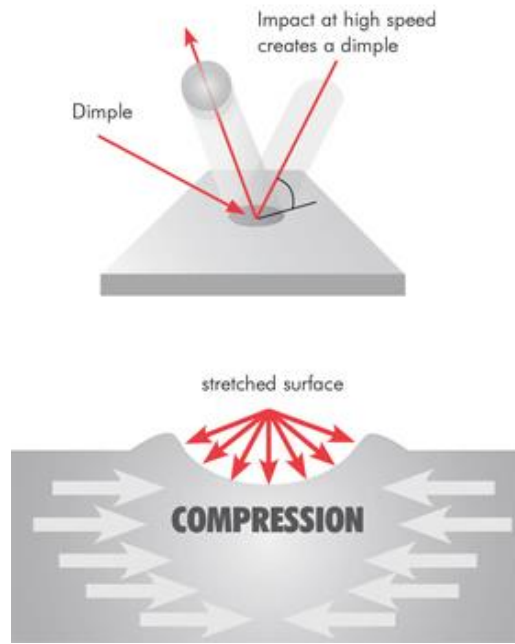


Figure 106: Illustration of shot-peening method used to prepare our samples²⁴⁴ High speed impact between the small balls and the materials modifies the surface by generating residual stresses in the material.

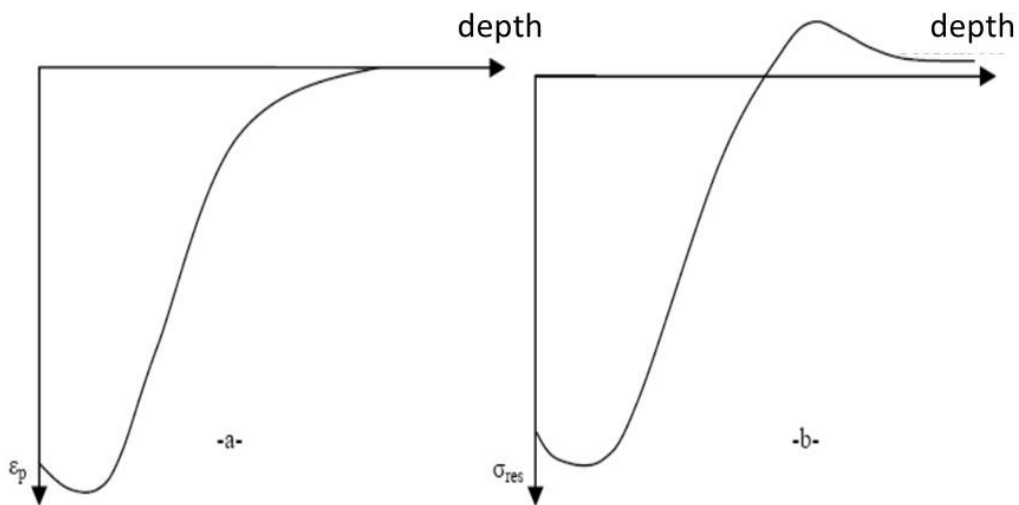


Figure 107: Characteristic profiles used in shot peening²⁴⁵: (a) plastic deformation profile, ϵ_p and (b) residual stress σ_{res} variations as a function of depth.

In order to optimize this process, several parameters can be changed and affect the residual stress state introduced. The main shot-peening parameters which influence the residual stress are: the shot peening time, the diameter, the nature and weight of shot and the projection speed. For a given ball diameter and a given projection rate, the greater the peening time is plus the higher the shot-peening influence depth and the compression stress are. The peak of the maximum of the compression stress increases and shifts in the inside direction. Similarly, the increase in projection speed has the same effect as increasing the duration of treatment.

Increasing the diameter of the balls causes an increase in the depth affected by the compressive residual stress, but does not alter notoriously the value of the compressive stress.

These parameters and their influences are summarized in **Figure 108**.

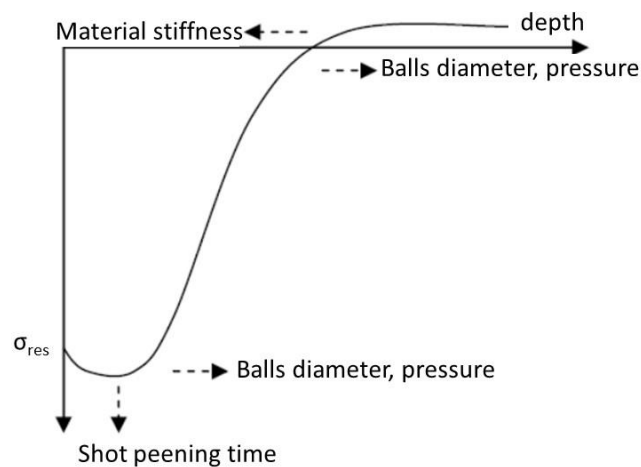


Figure 108: Schematic of the effect of some parameters on the shot-peening stress profile²⁴⁵.

For our study, shot-peening was realized during 10 minutes on rectangular 80 x 40 x 2mm zirconium plates. The parameters were chosen to introduce residual stresses in a stratum of about 300 μm thick under the metal surface. The process uses tungsten carbide balls of 2 mm of diameter and a sonotrode vibrating at 20 kHz with an amplitude of 24 μm ²¹⁷.

4.3.1.2. Obtaining of the stress profile by incremental hole-drilling method

The incremental hole-drilling method is a quite simple technique to measure residual stress in materials. Considered as a semi-destructive, indirect method, the residual stress distribution is measured following one direction, a sense and a magnitude depending on the depth of the hole. It consists in a hole drilled in the material at the location where one want to measure the residual stresses. Due to the drilling of the hole the locked up residual stresses are relieved and the corresponding strains on the surface are measured using suitable strain gauges bonded around the hole on the surface. From the strains measured around the hole, the residual stresses are calculated using appropriate calibration constants²⁴⁶.

Figure 109 presents the residual stress profile for 10 min shot-peened sample. The measurements show a particular shape of the stress distribution: the most superficial layers are slightly compressed then deeper the negative stress gradient leads to a minimum algebraic value located at circa 100 μm of depth followed by an inversion of the gradient sign leading to positive values (tensile stress). This kind a profile is well known in literature²¹⁷.

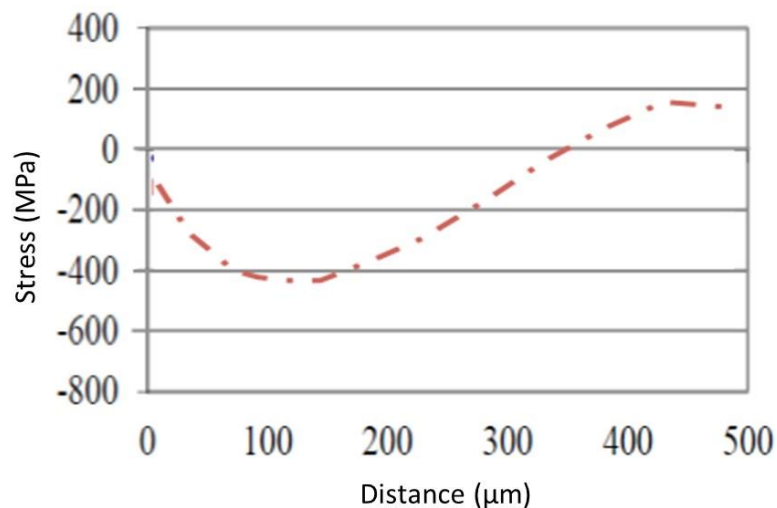


Figure 109: Residual stress profile of shot-peened Zr obtained by incremental hole-drilling method²¹⁷.

4.3.1.3. Scanning Microwave Microscopy for residual stress measurements

The shot-peened Zr sample was then analyzed by SMM at a given frequency of 8 GHz.

As the imaging mode of the SMM is limited of $80 \times 80 \mu\text{m}$ area scan, several images were realized and superimposed to reconstruct the complete zone of interest (**Figure 110**). The shot peening surface is represented by the number 5 on **Figure 110**.

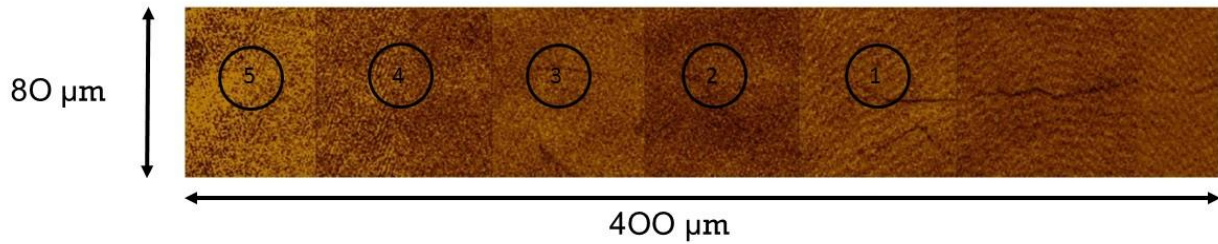


Figure 110: SMM amplitude images realized on the shot peened Zr sample (image full size: $80 \times 400 \mu\text{m}$). Regions (1) to (5) represent successive images obtained across the region of interest.

One notice that there is no major contrast changes between the images 1,2,3,4 and 5 as we observed in the case of the oxygen diffusion. However, small contrast variation are observed between images. To compare these images, we extracted for each image the most prevalent value of the phase shift (**Figure 111b**). Then, we plotted this value as a function of the distance for each image. The residual phase profile obtained by SMM measurement is given in **Figure 111a**.

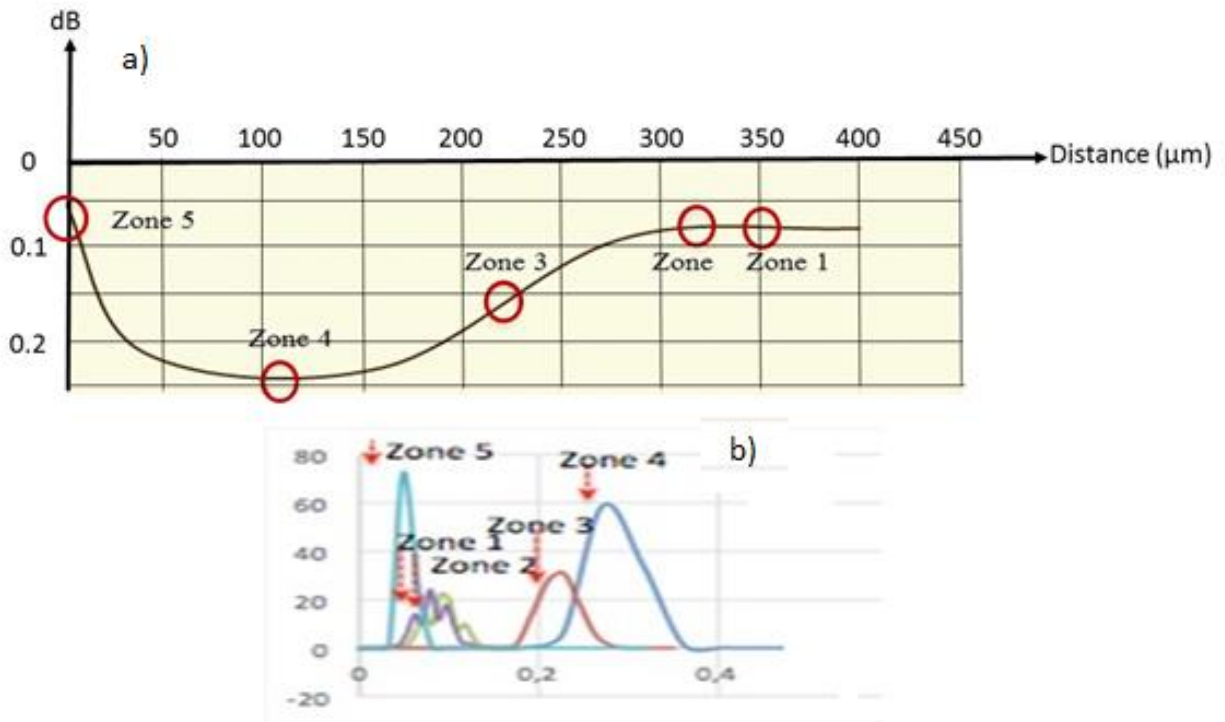


Figure 111: Phase profile on a shot-peening sample realized by SMM. a) Phase profile obtained by measuring the amplitude of the largest peak for each one of the zones. b) Spectrum obtained by averaging the collection of spectra obtained for each image in **Figure 110**.

The profile obtained by SMM is completely similar to the one realized with the incremental hole-drilling method. The curve show perfectly the compression and the traction areas, a contrary to the hole-drilling the SMM results are obtained in a direct way.

Imaging being not a necessary condition in that kind of study and taking into account the spatial distribution of the residual stress effect (macroscopic effect), we modified the analyze method to make it faster and easier.

Instead of realizing a set of picture, for each point of measure (every 50 μm in that case) we realized an amplitude spectrum (**Figure 112**) in using the displacement of the motorized stage allowing a measure step from 5 μm to a few millimeters. Then, for a fixed frequency (represented by the black line on **Figure 112**), we plot the amplitude variation as a function of the distance. This method will be from now used for the determination of stress profile shape.

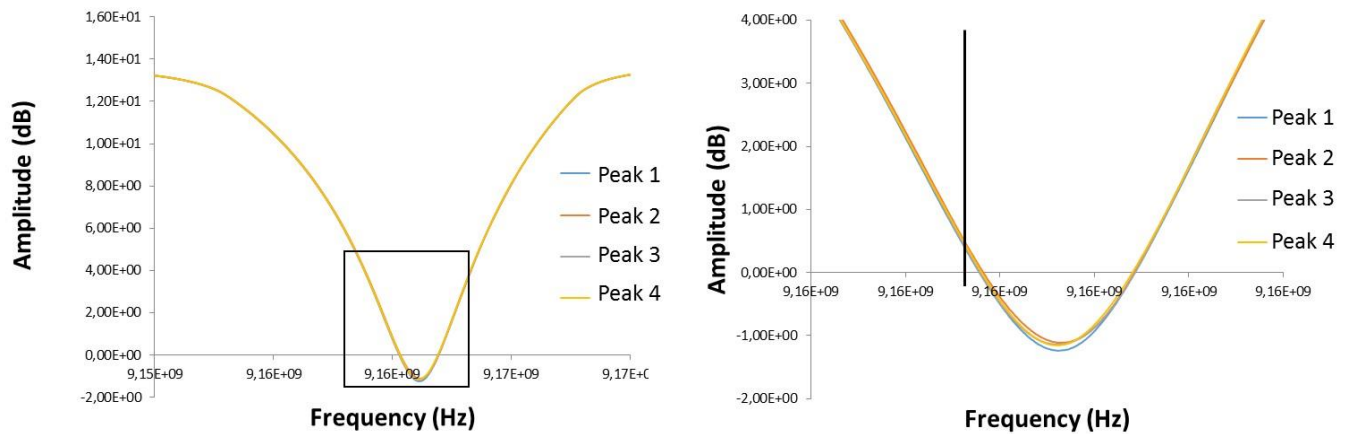


Figure 112: Representation of the SMM amplitude peaks versus frequency. Each peak provide from a different area of the shot peened sample to analyze.

Consequently, the measurement of the shot-peened Zr sample were realized with the procedure previously described. The shot-peening profile can be observed in **Figure 113**. One can notice again the excellent correlation between the profile obtained by SMM and the one obtained by indentation measurement²¹⁷. The interesting point to notice is that the SMM gives directly the profile of the residual stress without any intermediate calculations.

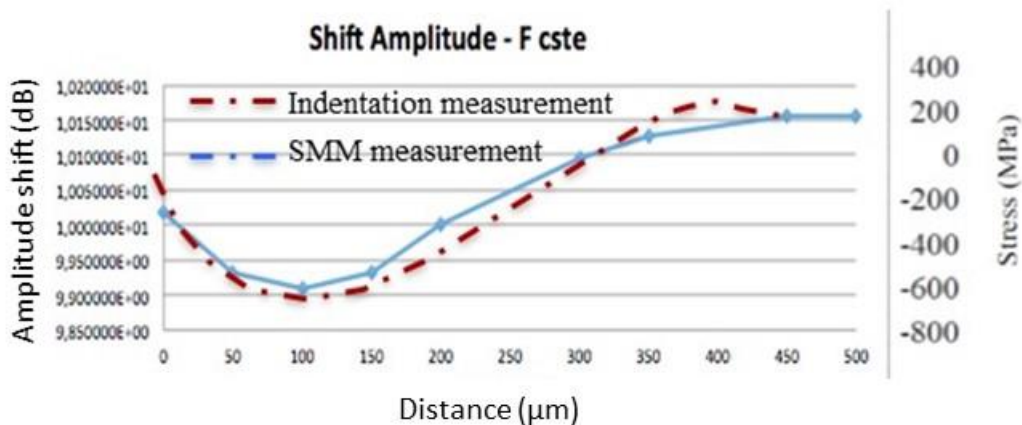


Figure 113: SMM measurements compared to the indentation profile showing a good agreement.

4.3.2. Study of shot-peening treatment on a brass sample

Now that the first evidence of the sensitivity of SMM to stress inside a material have been highlighted, it is necessary to confirm these results by the study of another kind of material.

That's why we focused on a brass sample presenting different shot-peening times.

SMM measurement were realized as previously described.

Previously, we showed that a shot-peening treatment leads to an increase of the compression stress peak as well as its shift to the inside of the sample (**Figure 108**). The phenomena is checked here and presented in **Figure 114** which perfectly highlights the shot-peening treatment time impact. Indeed, the shot-peening treatment impact distance previously estimated at $950\mu\text{m}$ for a 20 minutes shot-peened sample rises until $1150\mu\text{m}$ for a 40 minutes shot-peened sample.

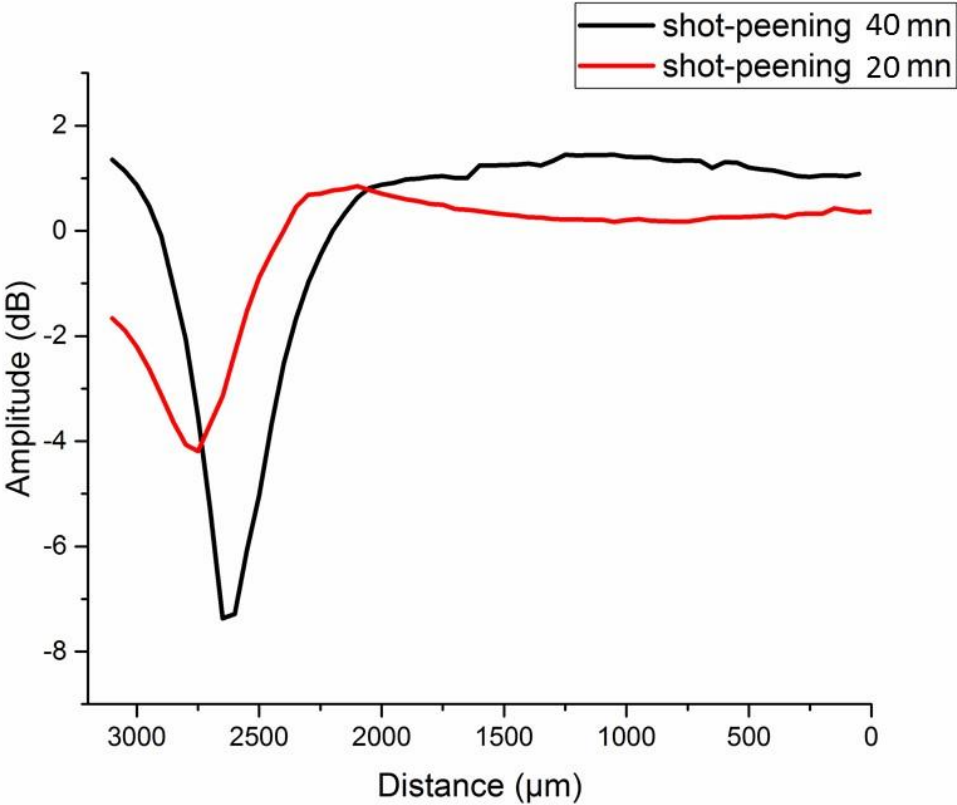


Figure 114: Influence of the shot-peening time - Comparison between 20min and 40min shot peened samples (the shot-peened surface is located on the left part of the graphic representation) showing a shift in frequency and a change in amplitude that may be used for quantitative analysis.

4.3.2.4. Conclusion

In the case of the study of different materials, we highlighted the potential of the SMM technique for non-destructive and direct stress profile measurement. The shot-peening surface studied presents a stress profile comparable to the one we expected.

Namely, we assume that SMM technique could provide a direct access to the residual stress profile with a sensitivity to the compression and tensile stress. The next step would be to realize a calibration that directly links the amplitude variation (in dB) with the MPa variation.

4.4. Conclusion

In this chapter we highlighted the high potential of SMM for tomographic investigation of metallic samples. Due to the high sensitivity of the technique to local changes in the conductivity of materials, the diffusion of light chemical element inside zirconium was observed. Moreover, we assume that the technique could allow to measure a stress profile in material in a direct and easy way with high reproducibility. This advance in characterization could lead to a great advance in qualification and quantification of stress in materials. The preliminary results obtained lead to the creation of a laboratory in collaboration with ARDPI Company. We focus now on the optimization of this technique for the industry through the realization of a portative prototype to realize in situ analyses.

Conclusion

This thesis reports my PhD work carried out during the years of 2013 to 2016 at the *Optique Submicronique et Nano Capteurs* team of the Institut Carnot de Bourgogne (ICB), under the supervision of Pr. Eric Lesniewska and Dr. Eric Bourillot.

The work was realized in collaboration with Dr. Laurène Tétard from the University of Central Florida, Pr. Alexandre Dazzi from Université Paris Sud (and Marie-Joelle Virolle from Université Paris Sud 11).

The main objectives of this thesis were to exploit and develop the subsurface nanoscale imaging by the use of Atomic Force Microscopy.

For the first time, the study of the influence of frequency parameters on the volume investigation by acoustic microscopy (MSAFM) was performed. Moreover, through the fabrication on nano-calibrated samples realized at the technological platform ARCEN (Applications, Recherches et Caractérisation à l'Echelle Nanométrique) of our laboratory, a numerical model, aimed at the understanding of the role of frequencies applied for the subsurface characterization, was developed and experimentally validated.

Next, MSAFM was applied to the characterization of dielectric and biological samples. Furthermore, the sensitivity of the technique to low density structures was revealed through the analysis of polymer samples and the tomographic reconstruction of the insulation profile of the polymer by electron beam lithography. Additionally, in order to achieve the complete understanding of biological samples, the AFM-IR – which provided chemical information – were combined to MSAFM to the study of the distribution of lipid vesicles inside *Streptomyces* bacteria. This allowed the study of the complex biological processes, such as biofuel production. A prototype of AFM-IR/MSAFM is being prepared, a disclosure invention was realized and the corresponding patent is currently in preparation.

However, the theoretical model developed for metal samples cannot be applied anymore on dielectric ones and a further study to have access to a perfect correlation between frequency and depth investigation in soft matter is being developed.

On the other hand, although the power of MSAFM technique combined to AFM-IR for in-volume and chemical characterization of biological samples was explored, the full characterization of metal samples still remains rather obscure. In this respect, the second part of the thesis focuses on the SMM, which possess a great sensitivity to local changes in material conductivity. This was demonstrated through the analyses of calibrated samples and applied to the study of diffusion of light chemical element (oxygen) in metal (zirconium). The promising results obtained by this techniques interested the industrial sector, and a research laboratory was developed with ARDPI industrial company.

Moreover, the thesis addresses the perspectives of the SMM technique for the determination of residual stress in materials. Interestingly, this technique turns out to offer great and promising characterization possibilities for the industry. Specifically, the ICB laboratory is involved in the development of an SMM portative version for in-situ measurements.

The next studies to realize consist in developing a data bank to calibrate the SMM on different materials and thus being able to link with high accuracy the amplitude and phase variations to the electric conductivity of the materials and to the stress value in MPa.

Actually, a study on metal alloys made of silver and gold is conducted to link the amplitude variations to the exact percentage of elements in the sample.

Moreover, it could be interesting to focus on the study of biological samples by SMM technique and to develop a liquid cell to be able to realize in-situ measurements.

As a conclusion, MSAFM and SMM techniques offer a whole set of thorough subsurface characterization methods, ranging from biological to metallic samples in a frequency range from MHz to GHz. The coupling of these two complementary techniques would allow a full, in situ characterization of many different materials.

As the continuation of my scientific research, I start a postdoctoral fellowship at the Institute of life science at the Université Catholique de Louvain (UCL, Belgium) in August under the direction of Pr. Yves Dufrêne. This new research topic focus on the interaction of bacteria with surfaces explored by AFM and force spectroscopy analysis.

References

- 1 Brown, M. R. & Williams, P. The influence of environment on envelope properties affecting survival of bacteria in infections. *Annual Reviews in Microbiology* **39**, 527-556 (1985).
- 2 Moghimi, S. M., Hunter, A. C. & Murray, J. C. Nanomedicine: current status and future prospects. *The FASEB journal* **19**, 311-330 (2005).
- 3 Nel, A., Xia, T., Mädler, L. & Li, N. Toxic potential of materials at the nanolevel. *Science* **311**, 622-627 (2006).
- 4 Werner, M. R. & Fahrner, W. R. Review on materials, microsensors, systems and devices for high-temperature and harsh-environment applications. *Industrial Electronics, IEEE Transactions on* **48**, 249-257 (2001).
- 5 Kinoshita, N. *et al.* Assessment of individual radionuclide distributions from the Fukushima nuclear accident covering central-east Japan. *Proceedings of the National Academy of Sciences* **108**, 19526-19529 (2011).
- 6 Rieber, R. W. & Carton, A. S. in *The collected works of LS Vygotsky* 29-51 (Springer, 1993).
- 7 McMahan, C. & Coffin, L. Mechanisms of damage and fracture in high-temperature, low-cycle fatigue of a cast nickel-based superalloy. *Metallurgical Transactions* **1**, 3443-3450 (1970).
- 8 Talreja, R. & Singh, C. V. *Damage and failure of composite materials*. (Cambridge University Press, 2012).
- 9 Yaméogo, S., Corthésy, R. & Leite, M. Influence of local heterogeneity on Doorstopper stress measurements. *International Journal of Rock Mechanics and Mining Sciences* **60**, 288-300 (2013).
- 10 Lichtman, J. W. & Conchello, J.-A. Fluorescence microscopy. *Nature methods* **2**, 910-919 (2005).
- 11 Herman, B. *Fluorescence microscopy*. (BIOS Scientific Publishers, 1998).
- 12 Young, J. W. *et al.* Measuring single-cell gene expression dynamics in bacteria using fluorescence time-lapse microscopy. *Nature protocols* **7**, 80-88 (2012).
- 13 Valeur, B. & Berberan-Santos, M. N. *Molecular fluorescence: principles and applications*. (John Wiley & Sons, 2012).
- 14 Armstrong, J. & Niven, J. Fluorescence microscopy in the study of nucleic acids; histochemical observations on cellular and virus nucleic acids. *Nature* **180**, 1335 (1957).
- 15 http://www.angiobodies.com/cnb_eng.asp.
- 16 Caron, D. A. Technique for enumeration of heterotrophic and phototrophic nanoplankton, using epifluorescence microscopy, and comparison with other procedures. *Appl Environ Microb* **46**, 491-498 (1983).
- 17 Wilson, T. Confocal microscopy. *Academic Press: London, etc* **426**, 1-64 (1990).
- 18 Sugawara, Y., Kamioka, H., Honjo, T., Tezuka, K.-i. & Takano-Yamamoto, T. Three-dimensional reconstruction of chick calvarial osteocytes and their cell processes using confocal microscopy. *Bone* **36**, 877-883 (2005).
- 19 Axelrod, D. Total internal reflection fluorescence microscopy in cell biology. *Traffic* **2**, 764-774 (2001).
- 20 Thompson, N. L. in *Topics in fluorescence spectroscopy* 337-378 (Springer, 1999).
- 21 Krenning, E. *et al.* Somatostatin receptor scintigraphy with [111In-DTPA-D-Phe1]-and [123I-Tyr3]-octreotide: the Rotterdam experience with more than 1000 patients. *European journal of nuclear medicine* **20**, 716-731 (1993).

- 22 Kharfi, F. *Principles and Applications of Nuclear Medical Imaging: A Survey on Recent Developments*. (INTECH Open Access Publisher, 2013).
- 23 Jolepalem, P. & Balon, H. R. The Role of Scintigraphy in Confirmation of Suspected Brain Death. *Journal of nuclear medicine technology* **41**, 306-307 (2013).
- 24 Marrie, T. & Costerton, J. Scanning and transmission electron microscopy of in situ bacterial colonization of intravenous and intraarterial catheters. *Journal of Clinical Microbiology* **19**, 687-693 (1984).
- 25 Lickfield, K. Transmission electron microscopy of bacteria. *Methods in microbiology* **9**, 127-176 (1976).
- 26 Frank, J. *Electron tomography*. (Springer, 1992).
- 27 Midgley, P. A. & Dunin-Borkowski, R. E. Electron tomography and holography in materials science. *Nature materials* **8**, 271-280 (2009).
- 28 McIntosh, R., Nicastro, D. & Mastronarde, D. New views of cells in 3D: an introduction to electron tomography. *Trends in cell biology* **15**, 43-51 (2005).
- 29 Bonetta, L. Zooming in on electron tomography. *Nature Methods* **2**, 139-145 (2005).
- 30 Parzuchowski, H. M., Reighard, M. K. & Kintz, K. G. (Google Patents, 1997).
- 31 Lorraine, P. W., Hewes, R. A. & Staver, P. R. (Google Patents, 1998).
- 32 Scruby, C. B. & Drain, L. E. *Laser ultrasonics techniques and applications*. (CRC Press, 1990).
- 33 Profunser, D. M., Vollmann, J., Bryner, J. & Dual, J. in *NDE For Health Monitoring and Diagnostics*. 21-30 (International Society for Optics and Photonics).
- 34 <http://tecnar.com/index.php/products/laser-ut>.
- 35 Murfin, A., Soden, R., Hatrick, D. & Dewhurst, R. J. Laser-ultrasound detection systems: a comparative study with Rayleigh waves. *Measurement Science and Technology* **11**, 1208 (2000).
- 36 Kundu, T. *Ultrasonic nondestructive evaluation: engineering and biological material characterization*. (CRC press, 2003).
- 37 Hauptmann, P., Hoppe, N. & Püttmer, A. Application of ultrasonic sensors in the process industry. *Measurement Science and Technology* **13**, R73 (2002).
- 38 <http://www.thefabricator.com/publication/tpj/issue/794>.
- 39 Hashimoto, M. Eddy current testing. *Metals and Technology(Japan)(Japan)* **69**, 21-27 (1999).
- 40 Schmidt, T. R. The remote field eddy current inspection technique. *Materials Evaluation* **42**, 225-230 (1984).
- 41 Fukutomi, H., Huang, H., Takagi, T. & Tani, J. Identification of crack depths from eddy current testing signal. *Magnetics, IEEE Transactions on* **34**, 2893-2896 (1998).
- 42 Bodnar, J. *et al.* Stimulated infrared thermography applied to help restoring mural paintings. *NDT & E International* **49**, 40-46 (2012).
- 43 Maldague, X. P. Introduction to NDT by active infrared thermography. *Materials Evaluation* **60**, 1060-1073 (2002).
- 44 Candoré, J. C., Bodnar, J. L., Detalle, V. & Grossel, P. Non-destructive testing of works of art by stimulated infrared thermography. *The European Physical Journal Applied Physics* **57**, 21002 (2012).
- 45 Avdelidis, N., Hawtin, B. & Almond, D. Transient thermography in the assessment of defects of aircraft composites. *Ndt & E International* **36**, 433-439 (2003).
- 46 Bison, P. G. *et al.* in *AeroSense 2003*. 318-327 (International Society for Optics and Photonics).
- 47 Meola, C. A new approach for estimation of defects detection with infrared thermography. *Materials Letters* **61**, 747-750 (2007).

- 48 Luong, M. P. Fatigue limit evaluation of metals using an infrared thermographic technique. *Mechanics of materials* **28**, 155-163 (1998).
- 49 Hayat, M. A. *Principles and techniques of scanning electron microscopy. Biological applications. Volume I.* (Van Nostrand Reinhold Company., 1974).
- 50 Unakar, N., Tsui, J. & Harding, C. Scanning electron microscopy. *Ophthalmic Research* **13**, 20-35 (1981).
- 51 Krumeick, F. Properties of electrons, their interactions with matter and applications in electron microscopy. *Laboratory of Inorganic Chemistry, disponível em <http://www.microscopy.ethz.ch/downloads/Interactions.pdf>, consultado em, 3-08 (2011).*
- 52 Défarge, C., Issa, O. M. & Trichet, J. Apports du cryo-microscope électronique à balayage à émission de champ à l'étude des matières organiques et des relations organo-minérales naturelles. Application aux croûtes microbiotiques des sols. *Comptes Rendus de l'Académie des Sciences-Series IIA-Earth and Planetary Science* **328**, 591-597 (1999).
- 53 Ngo, P. D. in *Failure Analysis of Integrated Circuits* 205-215 (Springer, 1999).
- 54 <http://www.nanoanalytics.com/en/analyticalservices/techniques/SEMEDS/index.php>.
- 55 Safaepour, M., Shahverdi, A. R., Shahverdi, H. R., Khorramizadeh, M. R. & Gohari, A. R. Green synthesis of small silver nanoparticles using geraniol and its cytotoxicity against fibrosarcoma-wehi 164. *Avicenna journal of medical biotechnology* **1**, 111-115 (2009).
- 56 Usher, D. Sodium ion migration in glass on electron beam irradiation. *Journal of Physics C: Solid State Physics* **14**, 2039 (1981).
- 57 Bouyne, E., Flower, H., Lindley, T. & Pineau, A. Use of EBSD technique to examine microstructure and cracking in a bainitic steel. *Scripta Materialia* **39**, 295-300 (1998).
- 58 Simkin, B., Ng, B., Bieler, T., Crimp, M. & Mason, D. Orientation determination and defect analysis in the near-cubic intermetallic γ -TiAl using SACP, ECCI, and EBSD. *Intermetallics* **11**, 215-223 (2003).
- 59 Wright, S. I. & Nowell, M. M. EBSD image quality mapping. *Microsc Microanal* **12**, 72-84 (2006).
- 60 Zhai, T., Wilkinson, A. & Martin, J. A crystallographic mechanism for fatigue crack propagation through grain boundaries. *Acta Mater* **48**, 4917-4927 (2000).
- 61 Uta, E., Gey, N., Bocher, P., Humbert, M. & Gilgert, J. Texture heterogeneities in α p/ α s titanium forging analysed by EBSD-Relation to fatigue crack propagation. *Journal of microscopy* **233**, 451-459 (2009).
- 62 Blochwitz, C., Brechbühl, J. & Tirschler, W. Analysis of activated slip systems in fatigue nickel polycrystals using the EBSD-technique in the scanning electron microscope. *Materials Science and Engineering: A* **210**, 42-47 (1996).
- 63 <http://www.edax.com/Products/EBSD/EBSD-Detectors.aspx>.
- 64 <https://www.ucl.ac.uk/mssl/detection/plasma-detection/research/electrostatic>.
- 65 Von Heimendahl, M., Bell, W. & Thomas, G. Applications of Kikuchi line analyses in electron microscopy. *Journal of Applied Physics* **35**, 3614-3616 (1964).
- 66 Johansson, S. A., Campbell, J. L. & Malmqvist, K. G. *Particle-induced X-ray emission spectrometry (PIXE)*. Vol. 133 (John Wiley & Sons, 1995).
- 67 Volfinger, M. & Robert, J.-L. Particle-induced-gamma-ray-emission spectrometry applied to the determination of light elements in individual grains of granite minerals. *Journal of radioanalytical and nuclear chemistry* **185**, 273-291 (1994).
- 68 Wilkens, B., Shepard, C. & Lanford, W. Nuclear reaction analysis profiling as direct evidence for lithium ion mass transport in thin film "rocking-chair" structures. *Energy (t&V)* **1**, 1.5 (1982).

- 69 Perrière, J. Rutherford backscattering spectrometry. *Vacuum* **37**, 429-432 (1987).
- 70 Abbe, E. Beiträge zur Theorie des Mikroskops und der mikroskopischen
Wahrnehmung. *Archiv für mikroskopische Anatomie* **9**, 413-418 (1873).
- 71 <http://www.olympus-global.com/en/>.
- 72 Betzig, E. & Trautman, J. K. Near-field optics: microscopy, spectroscopy, and surface
modification beyond the diffraction limit. *Science* **257**, 189-195 (1992).
- 73 Girard, C. & Dereux, A. Near-field optics theories. *Reports on Progress in Physics* **59**,
657 (1996).
- 74 Leviatan, Y. Study of near-zone fields of a small aperture. *Journal of applied physics*
60, 1577-1583 (1986).
- 75 Ferrell, T. L., Warmack, R. J. & Reddick, R. C. (Google Patents, 1991).
- 76 Goudonnet, J.-P. *et al.* in *OE/LASE'92*. 12-23 (International Society for Optics and
Photonics).
- 77 Bourillot, E., De Fornel, F., Salomon, L., Adam, P. & Goudonnet, J. Observation de
structures guidantes en microscopie à effet tunnel photonique. *Journal of optics* **23**, 57-
62 (1992).
- 78 Binnig, G., Quate, C. F. & Gerber, C. Atomic force microscope. *Physical Review Letters*
56, 930 (1986).
- 79 Binnig, G., Gerber, C., Stoll, E., Albrecht, T. & Quate, C. Atomic resolution with atomic
force microscope. *EPL (Europhysics Letters)* **3**, 1281 (1987).
- 80 Binnig, G. & Rohrer, H. Scanning tunneling microscopy. *Surf Sci* **126**, 236-244 (1983).
- 81 <https://www.bruker.com/>.
- 82 Meyer, G. & Amer, N. M. Simultaneous measurement of lateral and normal forces with
an optical-beam-deflection atomic force microscope. *Applied Physics Letters* **57**, 2089-
2091 (1990).
- 83 [http://www.parkafm.com/index.php/park-spm-modes/91-standard-imaging-mode/222-
lateral-force-microscopy-lfm](http://www.parkafm.com/index.php/park-spm-modes/91-standard-imaging-mode/222-lateral-force-microscopy-lfm).
- 84 Hölscher, H. AFM, Tapping Mode. *Encyclopedia of Nanotechnology*, 99-99 (2012).
- 85 Le Gnimellec, C., Lesniewska, É., Giocondi, M.-C., Finot, É. & Goudonnet, J.-P.
Simultaneous imaging of the surface and the submembrane cytoskeleton in living
cells by tapping mode atomic force microscopy. *Comptes Rendus de l'Académie des
Sciences-Series III-Sciences de la Vie* **320**, 637-643 (1997).
- 86 Hansma, P. *et al.* Tapping mode atomic force microscopy in liquids. *Applied Physics
Letters* **64**, 1738-1740 (1994).
- 87 <http://www.nanoscience.com/technology/afm-technology/afm-modes-2/>.
- 88 Pletikapić, G., Berquand, A., Radić, T. M. & Svetličić, V. Quantitative nanomechanical
mapping of marine diatom in seawater using peak force tapping atomic force
microscopy1. *Journal of Phycology* **48**, 174-185 (2012).
- 89 Pittenger, B., Erina, N. & Su, C. Quantitative mechanical property mapping at the
nanoscale with PeakForce QNM. *Application Note Veeco Instruments Inc* (2010).
- 90 Derjaguin, B. V., Muller, V. M. & Toporov, Y. P. Effect of contact deformations on the
adhesion of particles. *J Colloid Interf Sci* **53**, 314-326 (1975).
- 91 Lai, J., Chandrachud, M., Majumda, A. & Carrejo, J. Thermal detection of device
failure by atomic force microscopy. *Electron Device Letters, IEEE* **16**, 312-315 (1995).
- 92 Hammiche, A., Pollock, H., Song, M. & Hourston, D. Sub-surface imaging by scanning
thermal microscopy. *Measurement Science and technology* **7**, 142 (1996).
- 93 Luo, K., Shi, Z., Lai, J. & Majumdar, A. Nanofabrication of sensors on cantilever probe
tips for scanning multiprobe microscopy. *Applied Physics Letters* **68**, 325-327 (1996).

- 94 Lee, J.-H. & Gianchandani, Y. High-resolution scanning thermal probe with servocontrolled interface circuit for microcalorimetry and other applications. *Review of scientific instruments* **75**, 1222-1227 (2004).
- 95 <http://www.parkafm.com/index.php/park-spm-modes/99-thermal-properties/252-scanning-thermal-microscopy-sthm>.
- 96 Aubry, R. *et al.* SThM temperature mapping and nonlinear thermal resistance evolution with bias on AlGaIn/GaN HEMT devices. *Electron Devices, IEEE Transactions on* **54**, 385-390 (2007).
- 97 ANTONIOW, J. S., MAIGRET, J.-E., CHIRTOC, M., BEAUGRAND, J. & DOLE, P. Mise en évidence par micro-analyse thermique à balayage (SThM) de gradients de température de transitions vitreuses dans les parois lignocellulo-siques.
- 98 Dietzel, D., Chotikaprakhan, S., Bein, B. & Pelzl, J. in *Journal de Physique IV (Proceedings)*. 87-91 (EDP sciences).
- 99 Nonnenmacher, M. & Wickramasinghe, H. Scanning probe microscopy of thermal conductivity and subsurface properties. *Applied Physics Letters* **61**, 168-170 (1992).
- 100 Fryer, D. S., Nealey, P. F. & de Pablo, J. J. Thermal probe measurements of the glass transition temperature for ultrathin polymer films as a function of thickness. *Macromolecules* **33**, 6439-6447 (2000).
- 101 Bond, L. *et al.* Differential scanning calorimetry and scanning thermal microscopy analysis of pharmaceutical materials. *International journal of pharmaceutics* **243**, 71-82 (2002).
- 102 <https://www.asylumresearch.com/Products/Ztherm/Ztherm.shtml>.
- 103 Rao, C. N. R. Chemical applications of infrared spectroscopy. (1963).
- 104 Hammiche, A. *et al.* Photothermal FT-IR spectroscopy: A step towards FT-IR microscopy at a resolution better than the diffraction limit. *Applied spectroscopy* **53**, 810-815 (1999).
- 105 Müller, T. *et al.* Nanoscale spatially resolved infrared spectra from single microdroplets. *Lab on a Chip* (2014).
- 106 Policar, C. *et al.* Subcellular IR imaging of a metal-carbonyl moiety using photothermally induced resonance. *Angewandte Chemie* **123**, 890-894 (2011).
- 107 Dazzi, A. *et al.* AFM-IR: combining atomic force microscopy and infrared spectroscopy for nanoscale chemical characterization. *Applied spectroscopy* **66**, 1365-1384 (2012).
- 108 Prater, C., Kjoller, K. & Shetty, R. Nanoscale infrared spectroscopy. *Materials Today* **13**, 56-60 (2010).
- 109 Deniset-Besseau, A., Prater, C. B., Virolle, M.-J. & Dazzi, A. Monitoring TriAcylGlycerols Accumulation by Atomic Force Microscopy Based Infrared Spectroscopy in Streptomyces Species for Biodiesel Applications. *The Journal of Physical Chemistry Letters* **5**, 654-658 (2014).
- 110 Kessler, L. W. & Yuhas, D. E. in *IEEE Proceedings*. 526-536.
- 111 Sokoloff, S. (Google Patents, 1939).
- 112 Sokolov, S. On the problem of the propagation of ultrasonic oscillations in various bodies. *Elek Nachr Tech* **6**, 92 (1929).
- 113 Sokolov, S. Y. Ultrasonic methods of detecting internal flaws in metal articles. *Zavodskaya Laboratoriya* **4** (1935).
- 114 Sokolov, S. Y. Ultraacoustic methods of studying properties of hardened steel and detecting intrinsic flaws of metal articles. *Zh. Tekh. Fiz* **11**, 160-169 (1941).
- 115 http://www.akin.ru/e_main.htm.
- 116 Lemons, R. & Quate, C. Acoustic microscope—scanning version. *Applied Physics Letters* **24**, 163-165 (1974).

- 117 Weiss, E. C., Lemor, R. M., Pilarczyk, G., Anastasiadis, P. & Zinin, P. V. Imaging of focal contacts of chicken heart muscle cells by high-frequency acoustic microscopy. *Ultrasound in medicine & biology* **33**, 1320-1326 (2007).
- 118 Prasad, M., Manghnani, M., Wang, Y., Zinin, P. & Livingston, R. Acoustic microscopy of portland cement mortar aggregate/paste interfaces. *J Mater Sci* **35**, 3607-3613 (2000).
- 119 Yamanaka, K., Ogiso, H. & Kolosov, O. Ultrasonic force microscopy for nanometer resolution subsurface imaging. *Applied Physics Letters* **64**, 178-180 (1994).
- 120 Chilla, E., Hesjedal, T. & Fröhlich, H.-J. Nanoscale determination of phase velocity by scanning acoustic force microscopy. *Physical Review B* **55**, 15852 (1997).
- 121 Rabe, U. in *Applied Scanning Probe Methods II* 37-90 (Springer, 2006).
- 122 Yamanaka, K. & Tsuji, T. Ultrasonic Atomic Force Microscopy. *Characterization of Materials* (2013).
- 123 Yamanaka, K. Ultrasonic force microscopy. *MRS Bulletin* **21**, 36-41 (1996).
- 124 Rohrbeck, W. & Chilla, E. Detection of surface acoustic waves by scanning force microscopy. *physica status solidi (a)* **131**, 69-71 (1992).
- 125 Kolosov, O. & Yamanaka, K. Nonlinear detection of ultrasonic vibrations in an atomic force microscope. *Japanese journal of applied physics* **32**, L1095 (1993).
- 126 Yamanaka, K. & Nakano, S. Ultrasonic atomic force microscope with overtone excitation of cantilever. *Japanese journal of applied physics* **35**, 3787-3792 (1996).
- 127 Heuberger, M., Dietler, G. & Schlapbach, L. Mapping the local Young's modulus by analysis of the elastic deformations occurring in atomic force microscopy. *Nanotechnology* **6**, 12 (1995).
- 128 Radmacher, M., Fritz, M., Kacher, C. M., Cleveland, J. P. & Hansma, P. K. Measuring the viscoelastic properties of human platelets with the atomic force microscope. *Biophys J* **70**, 556-567 (1996).
- 129 Maivald, P. *et al.* Using force modulation to image surface elasticities with the atomic force microscope. *Nanotechnology* **2**, 103 (1991).
- 130 Kolosov, O. V. *et al.* Imaging the elastic nanostructure of Ge islands by ultrasonic force microscopy. *Physical Review Letters* **81**, 1046 (1998).
- 131 Rabe, U. & Arnold, W. Acoustic microscopy by atomic force microscopy. *Applied Physics Letters* **64**, 1493-1495 (1994).
- 132 Hurley, D., Shen, K., Jennett, N. & Turner, J. A. Atomic force acoustic microscopy methods to determine thin-film elastic properties. *Journal of applied physics* **94**, 2347-2354 (2003).
- 133 Rabe, U. *et al.* Quantitative determination of contact stiffness using atomic force acoustic microscopy. *Ultrasonics* **38**, 430-437 (2000).
- 134 McMaster, R. C. *Nondestructive testing handbook. Volume 1-Leak testing.* (1982).
- 135 Shibata, M., Yamashita, H., Uchihashi, T., Kandori, H. & Ando, T. High-speed atomic force microscopy shows dynamic molecular processes in photoactivated bacteriorhodopsin. *Nature nanotechnology* **5**, 208-212 (2010).
- 136 Kodera, N., Yamamoto, D., Ishikawa, R. & Ando, T. Video imaging of walking myosin V by high-speed atomic force microscopy. *Nature* **468**, 72-76 (2010).
- 137 Bosisio, R., Giroux, M. & Couderc, D. Paper sheet moisture measurements by microwave phase perturbation techniques. *J. Microwave Power* **5**, 25-34 (1970).
- 138 Seifert, W., Gerner, E., Stachel, M. & Dransfeld, K. Scanning Tunneling Microscopy at Microwave-Frequencies. *Ultramicroscopy* **42**, 379-387, doi:Doi 10.1016/0304-3991(92)90296-V (1992).
- 139 Vitry, P. *et al.* Advances in quantitative nanoscale subsurface imaging by mode-synthesizing atomic force microscopy. *Applied Physics Letters* **105**, 053110 (2014).

- 140 Bourillot, E. *et al.* Solid Solution Characterization in Metal by Original Tomographic Scanning Microwave Microscopy Technique. *Characterization of Minerals, Metals, and Materials 2015*, 65-72.
- 141 Ewald, M. *et al.* From surface to intracellular non-invasive nanoscale study of living cells impairments. *Nanotechnology* **25**, 295101 (2014).
- 142 Tetard, L. *et al.* Imaging nanoparticles in cells by nanomechanical holography. *Nature nanotechnology* **3**, 501-505 (2008).
- 143 Vitry, P. *et al.* Mode-synthesizing atomic force microscopy for 3D reconstruction of embedded low-density dielectric nanostructures. *Nano Research*, 1-7 (2015).
- 144 Passian, A., Thundat, T. G. & Tetard, L. (Google Patents, 2013).
- 145 Shekhawat, G. & Dravid, V. Seeing the invisible: scanning near-field ultrasound holography (SNFUH) for high resolution sub-surface imaging. *Microsc Microanal* **12**, 1214-1215 (2006).
- 146 Passian, A., Thundat, T. G. & Tetard, L. (Google Patents, 2014).
- 147 Tetard, L., Passian, A. & Thundat, T. New modes for subsurface atomic force microscopy through nanomechanical coupling. *Nature nanotechnology* **5**, 105-109 (2010).
- 148 Tetard, L., Passian, A., Farahi, R. & Thundat, T. Atomic force microscopy of silica nanoparticles and carbon nanohorns in macrophages and red blood cells. *Ultramicroscopy* **110**, 586-591 (2010).
- 149 Striegler, A. *et al.* Detection of buried reference structures by use of atomic force acoustic microscopy. *Ultramicroscopy* **111**, 1405-1416 (2011).
- 150 Tetard, L., Passian, A., Farahi, R. H., Voy, B. H. & Thundat, T. Applications of Subsurface Microscopy. *Nanotoxicity: Methods and Protocols*, 331-343 (2012).
- 151 Shekhawat, G. S., Avasthy, S., Srivastava, A. K., Tark, S.-H. & Dravid, V. P. Probing buried defects in extreme ultraviolet multilayer blanks using ultrasound holography. *Nanotechnology, IEEE Transactions on* **9**, 671-674 (2010).
- 152 Verbiest, G., Oosterkamp, T. & Rost, M. Subsurface-AFM: sensitivity to the heterodyne signal. *Nanotechnology* **24**, 365701 (2013).
- 153 Cantrell, S. A., Cantrell, J. H. & Lillehei, P. T. Nanoscale subsurface imaging via resonant difference-frequency atomic force ultrasonic microscopy. *Journal of applied physics* **101**, 114324 (2007).
- 154 Fukuma, T., Kimura, K., Kobayashi, K., Matsushige, K. & Yamada, H. Frequency-modulation atomic force microscopy at high cantilever resonance frequencies using the heterodyne optical beam deflection method. *Review of scientific instruments* **76**, 126110 (2005).
- 155 Rabe, U., Janser, K. & Arnold, W. Vibrations of free and surface-coupled atomic force microscope cantilevers: theory and experiment. *Review of scientific instruments* **67**, 3281-3293 (1996).
- 156 Crozier, K. *et al.* Thin film characterization by atomic force microscopy at ultrasonic frequencies. *Applied Physics Letters* **76**, 1950-1952 (2000).
- 157 Cuberes, M. T., Assender, H., Briggs, G. A. D. & Kolosov, O. Heterodyne force microscopy of PMMA/rubber nanocomposites: nanomapping of viscoelastic response at ultrasonic frequencies. *Journal of Physics D: Applied Physics* **33**, 2347 (2000).
- 158 Cuberes, M., Briggs, G. & Kolosov, O. Nonlinear detection of ultrasonic vibration of AFM cantilevers in and out of contact with the sample. *Nanotechnology* **12**, 53 (2001).
- 159 Cuberes, M., Stegemann, B., Kaiser, B. & Rademann, K. Ultrasonic force microscopy on strained antimony nanoparticles. *Ultramicroscopy* **107**, 1053-1060 (2007).

- 160 Tetard, L. *et al.* Elastic phase response of silica nanoparticles buried in soft matter. *Applied Physics Letters* **93**, 133113 (2008).
- 161 Verbiest, G., Simon, J., Oosterkamp, T. & Rost, M. Subsurface atomic force microscopy: towards a quantitative understanding. *Nanotechnology* **23**, 145704 (2012).
- 162 Shekhawat, G., Srivastava, A., Avasthy, S. & Dravid, V. Ultrasound holography for noninvasive imaging of buried defects and interfaces for advanced interconnect architectures. *Applied Physics Letters* **95**, 263101 (2009).
- 163 Tetard, L. *et al.* Virtual resonance and frequency difference generation by van der Waals interaction. *Physical Review Letters* **106**, 180801 (2011).
- 164 Cantrell, J. H. & Cantrell, S. A. Analytical model of the nonlinear dynamics of cantilever tip-sample surface interactions for various acoustic atomic force microscopies. *Physical Review B* **77**, 165409 (2008).
- 165 Rose, J. L. & Nagy, P. B. Ultrasonic waves in solid media. *The Journal of the Acoustical Society of America* **107**, 1807-1808 (2000).
- 166 Vitry, P. *et al.* Mode-synthesizing atomic force microscopy for volume characterization of mixed metal nanoparticles. *Journal of microscopy* (2016).
- 167 Ash, E. & Nicholls, G. Super-resolution aperture scanning microscope. (1972).
- 168 Tabib-Azar, M., Su, D.-P., Pohar, A., LeClair, S. & Ponchak, G. 0.4 μm spatial resolution with 1 GHz ($\lambda = 30\text{ cm}$) evanescent microwave probe. *Review of scientific instruments* **70**, 1725-1729 (1999).
- 169 Hyde, J. S. (Google Patents, 1966).
- 170 Ash, E. & Nicholls, G. Super-resolution aperture scanning microscope. *Nature* **237**, 510-512 (1972).
- 171 Mosig, J. R., Besson, J.-C., Gex-Fabry, M. & Gardiol, F. E. Reflection of an open-ended coaxial line and application to nondestructive measurement of materials. *Instrumentation and Measurement, IEEE Transactions on* **1001**, 46-51 (1981).
- 172 Pond, J. *et al.* Penetration depth and microwave loss measurements with a YBa₂Cu₃O_{7- δ} /LaAlO₃/YBa₂Cu₃O_{7- δ} trilayer transmission line. *Applied physics letters* **59**, 3033-3035 (1991).
- 173 Manassen, Y. Scanning Probe microscopy and magnetic resonance. *Advanced Materials* **6**, 401-404 (1994).
- 174 Zhang, Z., Hammel, P. & Wigen, P. Observation of ferromagnetic resonance in a microscopic sample using magnetic resonance force microscopy. *Applied physics letters* **68**, 2005-2007 (1996).
- 175 Wago, K., Botkin, D., Yannoni, C. & Rugar, D. Paramagnetic and ferromagnetic resonance imaging with a tip-on-cantilever magnetic resonance force microscope. *Applied physics letters* **72**, 2757-2759 (1998).
- 176 Anlage, S. M., Talanov, V. V. & Schwartz, A. R. in *Scanning probe microscopy* 215-253 (Springer, 2007).
- 177 Black, R. *et al.* Microwave microscopy using a superconducting quantum interference device. *Applied physics letters* **66**, 99-101 (1995).
- 178 Jackson, J. D. & Fox, R. F. Classical electrodynamics. *American Journal of Physics* **67**, 841-842 (1999).
- 179 Osepchuk, J. M. Microwave power applications. *Microwave Theory and Techniques, IEEE Transactions on* **50**, 975-985 (2002).
- 180 Lorrain, P., Corson, D. R., Guthmann, C. & Lederer, D. *Champs et ondes électromagnétiques*. (Armand Colin, 1979).
- 181 Plassard, C. *et al.* Detection of defects buried in metallic samples by scanning microwave microscopy. *Physical Review B* **83**, doi:Artn 121409

Doi 10.1103/Physrevb.83.121409 (2011).

- 182 Tsuji, T. & Yamanaka, K. Observation by ultrasonic atomic force microscopy of reversible displacement of subsurface dislocations in highly oriented pyrolytic graphite. *Nanotechnology* **12**, 301 (2001).
- 183 Passeri, D. *et al.* Characterization of epoxy/single-walled carbon nanotubes composite samples via atomic force acoustic microscopy. *Physica E: Low-dimensional Systems and Nanostructures* **40**, 2419-2424 (2008).
- 184 Rose, J. L. A baseline and vision of ultrasonic guided wave inspection potential. *Journal of pressure vessel technology* **124**, 273-282 (2002).
- 185 Nielsen, J. C., Prahl, C. & Lonvaud-Funel, A. Malolactic fermentation in wine by direct inoculation with freeze-dried *Leuconostoc oenos* cultures. *American Journal of Enology and Viticulture* **47**, 42-48 (1996).
- 186 Guzzo, J., Jobin, M.-P. & Diviès, C. Increase of sulfite tolerance in *Oenococcus oeni* by means of acidic adaptation. *FEMS Microbiology Letters* **160**, 43-47 (1998).
- 187 Guzzo, J. *et al.* Regulation of stress response in *Oenococcus oeni* as a function of environmental changes and growth phase. *International journal of food microbiology* **55**, 27-31 (2000).
- 188 Guzzo, J. *et al.* A small heat shock protein from *Leuconostoc oenos* induced by multiple stresses and during stationary growth phase. *Letters in Applied Microbiology* **24**, 393-396 (1997).
- 189 Coucheney, F. *et al.* A small HSP, Lo18, interacts with the cell membrane and modulates lipid physical state under heat shock conditions in a lactic acid bacterium. *Biochimica et Biophysica Acta (BBA)-Biomembranes* **1720**, 92-98 (2005).
- 190 Weidmann, S., Rieu, A., Rega, M., Coucheney, F. & Guzzo, J. Distinct amino acids of the *Oenococcus oeni* small heat shock protein Lo18 are essential for damaged protein protection and membrane stabilization. *FEMS microbiology letters* **309**, 8-15 (2010).
- 191 Da Silveira, M. G., Golovina, E. A., Hoekstra, F. A., Rombouts, F. M. & Abee, T. Membrane fluidity adjustments in ethanol-stressed *Oenococcus oeni* cells. *Appl Environ Microb* **69**, 5826-5832 (2003).
- 192 Brown, L., Wolf, J. M., Prados-Rosales, R. & Casadevall, A. Through the wall: extracellular vesicles in Gram-positive bacteria, mycobacteria and fungi. *Nature Reviews Microbiology* **13**, 620-630 (2015).
- 193 Davis, J. R. & Sello, J. K. Regulation of genes in *Streptomyces* bacteria required for catabolism of lignin-derived aromatic compounds. *Appl Microbiol Biot* **86**, 921-929 (2010).
- 194 Ma, F. & Hanna, M. A. Biodiesel production: a review. *Bioresource Technol* **70**, 1-15 (1999).
- 195 Ranade, N. & Vining, L. C. Accumulation of intracellular carbon reserves in relation to chloramphenicol biosynthesis by *Streptomyces venezuelae*. *Canadian journal of microbiology* **39**, 377-383 (1993).
- 196 Hu, Q. *et al.* Microalgal triacylglycerols as feedstocks for biofuel production: perspectives and advances. *The Plant Journal* **54**, 621-639 (2008).
- 197 Kumar, P., Barrett, D. M., Delwiche, M. J. & Stroeve, P. Methods for pretreatment of lignocellulosic biomass for efficient hydrolysis and biofuel production. *Ind Eng Chem Res* **48**, 3713-3729 (2009).
- 198 Chen, F. & Dixon, R. A. Lignin modification improves fermentable sugar yields for biofuel production. *Nature biotechnology* **25**, 759-761 (2007).

- 199 Fischer, C. R., Klein-Marcuschamer, D. & Stephanopoulos, G. Selection and optimization of microbial hosts for biofuels production. *Metabolic engineering* **10**, 295-304 (2008).
- 200 Miao, X. & Wu, Q. Biodiesel production from heterotrophic microalgal oil. *Bioresource Technol* **97**, 841-846 (2006).
- 201 Atsumi, S. & Liao, J. C. Metabolic engineering for advanced biofuels production from *Escherichia coli*. *Current opinion in biotechnology* **19**, 414-419 (2008).
- 202 Lu, X., Vora, H. & Khosla, C. Overproduction of free fatty acids in *E. coli*: implications for biodiesel production. *Metabolic engineering* **10**, 333-339 (2008).
- 203 Bokinsky, G. *et al.* Synthesis of three advanced biofuels from ionic liquid-pretreated switchgrass using engineered *Escherichia coli*. *Proceedings of the National Academy of Sciences* **108**, 19949-19954 (2011).
- 204 Hopwood, D. A. *et al.* Cloning *Streptomyces* genes for antibiotic production. *Trends in Biotechnology* **1**, 42-48 (1983).
- 205 Butler, P., Brown, M. & Oliver, S. Improvement of antibiotic titers from *Streptomyces* bacteria by interactive continuous selection. *Biotechnology and bioengineering* **49**, 185-196 (1996).
- 206 Goodfellow, M., Williams, S. T. & Mordarski, M. *Actinomycetes in biotechnology*. (Academic, 1988).
- 207 Coze, F., Gilard, F., Tcherkez, G., Virolle, M.-J. & Guyonvarch, A. Carbon-Flux Distribution within *Streptomyces coelicolor* Metabolism: A Comparison between the Actinorhodin-Producing Strain M145 and Its Non-Producing Derivative M1146. *Plos One* **8**, e84151 (2013).
- 208 Vitry, P. *et al.* Combining infrared and mode synthesizing atomic force microscopy: Application to the study of lipid vesicles inside *Streptomyces* bacteria. *Nano Research*, 1-8.
- 209 Tetard, L. *et al.* Spectroscopy and atomic force microscopy of biomass. *Ultramicroscopy* **110**, 701-707 (2010).
- 210 Matthiessen, A. On the Electrical Conductivity of Alloys. *Ann. Physik. Chem* **110**, 190 (1860).
- 211 Haynes, W. M. *CRC handbook of chemistry and physics*. (CRC press, 2014).
- 212 Leani, J. J., Sánchez, H. c. J., Pérez, R. D. & Pérez, C. Depth profiling nano-analysis of chemical environments using resonant Raman spectroscopy at grazing incidence conditions. *Analytical chemistry* **85**, 7069-7075 (2013).
- 213 Fiedler, H. D. *et al.* Simultaneous Nondestructive Analysis of Palladium, Rhodium, Platinum, and Gold Nanoparticles Using Energy Dispersive X-ray Fluorescence. *Analytical chemistry* **85**, 10142-10148 (2013).
- 214 De Giacomo, A., Gaudiuso, R., Koral, C., Dell'Aglio, M. & De Pascale, O. Nanoparticle-enhanced laser-induced breakdown spectroscopy of metallic samples. *Analytical chemistry* **85**, 10180-10187 (2013).
- 215 Lühl, L., Mantouvalou, I., Schaumann, I., Vogt, C. & Kanngießer, B. Three-dimensional chemical mapping with a confocal XRF setup. *Analytical chemistry* **85**, 3682-3689 (2013).
- 216 Optasanu, V. *et al.* High-resolution characterization of the diffusion of light chemical elements in metallic components by Scanning Atomic Force Microscopy. *Nanoscale* (2014).
- 217 Raceanu, L., Optasanu, V., Montesin, T., Montay, G. & François, M. Shot-Peening of Pre-Oxidized Plates of Zirconium: Influence of Residual Stress on Oxidation. *Oxidation of metals* **79**, 135-145 (2013).

- 218 Seitz, F. On the theory of diffusion in metals. *Acta Crystallographica* **3**, 355-363 (1950).
- 219 Dugdale, J. & Basinski, Z. Mathiessen's Rule and Anisotropic Relaxation Times. *Physical Review* **157**, 552 (1967).
- 220 Chernyaeva, T., Stukalov, A. & Gritsina, V. Oxygen in zirconium. (1999).
- 221 Wypych, G. *Handbook of material weathering*. (2003).
- 222 Smith, D. J. Deep hole drilling. *Practical Residual Stress Measurement Methods*, 65-87 (2013).
- 223 Klug, H. P. & Alexander, L. E. *X-ray diffraction procedures*. Vol. 2 (Wiley New York, 1954).
- 224 Bacon, G. E. Neutron diffraction. 3. (1975).
- 225 Withers, P. & Bhadeshia, H. Residual stress. Part 1—measurement techniques. *Mater Sci Tech-Lond* **17**, 355-365 (2001).
- 226 Hauk, V. *Structural and residual stress analysis by nondestructive methods: Evaluation-Application-Assessment*. (Elsevier, 1997).
- 227 Totten, G. E. *Handbook of residual stress and deformation of steel*. (ASM international, 2002).
- 228 <http://www.ni.com/white-paper/3642/en/>.
- 229 Callister, W. D. & Rethwisch, D. G. *Materials science and engineering: an introduction*. Vol. 7 (Wiley New York, 2007).
- 230 Roland, T., Reirant, D., Lu, K. & Lu, J. Fatigue life improvement through surface nanostructuring of stainless steel by means of surface mechanical attrition treatment. *Scripta Materialia* **54**, 1949-1954 (2006).
- 231 Wagner, L. Mechanical surface treatments on titanium, aluminum and magnesium alloys. *Materials Science and Engineering: A* **263**, 210-216 (1999).
- 232 Prev y, P., Jayaraman, N. & Ravindranath, R. in *ASME Turbo Expo 2004: Power for Land, Sea, and Air*. 231-239 (American Society of Mechanical Engineers).
- 233 Schulze, V. *Modern mechanical surface treatment: states, stability, effects*. (John Wiley & Sons, 2006).
- 234 Champaigne, J. Shot Peening Method. *Metal Finishing* **6**, 160 (1996).
- 235 Schajer, G. Measurement of non-uniform residual stresses using the hole-drilling method. Part I—Stress calculation procedures. *Journal of Engineering Materials and Technology* **110**, 338-343 (1988).
- 236 Drilling, D.-H., Coring, R. & Boring, S. Deep-Hole Drilling.
- 237 Hilley, M. *Residual stress measurement by X-ray diffraction*. (Society of Automotive Engineers, 1980).
- 238 Allen, A., Hutchings, M., Windsor, C. & Andreani, C. Neutron diffraction methods for the study of residual stress fields. *Advances in Physics* **34**, 445-473 (1985).
- 239 Prevey, P. S. X-ray diffraction residual stress techniques. *ASM International, ASM Handbook*. **10**, 380-392 (1986).
- 240 <http://www.veqter.co.uk/>.
- 241 Marsh, K. J. Shot peening: techniques and applications. *Engineering Materials Advisory Service Ltd.(United Kingdom)*, 1993, 320 (1993).
- 242 Kobayashi, M., Matsui, T. & Murakami, Y. Mechanism of creation of compressive residual stress by shot peening. *International Journal of Fatigue* **20**, 351-357 (1998).
- 243 Dalaei, K., Karlsson, B. & Svensson, L.-E. Stability of shot peening induced residual stresses and their influence on fatigue lifetime. *Materials Science and Engineering: A* **528**, 1008-1015 (2011).
- 244 <http://www.wheelabratorgroup.com/en/sites/wheelabrator/content/home.aspx>.

- 245 Chajec, W. Advances in Mechanics: Theoretical, Computational and Interdisciplinary Issues.
- 246 Rossini, N., Dassisti, M., Benyounis, K. & Olabi, A. Methods of measuring residual stresses in components. *Mater Design* **35**, 572-588 (2012).

List of publications

- [1] Vitry, P., Bourillot, E., Tetard, L., Plassard, C., Lacroute, Y., Lesniewska, E. (2016). **Mode-Synthesizing Atomic Force Microscopy for volume characterization of mixed metal nanoparticles.** *Journal of Microscopy*.
- [2] Vitry, P., Rebois, R., Bourillot, E., Deniset-Besseau, A., Virolle, M.J., Lesniewska, E., Dazzi, A. (2016). **Combining Infra-Red and Mode-Synthesizing Atomic Force Microscopy: Application to the study of lipid vesicles inside Streptomyces bacteria.** *NanoResearch* 10.1007/s12274-016-1061-6.
- [3] Rocca-Smith, J.C., Karbowiak, T., Marcuzzo, E., Sensidoni, A., Piasente, F., Champion, D., Heintz, O., Vitry, P., Bourillot, E., Lesniewska, E., Debeaufort, F. (2016). **Impact of corona treatment on PLA film properties.** *Polymer Degradation and Stability Journal*.
- [4] Mouawad, O., Vitry, P., Strutynski, C., Picot-Clément, J., Désévéday, F., Gadret, G. & Smektala, F. (2015). **Atmospheric aging and surface degradation in As₂S₃ fibers in relation with suspended-core profile.** *Optical Materials* 44, 25-32.
- [5] Vitry P., Bourillot E., Plassard C., Lacroute Y., Calkins E., Tétard L., Lesniewska E. (2015). **Mode synthesizing atomic force microscopy for 3D reconstruction of embedded low density dielectric nanostructures.** *Nano Research* 8(7), 2199-2205.
- [6] Bourillot, E., Vitry, P., Optasanu, V., Plassard, C., Lacroute, Y., Montessin, T., & Lesniewska, E. (2015). **Solid Solution Characterization in Metal by Original Tomographic Scanning Microwave Microscopy Technique.** *Characterization of Minerals, Metals, and Materials* 2015, 65-72.
- [7] Optasanu, V., Bourillot, E., Vitry, P., Plassard, C., Beurenaut, L., Jacquinet, P. & Montessin, T. (2014). **High-resolution characterization of the diffusion of light chemical elements in metallic components by scanning microwave microscopy.** *Nanoscale*, 6(24), 14932-14938.
- [8] Vitry, P., Bourillot, E., Plassard, C., Lacroute, Y., Tetard, L., & Lesniewska, E. (2014). **Advances in quantitative nanoscale subsurface imaging by mode-synthesizing atomic force microscopy.** *Applied Physics Letters*, 105(5), 053110.
- [9] Bourillot E. , Carriou D. , Vitry P. , Weidmann S. , Aybeke E. , Guzzo J., Lesniewska E. **Direct observation of lipid bilayer protection by small heat shock proteins.** Submitted

Conferences and Contributions

- [1] **P. Vitry**, C. Plassard, L. Tétard, E. Bourillot, E. Lesniewska. Non-invasive observation of intracellular impairments in biological specimen with nanoscale resolution using micro-wave and ultrasound. 28-30 Octobre 2013: GDR Ondes, Dijon, France. – Oral presentation.
- [2] **P. Vitry**, E. Bourillot, V. Optasanu, L. Beurenaut, C. Plassard, P. Jacquinet, T. Montessin, E. Lesniewska. *Solid solution characterization by original tomographic Scanning Microwave Microscopy Technique*. Décembre 2013: Journée de la photonique, Dijon. – Oral presentation.
- [3] E. Lesniewska, **P. Vitry**, M. Ewald, G. Belliot, A. Dazzi, L. Tétard, E. Bourillot. From surface to intracellular non-invasive nanoscale study of bacteria using Mode Synthesizing Atomic Force Microscopy and Scanning Microwave microscopy. 31 Janvier-3 Février 2014: XVI Linz Winter Workshop, Linz, Austria. – Oral presentation.
- [4] **P. Vitry**, E. Bourillot, L. Tétard, C. Plassard, Y. Lacroute, A. Dazzi, E. Lesniewska. *Mode Synthesizing Atomic Force Microscopy for 3D reconstruction*. 16–18 Juin 2014: Conférence AFM Multifrequency Madrid. - Oral presentation.
- [5] E. Lesniewska, **P. Vitry**, L. Tétard, C. Plassard, A. Dazzi, E. Bourillot. *Acoustic, microwave and infrared imaging used for lipids investigations*. 29 Juin – 2 Juillet 2014: ISPM. 16th International Scanning Probe Meeting, Seoul, Corée. – Oral presentation.
- [6] E. Lesniewska, **P. Vitry**, L. Tétard, A. Dazzi, E. Bourillot. *Tomographic multi-frequency microscopy for depth investigation on soft samples*. 19-20 Novembre 2014: BRUKER User's meeting, Reims. – Oral presentation.
- [7] E. Lesniewska, **P. Vitry**, E. Bourillot. *AFM imaging to measure chemical-physics properties at the nanoscale*. Décembre 1-5 2014: Nanothermodynamics Workshop. Leiden, the Netherlands. – Oral presentation.
- [8] **P. Vitry**, E. Bourillot, C. Plassard, Y. Lacroute, L. Tétard, E. Lesniewska. *Study of metallic calibrated defects by subsurface nanoscale imaging*. 15-19 Mars 2015: TMS (The Mineral, Metals and Material Society) Orlando, Floride. – Oral presentation.
- [9] E. Lesniewska, **P. Vitry**, A. Dazzi, L. Tétard, E. Bourillot. *Combining acoustic and spectroscopic measurement to characterization biological entities*. 15-19 Mars 2015: TMS (The Mineral, Metals and Material Society) Orlando, Floride. – Oral presentation.
- [10] E. Bourillot, **P. Vitry**, V. Optasanu, T. Montessin, E. Lesniewska. *Solid solution characterization in metal by original tomographic Scanning Microwave Microscopy Technique*. 15-19 Mars 2015: TMS (The Mineral, Metals and Material Society) Orlando, Floride. – Oral presentation.
- [11] **P. Vitry**, E. Bourillot, R. Selon, E. Lesniewska. *New advances in Scanning Microwave Microscopy*. 23-29 Aout 2015: MCM (Multinational Congress of Microscopy) Eger, Hongrie. – Oral presentation.

- [12] **P. Vitry**, E. Bourillot, R. Selon, Y. Lacroute, A. Dazzi, V. Optasanu, L. Tetard, E. Lesniewska. *Multi-frequency Atomic Force Microscopy*. 03 Décembre 2015: Journée de la photonique, Besançon, France. – Oral presentation.
- [13] E. Lesniewska, **P. Vitry**, M. J. Virolle, A. Dazzi, L. Tetard, E. Bourillot. *Combining AFM-IR and Mode Synthesizing Atomic Force Microscopy: Application to the study of lipid vesicles inside bacteria*. 29 Janvier – 01 Février 2016: Annual Linz Winter Workshop, Linz, Austria. – Oral presentation.
- [14] **P. Vitry**, E. Bourillot, A. Dazzi, L. Tetard, E. Lesniewska. *Multi-frequency atomic force microscopy for tomography analyses*. 02-03 Mars 2016: Florida Chapter AVS, Orlando, Floride. – Oral presentation.
- [15] **P. Vitry**, D. Carriou, E. Bourillot, E. Lesniewska. Caractérisation de bicouches lipidiques supportées par microscopie à force atomique et HS-AFM – Interaction avec la sHSP Lo-18. Septembre 2012: Journée de la photonique de Besançon. – Poster.
- [16] **P. Vitry**, C. Plassard, E. Bourillot, S. Weidmann-Desroche, J. Guzzo, L. Tétard, A. Passian, E. Lesniewska. Characterization of bulk defect by Mode Synthesizing Atomic Force Microscopy – Application to the study of stressed *Oenococcus Oeni* bacteria. 30 Juin – 3 Juillet 2013: Congrès International Scanning Probe Microscopy (ISPM) Dijon. – Poster.
- [17] C. Plassard, E. Bourillot, **P. Vitry**, L. Beurenaut, Y. Lacroute, J. Rossignol, V. Optasanu, T. Montessin, E. Lesniewska. *New tomography technique applied on defects in metal sample based on Scanning Microwave Microscopy*. 30 Juin – 3 Juillet 2013: Congrès International Scanning Probe Microscopy (ISPM) Dijon. – Poster.
- [18] **P. Vitry**, E. Bourillot, L. Tétard, C. Plassard, A. Dazzi, M. Maitre, J. Guzzo, E. Lesniewska. *Mode Synthesizing Atomic Force Microscopy*. Mai 2014: Journée des écoles doctorales Besançon. – Poster.
- [19] **P. Vitry**, R. Rebois, E. Bourillot, L. Tétard, A. Deniset-Besseau, A. Dazzi, E. Lesniewska. *Combining Infra-Red and Mode Synthesizing Atomic Force Microscopy*. Mars 2016 : Conférence AVS Florida Chapter Orlando.- Poster.
- [20] **P. Vitry**, E. Bourillot, A. Dazzi, L. Tétard, E. Lesniewska. *Multi-frequency atomic force microscopy for tomography analysis*. Mars 2016: Conference AVS Florida Chapter Orlando.- Oral presentation.